UNIVERSITY OF CALIFORNIA

Santa Barbara

Heteroepitaxial Design of Long-Wavelength III-Nitride Light-Emitting Diodes

A dissertation submitted in partial satisfaction of the

requirements for the degree

Doctor of Philosophy

in

Materials

by

Cheyenne Lynsky

Committee in charge:

Professor James S. Speck, Chair

Professor Claude Weisbuch

Professor Steven P. DenBaars

Dr. Stacia Keller, Principal Development Engineer

December 2021

The dissertation of Cheyenne Lynsky is approved.

Stacia Keller

Steven P. DenBaars

Claude Weisbuch

James S. Speck, Committee Chair

December 2021

Heteroepitaxial Design of Long-Wavelength III-Nitride Light-Emitting Diodes

by

Cheyenne Lynsky

To my parents, Diane and Rick Lynsky

ACKNOWLEDGEMENTS

During my time at UCSB, I had the privilege to work, learn, and build relationships with countless exceptional individuals. It was these professors, scientists, peers, and friends who challenged me intellectually and supported me day after day. I am forever grateful for the opportunity graduate school gave me to expand my knowledge and grow both professionally and personally.

I would like to first thank my committee members for their guidance and support over the years. To my advisor, Jim Speck, who never ceased to impress me with his dedication to his research and students. Despite advising many students on a wide range of projects and traveling around the world for meetings and presentations, Jim always made time to answer my questions and guide my research. After just one interaction with Jim, it becomes immediately obvious that he has both incredible passion and determination. His rigorous pursuit of scientific knowledge and willingness to dissect every technical detail, set an exceptional example for all his students. This same commitment to scientific excellence can be said for Claude Weisbuch. Claude's vast knowledge of semiconductor physics, and desire to share with and teach students, made him an invaluable committee member. I am appreciative of the time and attention he gave to my research. Steve DenBaars expertise in MOCVD and enthusiasm for new ideas heavily shaped my research experience. He was always available to listen to my challenges related to growth or fabrication and was quick with a list of suggestions. In addition to his academic experience, Steve's business acumen and knowledge of technology are instrumental for helping his students to understand the scope of their research. Lastly, Stacia Keller's knowledge of MOCVD is unparalleled and I am so grateful for her desire to impart that knowledge on others. Her ability to locate data

and papers in her vast office library spanning decades of research will always amaze me. Stacia's approachability and scientific curiosity opened the door for many valuable conversations.

In addition to my committee members, I would like to acknowledge professors at UCSB that I had the pleasure of working with, including Shuji Nakamura, Umesh Mishra, and Mike Gordon. I also had the opportunity to participate in several collaborations. Thank you to Professors Saulius Marcinkevičius, Ramūnas Aleksiejūnas, Jacques Peretti, and Yuhrenn Wu as well as researchers Rinat Yapparov, Wiebke Hahn, and Mylène Sauty for performing countless experiments on my samples and for sharing your knowledge of semiconductor physics.

The staff and research scientists at UCSB were paramount to my research and academic progress. Thank you to Mike Iza, David Whitlatch, Brian Carralejo, and Stacia Keller for running the MOCVD lab and assisting the researchers who use it. To say the MOCVD lab is demanding to run is an understatement. To Mike Iza, I enjoyed chatting with you in lab and getting to know you over the years. Thank you for your support, in a multitude of ways, and for always being the calm in the storm that is sometimes graduate school. Within SSLEEC I also want to acknowledge Dan Cohen and Tal Margalith for their questions during meetings and management of the group. The Materials Department and SSLEEC staff members went above and beyond to be helpful over the years, thank you to Jocelyn Guzman, Alex Huddleston, Tawny Hernandez, Yukina Warner, Emi Sautot, and Tara Owens.

Materials characterization was one of my favorite aspects of research and I was fortunate to have access to exceptional facilities. The X-ray and microscopy staff members,

Youli Li, Miguel Zepeda-Rosales, Tom Mates, Aidan Taylor, and Claire Chisholm, played a critical role in keeping these facilities running. Special thanks go to Tom Mates for patiently teaching me how to do SIMS characterization and to Feng Wu for your excellent TEM characterization of my materials. Thank you to the many members of the nanofabrication staff who keep the fab running smoothly and support an impressive number and variety of research projects.

To my fellow MO5 growers, past and present, Yi Chao Chow, Pavel Shapturenka, Caroline Reilly, Jared Kearns, Ryan White, Jake Ewing, Panpan Li, Shubhra Pasayat, Ryan Anderson, Vineeta Muthuraj, we shared many experiences together and I am grateful to have had such wonderful lab mates. I had the opportunity to work closely with Yi Chao Chow, Jake Ewing, Ryan White, and Abdullah Alhassan and they have all made innumerable scientific contributions to the work presented in this dissertation. In particular, Jake Ewing contributed significantly to the epitaxial growth, device processing, and device characterization presented in Chapter 6. There were many other students and post-docs with whom I enjoyed both scientific and unscientific conversations, including Wan Ying Ho, Clayton Qwah, Camille Pivard, Ryan Ley, Matt Wong, Chris Zollner, Akhil Mauze, Kelsey Jorgensen, Jianfeng Wang, Phillip Chan, Nate Palmquist, Morteza Monavarian and many more. I would like to thank several past SSLEEC students who mentored and befriended me, Andrew Espenlaub, David Hwang, Daniel Myers, Abdullah Alhassan, and Thomas Malkowski. I must give a special acknowledgement to the post-docs I worked with, Guillaume Lheureux and Bastien Bonef. I am appreciative of not only their technical guidance, but also their life advice, positivity, and support.

I would like to thank the close friends I made in Santa Barbara, including Lesley Chan, Simone Tommaso Suran Brunelli, Chris Pynn, Brian Markman, Monica Volk, The Ranch, and the Italian espresso crew. I cannot imagine graduate school or my life without you.

Lastly, I must thank my family and loved ones. I want to acknowledge my grandmother Rosemary, whose commitment to education and perseverance to obtain a degree paved the way for me. My brother Ryan has always been my biggest cheerleader and I am so thankful for his positive energy and big heart. To Erik, thank you for supporting me throughout this journey, from near and far. Your optimistic attitude, ingenuity, and passion continue to amaze me. I am grateful to have had you by my side encouraging me to pursue my goals. To my parents, Rick and Diane, I have you to thank most of all. I could not have made it here without your unwavering love and support.

CURRICULUM VITAE

Cheyenne Lynsky

EDUCATION

University of California, Santa Barbara – Santa Barbara, CA *December 2021*
Ph.D., Materials
Advisor: Professor James S. Speck

Northwestern University – Evanston, IL *June 2015*
B.S., Materials Science and Engineering

EXPERIENCE

University of California, Santa Barbara – Santa Barbara, CA *2016 – Present*
Graduate Student Researcher, Speck Laboratory

IM Flash Technologies, LLC – Lehi, UT *2015 – 2016*
Process Engineer – Real-time Defect Analysis

Northwestern University – Chicago, IL *2013 – 2015*
Undergraduate Research Assistant, Stupp Laboratory

Dynamic Biosensors GmbH – Munich, Germany *2015*
Undergraduate Intern

University of Colorado Boulder – Boulder, CO *2014*
NSF Undergraduate Researcher, Schwartz Laboratory

Medtronic – Minneapolis, MN *2013*
Materials Engineering Summer Associate

PUBLICATIONS

F. Wu, **C. Lynsky**, J. Ewing, M. Iza, S. Nakamura, S. P. DenBaars, and J. S. Speck, "Structure of V-defects in long wavelength GaN-based light emitting diodes," *In Preparation*.

C. Lynsky, G. Lheureux, B. Bonef, K. S. Qwah, R. C. White, S. P. DenBaars, S. Nakamura, Y.-R. Wu, C. Weisbuch, and J. S. Speck, "Improved vertical carrier transport for green III-nitride LEDs using InGaN alloy quantum barriers," *Submitted*.

C. Lynsky, R. C. White, Y. C. Chow, W. Y. Ho, S. Nakamura, S. P. DenBaars, and J. S. Speck, "Role of V-defect density on the performance of III-nitride green LEDs on sapphire substrates," J. Cryst. Growth **560–561**, 126048 (2021).

Y. C. Chow, **C. Lynsky**, F. Wu, S. Nakamura, S. P. DenBaars, C. Weisbuch, and J. S. Speck, "Reduction of efficiency droop in c-plane InGaN/GaN light-emitting diodes using a thick single quantum well with doped barriers," Appl. Phys. Lett. **119**(22), 221102 (2021).

R. C. White, H. Li, M. Khoury, **C. Lynsky**, M. Iza, S. Keller, D. Sotta, S. Nakamura, and S. P. DenBaars, "InGaN-Based microLED Devices Approaching 1% EQE with Red 609 nm Electroluminescence on Semi-Relaxed Substrates," Crystals **11**(11), 1364 (2021).

R. C. White, M. Khoury, M. S. Wong, H. Li, **C. Lynsky**, M. Iza, S. Keller, D. Sotta, S. Nakamura, and S. P. DenBaars, "Realization of III-Nitride c-Plane microLEDs Emitting from 470 to 645 nm on Semi-Relaxed Substrates Enabled by V-Defect-Free Base Layers," Crystals **11**(10), 1168 (2021).

P. Li, H. Li, H. Zhang, **C. Lynsky**, M. Iza, J. S. Speck, S. Nakamura, and S. P. DenBaars, "Size-independent peak external quantum efficiency (>2%) of InGaN red micro-light-emitting diodes with an emission wavelength over 600 nm," Appl. Phys. Lett. **119**(8), 081102 (2021).

S. Marcinkevičius, R. Yapparov, Y. C. Chow, **C. Lynsky**, S. Nakamura, S. P. DenBaars, and J. S. Speck, "High internal quantum efficiency of long wavelength InGaN quantum wells," Appl. Phys. Lett. **119**(7), 071102 (2021).

P. Li, H. Li, Y. Yao, H. Zhang, **C. Lynsky**, K. S. Qwah, M. Iza, J. S. Speck, S. Nakamura, S. Nakamura, S. P. DenBaars, and S. P. DenBaars, "Fully transparent metal organic chemical vapor deposition-grown cascaded InGaN micro-light-emitting diodes with independent junction control," Opt. Express, OE **29**(14), 22001–22007 (2021).

P. Li, H. Li, Y. Yao, H. Zhang, **C. Lynsky**, K. S. Qwah, J. S. Speck, S. Nakamura, and S. P. DenBaars, "Demonstration of high efficiency cascaded blue and green micro-light-emitting diodes with independent junction control," Appl. Phys. Lett. **118**(26), 261104 (2021).

C. Lynsky, A. I. Alhassan, G. Lheureux, B. Bonef, S. P. DenBaars, S. Nakamura, Y.-R. Wu, C. Weisbuch, and J. S. Speck, "Barriers to carrier transport in multiple quantum well nitride-based c-plane green light emitting diodes," Phys. Rev. Materials **4**(5), 054604 (2020).

G. Lheureux, **C. Lynsky**, Y.-R. Wu, J. S. Speck, and C. Weisbuch, "A 3D simulation comparison of carrier transport in green and blue c-plane multi-quantum well nitride light emitting diodes," J. Appl. Phys. **128**(23), 235703 (2020).

R. Yapparov, Y. C. Chow, **C. Lynsky**, F. Wu, S. Nakamura, J. S. Speck, and S. Marcinkevičius, "Variations of light emission and carrier dynamics around V-defects in InGaN quantum wells," J. Appl. Phys. **128**(22), 225703 (2020).

R. Yapparov, **C. Lynsky**, S. Nakamura, J. S. Speck, and S. Marcinkevičius, "Optimization of barrier height in InGaN quantum wells for rapid interwell carrier transport and low nonradiative recombination," Appl. Phys. Express **13**(12), 122005 (2020).

R. Aleksiejūnas, K. Nomeika, O. Kravcov, S. Nargelas, L. Kuritzky, **C. Lynsky**, S. Nakamura, C. Weisbuch, and J. S. Speck, "Impact of Alloy-Disorder-Induced Localization on Hole Diffusion in Highly Excited c-Plane and m-Plane (In,Ga)N Quantum Wells," Phys. Rev. Applied **14**(5), 054043 (2020).

S. S. Pasayat, R. Ley, C. Gupta, M. S. Wong, **C. Lynsky**, Y. Wang, M. J. Gordon, S. Nakamura, S. P. Denbaars, S. Keller, and U. K. Mishra, "Color-tunable <10 μm square InGaN micro-LEDs on compliant GaN-on-porous-GaN pseudo-substrates," Appl. Phys. Lett. **117**(6), 061105 (2020).

M. S. Wong, J. A. Kearns, C. Lee, J. M. Smith, **C. Lynsky**, G. Lheureux, H. Choi, J. Kim, C. Kim, S. Nakamura, J. S. Speck, and S. P. DenBaars, "Improved performance of AlGaInP red micro-light-emitting diodes with sidewall treatments," Opt. Express **28**(4), 5787 (2020).

R. Freeman, M. Han, Z. Álvarez, J. A. Lewis, J. R. Wester, N. Stephanopoulos, M. T. McClendon, **C. Lynsky**, J. M. Godbe, H. Sangji, E. Luijten, and S. I. Stupp, "Reversible self-assembly of superstructured networks," Science **362**(6416), 808–813 (2018).

PATENTS

M. Monavarian, C. Weisbuch, **C. Lynsky**, G. Lheureux, J.S Speck, "Methods of volumetric hole injection via intentional V-defects in InAlGaN light-emitting diodes," US Patent Application UC Case No. 2020-058, 2019, (Filed).

PRESENTATIONS

C. Lynsky, G. Lheureux, F. Wu, Y. C. Chow, R. C. White, B. Bonef, S. P. DenBaars, S. Nakamura, Y.-R. Wu, C. Weisbuch, and J. S. Speck, "High Performance Green LEDs for Solid-State Lighting," presented at DOE Lighting R&D Workshop, Virtual (January 2021).

C. Lynsky, G. Lheureux, Y. C. Chow, R. C. White, B. Bonef, S. P. DenBaars, S. Nakamura, Y.-R. Wu, C. Weisbuch, and J. S. Speck, "High Performance Green LEDs for Solid-State Lighting," poster presented at DOE Lighting R&D Workshop, San Diego, CA (January 2020).

C. Lynsky, G. Lheureux, A. I. Alhassan, B. Bonef, R. C. White, S. Nakamura, S. P. Den Baars, Y.-R. Wu, C. Weisbuch, and J. S. Speck, "Contribution of polarization-induced barriers to excess forward voltage in c-plane green LEDs," presented at 13th International Conference on Nitride Semiconductors 2019 (ICNS-13), Bellevue, WA (July 2019).

C. Lynsky, R. C. White, G. Lheureux, B. Bonef, A. I. Alhassan, C. Weisbuch, S. P. DenBaars, S. Nakamura, and J. S. Speck, "High Performance Green LEDs for Solid-State Lighting," poster presented at DOE Lighting R&D Workshop, Dallas, TX (January 2019).

C. Lynsky, R. C. White, A. I. Alhassan, G. Lheureux, C. Weisbuch, S. P. DenBaars, S. Nakamura, and J. S. Speck, "Epitaxial Design of c-plane Green LEDs with Reduced Forward Voltage," poster presented at Solid State Lighting and Energy Electronics Center Annual Review, Santa Barbara, CA (November 2018).

HONORS AND AWARDS

Outstanding Graduate Student Research Achievement Award, Solid State Lighting and Energy Electronics Center (2021)

Magna Cum Laude, McCormick School of Engineering, Northwestern University (2015)

Departmental Honors, Materials Science and Engineering, Northwestern University (2015)

3rd Place Award, ASM International Undergraduate Design Competition (2014)

Tom McAuley Undergraduate Academic Achievement Scholarship, Northwestern University (2012)

ABSTRACT

Heteroepitaxial Design of Long-Wavelength III-Nitride Light-Emitting Diodes

by

Cheyenne Lynsky

The group III-nitride material system has emerged as the preferred choice for a wide range of semiconductor optoelectronic applications, ranging from light-emitting diodes (LEDs) for general illumination to red-green-blue micro-LEDs for next generation displays. Properties such as direct bandgaps spanning the visible spectrum, high defect tolerance, and excellent efficiency make InGaN-based LEDs attractive for replacing conventional lighting and display technologies. However, the optical and electrical efficiency decreases significantly when increasing the emission wavelength of nitride LEDs from blue to red, which can be explained in part by materials quality degradation and larger polarization-induced electric fields.

This dissertation focuses on the epitaxial growth and characterization of long-wavelength group III-nitride LEDs emitting in the green to red spectral range. The origin of low electrical efficiency in *c*-plane green LEDs is first explored using a combined experimental and simulation-based approach. LEDs are grown using metal organic chemical vapor deposition, fabricated into devices, and electrically tested. Three-dimensional LED device simulations based on the Localization Landscape theory of disorder are then conducted to relate nitride materials properties to device performance. These studies

demonstrate that polarization barriers at the GaN/InGaN interface and sequential filling of quantum wells (QWs) contribute to the low electrical efficiency in green LEDs.

The use of InGaN quantum barriers (QBs) is introduced as an approach to overcome barriers to carrier transport in green LEDs. Structures incorporating InGaN QBs have a reduced polarization discontinuity at the QW/QB interface and contribute an additional source of alloy disorder. Through experiments and three-dimensional simulations, it is shown that InGaN QBs improve electrical efficiency and introduce preferential pathways for vertical transport through regions of high indium content. Next, an approach using engineered V-defects, which have lower total polarization discontinuities for InGaN/GaN interfaces than *c*-plane, is proposed to mitigate polarization-induced potential barriers in green LEDs. Lastly, efforts to improve green LED performance are extended to red micro-LEDs, where materials degradation and polarization-induced electric fields become more severe. The results presented in this dissertation expand the understanding of long-wavelength LED efficiency and provide a path to realize high-performance green and red LEDs and micro-LEDs through careful heteroepitaxial growth and design.

TABLE OF CONTENTS

1

Introduction

1.1 Solid-State III-Nitride LEDs

The technological importance of light-emitting diodes (LEDs) cannot be fully appreciated without reflecting on the evolution of lighting technology throughout human history. Beginning first with the burning of wood, early methods of lighting included oil lamps, candles, kerosene, and gas. With the invention of electricity came filament incandescent lamps and then gas discharge (or fluorescent) lamps. Each new technology was accompanied by improvements in the efficiency and quality of the light source along with reductions in the cost. LEDs were the first lighting technology to rely on electroluminescence, which is the direct conversion of electricity into light. The LED was invented by Oleg Vladimirovich Lossev in the early 1920s when he observed light emission from direct biasing of silicon carbide and in 1928, he published these observations [1]. As material purity and the understanding of semiconductor physics improved, so did LED efficiency.

LEDs with different emission wavelengths were demonstrated on a variety of semiconductor materials; however, it was the invention of blue LEDs by Shuji Nakamura in 1993 that ultimately led to the widespread use of solid-state LEDs for white lighting [2,3]. To achieve white light, a blue LED is coated with a phosphor material which absorbs some

of the blue light and re-emits broad yellow luminescence. The combined broad-spectrum yellow and blue light creates the appearance of white light to the human eye. Even with some efficiency loss due to color conversion, LED lamps are more efficient than conventional incandescent lamps by a factor of 10 to 15. Additionally, the small size, low cost, and long lifetimes of solid-state lamps have made lights available to people across the world who previously lacked access. For additional information on the history of lighting and development of blue LEDs, see Refs [4] and [5].

The group III-nitrides, which consist of aluminum nitride (AlN), gallium nitride (GaN), indium nitride (InN), and their alloys, are the class of direct bandgap semiconductors that enabled efficient solid-state lighting. Further background on group III-nitride materials will be presented in Chapter 2. In blue LEDs, the active material that emits light is $In_xGa_{1-x}N$, where the fraction of indium x is approximately 0.15. The focus of this dissertation, however, is on LEDs that emit in the green spectral range and longer wavelengths. In the following sections, the primary technologies driving long-wavelength LED development are presented.

1.2 Motivation

1.2.1 Color-mixed White Lighting

Efficient solid-state lighting was enabled by blue LEDs combined with a phosphor downconverter material, such as cerium-doped yttrium aluminum garnet (Ce:YAG). Phosphor converted LEDs (pc-LEDs) are still the dominant architecture used for white LED lighting today due to their relative simplicity, temperature robustness, and color stability. The efficiency of an LED package is typically described in units of photopic lumens of light

(lm) created per input electrical watt (W). LEDs can be further characterized by their correlated color temperature (CCT), where cool white has a CCT of 5700 K and warm white has a CCT of 3000–3500 K. In 2019, the luminous efficacy of cool white and warm white pc-LEDs at 35 A cm^{-2} were approximately 185 lm/W and 165 lm/W [6], respectively, which is significantly higher than the 50–70 lm/W of a typical compact fluorescent lamp. However, phosphor down-conversion of a blue pump LED leads to significant Stokes losses, resulting in a predicted upper limit of ~250 lm/W for pc-LEDs [6]. Stokes loss in pc-LEDs is the energy loss in the form of heat that occurs during absorption of a high energy blue photon and subsequent emission of a lower energy photon.

Alternatively, color-mixed LEDs (cm-LEDs) produce white light from red, green, blue, and amber (RGBA) LEDs and have a higher expected luminous efficacy limit of 325 lm/W [6]. The cm-LED architecture also enables full-color-tuning where the CCT and chromaticity can be controlled. As the understanding of light science and the impact of light on human physiology improves, the demand for such tunable lights is likely to increase. Despite their significant potential, cm-LEDs currently have luminous efficacy values closer to 115 lm/W [6]. The poor performance of cm-LEDs relative to pc-LEDs is attributed to the low efficiency of direct green and amber emitters. To achieve higher efficiency LED lamps with improved tunability, continued development of solid-state green and amber LEDs is essential. For more on the status of solid-state lighting technology today and R&D opportunities, see Ref [6].

1.2.2 Display Technology

With high brightness, low power consumption, long lifetimes, and excellent stability, solid-state LEDs are attractive for use in next-generation displays. Displays using solid-state LEDs with dimensions less than 100 μm, known as micro-LEDs (or μLEDs) for the red-green-blue (RGB) pixels have many advantages over incumbent technologies, namely thin-film-transistor liquid crystal displays (TFT-LCDs) and organic LED (OLED) displays. To produce an image, modern TFT-LCDs rely on a matrix of liquid crystals, a solid-state LED backlight, and a series of polarizers and color filters; the polarizers and filters severely reduce the overall display efficiency. OLED displays emerged as an alternative to TFT-LCDs and are now found in a variety of consumer electronics, including smartphones and TVs. Because OLED pixels are self-emissive, have independent color emission, and can be individually turned on and off, they offer improved efficiency, color contrast, and blacks over TFT-LCDs.

However, displays incorporating μLEDs offer most of the benefits of OLEDs with the addition of having higher brightness, improved environmental stability, longer lifetimes, lower power consumption, faster response times, and wider color gamut. Perhaps the most significant advantage that OLEDs retain over μLEDs are their relatively facile manufacturability using vacuum deposition or solution processing (i.e., printing) methods. The assembly of μLEDs into arrays has proven to be a difficult technological challenge [7]. Mass transfer, also known as “pick-and-place”, technologies include laser lift-off, fluidic assembly, electrostatic array, and elastomer stamp and can be used for direct view TV or smartphone displays. For smaller, high-pixel density displays, monolithic fabrication methods are also an attractive approach. Other device level challenges exist for μLEDs [8],

such as the reduction in external quantum efficiency with size and achieving high efficiency across all wavelengths, which will be discussed in more detail in Chapter 6.

Despite possessing many of the desired characteristics of a superior display, μLEDs have yet to appear in the consumer electronic market. μLEDs are still a nascent technology compared to TFT-LCDs and OLEDs, but investments by companies such as Apple and Meta, and wall-size TVs offered by LG and Samsung, signal the relevance of μLED technology for next-generation displays.

1.3 Overview of Subsequent Chapters

This dissertation focuses on the growth and characterization of long-wavelength group III-nitride LEDs emitting in the green to red spectral range. Specific attention is given to understanding and improving the electrical efficiency in *c*-plane green LEDs. The experience gained during metal organic chemical vapor deposition (MOCVD) growth of green-emitting devices is then applied to realize high efficiency red LEDs.

Chapter 2 will provide necessary background information for this dissertation, including an introduction to the group III-nitride material system, semiconductor *p-n* junctions, LED device operation, and MOCVD growth. The role of alloy disorder in III-nitrides will also be discussed along with a high-level overview of the Localization Landscape theory of disorder [9-11] and the 3D drift-diffusion charge control (3D-DDCC) solver [12,13]. Chapter 3 will present a combined experimental and computational approach to explore the impact of quantum well (QW) number on forward voltage V_F in *c*-plane green LEDs. Chapter 4 will introduce $In_xGa_{1-x}N$ quantum barriers as an approach to overcome barriers to carrier transport in green LEDs; their impact on electrical device properties will

be examined computationally and experimentally. Chapter 5 will discuss V-defect engineering on sapphire substrates as another means to improve carrier transport and thus device efficiency. Chapter 6 will present the development of red μLEDs on silicon substrates, including epitaxial optimization, advanced materials characterization, and device results. Lastly, Chapter 7 will summarize the key conclusions from this dissertation and present recommendations for future work.

References

[1] O.V. Lossev, The London, Edinburgh, and Dublin Philosophical Magazine and Journal of Science **6**, 1024 (1928).

[2] S. Nakamura, M. Senoh, and T. Mukai, Jpn. J. Appl. Phys. **32**, L8 (1993).

[3] S. Nakamura, T. Mukai, and M. Senoh, Appl. Phys. Lett. **64**, 1687 (1994).

[4] C. Weisbuch, Comptes Rendus Physique **19**, 89 (2018).

[5] D. Feezell and S. Nakamura, Comptes Rendus Physique **19**, 113 (2018).

[6] DOE BTO Lighting R&D Program, "*2019 Lighting R&D Opportunities*".

[7] K. Ding, V. Avrutin, N. Izyumskaya, Ü. Özgür, and H. Morkoç, Applied Sciences **9**, 1206 (2019).

[8] J.J. Wierer and N. Tansu, Laser & Photonics Reviews **13**, 1900141 (2019).

[9] M. Filoche and S. Mayboroda, PNAS **109**, 14761 (2012).

[10] M. Filoche, M. Piccardo, Y.-R. Wu, C.-K. Li, C. Weisbuch, and S. Mayboroda, Phys. Rev. B **95**, 144204 (2017).

[11] D.N. Arnold, G. David, D. Jerison, S. Mayboroda, and M. Filoche, Phys. Rev. Lett. **116**, 056602 (2016).

[12] C.-K. Li, M. Piccardo, L.-S. Lu, S. Mayboroda, L. Martinelli, J. Peretti, J.S. Speck, C. Weisbuch, M. Filoche, and Y.-R. Wu, Phys. Rev. B **95**, 144206 (2017).

[13] See http://yrwu-wk.ee.ntu.edu.tw/ for "Optoelectronic device simulation laboratory".

2

Background

2.1 Group III-Nitride Materials

The prominence of group III-nitride materials, (Al,Ga,In)N, in a wide range of commercially available technologies can be attributed to their unique materials properties. Because this dissertation is focused on III-nitrides for LEDs, the focus here will be on the properties that are technologically relevant for optoelectronic applications. Specifically, (Al,Ga,In)N materials have the following properties of interest: a wide range of bandgap energies, direct bandgaps, Type I heterojunction band alignment, a wurtzite crystal structure, and internal polarization.

The direct bandgaps of the III-nitrides range from ~0.7 eV for InN to ~6.2 eV for AlN, with GaN having an intermediate bandgap of 3.4 eV. These bandgap energies correspond to wavelengths ranging from 1.8 μm (infrared) to 200 nm (mid-ultraviolet), meaning the entire visible portion of the electromagnetic spectrum can be realized. Using alloys of the binary compounds, such as $In_xGa_{1-x}N$ and $Al_yGa_{1-y}N$, allows for the bandgap to be tuned to intermediate values. (Al,Ga,In)N materials also possess direct bandgaps which is an important property for achieving efficient light-emitting devices, such as LEDs and laser diodes. In a direct bandgap semiconductor, the minimum energy state of the conduction band (CB) and the maximum energy state of the valence band (VB) occur at the same

crystal momentum, or k-vector. Radiative recombination occurs when an electron in the CB fills an empty VB state (hole) and the energy difference between the initial and final states is emitted as a photon. The requirement of particles to satisfy conservation of crystal momentum means that radiative recombination will be an efficient process in direct bandgap materials but an inefficient process in indirect bandgap materials, where radiative recombination involves absorption or emission of a phonon.

Heterojunctions, which are the interface between dissimilar semiconductors, are widely used to engineer III-V solid-state electronics, where a device consisting of multiple heterojunctions is known as a heterostructure [1,2]. Heterojunctions can be classified based on their band alignment as Type I (straddling gap), Type II (staggered gap), or Type III (broken gap), as shown in Fig. 2.1. (Al,Ga,In)N materials have Type I band alignments, which enable the formation of quantum well heterostructures and therefore efficient LEDs, as will be discussed later in this chapter.

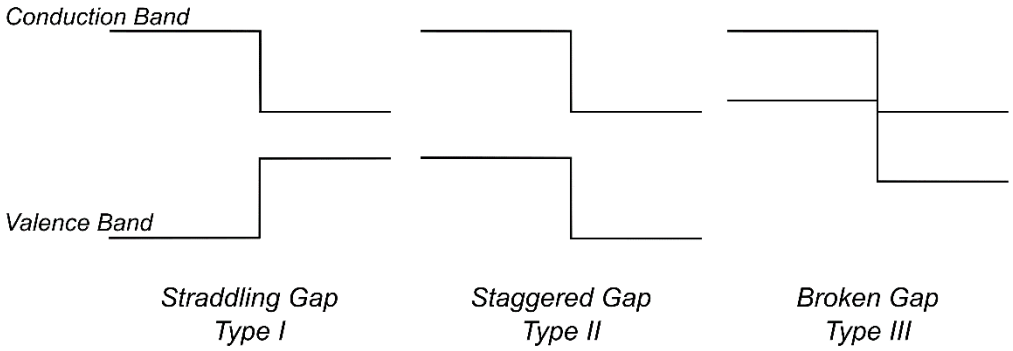

Figure 2.1. Heterojunction band alignments of (a) Type I (straddling gap), (b) Type II (staggered gap), and (c) Type III (broken gap).

Binary compounds in the III-nitride material system can exhibit a wurtzite or zinc blende crystal structure. Because zinc blende is less thermodynamically stable and is rarely

used in applications, this dissertation will be limited to the discussion of wurtzite (Al,Ga,In)N. Wurtzite is a hexagonal crystal system where for III-nitride materials each group III atom is tetrahedrally coordinated to four nitrogen atoms, and vice versa, as shown in Fig. 2.2. The wurtzite structure *appears* as close packed on the (0001) planes, where the (0001) planes consist of group III-N bilayers (formally, wurtzite is not a close packed structure due to the tetrahedral coordinate of each constituent atom). The (0001) stacking sequence is ABABAB, where A and B refer to III-N bilayers. The a lattice parameters for AlN, GaN, and InN are 3.112 Å, 3.189 Å, and 3.54 Å, respectively. Vegard's law [3] can be used to calculate the lattice parameters for $In_xGa_{1-x}N$ and $Al_yGa_{1-y}N$ alloys:

$$a_{InGaN} = x \cdot a_{InN} + (1 - x) \cdot a_{GaN}, \tag{2.1}$$

$$a_{AlGaN} = y \cdot a_{AlN} + (1 - y) \cdot a_{GaN}. \tag{2.2}$$

Pseudomorphic epitaxial growth is the growth of a single-crystal film on a different single-crystal film such that the atomic bonds remain fully coherent. During pseudomorphic growth of InGaN or AlGaN thin films on GaN, the film experiences biaxial compressive or tensile stress, respectively, due to lattice mismatch with the underlying crystal. Compressive or tensile plane stress results in either expansion or compression, respectively, along the *c*-axis, according to the Poisson effect. The large difference between the a lattice parameter of InN and GaN results in significant biaxial compressive stress and in practice limits the ability to grow high quality InGaN films.

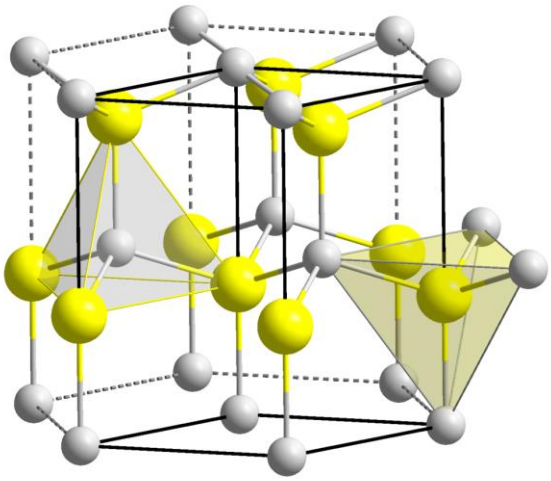

Figure 2.2. Wurtzite crystal structure of group III-nitride materials. Group III atoms are shown in yellow and nitrogen atoms are shown in grey. The tetrahedral coordination of atoms is highlighted as yellow and grey polyhedra.

The 6mm point group and $P6_3mc$ space group symmetry of wurtzite GaN is non-centrosymmetric, meaning it lacks an inversion center, and can be further classified as a polar crystallographic point group. A lack of inversion symmetry gives rise to interesting physical properties in GaN, namely, spontaneous electrical polarization $\mathbf{P}^{sp}$ and strain-induced piezoelectric polarization $\mathbf{P}^{pz}$. As previously described, lattice mismatch between (Al,Ga,In)N leads to strain in the film and therefore strain-induced piezoelectric polarization. From the strain distribution, $\mathbf{P}^{pz}$ can be evaluated by

$$\mathbf{P}^{pz} = [\mathbf{e}] \cdot [\varepsilon] = \begin{bmatrix} e_{15}\varepsilon_{xz} \\ e_{15}\varepsilon_{yz} \\ e_{31}(\varepsilon_{xx} + \varepsilon_{yy}) + e_{33}\varepsilon_{zz} \end{bmatrix}, \tag{2.3}$$

where ε_{xx}, ε_{yy}, ε_{zz} are normal strains and ε_{xy}, ε_{yz}, ε_{zx} are shear strains. e_{15}, e_{31}, e_{33} are the piezoelectric coefficients (Table 2.1) from the piezoelectric tensor, where the other tensor

terms are zero due to the 6mm point symmetry for the wurtzite crystal structure. The spontaneous polarization $\mathbf{P}^{sp}$ values, as related to the GaN buffer layer, are calculated from

$$\mathbf{P}^{sp} = ax + b(1-x) + cx(1-x), \tag{2.4}$$

where a, b, and c are coefficients given in Table 2.1 and x is the alloy composition of $In_xGa_{1-x}N$ or $Al_xGa_{1-x}N$. Both $\mathbf{P}^{sp}$ and $\mathbf{P}^{pz}$ are directed along the polar [0001] axis of the wurtzite crystal structure and the total polarization is given by $\mathbf{P}^{total}(\mathbf{r}) = \mathbf{P}^{pz} + \mathbf{P}^{sp}$.

Table 2.1. Piezoelectric polarization coefficients for GaN, InN, and AlN and spontaneous polarization coefficients for InGaN and AlGaN alloys [4,5].

Piezoelectric	$\boldsymbol{e_{15}}$ **(C cm^{-2})**	$\boldsymbol{e_{31}}$ **(C cm^{-2})**	$\boldsymbol{e_{33}}$ **(C cm^{-2})**
GaN	-0.40	-0.49	0.73
InN	-0.40	-0.49	0.73
AlN	-0.48	-0.58	1.55
Spontaneous	$\boldsymbol{a}$ **(C cm^{-2})**	$\boldsymbol{b}$ **(C cm^{-2})**	$\boldsymbol{c}$ **(C cm^{-2})**
InGaN alloy	-0.042	-0.034	0.037
AlGaN alloy	-0.090	-0.034	0.021

The presence of polarization means that different planes in a GaN crystal will exhibit different properties. Polar planes include Ga-polar (0001) and N-polar $(000\bar{1})$, with (0001) *c*-plane being the most common orientation for GaN LED growth. Nonpolar $\{11\bar{2}0\}$ *a*-plane and $\{1\bar{1}00\}$ *m*-plane are oriented perpendicular to the *c*-plane and the various semipolar planes are oriented with an inclination angle θ between 0° and 90°. Examples of different GaN growth planes are shown in Fig. 2.3.

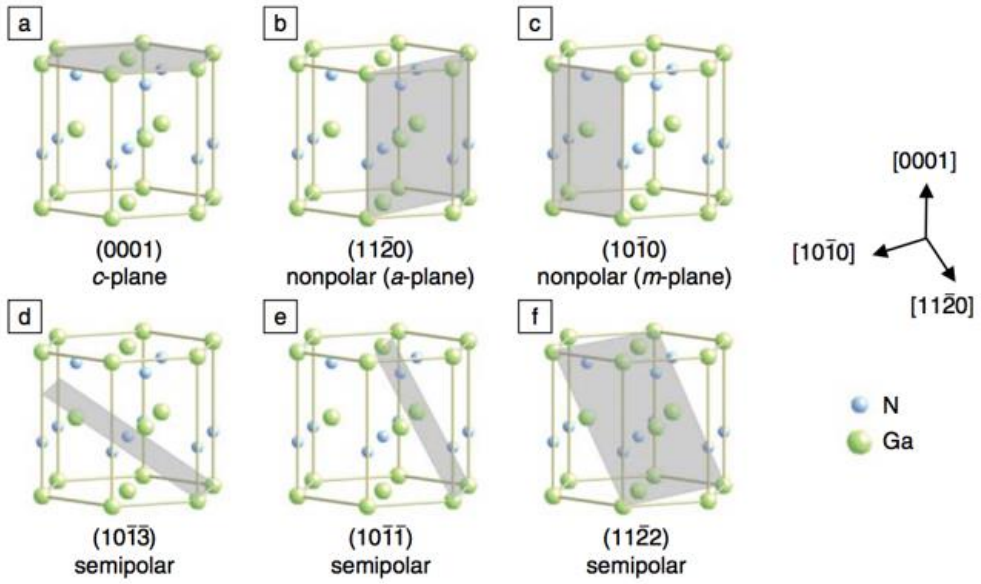

Figure 2.3. Schematic of GaN wurtzite crystal structures where the planes highlighted are the (a) polar *c*-plane, (b) nonpolar *a*-plane, (c) nonpolar *m*-plane, and (d-f) semipolar planes. Reprinted by permission from Springer Nature Customer Service Centre GmbH: Springer Nature MRS Bulletin [6], Copyright 2009.

Discontinuities in spontaneous and piezoelectric polarization at interfaces and surfaces are formed during pseudomorphic growth of III-nitride heterostructures. Taking the divergence of the total polarization $\mathbf{P}^{total}(\mathbf{r})$ over the entire domain gives the fixed polarization charge $\rho_{pol}(\mathbf{r})$,

$$\nabla \cdot \mathbf{P}^{total}(\mathbf{r}) = \rho_{pol}(\mathbf{r}). \tag{2.5}$$

Figure 2.4 shows the fixed polarization charges that form depending on orientation (Ga-polar or N-polar) and whether the stress in the film is compressive (i.e., InGaN on GaN) or tensile (i.e., AlGaN on GaN). Also shown in this figure are the directions of the spontaneous and piezoelectric polarization, along with the direction of the corresponding electric field. The orientation and film properties will therefore determine whether $\mathbf{P}^{sp}$ and

$\mathbf{P}^{pz}$ are in the same or opposite directions. For most commercially available visible LEDs, the heterostructures consist of InGaN films grown on GaN in the Ga-polar orientation, leading to $\mathbf{P}^{sp}$ and $\mathbf{P}^{pz}$ pointing in opposite directions. Using constants obtained by Bernardini *et al.*, piezoelectric fields as large as 3.5 MV/cm have been predicted in $In_{0.2}Ga_{0.8}N$ grown on polar GaN [7,8]. The difference between $\mathbf{P}^{pz}_{GaN}$ and $\mathbf{P}^{pz}_{InN}$ is defined as $\Delta\mathbf{P}^{pz}$ and similarly the difference between $\mathbf{P}^{sp}_{GaN}$ and $\mathbf{P}^{sp}_{InN}$ is defined as $\Delta\mathbf{P}^{sp}$. For InGaN films on GaN, $\Delta\mathbf{P}^{pz}$ has a much larger magnitude than $\Delta\mathbf{P}^{sp}$ due to the small difference between the spontaneous polarization in GaN (–0.029 C m^{-2}) and InN (–0.032 C m^{-2}). The implications of polarization on device design and performance will be discussed throughout this dissertation.

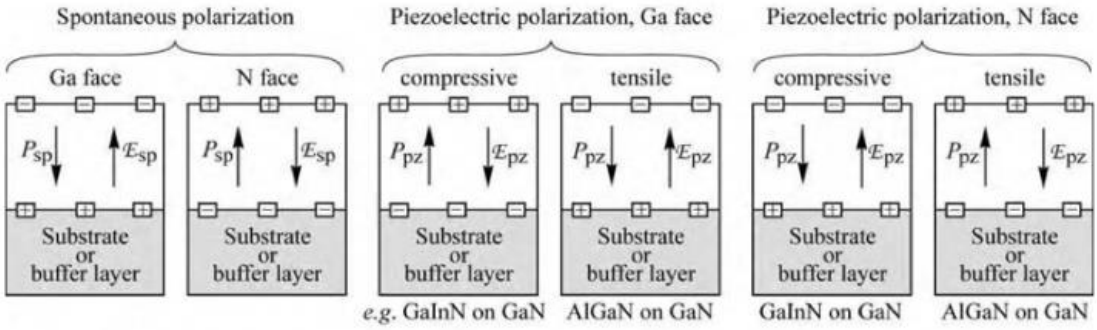

Figure 2.4. Fixed polarization charges and directions of spontaneous/piezoelectric polarization (along with corresponding electric field) for different orientations (Ga-polar or N-polar) and alloys (InGaN/AlGaN on GaN). Reproduced with permission of Cambridge University Press [9] Copyright 2006.

2.2 Semiconductor *p-n* Junctions

A core component of many semiconductor devices today are *p-n* junctions, which can be found in transistors, solar cells, laser diodes, and LEDs. A *p-n* junction is the junction between a *p*-type semiconductor material (doped with electron accepting impurities,

majority carrier type are holes) and an *n*-type semiconductor material (doped with electron donating impurities, majority carrier type are electrons). As will be seen throughout this dissertation, knowledge of *p*-*n* junctions, often referred to as diodes, provides an important foundation for understanding LED operation.

When a junction is formed between *p*-type and *n*-type materials, diffusion of carriers occurs due to large carrier concentration gradients. Electrons diffuse from the *n*-type to the *p*-type region leaving behind uncompensated donor ions N_D^+ and conversely, holes diffuse from the *p*-type to the *n*-type region leaving behind uncompensated acceptor ions N_A^-. A region around the junction is consequently formed that is depleted of mobile carriers and is known as the depletion region, which has a width W_D. The extent to which the depletion region penetrates the *n*-side and the *p*-side of the junction depends on the doping concentrations. The charge resulting from ionized donors and acceptors sets up an electric field and therefore a drift current that is opposite the diffusion current. In thermal equilibrium no net current can flow across the junction and the drift current exactly cancels the diffusion current.

Figure 2.5 shows the energy band diagram of a *p*-*n* junction in thermal equilibrium (no external applied bias). To achieve a constant Fermi level energy E_F (as required by thermal equilibrium) in a *p*-*n* junction, the CB and VB bend near in the depletion region W_D and lead to the appearance of a built-in potential V_{BI}. V_{BI} can be calculated according to

$$V_{BI} = \frac{k_B T}{q} \ln \frac{p_{p_o} n_{n_o}}{n_i^2}, \tag{2.6}$$

where q is the fundamental electron charge, k_B is the Boltzmann constant, T is temperature, $p_{p_0}$and n_{n_0} are the equilibrium majority carrier concentrations in the *p*- and *n*-regions,

respectively, and n_i is the intrinsic carrier concentration. The full-depletion approximation is frequently used in *p*-*n* junction analysis and assumes that the depletion region has defined edges and that the transition from the depleted to the quasi-neutral region is abrupt. The quasi-neutral region is adjacent to the depletion region and has a small electric field.

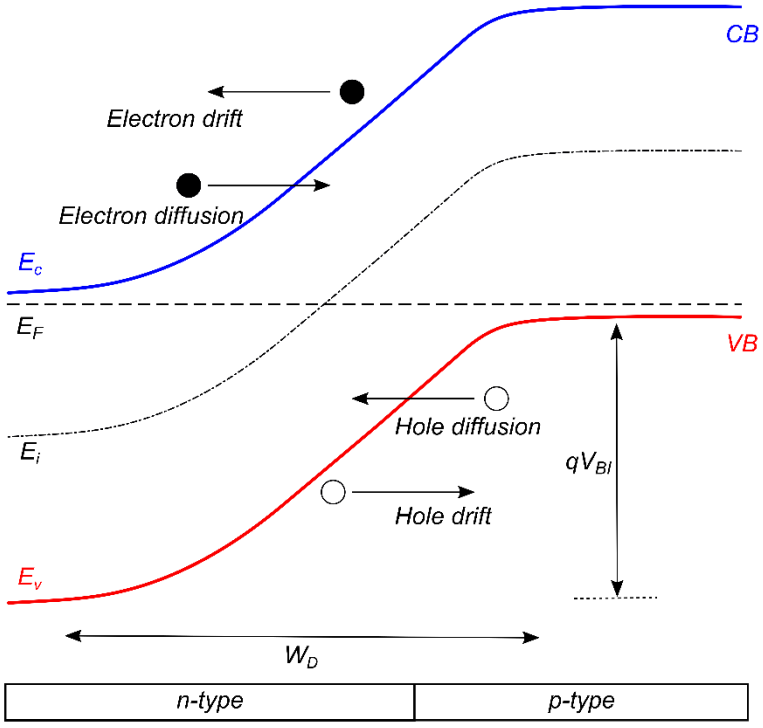

Figure 2.5. Energy band diagram of a *p*-*n* junction showing a constant Fermi level energy E_F, diffusion of holes from *p* to *n*, diffusion of electrons from *n* to *p*, drift of holes from *n* to *p*, drift of electrons from *p* to *n*, depletion width W_D, and built-in potential V_{BI}.

If an external bias V is applied to a *p*-*n* junction such that a positive voltage is applied to the *p*-type region relative to the *n*-type region, the diode is said to be forward-biased. Under forward bias, the electrostatic potential barrier is reduced to $V_{BI} - V$. The field across the depletion region also decreases because the applied electric field **E** is opposite the built-in electric field $\mathbf{E}_{BI}$. With a lower barrier height, diffusion current

increases as more carriers have sufficient thermal energy to overcome the smaller barrier and a net current flows in the forward direction. In the case of a reverse biased *p*-*n* junction, a negative voltage is applied to the *p*-type region relative to the *n*-type region. The potential barrier is increased to $V_{BI} + V$, resulting in a significantly reduced diffusion current and a small net drift current that flows in the reverse direction.

If both sides of the junction are long relative to the minority carrier diffusion length, the diode is called a "long diode". Neglecting recombination in the depletion region (ideal diode approximation), the total current density through the long diode for either forward or reverse bias is given by the Shockley diode equation

$$J_T = J_s\left(e^{qV/k_BT} - 1\right). \tag{2.7}$$

J_s is the reverse saturation current density and is given by

$$J_s = \frac{qp_{n_0}D_p}{L_p} + \frac{qn_{p_0}D_n}{L_n}, \tag{2.8}$$

where $p_{n_0}$and n_{p_0} are the equilibrium minority carrier concentrations in the *n*- and *p*-regions, D_n and D_p are the diffusion coefficients of electrons and holes, respectively, and L_n and L_p are the diffusion lengths of electrons and holes, respectively. J_s values as low as 2.6×10^{-7} A cm^{-2} have been demonstrated in GaN *p*-*n* junctions grown by molecular beam epitaxy [10]. Inspection of the diode equation shows that when V is positive and greater than several k_BT/q, the exponential term is much greater than one and J_T will increase exponentially with forward bias. When V is negative, the exponential term approaches zero and the current density is given by J_s, the reverse saturation current.

If the *p*-side or *n*-side of the diode are of a similar or smaller thickness relative to the minority carrier diffusion length in that region, the diode is referred to as a "short diode". In

this case the diode equation given by Eq. 2.7 remains the same. However, in the reverse saturation current density equation (Eq. 2.8), the minority carrier diffusion length on the short side of the diode (L_n, L_p, or both) are replaced with the width of the short side of the diode (W_p, W_n, or both). Deviations from ideality occur when there is generation and recombination within the depletion region. In this case the exponential term of the diode equation is replaced with $qV/\eta k_B T$, where η is known as the ideality factor and captures any departure from ideal diode characteristic.

2.3 LED Operation

Solid-state LEDs rely on heterostructures to achieve high efficiencies and to control the emission wavelength. (Al,Ga,In)N materials have Type I band alignment which allows for a material with a smaller bandgap (E_{g1}) to be placed in the middle of two wider bandgap materials (E_{g2}) to form a potential well. As shown in Fig. 2.6, both the conduction band and valence band have lower potentials in the narrow bandgap material region. Both electrons and holes will tend to accumulate in a potential well formed from materials with Type I band alignment. If the narrow bandgap material is sufficiently thin, on the order of the de Broglie wavelength of carriers, it is referred to as a quantum well (QW). When carriers are confined to a QW, they can only have discrete energy eigenstates, similar to those given by the finite well model. The rate of electron-hole recombination is higher in a QW relative to the bulk material due to the higher carrier density and the increase in electron-hole wavefunction overlap.

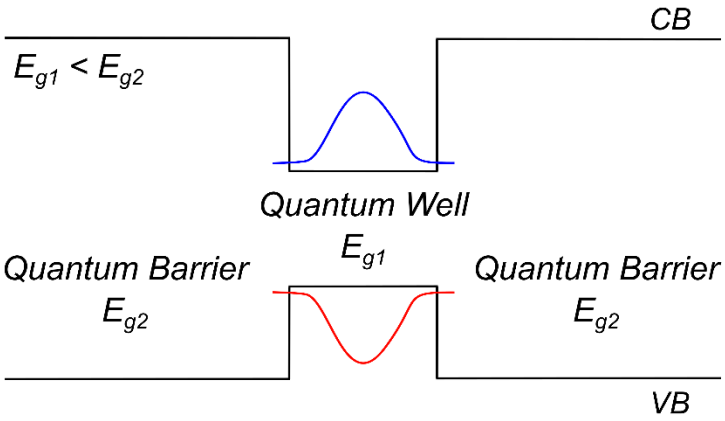

Figure 2.6. Schematic of a QW structure created by Type I band alignments between the QW material and the barrier material. The QW material has a bandgap of E_{g1} while the QB material has a bandgap of E_{g2}, where $E_{g1} < E_{g2}$; therefore, the electron and hole wavefunctions will be confined in the QW region.

Under forward bias, current increases exponentially, as given by the diode equation (Eq. 2.7), and a greater portion of injected carriers accumulate in the potential well. For an efficient LED, the majority of electron-hole recombination in the QW will be radiative (resulting in photon emission).

For group III-nitride LEDs emitting in the visible portion of the electromagnetic spectrum, $In_xGa_{1-x}N$ is used as the narrow bandgap material in the QW and the QW is clad by GaN quantum barrier (QB) layers with a wider bandgap. Increasing the fraction of indium x will decrease the QW bandgap, leading to a deeper potential well and a longer (red-shifted) emission wavelength. To achieve red emission (625 nm), high indium fractions are required whereas blue emission (450 nm) can be easily achieved with much lower indium fractions. It was previously described in Section 2.1 that pseudomorphic growth of InGaN films on GaN leads to biaxial compressive stress due to lattice mismatch and piezoelectric fields due to polarization discontinuities at interfaces. As the indium fraction is increased to achieve long-wavelength LEDs, these effects become more severe.

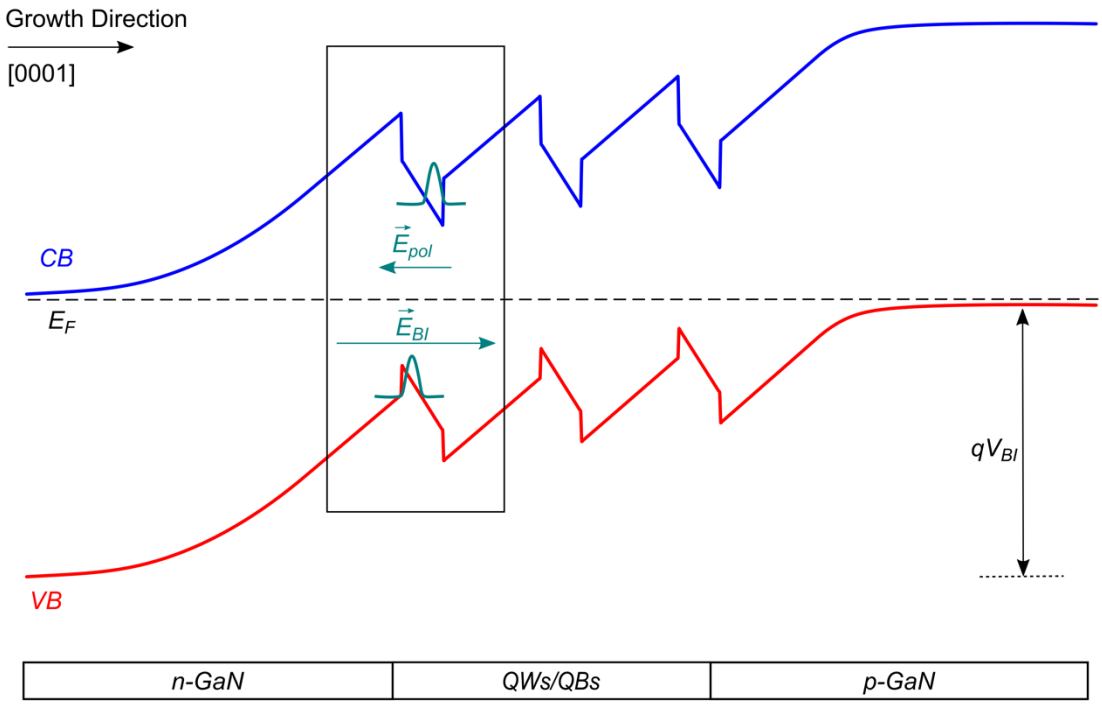

Figure 2.7. Energy band diagram of a three QW *c*-plane InGaN LED with no applied bias.

For Ga-polar InGaN on GaN, the component of the electric field due to spontaneous polarization $\mathbf{E}^{sp}$ is directed away from the substrate and the component of the electric field due to piezoelectric polarization field $\mathbf{E}^{pz}$ is directed toward the substrate (Fig. 2.4). The overall electric field due to polarization $\mathbf{E}_{pol}$ is directed toward the substrate as a result of $\mathbf{E}^{sp} < \mathbf{E}^{pz}$. Figure 2.7 shows an energy band diagram schematic of *c*-plane InGaN QWs in an unbiased LED where the polarization-induced electric field in the QW $\mathbf{E}_{pol}$ is greater than and opposite to the built-in electric field of the diode $\mathbf{E}_{BI}$. The large net electric field in the QW causes the potential to become sloped and the resulting triangular shaped well localizes electron and hole wavefunctions on opposite sides of the QW. In Fig. 2.8, the QW on the right has an applied electric field and therefore a sloped potential in the QW whereas the QW on the left has no applied electric field and the wavefunctions remain centered.

Spatial separation of wavefunctions reduces the rate of all recombination events, increasing the carrier density in the well at a given injection and QW thickness. As the electric field increases, the relative energies of the lowest electron and hole sub-bands decrease quadratically, bringing electrons and holes closer in potential, as shown in Fig. 2.8. The observed red-shift in the absorption edge upon application of an electric field perpendicular to a QW is known as the quantum confined Stark effect (QCSE) [11]. Therefore, QWs with high indium fraction will lead to greater wavefunction separation, lower recombination rates, and more strongly red-shifted emission due to the QCSE. At high carrier densities, free carriers injected into the QW will partially screen the polarization field and cause the emission to blue-shift.

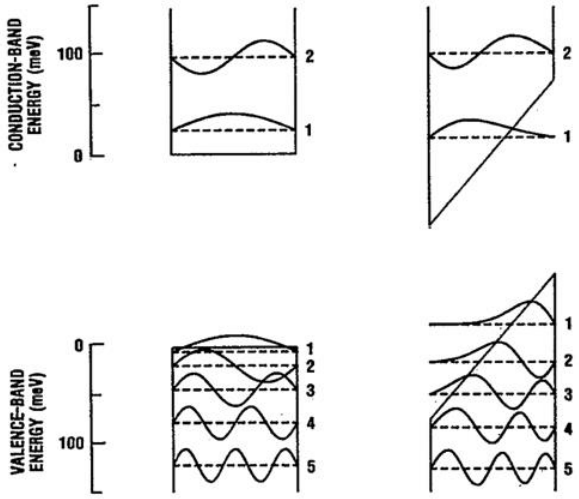

Figure 2.8. Conduction and valence bands of a QW (a) without an electric field and (b) with an electric field. The electric field causes the bands to tilt, creating a triangularly shaped potential. Reprinted with permission from [12] Copyright 1986 by the American Physical Society.

For many applications, and in the research presented in this dissertation, the goal is to realize high efficiency LEDs. To achieve this through optimized LED design, it is

important to understand the details of LED efficiency. An ideal LED would emit one photon for every injected electron and would thus have an internal quantum efficiency (IQE) of unity. Also in an ideal LED, emitted photons should escape from the LED and be emitted into free space. In this case, the light extraction efficiency (LEE) would be unity. In real LEDs, loss mechanisms such as photon absorption in metal contacts or reabsorption in the substrate cause LEE to be less than unity. As will be shown in Chapter 6, the choice of substrate and device configuration has a significant impact on the LEE. The external quantum efficiency (EQE) is the number of photons emitted into free space divided by the number of electrons injected into the LED, and can be defined as follows

$$EQE = \frac{L/h\nu}{I/q} = IQE \cdot LEE, \tag{2.9}$$

where L is the optical power emitted into free space, $h\nu$ is the photon energy, and I is the injected current. There can also be carrier overshoot or leakage along shunt paths that cause carriers to avoid recombination in the active region. The fraction of injected current that results in recombination current in the active region is called the injection efficiency η_{inj}.

Another component of LED efficiency is the electrical efficiency (EE),

$$EE = \frac{V_{ph}}{V_F}, V_{ph} = \frac{h\nu}{q} \tag{2.10}$$

where V_{ph} is the photon voltage and V_F is the forward voltage at a specific current density, typically 20 or 35 A cm^{-2}. Often V_F exceeds V_{ph} and the excess forward voltage is written as

$$\Delta V_F = V_F - V_{ph}. \tag{2.11}$$

Together, the EQE and EE are used to obtain the LED wall plug efficiency (WPE) or power conversion efficiency (PCE), which is given by

$$WPE = EQE \cdot EE = \frac{L/h\nu}{I/q} \cdot \frac{h\nu}{q} \cdot \frac{1}{V_F} = \frac{L}{I \cdot V_F}. \quad (2.12)$$

This equation can be understood as the ratio of the optical power output of an LED to the electrical power input.

The three main types of recombination processes known to occur in an LED are Shockley-Read-Hall (SRH) non-radiative recombination, band-to-band radiative recombination, and Auger non-radiative recombination, where each type has a different dependence on the carrier density n. A schematic showing the three recombination mechanisms is given in Fig. 2.9. Radiative recombination results in photon emission, whereas during non-radiative recombination, electron energy is converted to phonons (vibrational energy of lattice atoms). SRH recombination involves a free carrier relaxing into a trap state with an energy level E_T typically at mid-gap. The SRH rate will be determined by the relative speed of hole versus electron capture, but in both cases will become linear in either hole (p) or electron (n) concentration. For a non-degenerate direct bandgap semiconductor, radiative recombination is bimolecular and the rate is proportional to the product of electron and hole densities. In Auger recombination, an electron and hole recombine and the energy is transferred to another carrier, which can be an electron or a hole. If a high energy hot electron is produced, recombination is referred to as eeh Auger and if a hot hole is produced, it is referred to as ehh Auger. The Auger recombination rate is therefore proportional to either nnp or npp. At degenerate carrier densities, radiative recombination becomes monomolecular and Auger recombination becomes subcubic [13,14]; however, this regime is not reached under typical LED operating conditions.

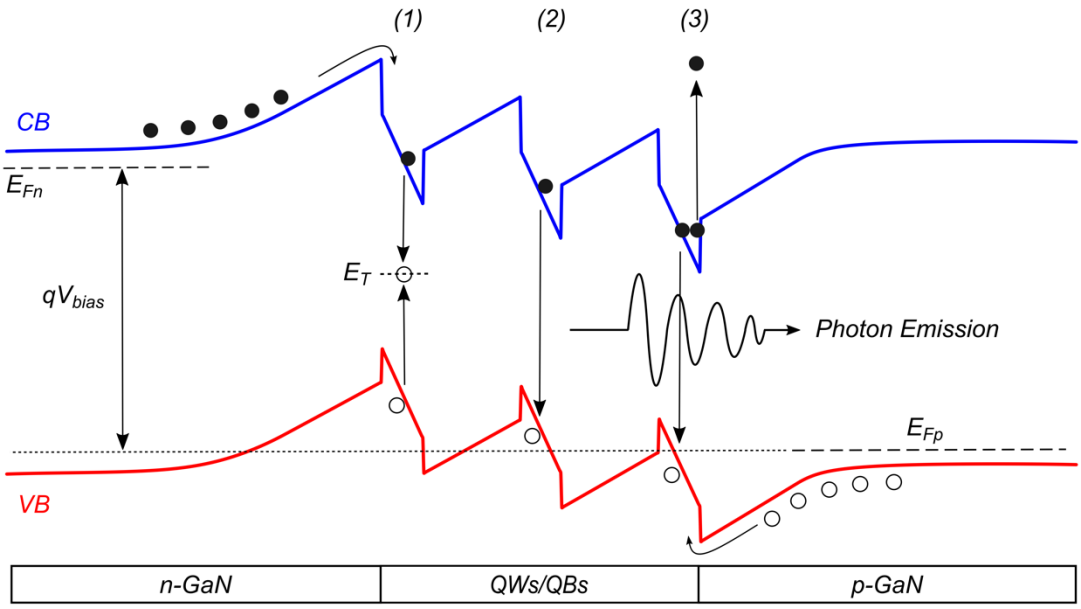

Figure 2.9. Forward biased three QW LED showing (1) Shockley-Read-Hall nonradiative recombination, (2) bimolecular radiative recombination, and (3) Auger (eeh) nonradiative recombination.

The following equation gives the recombination rate of charge carriers in the LED active region, assuming that the electron and hole densities are approximately equal ($n \sim p$)

$$\frac{dn}{dt} = \frac{J \cdot \eta_{inj}}{q \cdot d} - An - Bn^2 - Cn^3, \tag{2.13}$$

where J is the current density, d is the QW thickness, and A, B, and C are the SRH, radiative, and Auger recombination rate coefficients, respectively. The Auger coefficient C is taken to be an effective coefficient that accounts for both eeh and ehh Auger processes. Under steady state conditions ($dn/dt = 0$) and ideal injection efficiency ($\eta_{inj} = 1$), Eq. 2.13 can be reduced to

$$J = qd \cdot (An + Bn^2 + Cn^3). \tag{2.14}$$

The IQE, which was previously defined as the ratio of emitted photons to injected electrons, can be equivalently defined as the ratio of radiative recombination to total recombination,

$$IQE = \frac{Bn^2}{An + Bn^2 + Cn^3}. \tag{2.15}$$

What is known as the "ABC model" is employed to describe recombination of charge carriers in an LED active region and can be useful in evaluating the extent and origin of efficiency loss. IQE as a function of J is frequently plotted and the curve fit using the ABC model, where n is the internal variable connecting Eq. 2.14 and Eq. 2.15. In this context, the ABC model provides insight into the rates of the different recombination processes. In practice, IQE is obtained from Eq. 2.9, where EQE is measured experimentally and LEE is assumed to be constant with J. LEE depends on geometry and cannot be taken as constant when current crowding around metal contacts results in increased absorption of light; nevertheless, this complication is often ignored and fits of IQE and EQE using the ABC model are considered equivalent. Additional complexities that are often neglected in the ABC model include: inhomogeneous injection of carriers in multiple QW devices, carrier density dependence of the recombination coefficients, and localization effects resulting from fluctuations in indium composition. Despite these shortcomings, the ABC model is perhaps the most widely adopted model for describing carrier recombination in LEDs due to its relatively simple form.

It is impossible to cover the topic of efficiency in group III-nitride LEDs without discussing the phenomena known as efficiency droop, an issue which plagues even the best commercially available LEDs today. For an ideal LED, optical power L should increase linearly with injected current density J. In real LEDs which undergo efficiency droop, the

increase in L with increasing current is sublinear, as shown in Fig. 2.10(a). Droop can also be described in terms of efficiency and the framework of the ABC model. As injected current density is increased, so is the carrier density n; therefore, the IQE curve can be divided into different regimes based on the dependence of the recombination rates on n. At low carrier densities, IQE is dominated by trap-assisted SRH recombination (An). As n increases, radiative recombination (Bn^2) becomes the dominant mechanism. And finally at even higher n, Auger recombination (Cn^3) dominates and IQE begins to decrease. EQE is the experimentally measured parameter and in this case its dependence on J will be considered equivalent to the dependence of IQE on J. EQE as a function of J for a typical LED is given in Fig. 2.10(b), where EQE first rises sharply before reaching its maximum value, and then begins to slowly decay as J is further increased. This decrease in quantum efficiency after its maximum is efficiency droop. The exact shape of the EQE versus J curve will depend on the relative magnitude of the recombination coefficients A, B, and C.

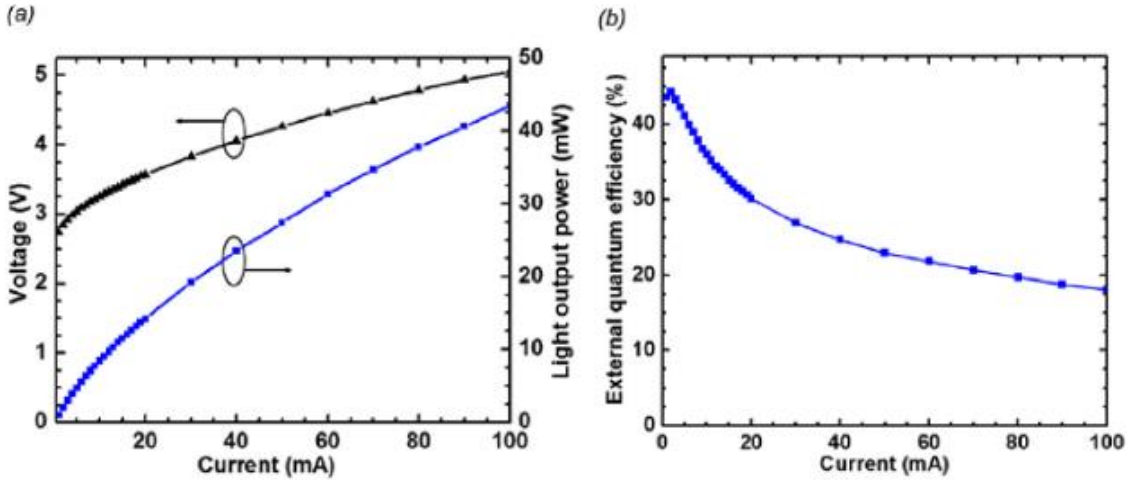

Figure 2.10. (a) Dependence of light output power L and voltage on injected current I and (b) Dependence of EQE on injected current I. Reprinted with permission from [15] Copyright The Optical Society.

The droop phenomenon has been well documented and its origin extensively studied and debated. The most frequently invoked explanations of droop include defect-assisted mechanisms [16], carrier leakage [17-19], and Auger recombination [20-24]. However, Auger recombination was demonstrated computationally to be strong enough in III-nitrides to be considered the dominant physical mechanism contributing to efficiency droop at high current densities [21,22]. Using a computational approach, Jones *et al*. reported that carrier localization due to random alloy fluctuations leads to a greater increase in C relative to B and to enhanced efficiency droop [23]. From device simulations which included random alloy fluctuations, it was also concluded that droop is dominated by Auger recombination and that alloy fluctuations exacerbate Auger-mediated droop [25-27]. Lastly, electron emission spectroscopy experiments by Iveland *et al*. directly measured Auger electrons, thus providing further support for Auger-mediated droop [24].

2.4 Metal Organic Chemical Vapor Deposition

The primary method of commercial III-nitride LED epitaxial growth, and the one used throughout this dissertation, is metal organic chemical vapor deposition (MOCVD). Epitaxial growth is broadly defined as the process of growing a crystalline layer on top of another crystal, where the layer orientation is determined by the underlying crystal. In MOCVD, high-purity gas phase precursors are injected into a reactor at high temperatures where they undergo pyrolysis. The subspecies adsorb onto the underlying crystal surface and react to form a new epitaxial layer. There are three primary growth regimes identified for MOCVD [28]. In the low-temperature, kinetically limited regime, the growth rate increases with temperature as adsorption of the subspecies increases. At intermediate temperatures in

the mass transport limited regime, the growth rate exhibits a weak temperature dependence. The majority of MOCVD growth takes place in the mass transport limited regime where the growth rate is determined by diffusion of the minority species (typically group III) to the growth surface. At higher temperatures in the desorption limited regime, the growth rate decreases with increasing temperature.

For MOCVD growth of (Al,Ga,In)N materials, the commonly used metalorganic (MO) group III precursors include trimethylaluminum (TMA), trimethylgallium (TMG), triethylgallium (TEG), and trimethylindium (TMI). The group V nitrogen precursor is gaseous ammonia (NH_3). Also required for semiconductor devices are dopant materials; for GaN, *p*-type doping is achieved using magnesium and *n*-type doping is achieved using silicon. The magnesium precursor bis(cyclopentadienyl)magnesium $Mg(C_5H_5)_2$ (referred to as Cp2Mg) is an MO dopant while the silicon precursor Si_2H_6 (referred to as disilane) is gaseous.

Because the MO precursors are either solid or liquid, bubblers and carrier gases are required to deliver the MO in a vapor phase into the reactor. H_2 and/or N_2 carrier gases are bubbled through the liquid or over the solid surface to pick up the MO vapor, where the vapor pressure of the MO is controlled by the bubbler temperature. The gas-phase NH_3 and Si_2H_6 are also combined with H_2 and/or N_2 carrier gases for delivery into the reactor. The flow of gases into the reactor are controlled by mass flow controllers (MFCs). To avoid pre-reactions, the group III and nitrogen precursors remain separate until they are injected into the reactor.

The choice of gallium precursor, TEG or TMG, will depend on the specific layer being grown. TMG has a high vapor pressure, enabling fast growth rates, and is typically

used for growing high temperature GaN layers. As the growth temperature is reduced, carbon impurity incorporation into the film is known to increase. The decomposition mechanisms for TMG and TEG are homolytic cleavage and β-hydride elimination, respectively, where β-hydride elimination results in reduced carbon incorporation. Therefore, TEG is often the preferred precursor for low temperature III-nitride growth despite its lower vapor pressure.

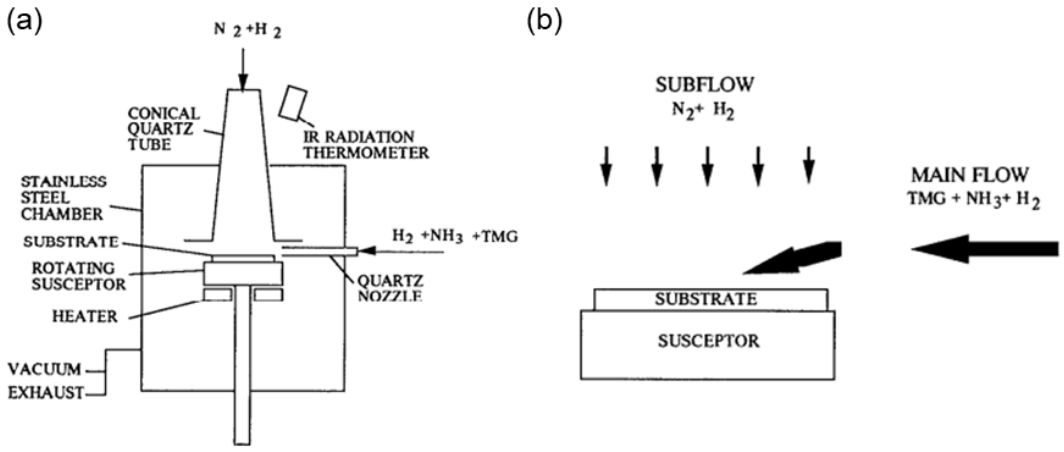

Figure 2.11. Schematics of the (a) horizontal two-flow reactor designed by Nakamura and (b) main flow and subflow of gases showing how the subflow is used to redirect the main flow toward the substrate. Reprinted from [29], with permission of AIP Publishing.

The reactor used in this dissertation for MOCVD growth is a horizontal "two-flow" reactor similar to the one designed by Nakamura and shown schematically in Fig. 2.11(a) [29]. In this reactor design, the MO precursors, NH_3, and H_2/N_2 carrier gases are injected horizontally over the substrate while a subflow of H_2 and/or N_2 is injected vertically. As depicted in Fig. 2.11(b), the vertical subflow redirects the main flow towards the substrate, thereby improving the boundary layer and enabling high quality GaN growth. The main flow rates and subflow rates are chosen to achieve laminar flow. The substrate is transferred

into the reactor on a graphite puck to then sit on a susceptor which rotates to realize a uniform growth rate across the substrate. A heater is used to achieve the high growth temperatures (550–1220 °C) required for III-nitride MOCVD growth.

Another important consideration for III-nitride epitaxy is the choice of substrate. Homoepitaxy of GaN on native GaN substrates has many advantages over heteroepitaxy; however, limitations in bulk GaN synthesis result in small substrate sizes and high costs. Therefore, most III-nitride LEDs are grown heteroepitaxially on non-native substrates such as (0001)-oriented sapphire (Al_2O_3), silicon carbide (6H-SiC), or (111)-oriented silicon (Si), with sapphire being by far the most common. Sapphire substrates have the advantages of producing high quality GaN films in addition to being low cost, optically transparent, and available in large sizes. For GaN growth on sapphire, which represents the majority of the growth in this dissertation, the mismatch in the a lattice constant and the coefficient of thermal expansion (CTE) are 16% and 34%, respectively. For GaN on sapphire, the CTE mismatch leads to high compressive film stress and extreme wafer bow. The large lattice mismatch of GaN on foreign substrates ultimately requires that a low temperature nucleation layer (also known as a buffer layer) of GaN or AlN first be grown on the substrate. The nucleation layer has a rough morphology and a high-degree of stacking disorder. As growth continues and the temperature is increased, high temperature (HT) GaN islands grow by a coarsening mechanism. The islands continue to grow laterally until eventually they rapidly coalesce into a smooth film.

The growth mechanism of GaN on sapphire detailed above leads to a high density of threading dislocations (TDs), which are extended crystallographic defects. TDs are electrically charged and can serve as nonradiative recombination centers and carrier leakage

pathways in an LED. The density of pure screw and mixed-character TDs is typically lower than the density of pure edge TDs. The HT GaN islands have been shown to contain one or a few mixed or pure screw TDs, while the majority of TDs are edge-component and are generated at the island coalescence boundary [30]. The total threading dislocation density (TDD) of GaN on sapphire is typically on the order of 10^8 cm^{-2}. For GaN on silicon, the TDD is on the order of 10^9 cm^{-2}. In addition to having a higher TDD and being optically absorbing, GaN films grown on silicon are subject to cracking due to high tensile film stress resulting from the 57% CTE mismatch. Despite these drawbacks, there is still interest in developing LED technology on Si. The wafers are available in larger sizes and lower costs than sapphire. There are also benefits associated with the maturity of the silicon semiconductor fabrication industry and the prospect of integrating LEDs and microelectronics. For more on the development of GaN-on-Si LEDs, see Ref [31] and the references therein.

The final aspect of III-nitride MOCVD growth that will be given closer attention is the growth of InGaN layers and their associated defects. Compared to GaN, InGaN requires lower growth temperatures to prevent indium desorption from the surface. At low growth temperatures, the adatom surface mobility decreases, which leads to poor surface morphology, and the incorporation of impurities such as carbon and oxygen increase. The 10% lattice mismatch between InN and GaN also causes significant biaxial stress in the InGaN film. When the InGaN film thickness exceeds the Matthews-Blakeslee critical thickness h_c, relaxation via misfit dislocation formation is energetically favorable [32-34]. However, the Matthews-Blakeslee critical thickness is purely based on energetics, not kinetics, and does not provide a mechanism for misfit dislocation formation. For InGaN

growth on semipolar orientations, there is a resolved shear stress on the (0001) slip plane, allowing for plastic relaxation via misfit dislocation glide. Thus, it is common for InGaN films to be grown at large thicknesses relative to h_c.

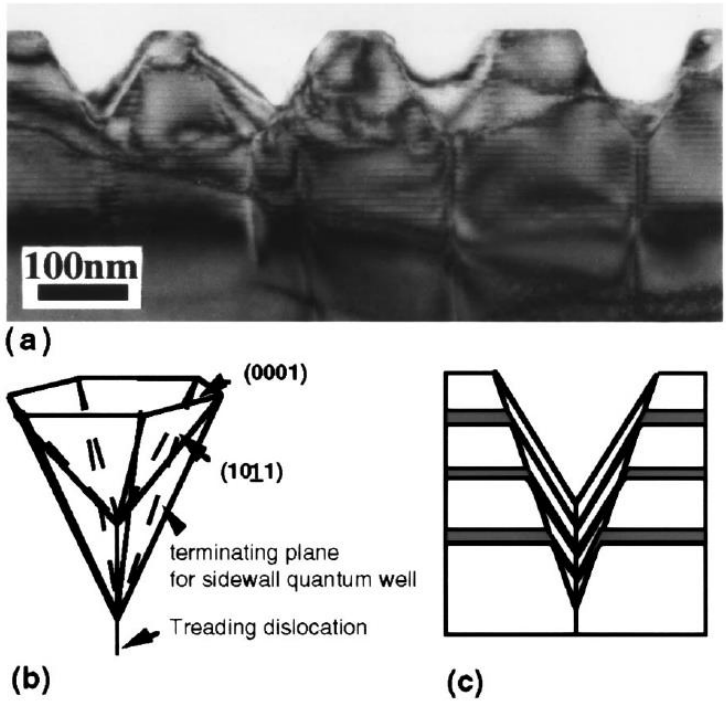

Figure 2.12. (a) Cross-section TEM image of an uncapped InGaN/GaN multiple QW structure. (b) Schematic of the hexagonal pyramid shape of a V-defect with {10$\bar{1}$1} sidewalls. (c) Cross-section schematic of a V-defect with planar and sidewall QWs. Reprinted from [36] with permission of AIP Publishing.

For *c*-plane LED growth, large three-dimensional defects known as V-defects are frequently observed [35] and are related to low temperature InGaN growth. V-defects are inverted hexagonal pyramids that nucleate at threading TDs due to the surface depression formed by a dislocation (Fig. 2.12) [36,37]. After nucleation, V-defects continue to grow due to kinetically limited growth. Furthermore, it is observed that higher indium compositions or period of InGaN/GaN layers promote V-defect growth [36,38]. Therefore

V-defects are frequently nucleated in the InGaN/GaN superlattice (SL) or QW regions. V-defects contain $\{10\bar{1}1\}$ semipolar sidewalls which have lower total polarization discontinuity for InGaN/GaN or AlGaN/GaN interfaces than polar *c*-plane [39]. When a V-defect extends through the multiple QW (MQW) active region of an LED, sidewall QWs and QBs are observed with reduced thickness and lower indium composition relative to those in the planar region [40,41]. More details on the role of V-defects on device performance will be discussed in Chapter 5.

2.5 Alloy Disorder and 3D Simulations

Ternary alloys have been essential in the development of modern compound semiconductor materials and devices. Alloying binary compounds enables various materials and electrical properties, most importantly the bandgap, to be controllably tuned. In an alloy material, atoms are randomly substituted at well-defined sites within the crystal lattice. Experimentally, alloy disorder can be observed in atom probe tomography (APT) measurements. The impact of alloy disorder in conventional III-V materials, such as III-arsenides and III-phosphides, is slight due to the small difference in bandgaps of constituent compounds. In contrast, the large difference in the bandgap of InN and GaN lead to InGaN QWs with extreme spatial variations in the energy landscape at nanometer length scales. Alloy disorder therefore strongly impacts carrier localization, transport, and recombination in III-nitride LED devices [26,42-45]. These effects become more pronounced for long-wavelength LEDs with high indium content InGaN QWs where alloy fluctuations are more severe [23,46].

Accounting for alloy disorder in conventional III-V materials can typically be done within the virtual crystal approximation (VCA). The VCA treats the disordered alloy by assuming that on each site, there is a virtual atom with properties that can be interpolated from the actual atoms. Despite its limitations, the VCA often produces useful results at a low computational cost. To better account for alloy disorder, perturbation theory is frequently applied to calculate energy shifts with respect to the values calculated using the VCA. However, the fluctuating potential in III-nitride alloys is too large to be treated as a perturbation and atomistic simulations are ultimately impractical for simulating the device behavior of a full LED structure.

To simulate the electrical behavior of III-nitride devices, a Poisson-Schrödinger-drift-diffusion solver should be used to solve the coupled equations self-consistently. To account for disorder-induced quantum effects, the Schrödinger equation should be solved in 3D for a disordered potential using a fine mesh (~0.2–1 nm) to correctly capture the physical scale of these phenomena. Self-consistently solving for the eigenstates in an alloy system using quantum mechanical calculations is too computationally demanding to be practical as the number of mesh nodes exceeds ~10^6 [27]. As an alternate approach, the Localization Landscape (LL) theory of disorder pioneered by Filoche and Mayboroda can be used to perform 3D device simulations that account for disorder effects [47-49].

In this section, the details of the device simulations presented in Chapters 3 and 4 of this dissertation are described. The 3D drift-diffusion charge control (3D-DDCC) solver developed by Professor Yuhrenn Wu is the tool used for these simulations [50,51].

The input parameters for each layer in the LED structure are first defined, including the thickness, dopant concentration and activation energy, carrier mobilities, nonradiative

lifetimes, radiative recombination coefficient, and Auger recombination coefficient. Figure 2.13(a) shows an example of the LED structure simulated using the 3D-DDCC solver in Ref [27]. The structures are then meshed using Gmsh [52,53] and the composition profiles used are based on those experimentally observed by APT [25,26]. In the 3D computations, the average indium (aluminum) composition of an InGaN (AlGaN) layer is first defined, and a random number generator is used to assign indium (aluminum) and gallium atoms to each cation lattice site. The Gaussian averaging method described extensively in Ref [27] is then used to realize a continuous fluctuating composition. Figures 2.13(b) and 2.13(c) show AlGaN and InGaN random alloy maps, respectively, that are generated using this approach. Although there are alloy fluctuations, the local bandgap E_g is retained. The local alloy composition is used to assign the bandgap E_g, dielectric constant ϵ_r, and effective mass m^* at each mesh node. For an $In_xGa_{1-x}N$ alloy with indium fraction x, these parameters are determined by interpolating between GaN and InN according to the following equations

$$E_g^{In_xGa_{1-x}N} = (1-x)E_g^{GaN} + xE_g^{InN} - 1.4x(1-x), \tag{2.16}$$

$$\epsilon_r^{In_xGa_{1-x}N} = (1-x)\epsilon_r^{GaN} + x\epsilon_r^{InN}, \tag{2.17}$$

$$m^{*,In_xGa_{1-x}N} = [(1-x)/m^{*,GaN} + xm^{*,InN}]^{-1}, \tag{2.18}$$

where Eq. 2.16 is in units of eV and the value of 1.4 eV is the bowing parameter.

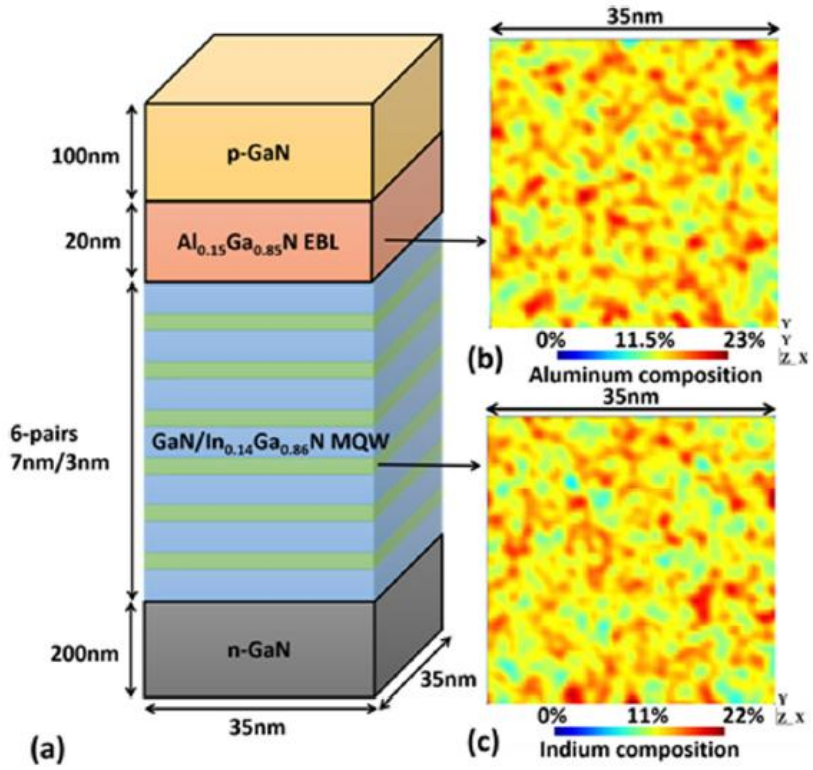

Figure 2.13. (a) Schematic of a simulated LED structure. (b) Distribution of aluminum in the *XY* plane of the AlGaN layer. (c) Distribution of indium in the *XY* plane of the InGaN QW. Reprinted with permission from [27] Copyright 2017 by the American Physical Society.

An *XY* map of the conduction band potential $E_c(\mathbf{r})$ in a QW is shown in Fig. 2.14, where the conduction band offsets between GaN and InGaN are taken to be 63% of the bandgap difference. However, the energy levels of electrons and holes are not given by the conduction and valence band potentials $E_{c,v}(\mathbf{r})$ as quantum effects occur due to the size and lateral dimensions of energy fluctuations. In the effective mass approximation, the true carrier energy levels are obtained by solving the Schrödinger equation obeyed by carriers in the fluctuating potential [54].

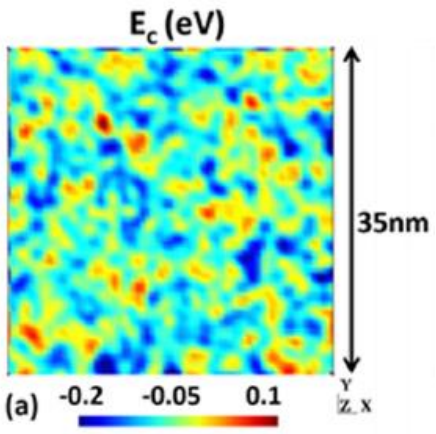

Figure 2.14. *XY* map of the conduction band potential computed by the 3D-DDCC solver. Reprinted with permission from [27] Copyright 2017 by the American Physical Society.

In the 3D-DDCC solver, the Schrödinger eigenvalue equation (Eq. 2.19) is replaced with the Landscape equation (Eq. 2.20)

$$\hat{H}\psi(\mathbf{r}) = E\psi(\mathbf{r}), \tag{2.19}$$

$$\hat{H}u_{e,h}(\mathbf{r}) = 1, \tag{2.20}$$

where the Hamiltonian for electrons and holes is given by

$$\hat{H} = -\frac{\hbar^2}{2m_{e,h}^*}\Delta + E_{c,v}(\mathbf{r}). \tag{2.21}$$

In these equations, $\psi(\mathbf{r})$ is the wavefunction, E is the eigenenergy, $m_{e,h}^*$ is the electron/hole effective mass, $\hbar$ is the reduced Planck's constant, $E_{c,v}(\mathbf{r})$ is the local conduction/valence band energy, and $u_{e,h}(\mathbf{r})$ is the Landscape function for electrons/holes. The Landscape equation is used to predict the energy levels and local density of states (LDOS) in place of the Schrödinger equation. The quantity $1/u_{e,h}(\mathbf{r})$ is interpreted as the effective potential for the carrier, accounting for their quantum nature and particular behavior, such as confinement

[49]. Thus, $1/u_{e,h}(\mathbf{r})$ is used directly to plot an effective band diagram for a given structure. The use of the Landscape equation in lieu of Schrödinger's equation leads to a 10^3 reduction in computation time [27], thus making 3D self-consistent computations possible.

Coherently grown III-nitride heterostructures in the [0001] orientation exhibit large internal electric fields resulting from discontinuities in spontaneous and piezoelectric polarization, which must be accounted for in device simulations. A 3D continuum stress-strain model is solved using the finite element method (FEM) to calculate the strain distribution. From the strain distribution, the strain-induced piezoelectric polarization $\mathbf{P}^{pz}$ is evaluated using Eq. 2.3. The spontaneous polarization $\mathbf{P}^{sp}$ and the polarization-induced charge $\rho_{pol}(\mathbf{r})$ are obtained from Eq. 2.4 and Eq. 2.5, respectively.

$\rho_{pol}(\mathbf{r})$ is solved once outside the self-consistency loop and is input into the Poisson equation to calculate the electrostatic potential $\varphi(\mathbf{r})$ and then $E_{c,v}(\mathbf{r})$. The Poisson equation is given by

$$\nabla \cdot \big(\epsilon \nabla \varphi(\mathbf{r})\big) = q\left(n - p + N_A^- - N_D^+ \pm \rho_{pol}(\mathbf{r})\right), \tag{2.22}$$

where ϵ is the dielectric constant, and N_A^- and N_D^+ are the ionized acceptor and donor densities. The electron and hole densities, n and p, respectively, are initially guessed. After obtaining $E_{c,v}(\mathbf{r})$, the Landscape equation (Eq. 2.20) is solved for the Landscape functions $u_{e,h}(\mathbf{r})$. The effective potentials $1/u_{e,h}(\mathbf{r})$ determine the bottom energy for the LDOS of the disordered system, which in Landscape theory can be computed from Weyl's law in 3D (Eq. 2.23) [49]. The carrier densities are then calculated from Eq. 2.24 and Eq. 2.25

$$\mathrm{LDOS}_{3\mathrm{D}}(E) = \frac{\sqrt{2}m_{e,h}^*}{\pi^2\hbar^3}\sqrt{\left|E - 1/u_{e,h}(\mathbf{r})\right|}, \tag{2.23}$$

$$n = \int_{1/u_e}^{+\infty} \mathrm{LDOS}_{3\mathrm{D}}(E) f_n(E) dE, \tag{2.24}$$

$$p = \int_{-\infty}^{1/u_h} \mathrm{LDOS}_{3\mathrm{D}}(E) f_p(E) dE, \tag{2.25}$$

where $f_n(E)$ and $f_p(E)$ are the Fermi-Dirac distributions for electrons and holes, respectively.

The carrier densities are input into the drift-diffusion (Eqs. 2.26 and 2.27) and recombination (Eqs. 2.28 and 2.29) equations, which are given by

$$J_n = n\mu_n \nabla E_{F_n}, \tag{2.26}$$

$$J_p = p\mu_p \nabla E_{F_p}, \tag{2.27}$$

$$\nabla \cdot (J_{n,p}) = \pm q[A_0 + B_0 np + C_0(n^2 p + np^2)], \tag{2.28}$$

$$A_0 = \frac{np - {n_i}^2}{\tau_n \left(p + n_i e^{\frac{(E_i - E_T)}{k_B T}}\right) + \tau_p \left(n + n_i e^{\frac{(E_T - E_i)}{k_B T}}\right)}. \tag{2.29}$$

J_n and J_p are the electron and hole current densities, μ_n and μ_p are the electron and hole mobilities, and E_{Fn} and E_{Fp} are the quasi-Fermi levels of electrons and holes. The Shockley-Read-Hall (SRH) model is used to account for nonradiative recombination due to defects through the rate A_0 (Eq. 2.29). τ_n and τ_p are the nonradiative electron and hole lifetimes, n_i is the intrinsic carrier density, E_i is the intrinsic energy level, and E_T is the trap energy level, which is assumed to be at midgap. B_0 and C_0 are the radiative and Auger nonradiative recombination coefficients, respectively, of bulk materials without disorder or electric field (see Ref. [27] for a more complete discussion on the choice of these coefficient values).

In the simulation process, the spatial dependence of the total polarization $\mathbf{P}^{total}(\mathbf{r})$ is first calculated to obtain the induced polarization charge $\rho_{pol}(\mathbf{r})$. Next, the Poisson equation is solved for the electrostatic potential $\varphi(\mathbf{r})$ which is used to calculate $E_c(\mathbf{r})$ and $E_v(\mathbf{r})$. The Landscape equations $\widehat{H}u_e(\mathbf{r}) = 1$ and $\widehat{H}u_h(\mathbf{r}) = 1$ are then solved for $u_e(\mathbf{r})$ and $u_h(\mathbf{r})$. From the effective potentials $1/u_e(\mathbf{r})$ and $1/u_h(\mathbf{r})$, the carrier densities of electrons and holes are calculated and fed back into the Poisson-DD equations to be solved in a self-consistent manner. Convergence is achieved when the potential energy difference between two consecutive iterations is less than 10^{-5} eV.

2.6 Long-wavelength LEDs

Long-wavelength LEDs are achieved by increasing the indium content in the InGaN QWs, which has several deleterious effects on the IQE. Some of these effects are related to the increased alloy fluctuations, while some are not. To increase indium incorporation, InGaN QWs are grown at lower temperatures, leading to poorer material quality, presumably due to a higher density of intrinsic point defects and extrinsic impurities that result in a higher SRH nonradiative recombination rate An [55,56]. Additionally, the polarization discontinuity at the QW and QB interface becomes larger as the indium fraction of the InGaN QW is increased. The resulting electric fields in the QW spatially separate electron and hole wavefunctions, thereby reducing their overlap and the bimolecular radiative recombination rate Bn^2. Lastly, increased alloy fluctuations in high indium fraction QWs lead to stronger in-plane carrier localization and a higher Auger nonradiative recombination rate Cn^3 [23,25-27]. The reduced vertical wavefunction overlap in high

indium content QWs also leads to higher overall carrier densities, thereby increasing Auger recombination at a given current density (Eq. 2.14) [57,58].

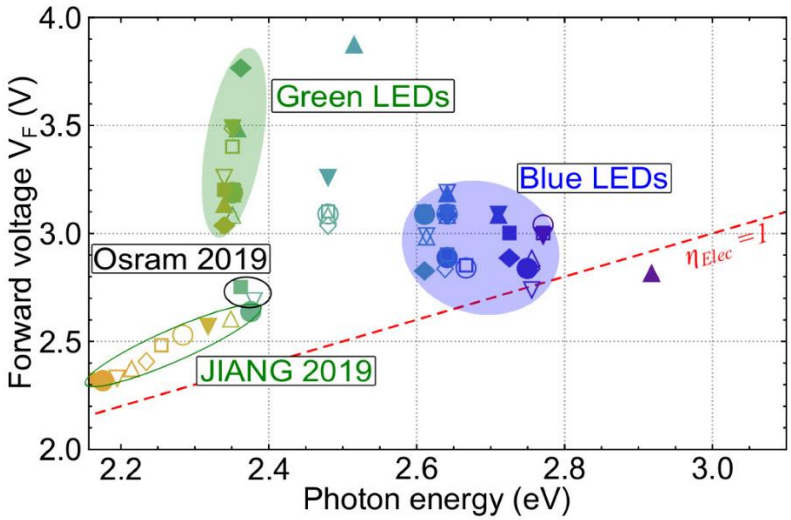

Figure 2.15. LED forward voltage at current densities ranging from 10 to 40 A cm^{-2} reported in the literature and by commercial LED producers. The red dashed line indicates where $h\nu/qV_F$ = 1. The references used for this figure can be found in the supplementary material of Ref [59]. Reproduced from [59], with the permission of AIP Publishing.

In addition to a lower IQE, state-of-the-art long-wavelength LEDs operate with significant excess forward voltage ΔV_F (Eq. 2.11) and therefore low EE (Eq. 2.10). Compared to blue LEDs, typical green LEDs suffer from poor WPE in part due to their large ΔV_F. Figure 2.15 shows the dependence of V_F on photon energy qV_{ph} as reported by commercial LED producers and in the literature at current densities ranging from 10 to 40 A cm^{-2}. From this figure, the large ΔV_F of green LEDs relative to blue LEDs can be visualized. A notable exception to the high V_F observed in green LEDs occurs when carrier injection is achieved laterally by V-defect side injection [35,60] instead of vertical injection through the QW stack as in usual LEDs. V-defect containing LEDs with wavelengths ranging from

green to amber are indicated in Fig. 2.15 as devices reported by Jiang 2019 and Osram 2019 [35].

The LED WPE can be written as

$$WPE = IQE \cdot LEE \cdot \frac{V_{ph}}{V_F}. \tag{2.30}$$

to highlight how V_F and IQE play an equal role in the overall device efficiency. While numerous publications have focused on understanding the low IQE of green LEDs [46,55-57,61], significantly less research has been devoted to identifying the barriers to carrier transport that lead to their low EE [62-64]. Chapter 3 will be primarily concerned with understanding the low EE of long-wavelength LEDs while Chapters 4 and 5 will explore approaches for its improvement.

References

[1] H. Kroemer, Proceedings of the IEEE **70**, 13 (1982).

[2] H. Kroemer, Rev. Mod. Phys. **73**, 783 (2001).

[3] A.R. Denton and N.W. Ashcroft, Phys. Rev. A **43**, 3161 (1991).

[4] O. Ambacher, J. Majewski, C. Miskys, A. Link, M. Hermann, M. Eickhoff, M. Stutzmann, F. Bernardini, V. Fiorentini, V. Tilak, B. Schaff, and L.F. Eastman, J. Phys.: Condens. Matter **14**, 3399 (2002).

[5] V. Fiorentini, F. Bernardini, and O. Ambacher, Appl. Phys. Lett. **80**, 1204 (2002).

[6] D.F. Feezell, M.C. Schmidt, S.P. DenBaars, and S. Nakamura, MRS Bulletin **34**, 318 (2009).

[7] O. Mayrock, H.-J. Wünsche, and F. Henneberger, Phys. Rev. B **62**, 16870 (2000).

[8] F. Bernardini, V. Fiorentini, and D. Vanderbilt, Phys. Rev. B **56**, R10024 (1997).

[9] E.F. Schubert, *Light-Emitting Diodes*, 2nd ed. (Cambridge University Press, 2006).

[10] C.A. Hurni, O. Bierwagen, J.R. Lang, B.M. McSkimming, C.S. Gallinat, E.C. Young, D.A. Browne, U.K. Mishra, and J.S. Speck, Appl. Phys. Lett. **97**, 222113 (2010).

[11] D.A.B. Miller, D.S. Chemla, T.C. Damen, A.C. Gossard, W. Wiegmann, T.H. Wood, and C.A. Burrus, Phys. Rev. Lett. **53**, 2173 (1984).

[12] D.A.B. Miller, D.S. Chemla, and S. Schmitt-Rink, Physical Review B **33**, 6976 (1986).

[13] A. David and M.J. Grundmann, Appl. Phys. Lett. **96**, 103504 (2010).

[14] J. Hader, J.V. Moloney, and S.W. Koch, Appl. Phys. Lett. **87**, 201112 (2005).

[15] A.I. Alhassan, R.M. Farrell, B. Saifaddin, A. Mughal, F. Wu, S.P. DenBaars, S. Nakamura, and J.S. Speck, Opt. Express, OE **24**, 17868 (2016).

[16] J. Hader, J.V. Moloney, and S.W. Koch, Appl. Phys. Lett. **96**, 221106 (2010).

[17] Q. Dai, Q. Shan, J. Wang, S. Chhajed, J. Cho, E.F. Schubert, M.H. Crawford, D.D. Koleske, M.-H. Kim, and Y. Park, Appl. Phys. Lett. **97**, 133507 (2010).

[18] M.-H. Kim, M.F. Schubert, Q. Dai, J.K. Kim, E.F. Schubert, J. Piprek, and Y. Park, Appl. Phys. Lett. **91**, 183507 (2007).

[19] Ü. Özgür, X. Ni, X. Li, J. Lee, S. Liu, S. Okur, V. Avrutin, A. Matulionis, and H. Morkoç, Semicond. Sci. Technol. **26**, 014022 (2011).

[20] Y.C. Shen, G.O. Mueller, S. Watanabe, N.F. Gardner, A. Munkholm, and M.R. Krames, Appl. Phys. Lett. **91**, 141101 (2007).

[21] E. Kioupakis, P. Rinke, K.T. Delaney, and C.G. Van de Walle, Appl. Phys. Lett. **98**, 161107 (2011).

[22] E. Kioupakis, D. Steiauf, P. Rinke, K.T. Delaney, and C.G. Van de Walle, Physical Review B **92**, (2015).

[23] C.M. Jones, C.-H. Teng, Q. Yan, P.-C. Ku, and E. Kioupakis, Appl. Phys. Lett. **111**, 113501 (2017).

[24] J. Iveland, L. Martinelli, J. Peretti, J.S. Speck, and C. Weisbuch, Phys. Rev. Lett. **110**, 177406 (2013).

[25] Y.-R. Wu, R. Shivaraman, K.-C. Wang, and J.S. Speck, Appl. Phys. Lett. **101**, 083505 (2012).

[26] T.-J. Yang, R. Shivaraman, J.S. Speck, and Y.-R. Wu, Journal of Applied Physics **116**, 113104 (2014).

[27] C.-K. Li, M. Piccardo, L.-S. Lu, S. Mayboroda, L. Martinelli, J. Peretti, J.S. Speck, C. Weisbuch, M. Filoche, and Y.-R. Wu, Phys. Rev. B **95**, 144206 (2017).

[28] D.H. Reep and S.K. Ghandhi, J. Electrochem. Soc. **130**, 675 (1983).

[29] S. Nakamura, Y. Harada, and M. Seno, Appl. Phys. Lett. **58**, 2021 (1991).

[30] X.H. Wu, P. Fini, E.J. Tarsa, B. Heying, S. Keller, U.K. Mishra, S.P. DenBaars, and J.S. Speck, Journal of Crystal Growth **189–190**, 231 (1998).

[31] F. Jiang, J. Zhang, S. Qian, and Z. Quan, *Light-Emitting Diodes: Materials, Processes, Devices and Applications*, Ed. by J. Li and G.Q. Zhang, (Springer, 2019), p. 133–170.

[32] J.W. Matthews and A.E. Blakeslee, Journal of Crystal Growth **27**, 118 (1974).

[33] A.E. Romanov, E.C. Young, F. Wu, A. Tyagi, C.S. Gallinat, S. Nakamura, S.P. DenBaars, and J.S. Speck, Journal of Applied Physics **109**, 103522 (2011).

[34] D. Holec, P.M.F.J. Costa, M.J. Kappers, and C.J. Humphreys, Journal of Crystal Growth **303**, 314 (2007).

[35] F. Jiang, J. Zhang, L. Xu, J. Ding, G. Wang, X. Wu, X. Wang, C. Mo, Z. Quan, X. Guo, C. Zheng, S. Pan, and J. Liu, Photonics Res. **7**, 144 (2019).

[36] X.H. Wu, C.R. Elsass, A. Abare, M. Mack, S. Keller, P.M. Petroff, S.P. DenBaars, J.S. Speck, and S.J. Rosner, Appl. Phys. Lett. **72**, 692 (1998).

[37] B. Heying, E.J. Tarsa, C.R. Elsass, P. Fini, S.P. DenBaars, and J.S. Speck, Journal of Applied Physics **85**, 6470 (1999).

[38] I.-H. Kim, H.-S. Park, Y.-J. Park, and T. Kim, Appl. Phys. Lett. **73**, 1634 (1998).

[39] A.E. Romanov, T.J. Baker, S. Nakamura, and J.S. Speck, J. Appl. Phys. **100**, 023522 (2006).

[40] S. Tomiya, Y. Kanitani, S. Tanaka, T. Ohkubo, and K. Hono, Appl. Phys. Lett. **98**, 181904 (2011).

[41] F. Wu, C. Lynsky, J. Ewing, M. Iza, S. Nakamura, S.P. DenBaars, and J.S. Speck, *In Preparation*.

[42] D.A. Browne, B. Mazumder, Y.-R. Wu, and J.S. Speck, Journal of Applied Physics **117**, 185703 (2015).

[43] W. Hahn, J.-M. Lentali, P. Polovodov, N. Young, S. Nakamura, J.S. Speck, C. Weisbuch, M. Filoche, Y.-R. Wu, M. Piccardo, F. Maroun, L. Martinelli, Y. Lassailly, and J. Peretti, Phys. Rev. B **98**, 045305 (2018).

[44] R. Aleksiejunas, K. Nomeika, O. Kravcov, S. Nargelas, L. Kuritzky, C. Lynsky, S. Nakamura, C. Weisbuch, and J.S. Speck, Phys. Rev. Applied **14**, 054043 (2020).

[45] K.S. Qwah, M. Monavarian, G. Lheureux, J. Wang, Y.-R. Wu, and J.S. Speck, Appl. Phys. Lett. **117**, 022107 (2020).

[46] M. Auf der Maur, A. Pecchia, G. Penazzi, W. Rodrigues, and A. Di Carlo, Phys. Rev. Lett. **116**, 027401 (2016).

[47] M. Filoche and S. Mayboroda, PNAS **109**, 14761 (2012).

[48] M. Filoche, M. Piccardo, Y.-R. Wu, C.-K. Li, C. Weisbuch, and S. Mayboroda, Phys. Rev. B **95**, 144204 (2017).

[49] D.N. Arnold, G. David, D. Jerison, S. Mayboroda, and M. Filoche, Phys. Rev. Lett. **116**, 056602 (2016).

[50] C.-K. Wu, C.-K. Li, and Y.-R. Wu, J. Comput. Electron. **14**, 416 (2015).

[51] See http://yrwu-wk.ee.ntu.edu.tw/ for "Optoelectronic device simulation laboratory".

[52] C. Geuzaine and J.-F. Remacle, Int. J. Numer. Meth. Engng. **79**, 1309 (2009).

[53] See http://gmsh.info/ for more information about Gmsh, a three-dimensional finite element mesh generator.

[54] D. Watson-Parris, M.J. Godfrey, P. Dawson, R.A. Oliver, M.J. Galtrey, M.J. Kappers, and C.J. Humphreys, Phys. Rev. B **83**, 115321 (2011).

[55] A. David, N.G. Young, C.A. Hurni, and M.D. Craven, Phys. Rev. Applied **11**, 031001 (2019).

[56] A.M. Armstrong, M.H. Crawford, and D.D. Koleske, Appl. Phys. Express **7**, 032101 (2014).

[57] E. Kioupakis, Q. Yan, and C.G. Van de Walle, Appl. Phys. Lett. **101**, 231107 (2012).

[58] A. David and M.J. Grundmann, Appl. Phys. Lett. **97**, 033501 (2010).

[59] G. Lheureux, C. Lynsky, Y.-R. Wu, J.S. Speck, and C. Weisbuch, J. Appl. Phys. **128**, 235703 (2020).

[60] C.-K. Li, C.-K. Wu, C.-C. Hsu, L.-S. Lu, H. Li, T.-C. Lu, and Y.-R. Wu, AIP Advances **6**, 055208 (2016).

[61] F. Nippert, S.Yu. Karpov, G. Callsen, B. Galler, T. Kure, C. Nenstiel, M.R. Wagner, M. Straßburg, H.-J. Lugauer, and A. Hoffmann, Appl. Phys. Lett. **109**, 161103 (2016).

[62] S.J. Chang, W.C. Lai, Y.K. Su, J.F. Chen, C.H. Liu, and U.H. Liaw, IEEE Journal of Selected Topics in Quantum Electronics **8**, 278 (2002).

[63] C.S. Xia, Z.M. Simon Li, Z.Q. Li, Y. Sheng, Z.H. Zhang, W. Lu, and L.W. Cheng, Appl. Phys. Lett. **100**, 263504 (2012).

[64] J.-Y. Chang, Y.-K. Kuo, and M.-C. Tsai, Physica Status Solidi (a) **208**, 729 (2011).

3

Excess Voltage in *c*-plane Green LEDs

3.1 Introduction

As was previously described in detail in Chapter 2, coherently grown heterostructures, such as InGaN quantum wells (QWs) and GaN quantum barriers (QBs), in the *c*-axis [0001] orientation have large internal electric fields due to discontinuities in total polarization (sum of spontaneous and piezoelectric polarization) resulting from the 6mm symmetry of the wurtzite crystal structure [1]. Additionally, the large difference in bandgaps of the constituent compounds (AlN, GaN, and InN) results in significant spatial variations in the band energy of their alloys (AlGaN and InGaN) as well as large conduction and valence band offsets in heterostructures [2]. Both the energy band fluctuations resulting from alloy disorder and the large band offsets directly impact carrier localization and transport. The presence of alloy disorder in the III-nitrides material system necessitates the use of full 3D simulations to accurately capture carrier behavior and achieve simulations that are consistent with experimental observations [2,3]. The purpose of the research in this chapter is to identify the impact of large band discontinuities and internal electric fields on excess forward voltage in multiple QW green LEDs.

The role of QW number on LED device performance has been explored in several previous publications. In an early report, Chang *et al.* measured an increase in V_F with QW

number in blue and green LEDs, which they partially attributed to an increase in series resistance and partially to the built-in voltage V_{BI} of the entire heterostructure [4]. Relative to the blue LED devices, they observed higher V_F in the green LEDs, which they ascribed to a higher resistivity of the green LED active region resulting from lower growth temperature. Xia *et al.* simulated an increase in V_F with higher QW number in blue LEDs, which they also attributed to an increase in series resistance [5]. Chang *et al.* performed simulations on blue LEDs with either InGaN or GaN QBs and one or five QWs [6]. The authors explained the lower voltage in InGaN barrier LEDs by reduced polarization-induced triangular barriers. They also concluded that the number of triangular barriers (number of QWs) influences electrical properties. It is demonstrated here that the addition of QWs should not change the built-in voltage of the diode and the polarization-related barriers cannot be described as the addition of a simple series resistance.

In this chapter, a combined experimental and computational approach based on the Localization Landscape theory of disorder [3,7-9], is used to explore the impact of QW number on V_F in *c*-plane green LEDs. The experimental LED growth and characterization is discussed first and is followed by device simulation results on similar structures. Lastly, a simulation comparison of green and blue MQW LEDs is presented. Combined, these data support a unified narrative that polarization discontinuities at the heterointerfaces and sequential carrier injection of QWs contribute to the large ΔV_F in MQW *c*-plane green LED structures [10,11].

3.2 Experimental

3.2.1 Methods

Green LEDs with varying number of QWs (one, two, three, five, and seven QWs) were grown by atmospheric pressure MOCVD on (0001) patterned sapphire substrates (PSS). A low temperature GaN nucleation layer was followed by a 3-μm high temperature unintentionally doped (UID) GaN layer, a 2-μm Si-doped *n*-GaN layer ([Si] = 6×10^{18} cm^{-3}), a ten-period *n*-$In_{0.05}Ga_{0.95}N$ (3 nm)/GaN (5 nm) superlattice layer ([Si] = 6×10^{18} cm^{-3}), and an 8 nm UID GaN layer. Next, the active region was grown undoped and consisted of 3-nm $In_{0.22}Ga_{0.78}N$ QWs, 2-nm $Al_{0.20}Ga_{0.80}N$ capping layers, and 8-nm GaN barriers. The active region was followed by 25 nm of highly doped *p*-GaN ([Mg] = 1.5×10^{20} cm^{-3}), 90 nm of *p*-GaN ([Mg] = 3×10^{19} cm^{-3}), and a 10-nm highly doped *p*-GaN contact layer. The epitaxial structure of the LEDs is shown in Fig. 3.1. The active region design of these LEDs was optimized in previous work to improve the green LED power and EQE [12-14]. The use of an AlGaN capping layer after the QW allows for aggressive growth conditions in the QBs, such as high temperature GaN growth and the introduction of H_2 carrier gas. All samples were grown to minimize V-defect formation and thus the electron and hole injection into the QWs is through the *c*-plane interface.

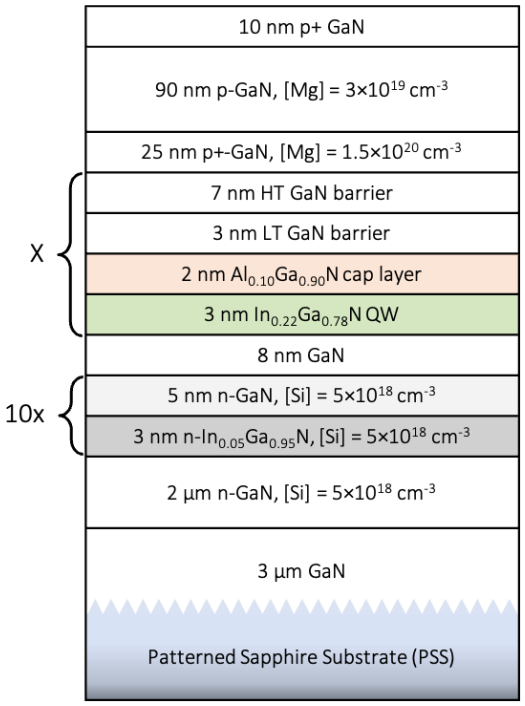

Figure 3.1. Epitaxial structure of LEDs grown by MOCVD with varying active region period X, where X = 1, 2, 3, 5, 7.

All samples underwent a post-growth anneal in N_2/O_2 at 600 °C for 15 minutes to activate the Mg-doped layers. The samples were then fabricated into LEDs using standard mesa isolation and contact deposition. Figure 3.2 shows the process flow for device fabrication. The mesa was first defined lithographically and a $Cl_2/SiCl_4$ reactive ion etch (RIE) was used to etch the GaN material. Plasma enhanced chemical vapor deposition (PECVD) was used to blanket deposit SiO_2 over the sample surface. The *p*-contacts were lithographically defined and SiO_2 was removed from the contact openings using a buffered hydrofluoric acid (BHF) wet etch. A metal stack of 30/400 nm Pd/Au was used as the contact to *p*-GaN for simple fabrication and reliable voltage determination. The device area was taken to be the area of the contact pad deposited on the mesa, where the contact pad area was 90% that of the mesa area. Lastly, the contact areas to *n*-GaN were lithographically

defined, SiO_2 was removed using BHF, and a metal stack consisting of 100/100/300 nm of Al/Ni/Au was deposited. Both contact metal stacks were deposited using electron-beam deposition.

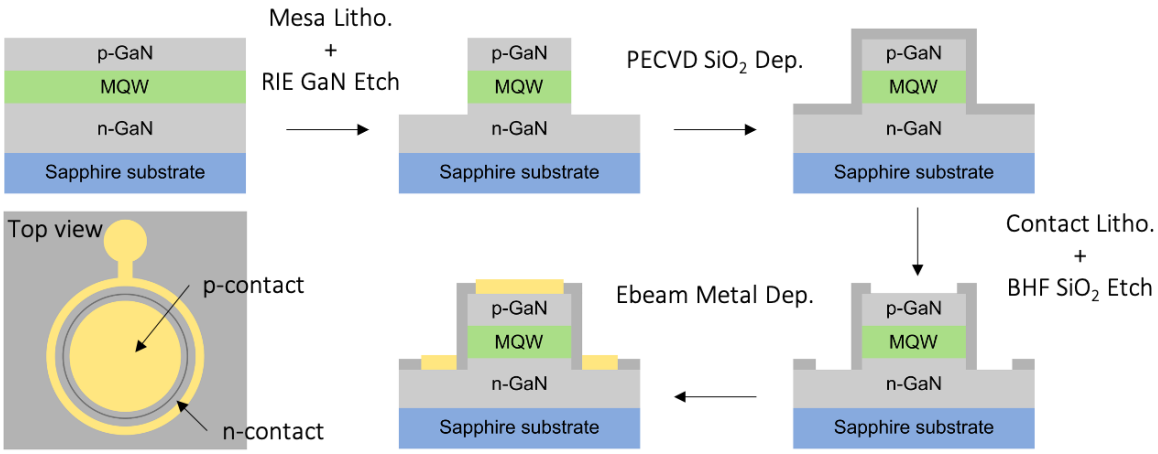

Figure 3.2. Process flow for fabrication of epitaxial material into an LED device with SiO_2 sidewall passivation, Pd/Au metal contacts to *p*-GaN, and Al/Ni/Au metal contacts to *n*-GaN. Note that the schematic is not drawn to scale.

Simulations of the optical and electrical properties of green LEDs require prior knowledge of the composition and thickness of the InGaN and AlGaN layers comprising the active region [2,3]. Detailed layer thicknesses and composition information can be obtained using atom probe tomography (APT) [3,15,16].The APT measurements shown here for the five-QW sample were performed by Dr. Bastien Bonef. Details of the APT sample preparation, evaporation, and reconstruction parameters can be found in Ref [15].

Figure 3.3(a) shows the APT reconstruction of the five-QW sample. The five InGaN/AlGaN/GaN QWs/cap layers/QBs can be clearly observed in the figure. Figure 3.3(b) is a 1D concentration profile showing the indium and aluminum III-site fraction variations in the active layer along the [0001] direction. The peak indium fractions measured

in the different InGaN QWs are 0.22 ± 0.02, 0.22 ± 0.02, 0.23 ± 0.02, 0.22 ± 0.02, and 0.22 ± 0.02 from the bottom to the top of the structure, which indicates well-controlled growth of the InGaN layers. The average aluminum composition in the capping layers was ~0.20, which is consistent with the composition expected from growth calibrations. Despite the inability of APT to resolve atomic planes in the [0001] direction in group III-N materials [17,18], the thickness of QWs can be estimated from the concentration profile in Fig. 3.3(b). The full width at half maximum (FWHM) of the indium profiles are used to measure the QW thicknesses. From the bottom to the top of the structure, the measured thicknesses are 2.8 nm, 2.9 nm, 2.9 nm, 3 nm, and 2.8 nm, which again closely agrees with values predicted from InGaN growth rate calibrations.

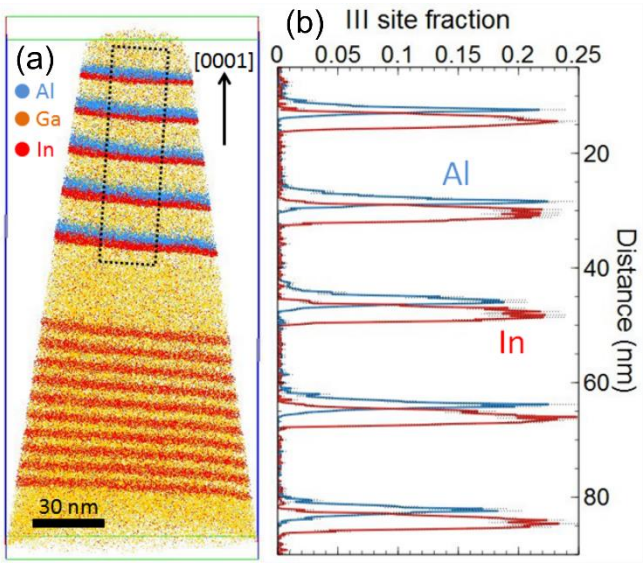

Figure 3.3. (a) Atom probe tomography 3D reconstruction of the active region for the five-QW sample. The InGaN/GaN superlattice and the five-period InGaN/AlGaN/GaN QWs/cap layers/QBs can be observed in the reconstruction. (b) 1D concentration profile of indium and aluminum measured along the [0001] direction and in the region defined in (a). Reprinted with permission from [10] Copyright 2020 by the American Physical Society.

Finally, statistical distribution analyses (SDA) were performed on the InGaN QWs to investigate their respective alloy distributions [19]. The experimental alloy distribution measured by APT are compared to the binomial distribution expected for random alloys, as described in Refs. [16] and [20]. SDA revealed that the five-QWs alloy compositions are randomly distributed in the QW plane, as usually observed for *c*-plane InGaN [21,22]. The results from APT are therefore reliable inputs for device simulations.

3.2.2 Results

The experimentally measured V_F values at 20 A cm^{-2} and 100 A cm^{-2} are plotted in Fig. 3.4. At a given current density, a systematic increase in V_F is observed as the QW number increases. The peak electroluminescence (EL) wavelength at 20 A cm^{-2} for the samples with one, two, three, five, and seven QWs are 508, 519, 515, 524, and 516 nm, respectively, as shown in Fig. 3.5(a). The integrated EL intensity at 20 A cm^{-2} is plotted in Fig. 3.5(b). Due to the large variation in devices measured on a given sample, no clear trend in integrated EL intensity can be discerned. All samples in this series, including the one-QW sample, showed large excess voltage relative to V_{ph}. A portion of this excess voltage can be attributed to the high aluminum content in the AlGaN capping layers, based on previous findings [23]. Another known contribution to V_F is the nonideal contact resistance between Pd/Au and *p*-GaN in these samples which leads to higher series resistance.

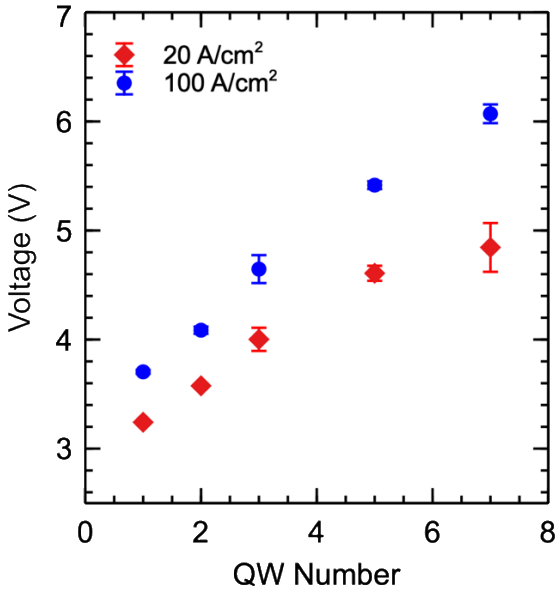

Figure 3.4. Forward voltage at 20 and 100 A cm^{-2} of green LEDs with varying QW period. A systematic increase in V_F is observed as the QW period is increased.

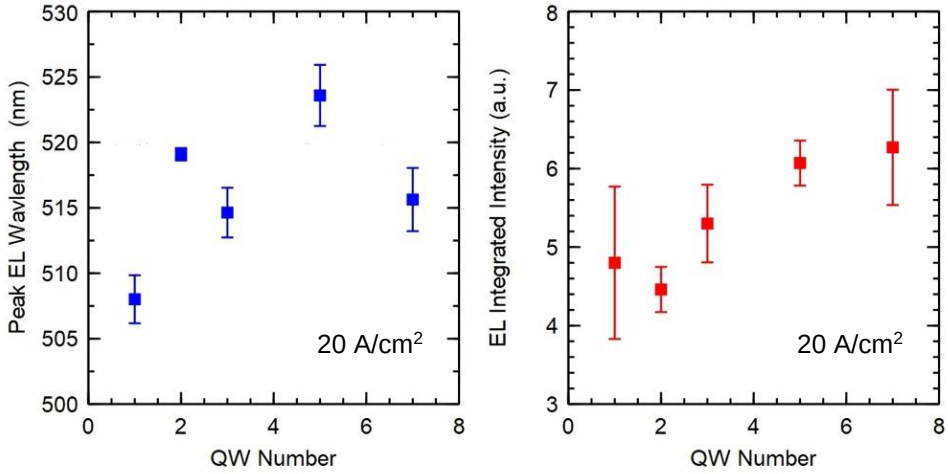

Figure 3.5. (a) Peak electroluminescence (EL) wavelength and (b) EL integrated intensity at 20 A cm^{-2} for green LEDs with varying QW period.

Circular transmission line measurement (CTLM) structures, such as the one shown in Fig. 3.6(a), on final fabricated devices typically allow for electrical characterization of the metal-semiconductor contacts. The circular test structures consist of a conducting inner

region of radius L, a gap of width d, and a conducting outer region. For these samples, the conducting regions were Pd/Au metal deposited on *p*-GaN and the gaps were bare *p*-GaN material with widths ranging from 5 μm to 55 μm. An important value obtained from this analysis is the transfer length L_T, which can be understood as the distance over which most of the current transfers from metal to semiconductor or from semiconductor to metal. The transfer length is defined by the specific contact resistivity ρ_c and the sheet resistance R_{sh} according to $L_T = \sqrt{\rho_c / R_{sh}}$. If $L \gg 4L_T$, the total resistance between the external and internal contacts is given by [24],

$$R_T = \frac{R_{sh}}{2\pi}\left[\frac{L_T}{L} + \frac{L_T}{L+d} + ln\left(1 + \frac{d}{L}\right)\right]. \tag{3.2}$$

Experimentally, I-V measurements were taken for each gap size and a linear fit was performed to calculate R_T. Equation 3.2 was used to fit R_T as a function of d and extract L_T and R_{sh}, from which ρ_c was then determined. Figure 3.6(b) shows the experimental CTLM I-V data for different gap widths along with linear fits to the data. The dependence of current on voltage exhibits rectifying behavior for small gap sizes as seen by the "S-shape" of the curves. Figure 3.6(c) shows the calculated resistance versus gap size along with the fit to Eq. 3.2. From the CTLM analysis, a specific contact resistivity of ρ_c = 0.015 Ω cm^2 was obtained. However, arriving at this value requires the assumption early on that the contacts are ohmic and the CTLM I-V data is linear, which is not the case here. Thus, specific contact resistivity values calculated from the CTLM data are not reported here due to the inaccuracy of performing this calculation on contacts with nonlinear I-V characteristic. By measuring and analyzing the CTLM data on all the reported LEDs, it is confirmed that the

voltage contributions from slight rectifying behavior of the *p*-contacts are the same for all samples and therefore do not impact the observed voltage trend with QW number.

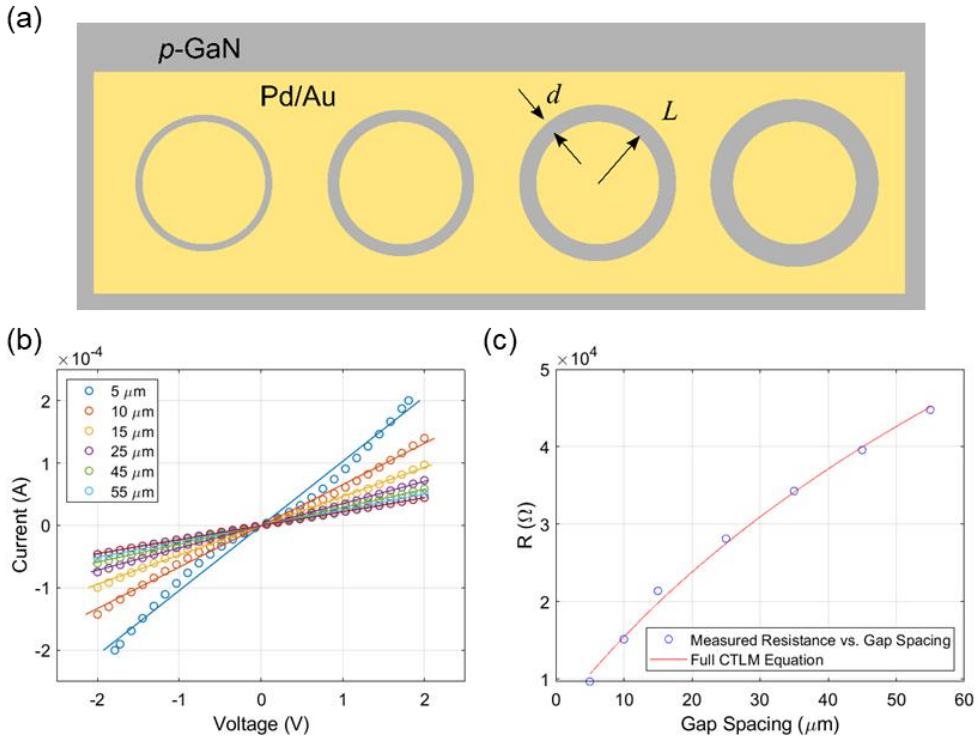

Figure 3.6 (a) Schematic of CTLM test structure with inner radius L and gap size d, where the gold regions are Pd/Au metal and the grey regions are *p*-GaN semiconductor. (b) Measured I-V data for CTLM patterns with varying gap sizes. Circles represent data points and lines represent a linear fit of the data. (c) Calculated resistance versus gap spacing is given as circles and the line is a fit of the data using Eq. 3.2.

The resistance due to the metal to *p*-type semiconductor contact will contribute to the overall series resistance. Therefore, as an alternative to the CTLM analysis, the linear portion of the experimental J-V curves were fit to extract the specific resistivity for each sample. This calculation yielded specific resistivity values of 3.8×10^{-3}, 4.0×10^{-3}, 4.5×10^{-3}, 4.5×10^{-3}, 6.7×10^{-3} Ω cm^2 for the samples with one, two, three, five, and seven QWs, respectively. The similar values for ρ again confirm that the series resistance, which is likely

dominated by the *p*-contacts and *p*-GaN layer, is similar for all samples and does not impact the overall voltage trend. The average specific resistivity, ρ = 4.7×10^{-3} Ω cm^2, was used to adjust the 1D and 3D simulation J-V curves shown in Fig. 3.8. The simulation data were corrected by plotting J as a function of V_{adj}, where $V_{adj} = V_{original} + (J \cdot \rho)$.

3.3 Device Simulations – Green LEDs

3.3.1 Methods

Rational heterostructure design via realistic 3D simulations is central to realizing reduced V_F. The random alloys in the active region of LEDs, such as InGaN and AlGaN, have intrinsic compositional fluctuations which translate into potential fluctuations. These in turn give rise to local potential barriers and minima that directly impact carrier localization, transport, and recombination. To capture the inherent 3D nature of nitride LEDs, the 3D-DDCC solver [25] is used here to simulate the electrical behavior of LED devices. The complete description of the method and parameters used are described in Chapter 2. All simulations presented here use 100% of the known values for the spontaneous and piezoelectric polarization parameters [1].

The green LED structure was first defined by specifying the thickness, doping, and carrier lifetimes of the different layers. The simulated structures were similar to the experimental structures described in Section 3.2, with the exceptions of thinner *p*-GaN and *n*-GaN layers of 40 nm and exclusion of the superlattice to limit the number of mesh points. The differences between the simulated and experimental structures do not impact the final results. The active region was composed of n × 3 nm $In_{0.22}Ga_{0.78}N$ QWs, n × 2 nm $Al_{0.20}Ga_{0.80}N$ cap layers, and (n + 1) × 8 nm GaN barriers, where n is the number of QWs.

The lateral dimension of the domain was 30 nm × 30 nm and Born-Von-Karman boundary conditions were applied such that the simulated system behaves as a semi-infinite medium. The domain was then meshed into small elements using Gmsh [26,27]. The mesh size was refined around the alloy regions of the structure (InGaN QWs and AlGaN cap layers). The mesh size in the *XY* lateral dimension was 0.5 nm × 0.5 nm and ranges between 0.2 to 1 nm in the *Z* direction. Finally, the alloy composition map was randomly generated using a Gaussian average weight method and affected to the node of the mesh. The five-QW LED structure is shown in Fig. 3.7 along with the aluminum and indium alloy maps in the *XY* plane of the AlGaN cap and InGaN QW, respectively. The strain and polarization fields (spontaneous and piezoelectric) were calculated before entering the self-consistency loop [3].

1D simulations were also performed for comparison with experiment and 3D simulations. The 1D drift-diffusion charge control (1D-DDCC) solver [25] was used and assumes 100% polarization fields. These 1D simulations cannot account for in-plane alloy fluctuations. The InGaN QW and AlGaN cap concentration profiles in the *Z* direction are described by step functions, rather than the Gaussian profiles used in 3D simulations.

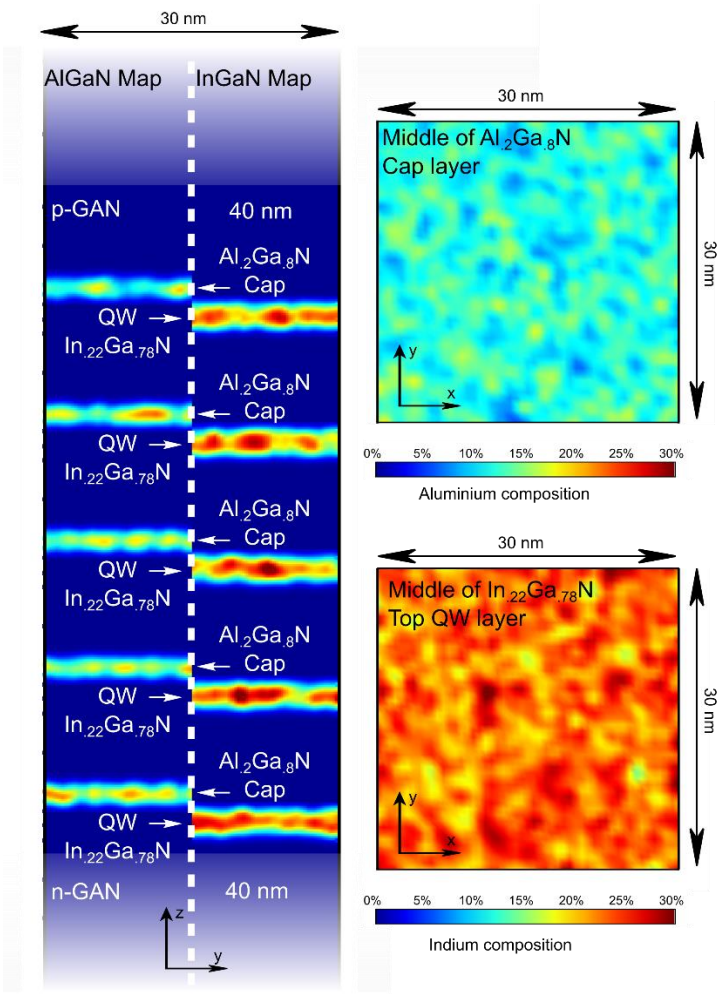

Figure 3.7. Simulated alloy map of a five-QW *c*-plane green LED with $In_{0.22}Ga_{0.78}N$ QWs and $Al_{0.20}Ga_{0.80}N$ capping layers. The random alloy fluctuations are visible as indium-rich and indium-poor regions in the QW and aluminum-rich and aluminum-poor regions in the capping layer. Reprinted with permission from [10] Copyright 2020 by the American Physical Society.

3.3.2 Results

Experimental *J-V* characteristics of the LEDs are shown as solid curves in Fig. 3.8; for a given current density, an increase in V_F is observed with increasing number of QWs. The *J-V* curves simulated using the 1D-DDCC algorithm are shown as dashed curves in Fig. 3.8(a) and the *J-V* curves for 3D simulated structures are shown as dotted curves in Fig. 3.8(b). Both the 1D and 3D *J-V* curves were adjusted based on the average experimental

specific resistivity, as discussed in Section 3.2. Compared to 1D, 3D simulations consistently predict a lower V_F and are in better agreement with experimental results. 3D simulations allow for the inclusion of in-plane alloy fluctuations, which were shown to play a key role in carrier transport for blue LEDs by providing preferential current paths for carriers, leading to lower turn-on voltages [2,3,28]. The same conclusion can be made for green LEDs where considering the 3D description of alloys delivers simulations with improved predictive capability. At 100 A cm^{-2} the average voltage added per QW is 0.41 V from experimental data and 0.48 V from 3D simulations.

Reasonable agreement between 3D simulations and experimental results was achieved without the need to adjust the polarization parameters, whereas in much 1D commercial software, the known polarization values [1] are reduced by as much as 50% to predict voltages consistent with experiments. Despite the improved predictive capability of the 3D simulations, discrepancies between the experimental and simulated J-V curves exist. In the low current density regime near diode turn-on, the shape of the J-V curves for the simulations and experiments deviate. The model used here is not able to capture certain physical phenomena which occur near LED turn-on. Namely, carrier tunneling and parallel shunt pathways may alter injection at low current densities and, in addition, unintentionally nucleated V-defects may provide a lower voltage barrier to carrier injection. The absence of these phenomena in the model may explain some of the differences which exist between experimental and simulation results. A semilogarithmic plot of the experimental J-V data is included in Fig. 3.8(c) to highlight the low current density device behavior.

Such a voltage penalty per QW is not measured in similar experimental or simulated MQW LED structures emitting in the blue spectral range. In previous work, a simulated V_F

= 2.9 V at 20 A cm^{-2} was reported for a six-QW blue *c*-plane LED [3], which is close to the photon voltage (V_{ph} = 2.76 V at λ = 450 nm). The results presented here suggest that the voltage penalty and its increase with QW number is inherent to *c*-plane LEDs emitting in the green spectral range and longer.

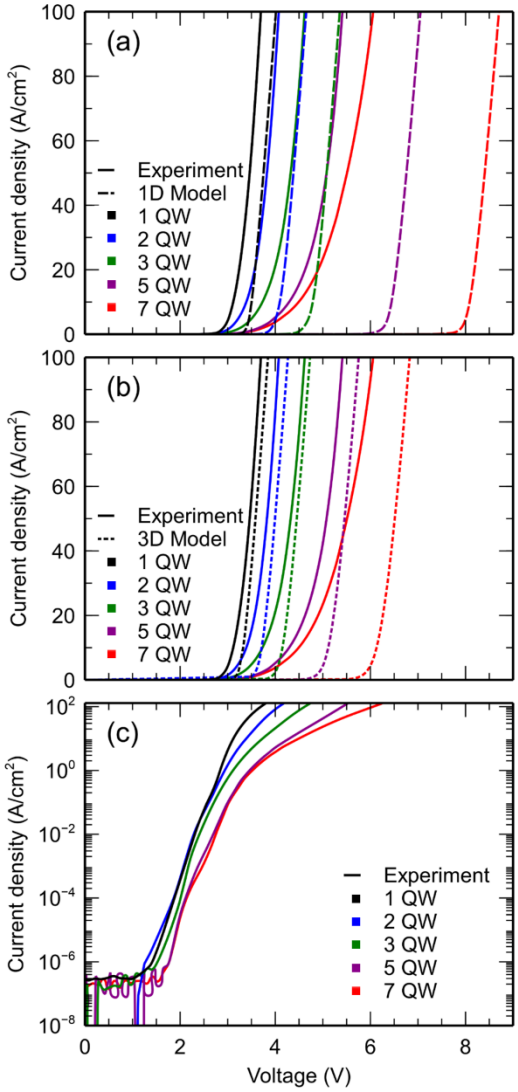

Figure 3.8. (a) Experimental *J*-*V* curves (solid) and 1D simulated *J*-*V* curves (dashed) for LEDs with varying number of QWs. (b) Experimental *J*-*V* curves (solid) and 3D simulated *J*-*V* curves (dotted) for LEDs with varying number of QWs. The 1D simulations predict significantly higher forward voltage compared to their 3D counterparts. (c) Experimental *J*-*V* curves on a semilogarithmic scale show the low current density device behavior. Reprinted with permission from [10] Copyright 2020 by the American Physical Society.

To further elucidate the role of QW number on V_F, the effective band diagrams of each structure are examined. In Fig. 3.9(a) the average indium and aluminum composition in the Z direction indicate the position of the InGaN QWs and AlGaN cap layers, respectively. The effective band diagram and V_F obtained by the 3D-DDCC solver for structures with one, three, five, and seven QWs are shown at 0 A cm^{-2} [Fig. 3.9(b)] and 10 A cm^{-2} [Fig. 3.9(c)]. The 0 eV position corresponds to the bottom of the $1/u_e$ potential on the *n*-GaN side of the LED, equal to the conduction band edge. The inset of Fig. 3.9(b) highlights the polarization barriers (fixed negative polarization-related charge) appearing at the GaN/InGaN (lower QB/QW) interfaces which prevent electrons from flowing inside the QWs where they can recombine. From the experimental and 3D simulated J-V curves [Fig. 3.8(b)], LED structures with more QWs require significantly more forward bias than the one-QW structure to reach the same current density. This trend is also clear in the effective band diagrams where the structures with three, five, and seven QWs are beyond flat band operation at 10 A cm^{-2}, further demonstrating how each additional QW results in a voltage penalty.

The band structures are also consistent with the experimental data which shows that at 10 A cm^{-2} the LEDs with three, five, and seven QWs are operating at voltages above V_{BI} (~3.3 V). Figure 3.9(d) shows the simulated "overshoot", or "overflow", fraction of injected current versus current density for LEDs with varying QW number. These predictions differ from those calculated for blue LEDs [3], where overflow only becomes significant for current densities in excess of ~1 kA cm^{-2}. The large overflow current for green LEDs, relative to blue LEDs, contributes to their low WPE. The simulated overflow is due in part to the diode bias approaching or exceeding V_{BI} at 10 A cm^{-2}. However, because the

simulated voltage exceeds the experimental voltage, overflow may be overemphasized by the simulations.

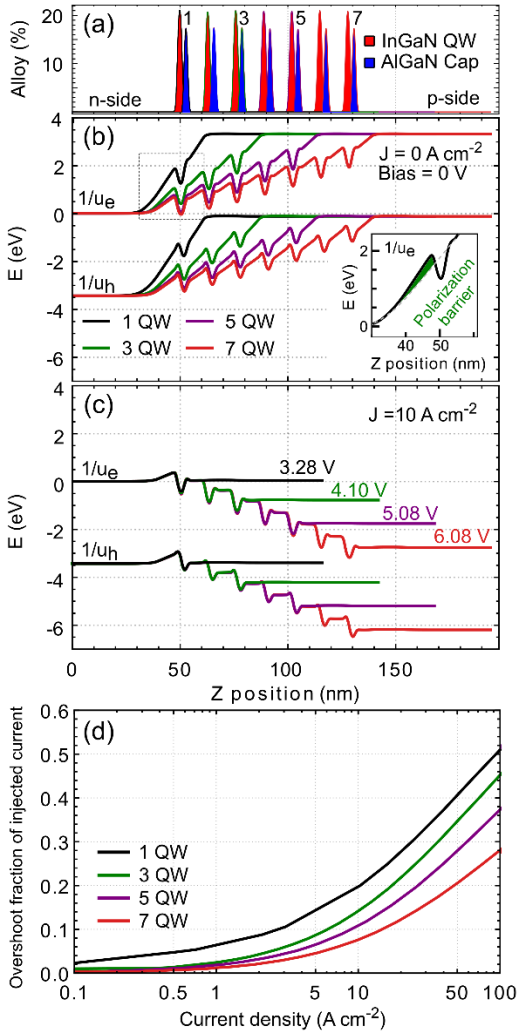

Figure 3.9. (a) Indium and aluminum profiles for the InGaN QW and AlGaN cap layers in the LED active region. Effective band diagrams for LEDs with one, three, five, and seven QWs at (b) 0 A cm^{-2} and (c) 10 A cm^{-2}. (d) Overshoot, or overflow, fraction of injected current versus current density for LEDs with one, three, five, and seven QWs. Reprinted with permission from [10] Copyright 2020 by the American Physical Society.

3.4 Device Simulations – Blue and Green LED Comparison

In the previous sections, polarization barriers were identified as a contributing factor to high V_F in MQW green devices. In this section, the differences between blue and green-emitting devices are explored in greater detail using the 3D-DDCC solver. A simulation-based approach allows for the role of polarization to be isolated from other effects. The findings presented here indicate that, in addition to strong piezoelectric fields, large band offsets between the barriers and QWs in green LEDs have an important impact on the excess turn-on voltage. Through simulations of *c*-plane blue and green LEDs with different numbers of QWs and either 100% or 0% polarization, it is shown that polarization barriers only partly explain the excess voltage for green LEDs. Theoretical evidence of sequential carrier injection of QWs as an additional contribution to excess voltage in MQW *c*-plane green LED structures is proposed.

3.4.1 Methods

In these simulations, the simplified *c*-plane LED structures presented in Fig. 3.10 were used. A 40-nm *n*-GaN layer (N_D = 6×10^{18} cm^{-3}) was followed by the active region composed of n × 3-nm In$_x$Ga$_{1-x}$N QWs and (n + 1) × 8-nm GaN barriers, where n is the number of QWs and x is the indium composition. The structure was completed by a 10-nm *p*-GaN layer (N_A = 3×10^{19} cm^{-3}) and a 40-nm *p*-GaN layer (N_A = 2×10^{19}cm^{-3}). The number of QWs was either one or five and the mean indium composition in the InGaN QW was 15% for the blue LED structure and 24% for the green LED structure. These concentrations are consistent with APT measurements of blue and green LEDs grown by MOCVD. The indium alloy maps in the XY plane of the QW for the blue and green LED structures are shown in

Fig 3.10. The structures were meshed using Gmsh [26,27]. A constant mesh size of 0.6 nm in the *XY* planes was used along with a variable mesh size in the *Z* direction that varied between 1 nm in the *p*- or *n*-GaN to 0.1 nm in the QW layers and at the layer boundaries.

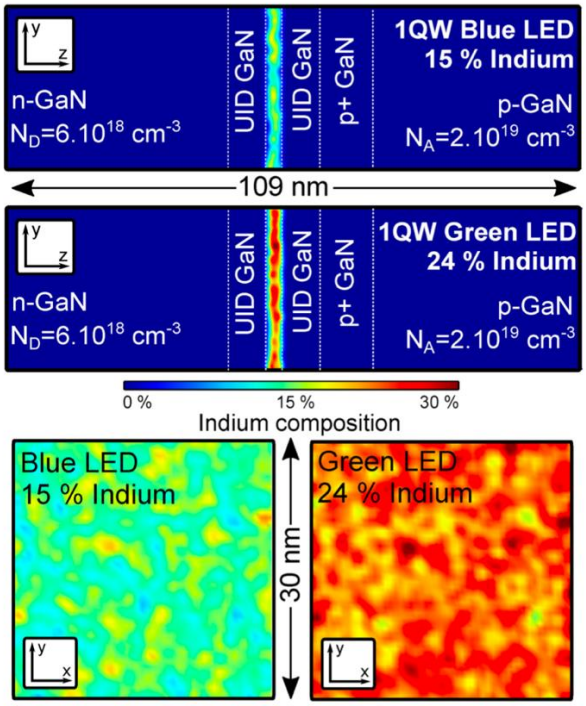

Figure 3.10. Top panel: Maps of the *YZ* plane showing the single QW LED structures and indium composition. The same structures are used for the blue ($In_{0.15}Ga_{0.85}N$ QW) and green ($In_{0.24}Ga_{0.76}N$ QW) LEDs. Bottom panel: *XY* map of indium distribution in the InGaN QW for blue (left) and green (right) LED structures. Reproduced from [11], with the permission of AIP Publishing.

3.4.2 Results

The simulated *J*-*V* curves for green (24% indium) and blue (15% indium) LEDs with one and five QWs are presented in Fig. 3.11(a). The *J*-*V* characteristics are shown as solid lines for the single QW structures and dashed lines for the five-QW structures. For the blue LED structures, V_F increases moderately with the addition of QWs. At a current density of 10 A cm^{-2}, the single QW blue LED has a V_F of 3.04 V, whereas the five QW structure has a

V_F of 3.44 V. In contrast, at 10 A cm^{-2}, the green LEDs have a V_F of 3.32 V and 5.06 V for the one-QW and five-QW structures, respectively. Figures 3.11(b) and 3.11(c) show the effective band diagrams ($1/u_e$ and $1/u_h$) of the blue and green LED structures at J = 10 A cm^{-2}. The 0 eV position is defined at the bottom of the effective conduction band at the *n*-side. Both blue LED structures operate in the flat band regime, near V_{BI}, whereas the five-QW green LED operates at a severe over-biased condition.

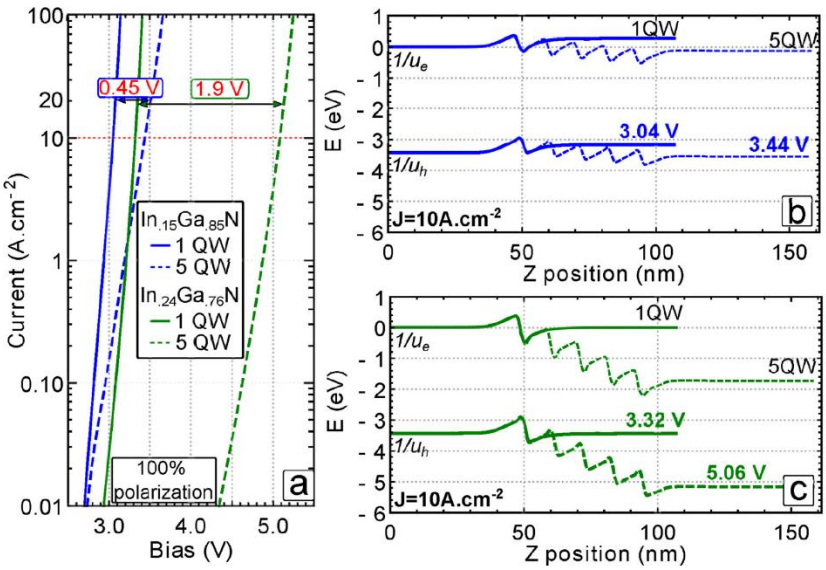

Figure 3.11. (a) Simulated J-V characteristics for LEDs with one QW (solid) or five QWs (dashed) and 15% (blue) or 24% (green) indium in the InGaN QW. 100% of the known polarization values were used. Effective band diagrams for the (b) blue and the (c) green LED structures. A clear voltage drop in the active region is visible for the five-QW green LED structure. Reproduced from [11], with the permission of AIP Publishing.

To understand the simulated J-V characteristics, the differences in carrier distribution and recombination in blue and green MQW LEDs were examined. The mean electron $\bar{n}$ and hole $\bar{p}$ carrier densities in the different QWs can be calculated using the following equations,

$$\bar{n} = \frac{\int_{Z_{min}}^{Z_{max}} n(z)dz}{Z_{max} - Z_{min}}, \tag{3.4a}$$

$$\bar{p} = \frac{\int_{Z_{min}}^{Z_{max}} p(z)dz}{Z_{max} - Z_{min}}, \tag{3.4b}$$

where Z_{min} and Z_{max} are the bottom and top position of the considered QW, respectively. Figure 3.12(a) shows $\bar{n}$ and $\bar{p}$ in each QW for the five-QW structures at J = 100 A cm^{-2}. In this figure, the QW number 1 is the bottom (*n*-side) QW and QW number 5 is the top (*p*-side) QW. In both blue and green LEDs, for a given QW number, the populations of electrons and holes are similar. However, the topmost QW exhibits much higher mean carrier densities than the bottom QWs in both structures.

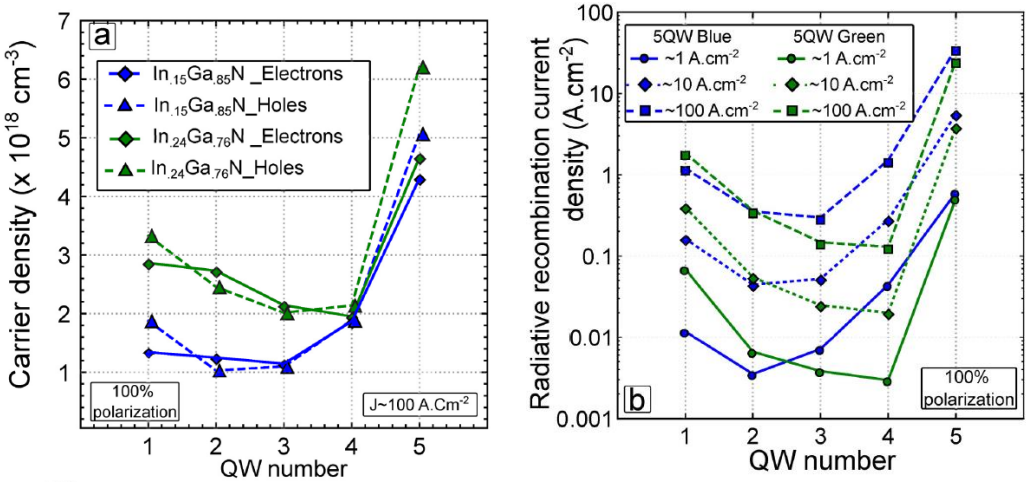

Figure 3.12. (a) Integrated electron (solid, diamond) and hole (dashed, triangle) densities for the different QWs in blue and green five-QW LED structures at 100 A cm^{-2}. (b) Comparison of the radiative recombination current density J_{Rad} in the different QWs in blue and green five-QW LEDs at 1 A cm^{-2} (solid, circle), 10 A cm^{-2} (dotted, diamond), and 100 A cm^{-2} (dashed, square) for 100% of polarization. Reproduced from [11], with the permission of AIP Publishing.

From $\bar{n}$ and $\bar{p}$, the radiative recombination current density J_{rad} in each QW can be calculated by

$$J_{Rad} = e \cdot L_z \int_{L_z} R_{Rad}(z)dz. \tag{3.5}$$

In Eq. 3.5, $R_{Rad}(z)$ is the radiative recombination rate and L_z is the QW width. R_{Rad} is equal to $B_0 np$ as described in Chapter 2, where B_0 is the radiative recombination coefficient of hypothetical bulk material without disorder or electric field. More details about the computation of R_{Rad} are discussed in Refs [3,8]. Figure 3.12(b) shows the calculated J_{rad} in each QW for the blue and green five-QW LED structures for current densities ranging from 1 to 100 A cm^{-2}. For most of the QWs, the blue LED exhibits a higher J_{Rad} than the green LED due to the smaller QCSE. There is also only a small change in the carrier distribution among the QWs as the current density is increased. In both structures, the top QW is the primary contributor to the overall radiative recombination current. This is consistent with previous findings which demonstrate that for III-nitride LEDs, *nearly all* emission comes from the top, *p*-side QW [3,29,30].

Polarization discontinuities give rise to energetic barriers for carrier transport and contribute to the voltage penalty in green LEDs [10]. It is commonly assumed that this is the only contribution to the voltage penalty [5,31-35]. To explore this hypothesis, the polarization was artificially turned off in the simulations by setting all piezoelectric coefficients and spontaneous polarization values to zero. This is equivalent to centrosymmetric GaN (not zinc blende GaN, which still shows piezoelectricity). The other parameters were kept the same as those used in other simulated *c*-plane structures. These simulations with the polarization turned off (0% polarization) cannot be considered as

equivalent to simulations of *m*-plane structures given that several parameters are different from the *c*-plane case [36]. The simulated *J*-*V* curves for one- and five-QW blue and green LED structures with 0% polarization are shown in Fig. 3.13(a).

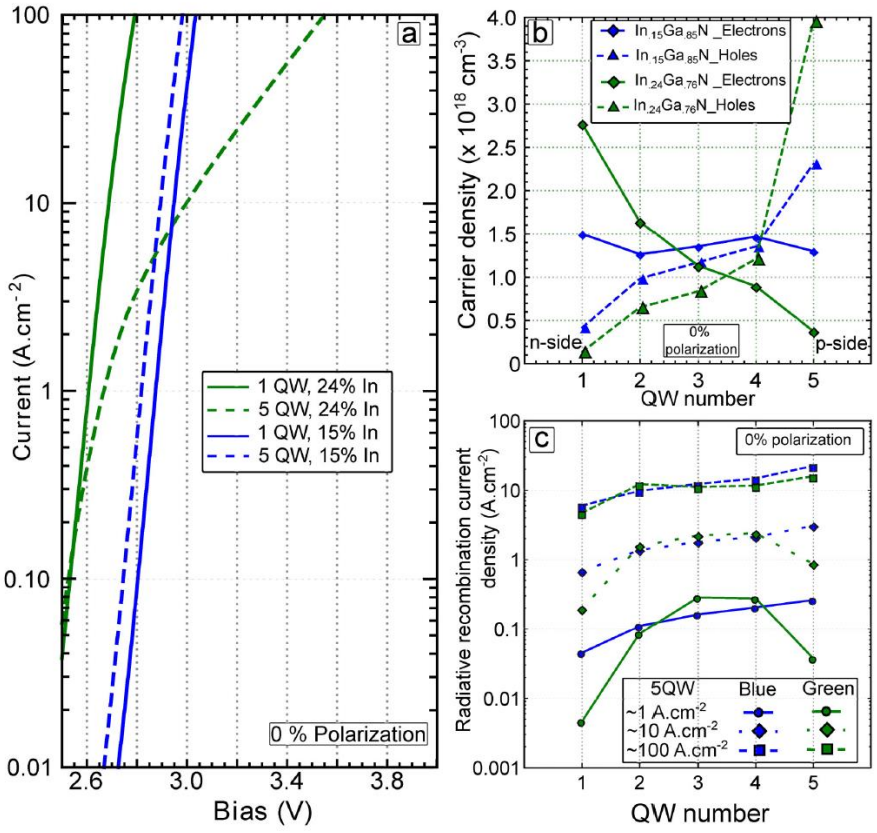

Figure 3.13. (a) Simulated 0% polarization *J*-*V* curves for LEDs containing 15% (blue) and 24% (green) indium with one QW (solid) and five QWs (dashed). (b) Average integrated electron (solid, diamond) and hole (dashed, triangle) densities for the different QW of 0% polarization MQW LED structures at J = 100 A cm^{-2}. (c) Comparison of the radiative recombination current density J_{Rad} in the different QWs for 0% polarization MQW LEDs at 1 A cm^{-2} (solid, circle), 10 A cm^{-2} (dotted, diamond), and 100 A cm^{-2} (dashed, square). Reproduced from [11], with the permission of AIP Publishing.

For the blue LED structures, in the absence of polarization, there is a small difference of 0.05 V between the single and five-QW structures. The primary barrier to carrier transport in the five-QW blue LED structure is therefore the 0.4 V piezoelectric

barrier, which can be seen when comparing Fig. 3.11(a) with 100% polarization and Fig. 3.13(a) with 0% polarization. The observed trends are different for green LED structures when polarization is turned off. The *J-V* curves for the one- and five-QW structures in Fig. 3.13(a) are very close for current densities below 1 A cm^{-2}; however, the curves diverge at higher current densities. For the five-QW structure, the *J-V* exhibits a strong slope modification, indicating another transport mechanism is present that is not observed in the one-QW green, one-QW blue, or five-QW blue structures. It is hypothesized that the change in transport is a result of sequential injection of carriers in the QWs. This effect arises due to the large band offsets between InGaN QWs and GaN QBs. To optimize carrier transport at a given bias, an inhomogeneous voltage drop occurs between QWs, with charges accumulating in the terminal QWs. Reaching the next QWs then requires an additional bias.

Figure 3.13(b) shows the mean electron and hole carrier densities (calculated according to Eq. 3.4) for blue and green five-QW structures with 0% polarization at J = 100 A cm^{-2}. Both structures exhibit more unbalanced electron and hole populations compared to the case of 100% polarization [Fig. 3.12(a)]. For the MQW blue LED, the electron population is relatively constant, and the imbalance is dominated by poor hole transport from the *p*-side to the *n*-side of the active region. The difference between electron and hole populations for a given QW is more pronounced in the green LED structures, where electron injection inhomogeneity mirrors that of holes. The *n*-side QWs are electron rich while the *p*-side QWs are hole rich. This is believed to be an indication of sequential injection of the QWs which results in the terminal QWs becoming populated before the central QWs. The sequential injection phenomenon is also present in the simulations using 100% polarization; however, because of the piezoelectric barriers, the 100% polarization structures operate at

higher bias. The sequential filling is thus obscured and can only be clearly seen in the 0% polarization case at lower bias.

Figure 3.13(c) shows the radiative recombination current density (Eq. 3.5) in each QW at different current densities for structures with 0% polarization. For the blue LED, the distribution of J_{rad} between the QWs does not change when the current density is increased. Compared to the 100% polarization case shown in Fig. 3.12(b), here the distribution of J_{rad} between the QWs is more balanced, with each QW contributing relatively equally to the overall radiative recombination current. For the five-QW green LED at a low current density of 1 A cm^{-2}, the highly unbalanced populations of carriers due to sequential injection results in an atypical distribution of J_{rad} [Fig. 3.13(c)]. Emission is primarily coming from the central (third and fourth) QWs where both carrier types are present. When the current density is increased to 100 A cm^{-2}, the J_{rad} distribution between QWs is similar to that observed for blue LEDs, with each QW contributing in a more equal way to the total radiative recombination current. However, the unbalanced electron and hole carrier densities in the green QWs at 100 A cm^{-2} [Fig. 3.13(b)] shows that sequential injection is present at high J, even if the radiative recombination is more uniform.

The sequential injection phenomenon should occur whenever large band offsets are present, and it should be addressed through device design. It has been experimentally observed in electron transport in photoexcited III-nitride MQWs and other materials that the QWs are not equally populated [30,37,38]. Moreover, these experimental papers tend to prove that the interwell transport in MQW structures is dominated by thermionic emission, similar to the hypothesis here of drift-diffusion transport in quasi-equilibrium. One solution to avoid sequential injection through stacked QWs could be provided by lateral injection in

the MQW [39,40]. In Fig. 2.15, the series of LEDs with wavelengths ranging from 525 nm to 600 nm from Jiang *et al.* and a series of Osram green LEDs are at considerably lower V_F than other commercially available and published results [41]. In both cases, V-defects are intentionally nucleated and propagate through the active region to provide a low barrier path for hole injection across the semipolar sidewalls. V-defects therefore help the carriers to avoid the energy barriers that are present when the carriers are sequentially injected in vertical QW layer stacks [42-45]. Thus, the mechanism leading to the excess voltage described here does not exist in LEDs with engineered V-defects.

3.5 Conclusions

Through experiment and simulation, two mechanisms are identified that contribute to the increase in V_F with QW number in green LEDs: polarization-induced barriers [10] and sequential filling of QWs [11]. The polarization barriers (fixed negative polarization-related charge) appearing at the GaN/InGaN (lower barrier/QW) interfaces prevent electrons from flowing inside the QWs where they can recombine. With the fraction of indium in green emitting QWs being higher than that of blue, green LEDs will have larger polarization barriers and thus exhibit a greater increase in V_F with the number of QWs. The result is a penalty in voltage with larger QW number as it becomes increasingly difficult for electrons to reach the most active *p*-side QW [29]. Indeed, a 3D simulation comparison of blue and green LEDs with one and five QWs showed a larger increase in V_F with the number of QWs for the green LEDs.

To assess the impact of the spontaneous and piezoelectric polarization barriers on V_F, simulations were performed using 0% of the known polarization values. The blue LED

structures with one- and five-QWs have a similar V_F; however, the five-QW green structure still presents a higher V_F than the single QW structure. The second mechanism that contributes to ΔV_F when there is 0% polarization is the sequential injection of QWs, which is related to the depth of the QW potential [30,37,38]. The effect is more pronounced in high indium content QWs which have a smaller bandgap and thus a deeper potential. For the green LEDs at 100 A cm^{-2}, approximately half of the excess voltage of the five-QW structure relative to the one-QW structure can be attributed to the polarization barriers while half can be attributed to the large band offsets. This is seen by comparing the J-V curves of the one- and five-QW green LED structures with 100% and 0% polarization. Sequential injection is a fundamental issue of materials with large bandgap differences and needs to be addressed through advanced design of LEDs, such as the use of alloy QBs or engineered V-defects, which will be discussed in Chapters 4 and 5, respectively. The results presented in this chapter indicate that, in addition to polarization fields, the large band offsets between InGaN QWs and GaN barriers must be considered for the design of high WPE long-wavelength III-nitride LEDs.

References

[1] F. Bernardini, V. Fiorentini, and D. Vanderbilt, Phys. Rev. B **56**, R10024 (1997).

[2] T.-J. Yang, R. Shivaraman, J.S. Speck, and Y.-R. Wu, Journal of Applied Physics **116**, 113104 (2014).

[3] C.-K. Li, M. Piccardo, L.-S. Lu, S. Mayboroda, L. Martinelli, J. Peretti, J.S. Speck, C. Weisbuch, M. Filoche, and Y.-R. Wu, Phys. Rev. B **95**, 144206 (2017).

[4] S.J. Chang, W.C. Lai, Y.K. Su, J.F. Chen, C.H. Liu, and U.H. Liaw, IEEE Journal of Selected Topics in Quantum Electronics **8**, 278 (2002).

[5] C.S. Xia, Z.M. Simon Li, Z.Q. Li, Y. Sheng, Z.H. Zhang, W. Lu, and L.W. Cheng, Appl. Phys. Lett. **100**, 263504 (2012).

[6] J.-Y. Chang, Y.-K. Kuo, and M.-C. Tsai, Physica Status Solidi (a) **208**, 729 (2011).

[7] M. Filoche and S. Mayboroda, PNAS **109**, 14761 (2012).

[8] M. Filoche, M. Piccardo, Y.-R. Wu, C.-K. Li, C. Weisbuch, and S. Mayboroda, Phys. Rev. B **95**, 144204 (2017).

[9] D.N. Arnold, G. David, D. Jerison, S. Mayboroda, and M. Filoche, Phys. Rev. Lett. **116**, 056602 (2016).

[10] C. Lynsky, A.I. Alhassan, G. Lheureux, B. Bonef, S.P. DenBaars, S. Nakamura, Y.-R. Wu, C. Weisbuch, and J.S. Speck, Phys. Rev. Materials **4**, 054604 (2020).

[11] G. Lheureux, C. Lynsky, Y.-R. Wu, J.S. Speck, and C. Weisbuch, J. Appl. Phys. **128**, 235703 (2020).

[12] Y.-L. Hu, R.M. Farrell, C.J. Neufeld, M. Iza, S.C. Cruz, N. Pfaff, D. Simeonov, S. Keller, S. Nakamura, S.P. DenBaars, U.K. Mishra, and J.S. Speck, Appl. Phys. Lett. **100**, 161101 (2012).

[13] A.I. Alhassan, R.M. Farrell, B. Saifaddin, A. Mughal, F. Wu, S.P. DenBaars, S. Nakamura, and J.S. Speck, Opt. Express, OE **24**, 17868 (2016).

[14] A.I. Alhassan, N.G. Young, R.M. Farrell, C. Pynn, F. Wu, A.Y. Alyamani, S. Nakamura, S.P. DenBaars, and J.S. Speck, Opt. Express, OE **26**, 5591 (2018).

[15] B. Bonef, M. Catalano, C. Lund, S.P. Denbaars, S. Nakamura, U.K. Mishra, M.J. Kim, and S. Keller, Appl. Phys. Lett. **110**, 143101 (2017).

[16] M. Khoury, H. Li, B. Bonef, L.Y. Kuritzky, A.J. Mughal, S. Nakamura, J.S. Speck, and S.P. DenBaars, Appl. Phys. Express **11**, 036501 (2018).

[17] F. Tang, M.P. Moody, T.L. Martin, P.A.J. Bagot, M.J. Kappers, and R.A. Oliver, Microscopy and Microanalysis **21**, 544 (2015).

[18] L. Rigutti, B. Bonef, J. Speck, F. Tang, and R.A. Oliver, Scripta Materialia **148**, 75 (2018).

[19] M.P. Moody, L.T. Stephenson, A.V. Ceguerra, and S.P. Ringer, Microsc. Res. Tech. **71**, 542 (2008).

[20] F. Tang, T. Zhu, F. Oehler, W.Y. Fu, J.T. Griffiths, F.C.-P. Massabuau, M.J. Kappers, T.L. Martin, P.A.J. Bagot, M.P. Moody, and R.A. Oliver, Appl. Phys. Lett. **106**, 072104 (2015).

[21] M.J. Galtrey, R.A. Oliver, M.J. Kappers, C.J. Humphreys, D.J. Stokes, P.H. Clifton, and A. Cerezo, Appl. Phys. Lett. **90**, 061903 (2007).

[22] M. Piccardo, C.-K. Li, Y.-R. Wu, J.S. Speck, B. Bonef, R.M. Farrell, M. Filoche, L. Martinelli, J. Peretti, and C. Weisbuch, Phys. Rev. B **95**, 144205 (2017).

[23] T. Shioda, H. Yoshida, K. Tachibana, N. Sugiyama, and S. Nunoue, Physica Status Solidi (a) **209**, 473 (2012).

[24] D. Schroder, *Semiconductor Material and Device Characterization*, Third Edition (John Wiley & Sons, Inc., 2006).

[25] See http://yrwu-wk.ee.ntu.edu.tw/ for "Optoelectronic device simulation laboratory".

[26] C. Geuzaine and J.-F. Remacle, Int. J. Numer. Meth. Engng. **79**, 1309 (2009).

[27] See http://gmsh.info/ for more information about Gmsh, a three-dimensional finite element mesh generator.

[28] Y.-R. Wu, R. Shivaraman, K.-C. Wang, and J.S. Speck, Appl. Phys. Lett. **101**, 083505 (2012).

[29] A. David, M.J. Grundmann, J.F. Kaeding, N.F. Gardner, T.G. Mihopoulos, and M.R. Krames, Appl. Phys. Lett. **92**, 053502 (2008).

[30] S. Marcinkevičius, R. Yapparov, L.Y. Kuritzky, Y.-R. Wu, S. Nakamura, S.P. DenBaars, and J.S. Speck, Appl. Phys. Lett. **114**, 151103 (2019).

[31] S. Tanaka, Y. Zhao, I. Koslow, C.-C. Pan, H.-T. Chen, J. Sonoda, S. DenBaars, and S. Nakamura, in (2011).

[32] Y.P. Zhang, Z.-H. Zhang, W. Liu, S.T. Tan, Z.G. Ju, X.L. Zhang, Y. Ji, L.C. Wang, Z. Kyaw, N. Hasanov, B.B. Zhu, S.P. Lu, X.W. Sun, and H.V. Demir, Opt. Express, OE **23**, A34 (2015).

[33] F. Akyol, D.N. Nath, S. Krishnamoorthy, P.S. Park, and S. Rajan, Appl. Phys. Lett. **100**, 111118 (2012).

[34] J. Xu, M.F. Schubert, A.N. Noemaun, D. Zhu, J.K. Kim, E.F. Schubert, M.H. Kim, H.J. Chung, S. Yoon, C. Sone, and Y. Park, Appl. Phys. Lett. **94**, 011113 (2009).

[35] D. Zhu, J. Xu, A.N. Noemaun, J.K. Kim, E.F. Schubert, M.H. Crawford, and D.D. Koleske, Appl. Phys. Lett. **94**, 081113 (2009).

[36] Y. Zhao, R.M. Farrell, Y.-R. Wu, and J.S. Speck, Jpn. J. Appl. Phys. **53**, 100206 (2014).

[37] H. Schneider and K. v. Klitzing, Phys. Rev. B **38**, 6160 (1988).

[38] K. Fröjdh, S. Marcinkevičius, U. Olin, C. Silfvenius, B. Stålnacke, and G. Landgren, Appl. Phys. Lett. **69**, 3695 (1996).

[39] J.-W. Shi, S.-H. Guol, C.-S. Lin, J.-K. Sheu, K.-H. Chang, W.-C. Lai, C.-H. Kuo, C.-J. Tun, and J.-I. Chyi, IEEE Journal of Selected Topics in Quantum Electronics **15**, 1292 (2009).

[40] P. Kivisaari, J. Oksanen, and J. Tulkki, Journal of Applied Physics **111**, 103120 (2012).

[41] F. Jiang, J. Zhang, L. Xu, J. Ding, G. Wang, X. Wu, X. Wang, C. Mo, Z. Quan, X. Guo, C. Zheng, S. Pan, and J. Liu, Photonics Res. **7**, 144 (2019).

[42] Z. Quan, J. Liu, F. Fang, G. Wang, and F. Jiang, J. Appl. Phys. **118**, 193102 (2015).

[43] Z. Quan, L. Wang, C. Zheng, J. Liu, and F. Jiang, J. Appl. Phys. **116**, 183107 (2014).

[44] X. Jiang, C. Zheng, C. Mo, X. Wang, J. Zhang, Z. Quan, J. Liu, and F. Jiang, Optical Materials **89**, 505 (2019).

[45] C.-K. Li, C.-K. Wu, C.-C. Hsu, L.-S. Lu, H. Li, T.-C. Lu, and Y.-R. Wu, AIP Advances **6**, 055208 (2016).

4

InGaN Alloy Quantum Barriers

4.1 Introduction

In Chapter 3, it was demonstrated experimentally and through 3D simulations based on the Localization Landscape theory of disorder that polarization barriers and band offsets at the GaN/InGaN (lower QB/QW) interface and sequential filling of QWs contribute to the large excess forward voltage in green III-nitride LEDs [1,2]. In addition to identifying a contributing factor to the low WPE of green LEDs, these findings highlighted the importance of using 3D as opposed to 1D simulations to accurately describe carrier transport in III-nitride LEDs with alloy disorder. A natural extension is the investigation of device structures that overcome these barriers to carrier transport in high indium composition QWs.

Kuo *et al*. previously explored the advantages of $In_{0.1}Ga_{0.9}N$ barriers in blue LEDs using APSYS simulations [3]. The authors propose that using InGaN barriers leads to more uniform electron and hole distribution in a MQW structure resulting from the lower polarization discontinuity at the QW/QB interface. With more uniform carrier distribution, Auger recombination and thus efficiency droop are reduced. Experimentally, MQW blue LEDs with InGaN/InGaN QWs/QBs were demonstrated to have reduced efficiency droop, forward voltage, and wavelength shift with current compared to LEDs with GaN QBs [4]. Liu *et al*. also demonstrated that InGaN barriers led to improved carrier injection into deeper

(*n*-side) QWs as evidenced by relative EL intensity of lower green-emitting QWs to a top blue-emitting QW [5].

Prior experimental reports motivate the use of InGaN barriers in *c*-plane green LEDs as a means of improving transport [4-6]. To-date, simulations performed on such structures have not accounted for the impact of alloy disorder in the InGaN barriers [3]. Because compositional alloy fluctuations cannot be independently controlled in experiments, simulations present an attractive option for studying their impact on device performance. It was discussed in Chapters 2 and 3 that alloy disorder strongly impacts carrier localization and transport in LED devices [7-12] and that these effects become more pronounced for green LEDs with high indium content InGaN QWs. Therefore, to understand carrier behavior in a disordered potential, full 3D treatment of the system is required. For this, the computational approach based on the Localization Landscape theory of disorder is again leveraged to perform efficient 3D device simulations [13-16].

In the first two sections of this chapter, the impact of $In_xGa_{1-x}N$ quantum barriers on the electrical properties of green-emitting LEDs is examined computationally and experimentally [17]. Structures incorporating $In_xGa_{1-x}N$ QBs will have a reduced polarization discontinuity at the QW/QB interface and will also contribute an additional source of alloy disorder to the active region. In the third section of this chapter, $In_xGa_{1-x}N$ quantum barriers are demonstrated to improve interwell carrier transport in blue-emitting QWs as measured by time-resolved photoluminescence spectroscopy [18].

4.2 Device Simulations

4.2.1 Simulation Structures

The *c*-plane green LED structure presented in Fig. 4.1(a) was used for the 3D simulations. The single QW structure consisted of a 40-nm thick *n*-GaN layer (N_D = 5×10^{18} cm^{-3}), a 3-nm $In_{0.22}Ga_{0.78}N$ QW, 7-nm $In_xGa_{1-x}N$ QBs on either side of the QW, and a 50-nm thick *p*-GaN layer (N_A = 2×10^{19} cm^{-3}). The indium fraction x in the InGaN QB was varied from 0 to 0.05. The two-QW structure was identical to the one-QW structure, but an additional QW and QB were added to the active region. AlGaN capping layers were not used in these simulation structures. The AlGaN layers incorporated into the experimentally grown samples are thin and contain a low aluminum fraction, as measured by APT. These layers are not expected to strongly impact transport and are excluded from the simulations to avoid uncertainty in defining the complex InGaN/AlGaN/InGaN alloy profiles. Input parameters for each layer in the structure are provided in Table 4.1. The LED structures were meshed using Gmsh [19,20]. A constant mesh size of 0.6 nm was used in the XY planes and a variable mesh size was used in the Z direction, ranging from 1 nm in the *p*-GaN and *n*-GaN to 0.1 nm in the QWs and at the layer boundaries.

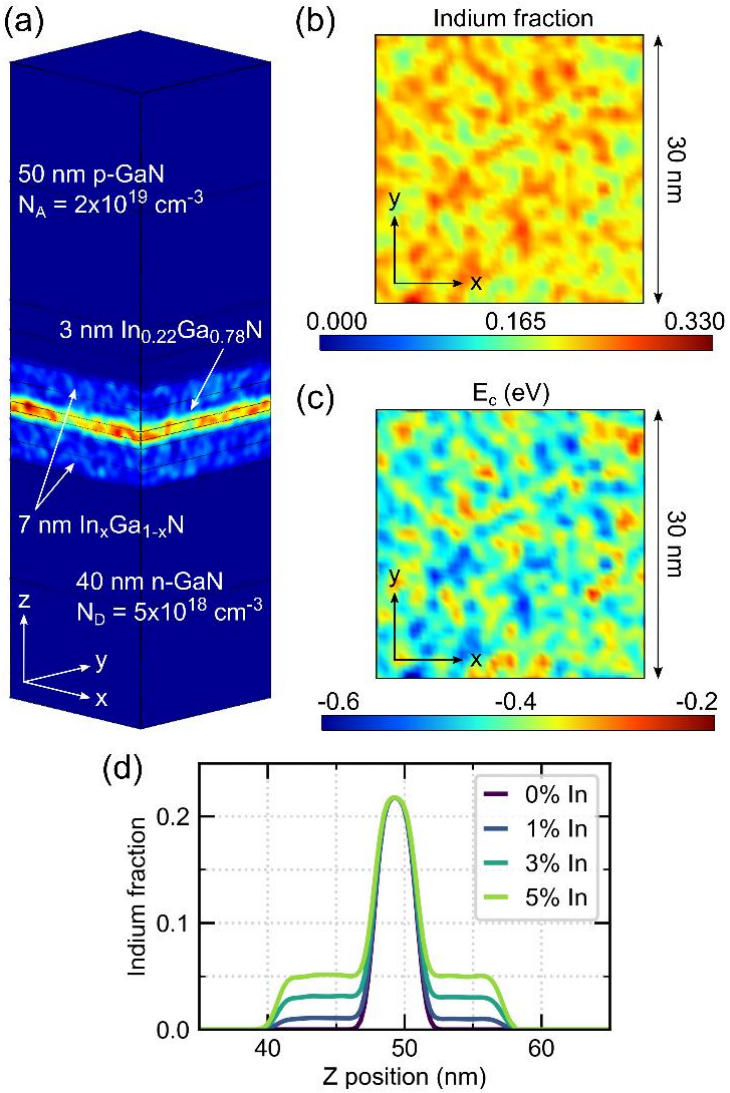

Figure 4.1. (a) Single QW LED structure used in 3D simulations. (b) XY map of indium distribution in the InGaN QW showing random lateral alloy fluctuations. (c) XY map of the conduction band potential $E_c(\mathbf{r})$ in the QW at a bias of 2.9 V. This map is the result of the compositional fluctuations in Fig. 4.1(b) and the associated variations in bandgap, electric field, and carrier injection. (d) Indium alloy composition averaged in the XY plane along the Z direction for the four simulated single QW structures with 22% indium in the QW and x% indium in the QBs, where x = 0, 1, 3, or 5.

The indium alloy composition averaged in the XY plane along the Z direction is shown in Fig. 4.1(d) for all InGaN QB compositions used in the simulations. The composition profiles are based on those observed experimentally by APT [7,21]. In the 3D

computations, the average indium composition of a layer is first defined, and a random number generator is used to assign indium and gallium atoms to each cation lattice site. The Gaussian averaging method described extensively in Ref [16] is used to realize a continuous fluctuating composition. Figure 4.1(b) shows the random alloy map that was generated; the XY slice in the QW exhibits random alloy fluctuations as evidenced by the indium-rich and indium-poor regions. Although there are alloy fluctuations, the local bandgap E_g is retained. The XY map of the conduction band potential $E_c(\mathbf{r})$ in the QW is shown in Fig. 4.1(c), where the conduction band offsets between GaN and InGaN are taken to be 63% of the bandgap difference. As discussed in Section 2.5, the energy levels of electrons and holes are obtained by solving the Schrödinger equation obeyed by carriers in the fluctuating potential [22]. In the 3D-DDCC solver, the Schrödinger equation (Eq. 2.19) is replaced with the Landscape equation (Eq. 2.20) [23].

Table 4.1. Simulation parameters used for each layer in the structure.

	n-GaN	InGaN QW	InGaN QB	*p*-GaN
Thickness (nm)	40	3	7	50
Doping (cm^{-3})	5×10^{18}	1×10^{17}	1×10^{17}	2×10^{19}
$\boldsymbol{E_a}$ **(meV)**	25	NA	NA	170
$\boldsymbol{\mu_e}$ **(cm^2/Vs)**	200	300	300	32
$\boldsymbol{\mu_h}$**(cm^2/Vs)**	23	10	10	5
$\boldsymbol{\tau_n^{NR}}$ **(s)**	10	1×10^{-7}	1×10^{-7}	6×10^{-10}
$\boldsymbol{\tau_p^{NR}}$ **(s)**	7×10^{-10}	1×10^{-7}	1×10^{-7}	10
$\boldsymbol{B_0}$ **(cm^3/s)**	2×10^{-11}	2×10^{-11}	2×10^{-11}	2×10^{-11}
$\boldsymbol{C_0}$ **(cm^6/s)**	6×10^{-31}	6×10^{-31}	6×10^{-31}	6×10^{-31}

4.2.2 *J-V* Characteristics

J-V curves obtained from 3D-DDCC simulations of the single QW structure are plotted in Fig. 4.2(a) to explore the effect of InGaN QBs on forward voltage V_F. As the indium composition in the QBs is increased from 0% to 5%, V_F systematically decreases. At 35 A cm^{-2}, the voltage decrease is 0.05 V per one percent indium in the QB. The same curves for the two-QW structures with varying QB indium composition are shown in Fig. 4.2(b). Again, a decrease in voltage occurs with increasing indium fraction of the QB. For a given indium content, the two-QW structures exhibit higher forward voltage compared to the one-QW structures. This result agrees with the findings presented in Chapter 3 which show that for planar LEDs without engineered V-defects, additional QWs with undoped barriers are accompanied by a voltage penalty [1,2]. Because the simulated structures used here are planar and do not contain V-defects, such as those found in Ref [24], a voltage penalty with increasing QW number is expected.

While overall the two-QW structures present higher V_F than the one-QW structures, the decrease in V_F with increasing QB indium composition is also more significant. Here the voltage decrease per one percent indium in the QB is 0.11 V at 35 A cm^{-2}. The advantage of InGaN alloy QBs on electrical properties is therefore cumulative with increasing QW number. By increasing the indium fraction in the QB, the barrier to transport associated with each QW is decreased. For the 0% indium QB case, the voltage penalty for going from one to two QWs is 0.45 V; in contrast, the voltage penalty is only 0.22 V for the 5% indium QB structures. These results may be significant for commercial LEDs where large numbers of QWs are frequently used to improve the optical efficiency of LEDs but come with the

drawback of worse electrical efficiency. InGaN QBs may provide a path to reduce the voltage penalty associated with increasing number of QWs.

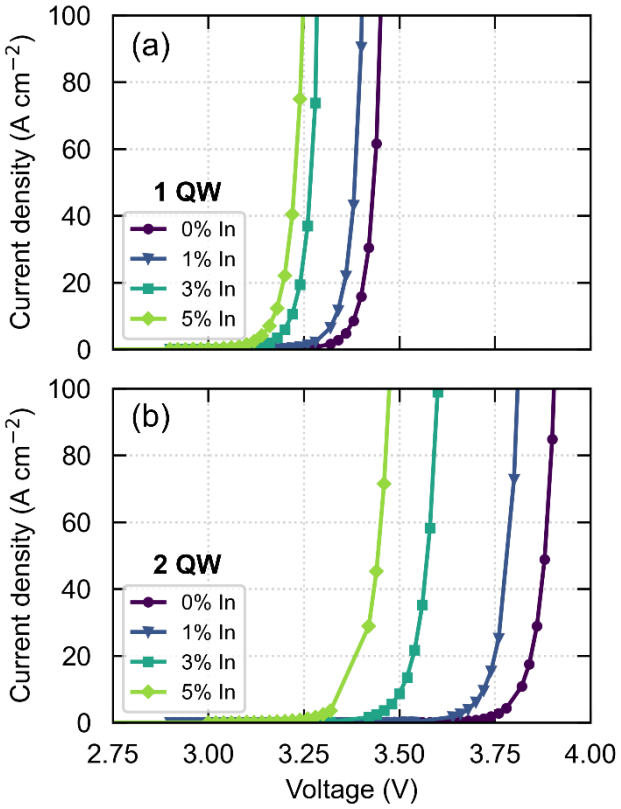

Figure 4.2. *J-V* curves from 3D simulations of green LED structures with $In_xGa_{1-x}N$ quantum barriers of varying indium composition and either (a) one QW or (b) two QWs.

4.2.3 Carrier Recombination

Simulations can also be used to assess the role of InGaN QBs on electron-hole recombination and hence provide additional insight into the reduction in V_F. Equation 2.14 gives the steady-state recombination rate of charge carriers in the LED active region, assuming ideal injection efficiency ($\eta_{inj} = 1$), steady state conditions ($dn/dt = 0$), and that the electron and hole densities are approximately equal ($n \sim p$). The recombination rate

coefficients have been shown to be proportional to the square of the wavefunction overlap F_{eh}, where $F_{eh} = \int \psi_e(z)\psi_h(z)dz$ [25,26]. A, B, and C can then be written as $A = A_0|F_{eh}|^2$, $B = B_0|F_{eh}|^2$, and $C = C_0|F_{eh}|^2$ where A_0, B_0, and C_0 are the bulk recombination rate coefficients. One mechanism that would then lead to an increase in A, B, and C is a reduction in the net electric field in the QW and the accompanying increase in F_{eh}. For a fixed QW thickness and crystallographic orientation, an increase in wavefunction overlap at a given current density implies a reduced net electric field in the QW layer due to the flattening of the conduction and valence bands. Evaluating the electron-hole wavefunction overlap is therefore one way to assess recombination and electric fields in the QW.

Because the Landscape equation is used here instead of the Schrödinger equation, the eigenvalues and eigenstates are not directly calculated. Instead, the carrier densities obtained in 3D are determined from the LDOS assuming Weyl's law (Eqs. 2.23 – 2.25) [15]. The normalized carrier densities for electrons and holes are calculated as follows,

$$n_{norm}(z) = \frac{n(z)}{\sqrt{\int_{Z_{min}}^{Z_{max}} n(z)^2 dz}}, \tag{4.1a}$$

$$p_{norm}(z) = \frac{p(z)}{\sqrt{\int_{Z_{min}}^{Z_{max}} p(z)^2 dz}}, \tag{4.1b}$$

$$\int_{Z_{min}}^{Z_{max}} n_{norm}(z)^2 dz = 1, \tag{4.2a}$$

$$\int_{Z_{min}}^{Z_{max}} p_{norm}(z)^2 dz = 1, \tag{4.2b}$$

where Z_{max} and Z_{min} are the domain boundaries where the normalized densities are defined. For the single QW structure investigated here, Z_{min} is chosen to be the middle of

the *n*-side quantum barrier (Z_{min} = 45 nm) and Z_{max} to be the middle of the *p*-side quantum barrier (Z_{max} = 55 nm). By defining the domain boundaries in this way, the carrier densities in the QBs are considered, representing the wavefunction penetration in the barriers, which is largely increased due to compositional fluctuations. Normalization allows $n_{norm}(z)$ and $p_{norm}(z)$ to be treated as the probability of electron and hole presence in the Z_{min} to Z_{maz} domain. $n_{norm}(z)$ and $p_{norm}(z)$ are then used to define the carrier density spatial overlap *CDSO*, a proxy for $|F_{eh}|^2$, where

$$CDSO = \int_{Z_{min}}^{Z_{max}} n_{norm}(z) * p_{norm}(z)\, dz. \tag{4.3}$$

The *CDSO* as a function of current density for the single QW LED structure with different QB indium compositions is given in Fig. 4.3(a). In all cases, the *CDSO* increases with current density due to progressive carrier injection into the QW and subsequent reduction of the QCSE by partial screening of the electric field. For a given current density, the *CDSO* increases with increasing QB indium composition. This trend is attributed to a decrease in the net electric field in the QW resulting from the reduced polarization discontinuity at the QW/QB interface and reduced band offsets when using InGaN barriers as opposed to GaN barriers. With InN and GaN having similar spontaneous polarization coefficients but large lattice mismatch, the spontaneous polarization-induced electric field in the QW is small relative to the electric field arising from piezoelectric polarization [27-29].

Increasing the *CDSO*, and thus the recombination rate in the QWs, should also lead to a decrease in the steady-state carrier density at a given current density according to Eq. 2.14. To explore this effect, the mean electron density $\bar{n}$ and mean hole density $\bar{p}$ in the single QW structure are computed according to Eq. 3.4. The dependence of the mean carrier

densities on current density for structures with different QB indium fraction are plotted in Fig. 4.3(b). As the indium fraction in the QB is increased, there is a very small change in $\bar{p}$ but a decrease in $\bar{n}$.

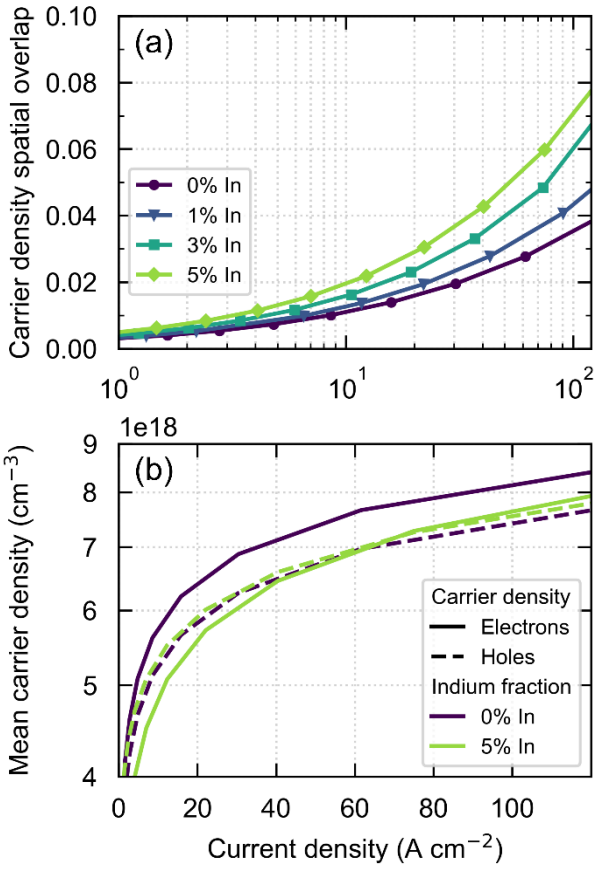

Figure 4.3. Simulated dependence of (a) carrier density spatial overlap *CDSO* and (b) mean electron (solid) and hole (dashed) carrier density on current density for single QW LEDs with different InGaN barrier compositions.

Because the A, B, and C coefficients are proportional to the square of the wavefunction overlap, a change in the *CDSO* is expected to impact the dependence of IQE on current density, where the IQE is defined in Eq. 2.15 as the ratio of the radiative recombination rate to the recombination rate due to all processes. Figure 4.4(a) shows the

IQE curves for single QW structures. While the peak IQE is similar for all structures, with higher QB indium fraction a slight increase in the current density at peak IQE and a significant reduction in droop are observed. The improvement in droop behavior can be explained by the lower steady-state carrier density and therefore reduced Auger rate (Cn^3) relative to the radiative rate (Bn^2).

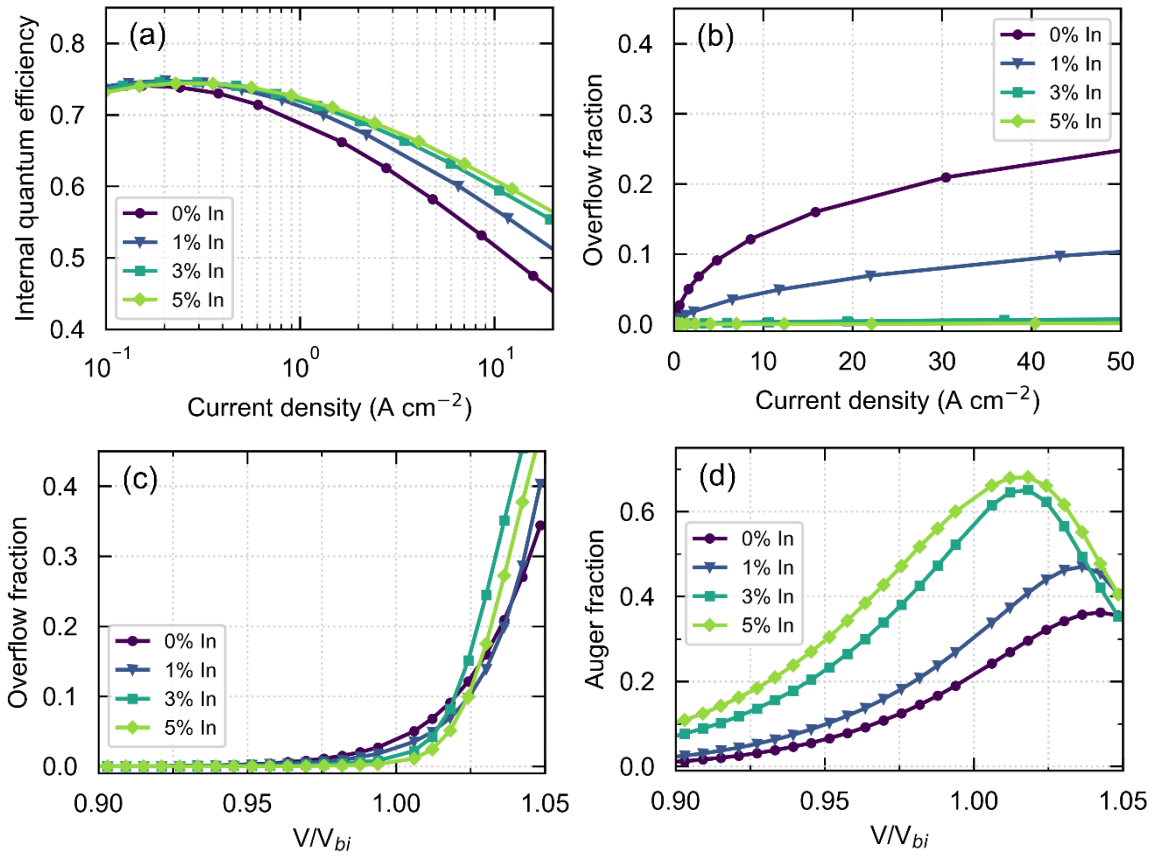

Figure 4.4. Simulated dependence of (a) internal quantum efficiency IQE at low current densities and (b) overflow fraction of current density for single QW LED structures. (c) Overflow fraction dependence on the ratio of applied voltage V to built-in diode voltage V_{BI}, where V_{BI} = 3.3 V. (d) Auger fraction dependence on V/V_{BI}.

An additional impact on carrier recombination is seen when looking at the fraction of current due to carrier overflow from the QW at higher currents, computed as the difference

between the injected current and the recombination currents. It is shown in Fig. 4.4(b) that at a given current density, the overflow fraction of current is smaller for structures with higher indium fraction in the barrier and that overflow becomes negligible for LEDs with 3% and 5% indium. This trend can be better understood by plotting the dependence of overflow fraction on the ratio of the applied voltage V to the built-in GaN *p-n* diode voltage V_{BI} (V_{BI} = 3.3 V for N_D = 5×10^{18} cm^{-3} and N_A = 2×10^{19} cm^{-3} and assuming 1% acceptor ionization). These results are shown in Fig. 4.4(c) where the curves for different QB indium fractions closely overlay one another. From the data in Figs. 4.4(b) and 4.4(c), it is observed that the overflow current is a result of applying a bias in excess of V_{BI}. This emphasizes that carrier overflow becomes significant only when V exceeds V_{BI} of the GaN *p-n* junction and that overflow is not connected to the turn-on voltage of the LED. Therefore, incorporating InGaN QBs in green LED structures not only reduces the forward voltage but also leads to lower carrier overflow. To further avoid overflow current at high diode voltages, an AlGaN electron blocking layer should be used. In Fig. 4.4(d), the dependence of the Auger fraction of current on V/V_{BI} is shown. Unlike overflow, there is an appreciable fraction of Auger at $V/V_{BI} < 1$, a regime where droop is observed in Fig. 4.4(a). The Auger fraction then begins to decrease with increasing V/V_{BI} as a smaller fraction of carriers are injected in the QW, corresponding to the increase in carrier overflow. At V/V_{BI} = 1.05, overflow and Auger have approximately the same contribution to the total current and therefore to droop.

4.2.4 Percolative Pathways

3D simulations allow for the determination of the percolative transport paths in III-nitride materials that arise due to random alloy fluctuations. Comparing structures with GaN

and InGaN barriers, spatial differences in electron current can be visualized. Figure 4.5 shows indium, electron current, and hole current maps in the XZ plane for one-QW structures with either GaN or $In_{0.05}Ga_{0.95}N$ QBs. The InGaN composition maps for the GaN and $In_{0.05}Ga_{0.95}N$ QB structures are shown in Figs. 4.5(a) and 4.5(d), respectively. At a current density of 8 A cm^{-2}, high electron current [Fig. 4.5(e)] and hole current [Fig. 4.5(f)] pathways are observed for the structure with InGaN barriers. In contrast, the electron current [Fig. 4.5(b)] and hole current [Fig. 4.5(c)] are more homogenous for the GaN QB structure and do not show the same regions of extreme high and low current. The inhomogeneous current maps indicate a secondary effect of InGaN barriers in addition to the average reduced polarization discontinuity at the QW/QB interface. From the current maps it is clear that there are preferential paths for carriers to flow through the barrier layers to then inject the QW. Alloy disorder, introduced through the addition of indium to the QB, is a likely explanation for the spatial variation in current through the structure. It is then of interest to identify which nanoscale variations in materials properties lead to the altered carrier transport.

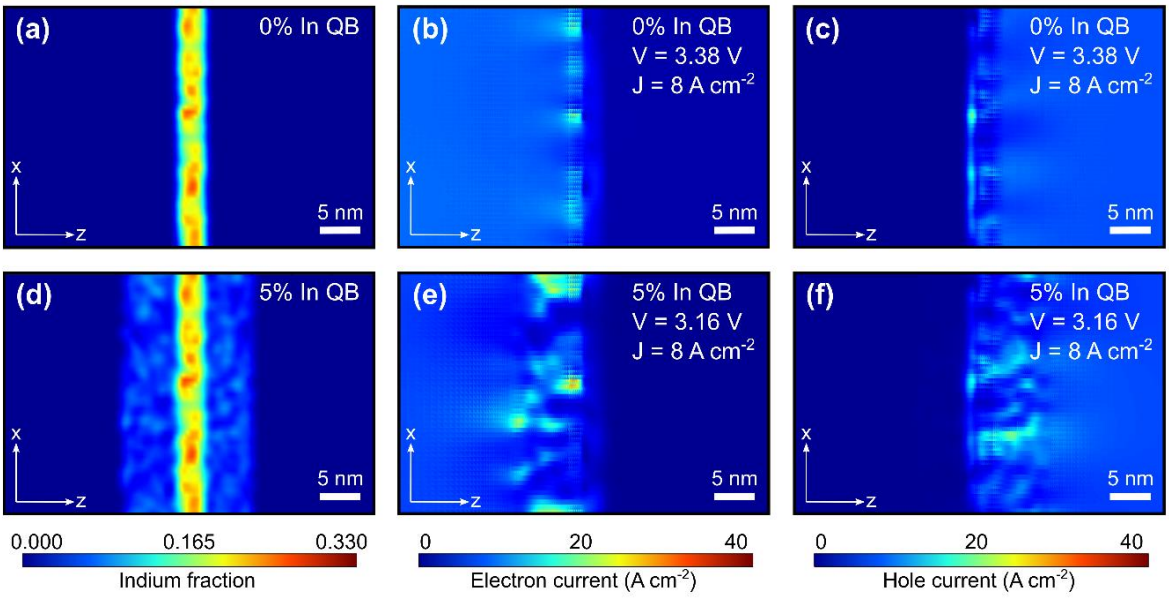

Figure 4.5. The XZ plane (a) indium composition map, (b) electron current map, and (c) hole current map for a one-QW LED with 0% indium barriers. The XZ plane (d) indium composition map, (e) electron current map, and (f) hole current map for a one-QW LED with 5% indium barriers. It can be seen that high indium composition quantum barrier structure results in high electron and hole current pathways.

To further explore the role of alloy fluctuations and percolative pathways on carrier transport, the magnitude of electron current $|J_n|$ in the *n*-side QB and the magnitude of hole current $|J_p|$ in the *p*-side QB are plotted as a function of indium composition in Fig. 4.6(a) and Fig. 4.6(b), respectively, for each computational node in the QBs. Note that scatter plots obtained using $|J_n|$ and $|J_p|$ are nearly identical to those using J_{nz} and J_{pz}, respectively. For both the *n*-side and *p*-side QBs, nodes are taken in the full 30 nm × 30 nm XY plane. The *n*-side QB domain is defined from Z = 41 nm to Z = 47 nm for a total number of 150 858 nodes and the *p*-side QB domain is defined from Z = 52 nm to Z = 57 nm for a total of 124 828 nodes. The scatter plots in Fig. 4.6 show the properties associated with each simulation node in the given domain. Here, the average indium fraction of the QB is fixed at 0.05 and the variations from approximately 0.02 to 0.08 represent the random alloy fluctuations for a

simulation node. A positive correlation is observed between electron current in the *n*-side barrier and indium fraction as well as hole current in the *p*-side barrier and indium fraction. This correlation indicates that the favorable path for carriers to transport through InGaN quantum barriers is along the regions of high indium content.

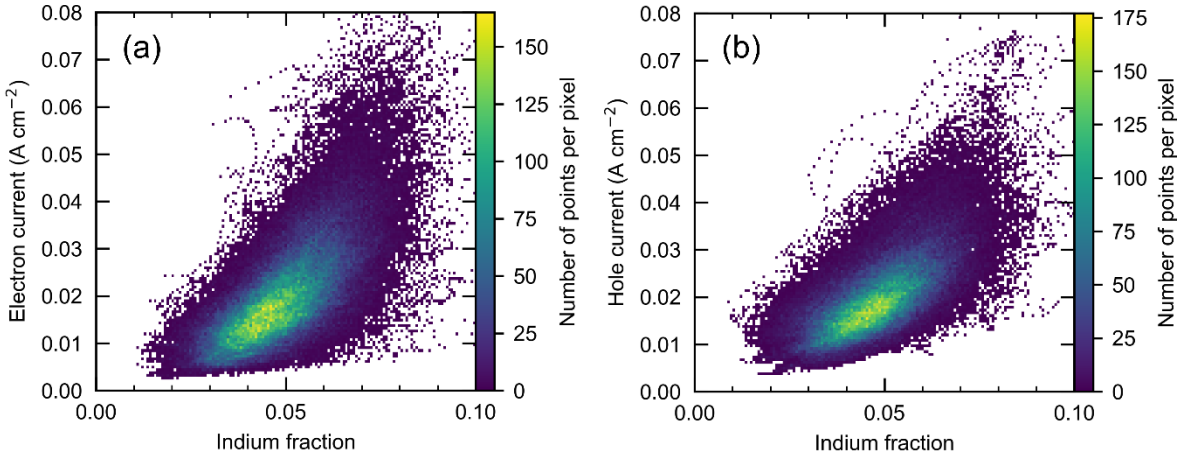

Figure 4.6. Correlation plots for the one-QW LED structure with 5% indium barriers (a) Electron current $|J_n|$ as a function of the indium composition in the *n*-side QB and (b) hole current $|J_p|$ as a function of the indium composition in the *p*-side QB at V = 2.9 V, below V_{BI}. Both the electron and hole current are higher in regions of high indium composition.

The physical reason behind this conclusion can be understood by looking at the effect of alloy composition on strain, and therefore strain-induced piezoelectric polarization $\mathbf{P}^{pz}$. Scatter plots of the dependence of the Z component normal strain ε_{zz} on indium composition in the QB are given in Fig. 4.7 for the 1%, 3%, and 5% indium barrier structures. The domain shown is for the *p*-side QB from Z = 52 nm to Z = 57 nm; however, similar results are obtained for the *n*-side QB. The average ε_{zz} values are approximately 0.5×10^{-3}, 1.5×10^{-3}, and 3.0×10^{-3} for the 1%, 3%, and 5% indium barrier structures, respectively. For all cases a negative correlation is observed where ε_{zz} decreases with increasing indium fraction in the *p*-side QB. At first the negative correlation result may seem

counterintuitive; for a uniform alloy, a larger ε_{zz} is expected for a higher indium composition InGaN film strained to an underlying GaN lattice. Indeed, this is the trend observed when comparing the average ε_{zz} for structures with different indium composition barriers.

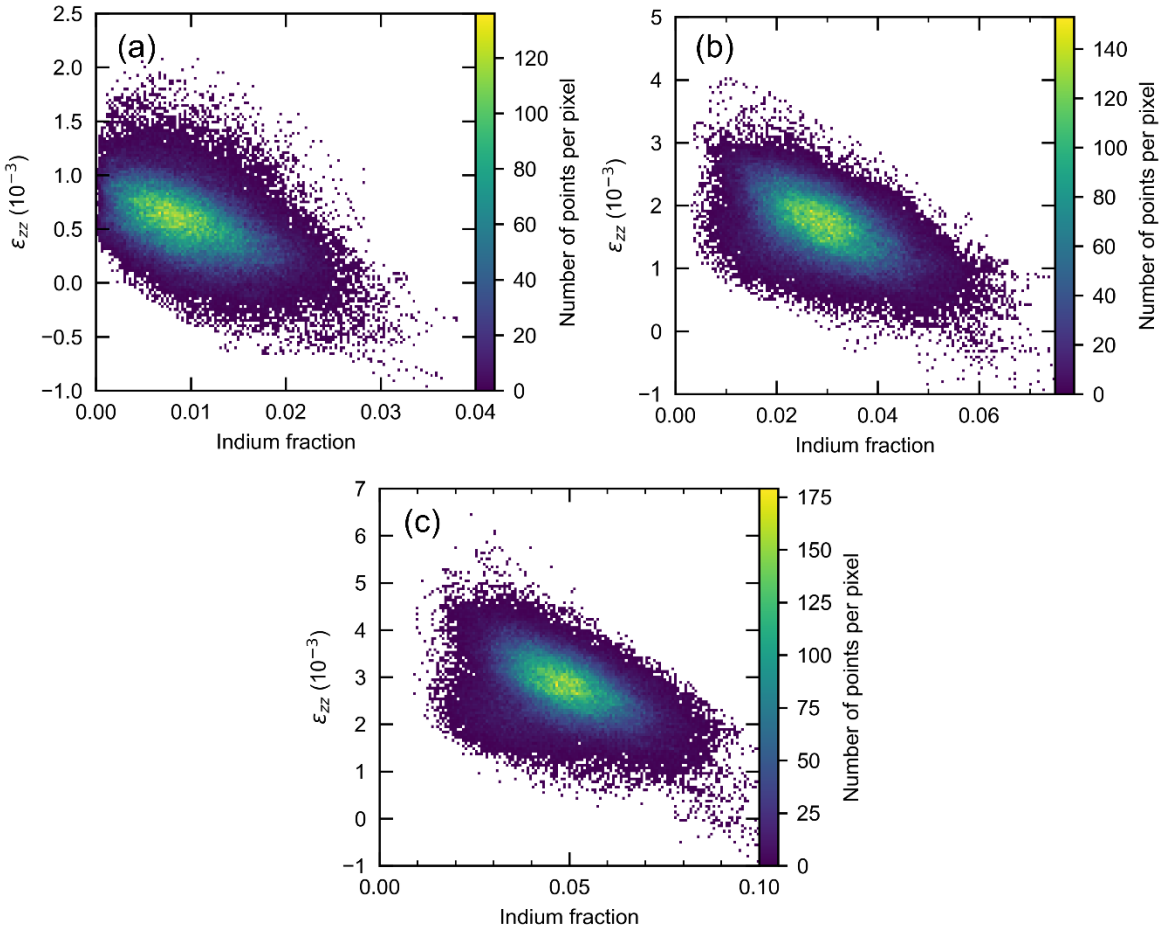

Figure 4.7. Correlation plots of the *p*-side QB showing the Z component normal strain ε_{zz} as a function of indium composition for one-QW LED structures with (a) 1%, (b) 3%, and (c) 5% indium in the quantum barrier. ε_{zz} decreases with indium composition in the QB for all cases but the average ε_{zz} is higher for structures with higher QB indium fraction.

To understand the negative correlation between ε_{zz} and indium composition within a given structure, it needs to be emphasized that a random alloy InGaN film with regions of

high and low indium composition is being considered. The regions of high indium composition will exhibit a smaller ε_{zz} as the lattice is constrained in the Z direction by the surrounding low indium composition regions. Conversely, the low indium compositions will have a larger ε_{zz} due to the surrounding regions of high indium composition. The negative correlation between ε_{zz} and indium fraction in the QB, for a structure with a fixed average indium fraction, indicates that areas of higher indium content have a relatively lower Z component of $\mathbf{P}^{pz}$. The high indium composition, low $\mathbf{P}^{pz}$, regions may further provide favorable, low barrier pathways for carriers to transport through the QBs and into the QWs. This agrees with previous results showing that polarization discontinuities at the QW/QB interface result in a polarization barrier for carrier transport and thus excess voltage in green LEDs [1].

4.3 Experimental

4.3.1 Methods

To experimentally study the effect of alloy quantum barriers, green LEDs were grown by atmospheric pressure MOCVD on (0001) patterned sapphire substrates (PSS) with either GaN or $In_{0.04}Ga_{0.96}N$ QBs and varying number of QWs. A low temperature GaN nucleation layer was followed by 3 μm of unintentionally doped GaN, 2 μm of *n*-GaN, and a 45-period *n*-type InGaN/GaN superlattice. The active region was undoped and consisted of 3-nm InGaN QWs, 2-nm $Al_{0.04}Ga_{0.96}N$ capping layers, and 8-nm GaN or $In_{0.04}Ga_{0.96}N$ QBs. Including AlGaN capping layers after the QW growth typically enables more aggressive GaN quantum barrier growth conditions, such as H_2 flow and high temperatures [24,30-36]. In the structures presented here, which use InGaN QBs, such aggressive growth conditions

cannot be used as they prevent efficient indium incorporation. Nevertheless, AlGaN capping layers are standard in long-wavelength LED growth and were therefore included in the experimental structures. High resolution x-ray diffraction (HRXRD) ω-2θ measurements of a thick InGaN calibration sample were performed on a Panalytical MRD PRO using Cu $K_{\alpha 1}$ radiation (λ = 1.5405 Å) to calibrate the InGaN QB growth rate and composition. The LED active region had either one, three, or five-QW periods. The *p*-side of the LED contained 10 nm of *p*+-GaN, 130 nm of *p*-GaN, and a 10 nm *p*+-GaN contact layer. The epitaxial structure of the samples described here is shown in Fig. 4.8.

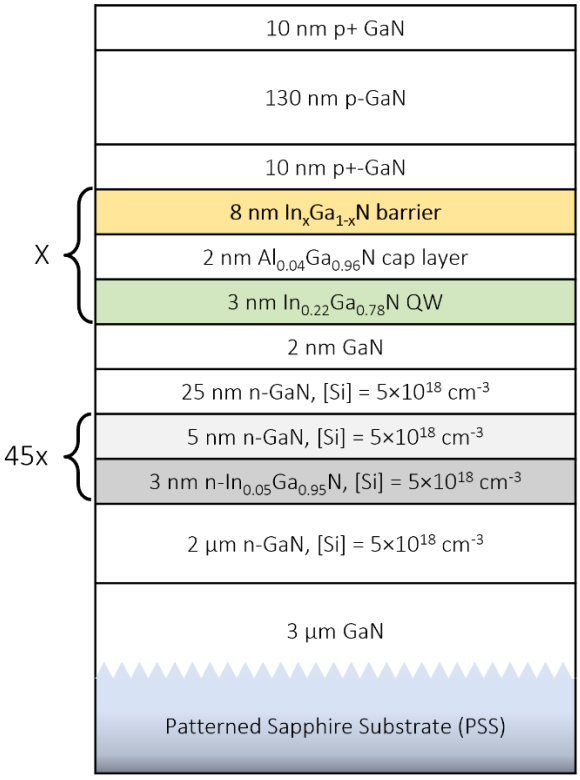

Figure 4.8. Epitaxial structure of green LEDs grown on PSS with either 0% or 4% indium in the quantum barriers and *X* number of QWs, where *X* = 1, 3, or 5.

A post-growth anneal in N_2/O_2 at 600 °C for 15 minutes was used to activate the Mg-doped layers. LEDs were fabricated using standard mesa isolation and contact deposition. Pd/Au was used as the *p*-contact to GaN to allow for reliable voltage determination. APT measurements were performed on all samples by Dr. Bastien Bonef to investigate the LED active region layer thicknesses and compositions. APT sample preparation, evaporation, and reconstruction details can be found in Ref. [37].

4.3.2 Results

To compare the simulation and experimental trends, the grown samples are characterized to identify whether the trend of lower voltage with InGaN barriers is observed. Figure 4.9(a) shows the APT reconstruction of the active region of the three-QW LED with InGaN barriers. The three InGaN QWs, AlGaN capping layers, and InGaN QBs can be clearly observed in this 3D reconstruction. The 1D concentration profiles for indium and aluminum are shown in Fig. 4.9(b); the indium and aluminum concentrations measured by APT are consistent with those expected from growth calibrations. In both Figs 4.9(a) and 4.9(b), a decrease in the indium fraction at the top side of the InGaN QB is observed. This thin layer can be explained by unintentional indium desorption from the QB during the growth pause (to allow for the substrate temperature to decrease) before the QW growth. A more uniform indium fraction in the QB could be achieved in future growths by reducing this growth pause.

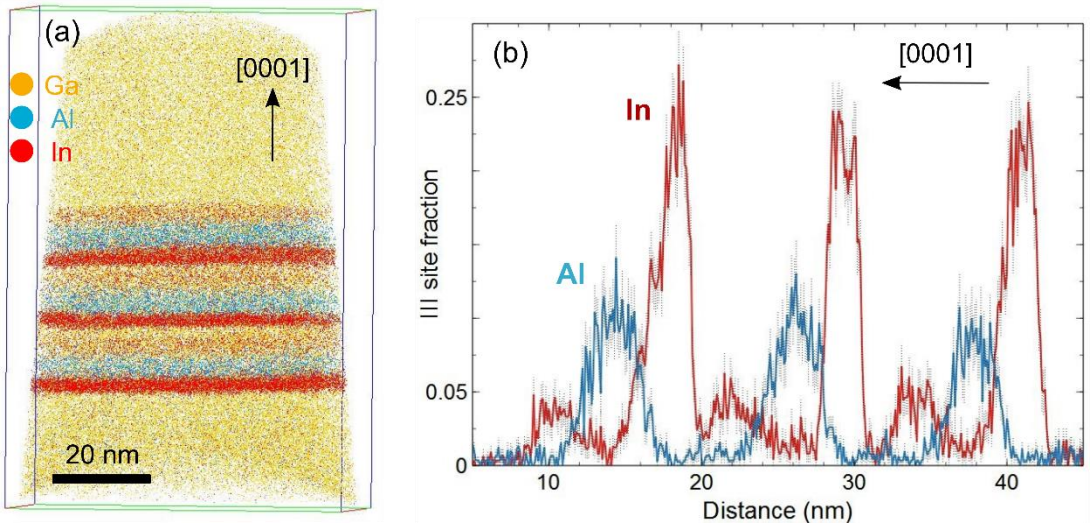

Figure 4.9. APT measurements of the three-QW LED with 4% indium InGaN quantum barriers showing the (a) 3D reconstruction of the active region and (b) 1D indium (red) and aluminum (blue) concentration profiles measured in the [0001] direction.

Figures 4.10(a) – 4.10(c) show the indium and aluminum fractions at the top of the InGaN QW, AlGaN cap layer, and InGaN QB. Statistical distribution analyses (SDAs) were performed on the InGaN QWs to investigate their respective alloy distributions [38]. In Figs. 4.10(d) – 4.10(f) the experimental alloy distribution measured by APT are compared to the binomial distribution expected for random alloys, as described in [39] and [40]. SDA showed that the InGaN QW, AlGaN cap layer, and InGaN QB alloy compositions are randomly distributed in the QW plane, consistent with expectations for *c*-plane alloys [41,42].

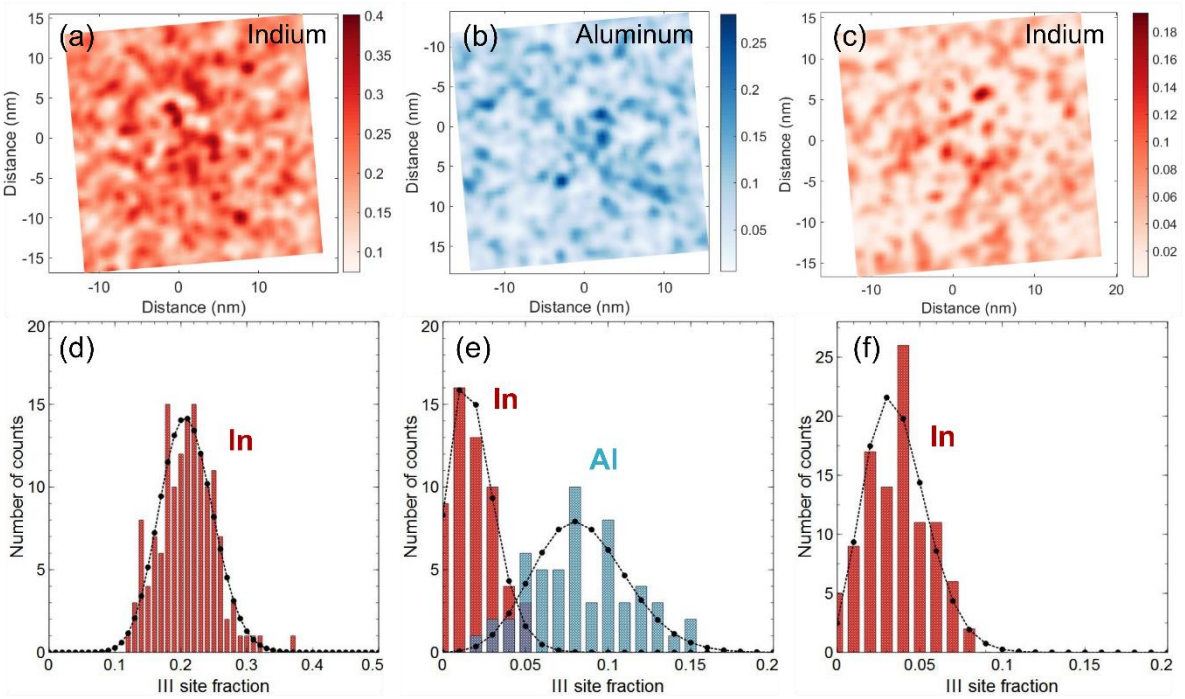

Figure 4.10. Top view of distribution of (a) indium in the InGaN QW, (b) aluminum in the AlGaN cap, and (c) indium in the InGaN QB for the three-QW LED with 4% indium QBs. Distribution of bin compositions of (d) indium in the QW, (e) aluminum in the cap, and (f) indium in the QB compared with the binomial distribution that would be expected in the case of a random alloy.

The six green LEDs were measured under electrical injection to elucidate the impact of alloy quantum barriers on electrical device properties. Consistent with simulations, for all samples, a decrease in forward voltage was observed for InGaN barriers relative to GaN barriers. The voltage at 20 A cm^{-2} for all LEDs are shown in Fig. 4.11(a) and the full *J*-*V* curves for representative one- and five-QW LEDs are shown in Fig. 4.11(b). For both the InGaN and GaN QB LEDs, V_F first increases from one to three QWs but remains constant from three to five QWs. Previous results on *c*-plane green LEDs with GaN QBs showed a large voltage increase with increasing QW number due to polarization related barriers to carrier transport [1]. The moderate increase in voltage with QW period here is attributed to

the inclusion of a high period InGaN/GaN SL that introduce inverted hexagonal pyramidal V-defects [43-46]. LEDs from previous studies which showed a large voltage penalty used a ten-period SL, whereas the structures reported here incorporate a 45-period SL. The role of V-defects in reducing the QW/QB polarization barriers is supported by recent literature on long-wavelength III-nitride LEDs which showed that V-defects may provide a path for carrier injection into the QWs via the semipolar sidewall, thus leading to lower V_F [24,47-50].

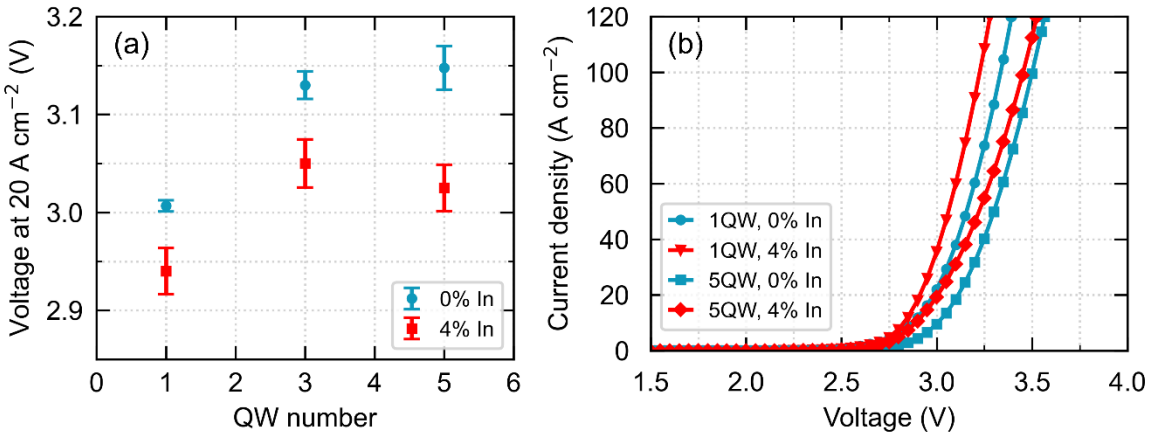

Figure 4.11. (a) Experimental V_F measured at 20 A cm^{-2} for LEDs with one, three, or five QWs and either 0% or 4% indium InGaN QBs. A reduction in V_F is measured for LED structures with InGaN quantum barriers. (b) J-V curves for LEDs with one or five QWs and 0% or 4% indium InGaN quantum barriers.

Accounting for the difference in superlattice period and therefore V-defect density, the experimental trend of reduced V_F with InGaN QBs is consistent with the simulation results. In addition, the peak EL wavelength was blue-shifted for LEDs with InGaN barriers, likely due to the reduced polarization discontinuity at the lower QB/QW interface and therefore reduced QCSE. The EL spectra for the one- and five-QW LEDs with 0% and 4%

indium QBs are shown in Fig. 4.12. The peak EL wavelength for the one, three, and five-QW samples with GaN barriers are 505, 515, and 541 nm, respectively. The peak EL wavelength for the one, three, and five-QW samples with InGaN barriers are 500, 498, and 500 nm, respectively. A blue-shift with decreasing QW number for the GaN barrier samples is also observed. This is attributed to an increase in the residual electric field of the *p-n* junction (due to a decrease in active region width) which cancels out a portion of the polarization-related electric field in the QW. The result is a decrease in the net electric field across the QW and a blue-shift as the QCSE is reduced.

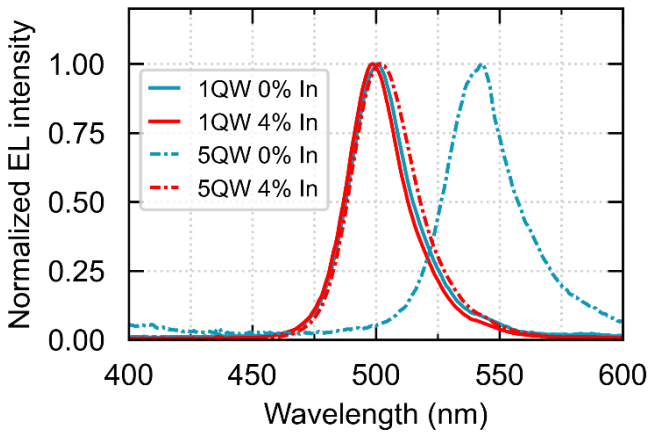

Figure 4.12. Normalized electroluminescence (EL) spectra for LEDs with one or five QWs and 0% or 4% indium InGaN quantum barriers.

4.4 Interwell Carrier Transport

4.4.1 Methods

In Section 4.2.4, InGaN alloy QBs were shown in simulations to introduce preferential pathways for carrier transport through regions of high indium content. For efficient operation, it is desirable to have uniform carrier distribution in the QWs of a MQW

LED structure. However, this goal is not easily realized due to the slow and inefficient nature of hole transport across QWs [51,52]. It is therefore of interest to explore heterostructure designs to achieve more uniform hole distribution. Previous studies by Marcinkevičius *et al*. showed that this could be achieved using InGaN alloy QBs [6].

Time-resolved photoluminescence (TRPL) spectroscopy was used to assess the impact of different QB layers on the interwell transport of carriers in MQW structures. Carrier transport was assessed using an optical marker technique where the rise in photoluminescence (PL) at the emission wavelength of a deep (*n*-side) detector QW is monitored [6,53,54]. The TRPL measurements and analysis shown here were performed at KTH Royal Institute by Professor Saulius Marcinkevičius and Rinat Yapparov. The samples were grown at UCSB.

The epitaxial structures for these experiments were grown on *c*-plane sapphire substrates by MOCVD. The structures consist of a 4.3-μm GaN buffer layer, a 3-nm $In_{0.18}Ga_{0.82}N$ detector QW (DQW), four 3-nm $In_{0.12}Ga_{0.88}N$ transport QWs (TQWs), and a 100-nm GaN cap layer. The four samples had either GaN, $In_{0.04}Ga_{0.96}N$, $In_{0.06}Ga_{0.94}N$, or $Al_{0.065}Ga_{0.935}N$ QBs with a fixed thickness of 8 nm. The structures were unintentionally doped (UID) with a background electron concentration of approximately 1×10^{17} cm^{-3}. A schematic of the epitaxial structure is shown in Fig. 4.13.

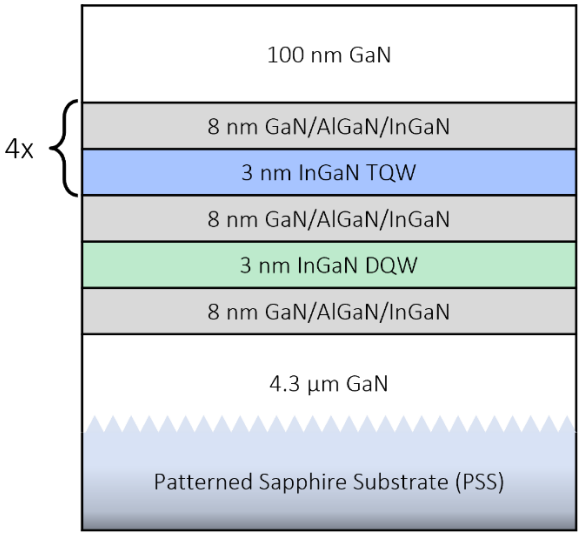

Figure 4.13. Epitaxial structure used for interwell transport experiments. The 8-nm QBs consisted of either GaN, $In_{0.04}Ga_{0.96}N$, $In_{0.06}Ga_{0.94}N$, or $Al_{0.065}Ga_{0.935}N$. The *n*-side detector QW has a longer emission wavelength than the top transport QWs.

TRPL spectroscopy measurements were used to study the interwell transport behavior for these structures. Comprehensive measurement details can be found in Ref. [18]. A Ti:sapphire laser with a 200-fs pulse duration and central wavelengths of 260, 390, and 430 nm was used to generate electron-hole pairs in the GaN cap layer, the TQWs, and the DQW, respectively. PL transients were registered with a time-correlated single photon counter. Time-integrated PL measurements from 12 K to 300 K were also performed. In this experimental setup, the photoexcited carrier density is much larger than the background electron concentration and therefore interwell transport is ambipolar and governed by holes [53]. A band diagram schematic of a structure similar to the one used here is given in Fig 4.14; the red dashed line indicates the approximate photogenerated carrier concentration profile.

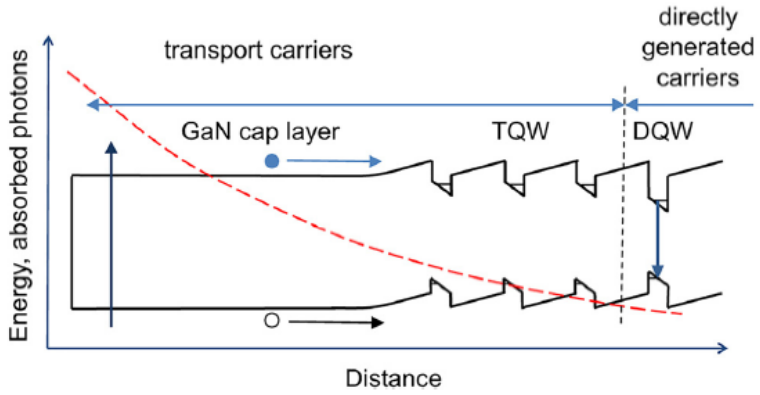

Figure 4.14. Schematic showing the band diagram of an epitaxial structure similar to the ones studied here, including the GaN cap layer, the transport QWs, and the detector QW. The red dashed line shows the approximate photogenerated carrier concentration profile. Reprinted from [6], with the permission of AIP Publishing.

4.4.2 Results

From the time-integrated PL spectra at 300 K in Fig. 4.15, an impact of QB type can be seen. The spectra shown are normalized to the intensity of the TQW peak, which occurs between approximately 410-420 nm. For the structures with InGaN barriers, there is significant signal at ~460-470 nm, corresponding to the DQW peak. In contrast, the structures with GaN and AlGaN barriers exhibit weak luminescence from the DQW. The different ratios of the DQW/TQW PL intensity indicate that the number of carriers which reach the deeper DQW depends on the QB composition and therefore the barrier height.

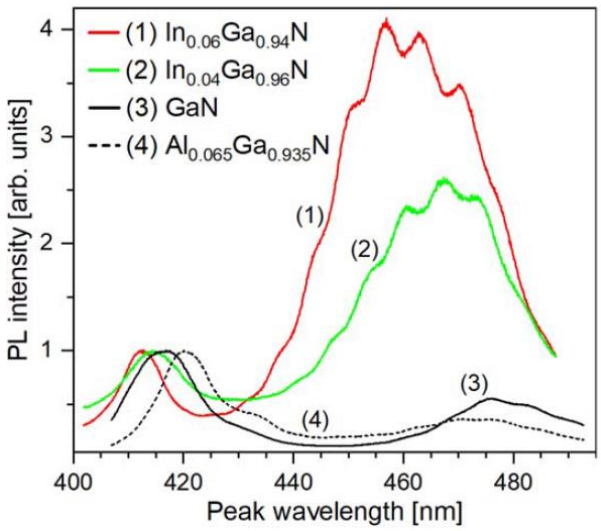

Figure 4.15. Time-integrated photoluminescence spectra at 300 K of structures with different QB layers. The spectra are normalized for each sample to the transport QW peak intensity. Reprinted from [18], Copyright 2020 The Japan Society of Applied Physics.

In these structures, the DQW serves as an optical marker and the interwell carrier transport can be evaluated by the rise of the DQW PL transients. For excitation using the 260 nm source, most of the electron-hole pairs are generated in the GaN cap layer. The rise in the PL signal from the DQW therefore captures carrier transport through the region containing the TQWs. Compared to the very fast sub-picosecond carrier capture into the QWs [55], the thermionic transport time is closer to the 100 ps to ns time range, indicating that thermionic emission can be assumed to be the limiting mechanism.

For the four structures, the DQW PL transients at 300 K are shown in Fig. 4.16. The inset shows the epitaxial structure for samples with InGaN barriers; the excitation and direction of carrier propagation are indicated. The transients exhibit a fast component of the PL rise which corresponds to radiative recombination of carriers directly excited in the DQW and surrounding barriers. There also exists a slow component that can be assigned to carriers excited in the GaN cap which then transport through the TQW region before

radiatively recombining in the DQW. There is no slow PL rise component in the case of the AlGaN barriers (yellow curve), signaling that carriers excited in the GaN cap do not reach the DQW. In the case of the GaN barriers (black curve), the slow PL rise component occurs over tens of ns, indicating that carrier transport through the TQW region to the DQW is slow. The situation is very different for the structures with InGaN barriers where the slow PL rise component is comparatively short. The slow rise extends from 0-4 ns and 0-2 ns for the structures with 4% (green curve) and 6% (red curve) indium in the barriers, respectively. These data show that interwell carrier transport through TQW regions containing InGaN barriers is efficient and fast relative to those containing GaN or AlGaN barriers. Furthermore, the time-integrated and time-resolved PL data are consistent with one another.

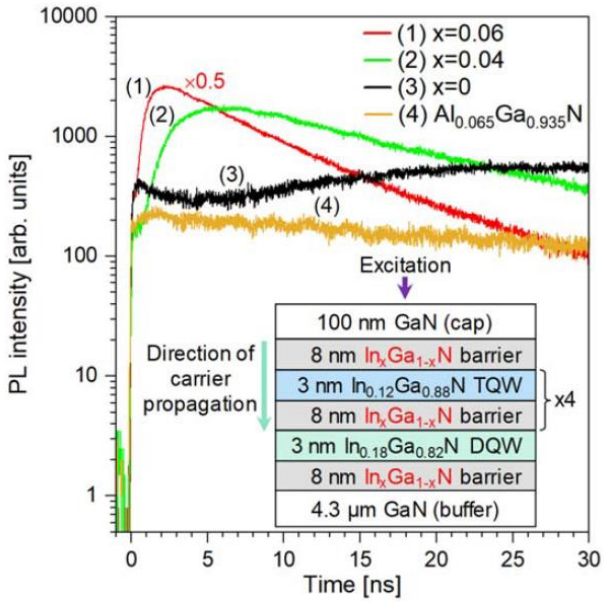

Figure 4.16. Detector QW photoluminescence transients at 300 K. The inset shows the epitaxial structure for the samples with $In_xGa_{1-x}N$ QBs, where x = 0.04 and 0.06. Reprinted from [18], Copyright 2020 The Japan Society of Applied Physics.

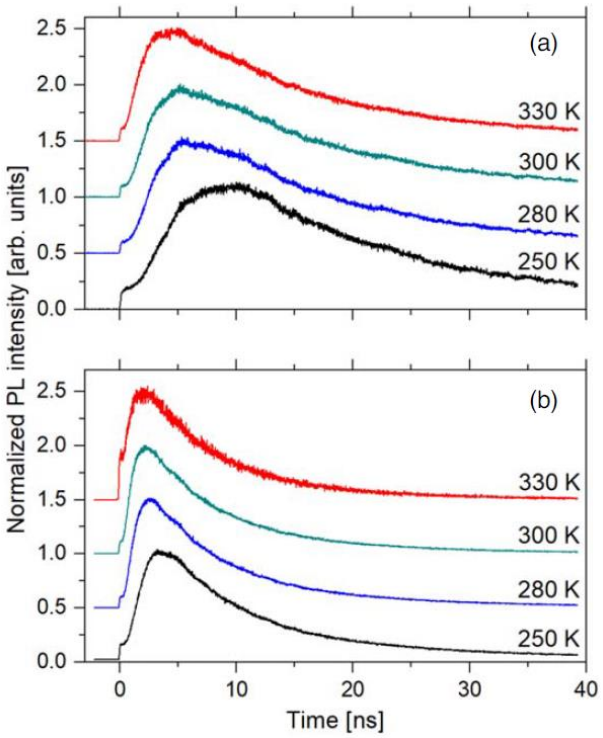

Figure 4.17. Normalized transients of the detector QW photoluminescence at 250, 280, 300, and 330 K for samples with (a) 4% and (b) 6% indium QBs. Reprinted from [18], Copyright 2020 The Japan Society of Applied Physics.

The PL rise times were determined by fitting the transients with the following empirical equation

$$I_{PL}(t) = A\left[\exp\left(-\frac{t}{\tau_r}\right) - \exp\left(-\frac{t}{\tau_d}\right)\right], \tag{4.4}$$

where A is a proportionality constant, τ_r is the slow DQW rise time, and τ_d is the decay time. By dividing τ_r by the number of TQWs, which is four in this case, the interwell transport time per TQW is calculated. At 300 K, the interwell transport times per TQW for the GaN, 4% indium, and 6% indium barrier samples are 2.5, 0.5, and 0.2 ns, respectively. The DQW PL transients collected from 250 K to 330 K on the InGaN barrier samples are shown in Fig. 4.17. For both structures, the PL rise times become shorter with increasing

temperature, indicating that thermionic transport of holes is the mechanism limiting interwell transport. This is due to the thermionic emission time τ_{TE} having an exponential dependence on the effective barrier height ΔE, $\tau_{TE} \propto \exp(\Delta E/kT)$ [56].

4.5 Conclusions

In this chapter, experimental and simulation-based results using InGaN alloy quantum barriers in *c*-plane green LED structures are presented to improve vertical carrier transport and reduce V_F. 3D device simulations that include random alloy fluctuations are used to understand carrier behavior in a disordered potential. Localization Landscape theory of disorder is incorporated self-consistently in the simulations to solve the coupled Poisson, Landscape, and drift-diffusion equations. The simulated J-V characteristics and *CDSO* indicate that increasing the indium fraction in the InGaN QBs leads to a reduced polarization discontinuity at the QB/QW interface, thereby reducing V_F and improving *CDSO*. At 35 A cm^{-2} from 0% to 5% QB indium fraction, the voltage decrease per one percent indium is 0.05 V for a single QW structure and 0.11 V for a two-QW structure.

LED structures with higher indium fraction in the barriers are also simulated to have reduced IQE droop and carrier overflow. The improvement in droop behavior can be explained by the lower steady-state carrier density and therefore reduced Auger recombination rate relative to the radiative recombination rate. At a given current density, structures with higher indium composition in the barriers have lower carrier overflow. By plotting overflow as a function of V/V_{BI}, it is shown that carrier overflow becomes significant only when V exceeds V_{BI} of the GaN *p*-*n* junction.

Simulated maps of electron and hole current through the device show a relatively homogenous distribution in the XY plane for structures using GaN quantum barriers; in contrast, preferential pathways for vertical transport are identified in structures with InGaN barriers as regions of high and low current. A positive correlation between hole (electron) current in the *p*-side (*n*-side) barrier and indium fraction reveals that preferential pathways exist in regions of high indium content. Furthermore, a negative correlation between the strain ε_{zz} and indium fraction shows that high indium content regions have reduced strain-induced piezoelectric polarization in the Z direction due to the mechanical constraint of the surrounding lower indium content regions.

Experimentally, multiple QW green LEDs with InGaN QBs exhibit lower V_F and blue-shifted wavelengths relative to LEDs with GaN QBs, consistent with simulation data. APT measurements of the LEDs with InGaN QBs show a thin layer at the upper QB/QW interface with lower indium composition which is attributed to the growth pause used to change temperature between the two layers. SDA of the APT data reveal that the InGaN QW, AlGaN cap layer, and InGaN QB alloy compositions are randomly distributed in the QW plane. Lastly, TRPL measurements on structures containing a deep (*n*-side) marker QW show that interwell carrier transport through blue-emitting transport QWs is more efficient and faster for structures with InGaN barriers relative to those containing GaN or AlGaN barriers. Detector QW PL transients measured at different temperatures confirm that thermionic transport of holes is the limiting mechanism for interwell transport.

The simulation-based and experimental results presented in this chapter can be used to inform heterostructure design of low V_F, long-wavelength LEDs. These studies also provide important insight into the nature of carrier transport in III-nitride alloy materials.

While presenting many benefits, the experimental use of InGaN QBs is not without challenges. To efficiently incorporate indium into the QBs, N_2 carrier gas and low temperatures are required. Unfortunately, these conditions are counter to those commonly used in high efficiency LED growth. For long-wavelength LEDs it has been shown to be particularly important to use H_2 carrier gas and high temperature QBs to recover the morphology from high indium QW growth and to minimize SRH-related nonradiative recombination [24,30-36]. Therefore, future studies should optimize the InGaN barrier growth conditions and explore the trade-off between InGaN barriers grown at lower temperature with N_2 carrier gas and GaN barriers grown at higher temperature with H_2 carrier gas.

References

[1] C. Lynsky, A.I. Alhassan, G. Lheureux, B. Bonef, S.P. DenBaars, S. Nakamura, Y.-R. Wu, C. Weisbuch, and J.S. Speck, Phys. Rev. Materials **4**, 054604 (2020).

[2] G. Lheureux, C. Lynsky, Y.-R. Wu, J.S. Speck, and C. Weisbuch, J. Appl. Phys. **128**, 235703 (2020).

[3] Y.-K. Kuo, J.-Y. Chang, M.-C. Tsai, and S.-H. Yen, Appl. Phys. Lett. **95**, 011116 (2009).

[4] J. Xu, M.F. Schubert, A.N. Noemaun, D. Zhu, J.K. Kim, E.F. Schubert, M.H. Kim, H.J. Chung, S. Yoon, C. Sone, and Y. Park, Appl. Phys. Lett. **94**, 011113 (2009).

[5] J.P. Liu, J.-H. Ryou, R.D. Dupuis, J. Han, G.D. Shen, and H.B. Wang, Appl. Phys. Lett. **93**, 021102 (2008).

[6] S. Marcinkevičius, R. Yapparov, L.Y. Kuritzky, Y.-R. Wu, S. Nakamura, S.P. DenBaars, and J.S. Speck, Appl. Phys. Lett. **114**, 151103 (2019).

[7] T.-J. Yang, R. Shivaraman, J.S. Speck, and Y.-R. Wu, Journal of Applied Physics **116**, 113104 (2014).

[8] D.A. Browne, B. Mazumder, Y.-R. Wu, and J.S. Speck, Journal of Applied Physics **117**, 185703 (2015).

[9] W. Hahn, J.-M. Lentali, P. Polovodov, N. Young, S. Nakamura, J.S. Speck, C. Weisbuch, M. Filoche, Y.-R. Wu, M. Piccardo, F. Maroun, L. Martinelli, Y. Lassailly, and J. Peretti, Phys. Rev. B **98**, 045305 (2018).

[10] R. Aleksiejūnas, K. Nomeika, O. Kravcov, S. Nargelas, L. Kuritzky, C. Lynsky, S. Nakamura, C. Weisbuch, and J.S. Speck, Phys. Rev. Applied **14**, 054043 (2020).

[11] K.S. Qwah, M. Monavarian, G. Lheureux, J. Wang, Y.-R. Wu, and J.S. Speck, Appl. Phys. Lett. **117**, 022107 (2020).

[12] M. Auf der Maur, A. Pecchia, G. Penazzi, W. Rodrigues, and A. Di Carlo, Phys. Rev. Lett. **116**, 027401 (2016).

[13] M. Filoche and S. Mayboroda, PNAS **109**, 14761 (2012).

[14] M. Filoche, M. Piccardo, Y.-R. Wu, C.-K. Li, C. Weisbuch, and S. Mayboroda, Phys. Rev. B **95**, 144204 (2017).

[15] D.N. Arnold, G. David, D. Jerison, S. Mayboroda, and M. Filoche, Phys. Rev. Lett. **116**, 056602 (2016).

[16] C.-K. Li, M. Piccardo, L.-S. Lu, S. Mayboroda, L. Martinelli, J. Peretti, J.S. Speck, C. Weisbuch, M. Filoche, and Y.-R. Wu, Phys. Rev. B **95**, 144206 (2017).

[17] C. Lynsky, G. Lheureux, B. Bonef, K.S. Qwah, R.C. White, S.P. Den Baars, S. Nakamura, Y.-R. Wu, C. Weisbuch, and J.S. Speck, *Submitted*.

[18] R. Yapparov, C. Lynsky, S. Nakamura, J.S. Speck, and S. Marcinkevičius, Appl. Phys. Express **13**, 122005 (2020).

[19] C. Geuzaine and J.-F. Remacle, Int. J. Numer. Meth. Engng. **79**, 1309 (2009).

[20] See http://gmsh.info/ for more information about Gmsh, a three-dimensional finite element mesh generator.

[21] Y.-R. Wu, R. Shivaraman, K.-C. Wang, and J.S. Speck, Appl. Phys. Lett. **101**, 083505 (2012).

[22] D. Watson-Parris, M.J. Godfrey, P. Dawson, R.A. Oliver, M.J. Galtrey, M.J. Kappers, and C.J. Humphreys, Phys. Rev. B **83**, 115321 (2011).

[23] See http://yrwu-wk.ee.ntu.edu.tw/ for "Optoelectronic device simulation laboratory".

[24] F. Jiang, J. Zhang, L. Xu, J. Ding, G. Wang, X. Wu, X. Wang, C. Mo, Z. Quan, X. Guo, C. Zheng, S. Pan, and J. Liu, Photonics Res. **7**, 144 (2019).

[25] A. David and M.J. Grundmann, Appl. Phys. Lett. **97**, 033501 (2010).

[26] E. Kioupakis, Q. Yan, and C.G. Van de Walle, Appl. Phys. Lett. **101**, 231107 (2012).

[27] F. Bernardini, V. Fiorentini, and D. Vanderbilt, Phys. Rev. B **56**, R10024 (1997).

[28] V. Fiorentini, F. Bernardini, and O. Ambacher, Appl. Phys. Lett. **80**, 1204 (2002).

[29] A.E. Romanov, T.J. Baker, S. Nakamura, and J.S. Speck, J. Appl. Phys. **100**, 023522 (2006).

[30] Y.-L. Hu, R.M. Farrell, C.J. Neufeld, M. Iza, S.C. Cruz, N. Pfaff, D. Simeonov, S. Keller, S. Nakamura, S.P. DenBaars, U.K. Mishra, and J.S. Speck, Appl. Phys. Lett. **100**, 161101 (2012).

[31] S.M. Ting, J.C. Ramer, D.I. Florescu, V.N. Merai, B.E. Albert, A. Parekh, D.S. Lee, D. Lu, D.V. Christini, L. Liu, and E.A. Armour, Journal of Applied Physics **94**, 1461 (2003).

[32] T. Shioda, H. Yoshida, K. Tachibana, N. Sugiyama, and S. Nunoue, Physica Status Solidi (a) **209**, 473 (2012).

[33] S. Saito, R. Hashimoto, J. Hwang, and S. Nunoue, Appl. Phys. Express **6**, 111004 (2013).

[34] D.D. Koleske, A.J. Fischer, B.N. Bryant, P.G. Kotula, and J.J. Wierer, Journal of Crystal Growth **415**, 57 (2015).

[35] A.I. Alhassan, R.M. Farrell, B. Saifaddin, A. Mughal, F. Wu, S.P. DenBaars, S. Nakamura, and J.S. Speck, Opt. Express, OE **24**, 17868 (2016).

[36] A.I. Alhassan, N.G. Young, R.M. Farrell, C. Pynn, F. Wu, A.Y. Alyamani, S. Nakamura, S.P. DenBaars, and J.S. Speck, Opt. Express, OE **26**, 5591 (2018).

[37] B. Bonef, M. Catalano, C. Lund, S.P. Denbaars, S. Nakamura, U.K. Mishra, M.J. Kim, and S. Keller, Appl. Phys. Lett. **110**, 143101 (2017).

[38] M.P. Moody, L.T. Stephenson, A.V. Ceguerra, and S.P. Ringer, Microsc. Res. Tech. **71**, 542 (2008).

[39] M. Khoury, H. Li, B. Bonef, L.Y. Kuritzky, A.J. Mughal, S. Nakamura, J.S. Speck, and S.P. DenBaars, Appl. Phys. Express **11**, 036501 (2018).

[40] F. Tang, T. Zhu, F. Oehler, W.Y. Fu, J.T. Griffiths, F.C.-P. Massabuau, M.J. Kappers, T.L. Martin, P.A.J. Bagot, M.P. Moody, and R.A. Oliver, Appl. Phys. Lett. **106**, 072104 (2015).

[41] M.J. Galtrey, R.A. Oliver, M.J. Kappers, C.J. Humphreys, D.J. Stokes, P.H. Clifton, and A. Cerezo, Appl. Phys. Lett. **90**, 061903 (2007).

[42] M. Piccardo, C.-K. Li, Y.-R. Wu, J.S. Speck, B. Bonef, R.M. Farrell, M. Filoche, L. Martinelli, J. Peretti, and C. Weisbuch, Phys. Rev. B **95**, 144205 (2017).

[43] B. Heying, E.J. Tarsa, C.R. Elsass, P. Fini, S.P. DenBaars, and J.S. Speck, Journal of Applied Physics **85**, 6470 (1999).

[44] X.H. Wu, C.R. Elsass, A. Abare, M. Mack, S. Keller, P.M. Petroff, S.P. DenBaars, J.S. Speck, and S.J. Rosner, Appl. Phys. Lett. **72**, 692 (1998).

[45] M. Shiojiri, C.C. Chuo, J.T. Hsu, J.R. Yang, and H. Saijo, Journal of Applied Physics **99**, 073505 (2006).

[46] I.-H. Kim, H.-S. Park, Y.-J. Park, and T. Kim, Appl. Phys. Lett. **73**, 1634 (1998).

[47] Z. Quan, L. Wang, C. Zheng, J. Liu, and F. Jiang, J. Appl. Phys. **116**, 183107 (2014).

[48] C.-K. Li, C.-K. Wu, C.-C. Hsu, L.-S. Lu, H. Li, T.-C. Lu, and Y.-R. Wu, AIP Advances **6**, 055208 (2016).

[49] S. Zhang, J. Zhang, J. Gao, X. Wang, C. Zheng, M. Zhang, X. Wu, L. Xu, J. Ding, Z. Quan, and F. Jiang, Photonics Res. **8**, 1671 (2020).

[50] C.-H. Ho, J.S. Speck, C. Weisbuch, and Y.-R. Wu, ArXiv:2109.08824 [Physics] (2021).

[51] A. David, M.J. Grundmann, J.F. Kaeding, N.F. Gardner, T.G. Mihopoulos, and M.R. Krames, Appl. Phys. Lett. **92**, 053502 (2008).

[52] J.H. Zhu, S.M. Zhang, H. Wang, D.G. Zhao, J.J. Zhu, Z.S. Liu, D.S. Jiang, Y.X. Qiu, and H. Yang, Journal of Applied Physics **109**, 093117 (2011).

[53] K. Fröjdh, S. Marcinkevičius, U. Olin, C. Silfvenius, B. Stålnacke, and G. Landgren, Appl. Phys. Lett. **69**, 3695 (1996).

[54] H. Hillmer and S. Marcinkevičius, Applied Physics B: Lasers and Optics **66**, 1 (1998).

[55] Ü. Özgür, M.J. Bergmann, H.C. Casey, H.O. Everitt, A.C. Abare, S. Keller, and S.P. DenBaars, Appl. Phys. Lett. **77**, 109 (2000).

[56] H. Schneider and K. v. Klitzing, Phys. Rev. B **38**, 6160 (1988).

5

V-defect Engineering on Sapphire

5.1 Introduction

Contributions to the large excess voltage in green III-nitride LEDs were discussed in Chapter 3. In Chapter 4, InGaN alloy QBs were proposed as one approach to minimize the barriers to carrier transport by reducing the polarization discontinuity at the QW/QB interface and introducing an additional source of alloy disorder in the active region. In this chapter, V-defect engineering is presented as an alternative method to reduce V_F in long-wavelength LEDs. Considerable progress on improving the WPE of green- to red-emitting LEDs was demonstrated by Jiang *et al*., where the impressive results were attributed to the use of V-defects that allow hole injection into lower QWs [1,2]. This result is significant because in typical planar LEDs under electrical pumping, only the top, *p*-side QW contributes to luminescence due to limited hole injection to the lower, *n*-side QWs [3,4].

Background on the formation and structure of V-defects were discussed in Chapter 2 [5-10]. In the past, V-defects were predominately believed to be detrimental to device performance and thus significant research was devoted to minimizing their size and density [11,12]. However, a growing body of research suggests that, if engineered carefully, V-defects can improve the WPE of long-wavelength LEDs [1,2,13-16]. Quan *et al*. showed using numerical simulations that V-defects can improve LED quantum efficiency by

enhancing hole injection [13]. This is possible due to the lower polarization charge densities at the InGaN/GaN and AlGaN/GaN interfaces on the semipolar $\{10\bar{1}1\}$ sidewalls relative to the planar region. In a four-QW LED structure, they calculated a significant increase in hole concentration in the central two QWs for a structure with a V-defect compared to one without a V-defect. In subsequent simulation studies, Li *et al*. demonstrated that higher densities and larger size V-defects lead to a reduced V_F in MQW LEDs [14]. Similar to Quan *et al*., they observed hole current flowing along the inclined sidewall QWs of the V-defect in addition to the planar QWs, thus allowing for more uniform hole injection of deeper (*n*-side) QWs. From these simulations, Li *et al*. concluded that increasing the V-defect size and density provides a larger area for sidewall carrier injection. Jiang *et al*. and Zhang *et al*. built upon these efforts and demonstrated experimentally III-nitride LEDs (λ ranging from ~522 nm to ~622 nm) with engineered V-defects on silicon substrates with low ΔV_F and high WPE [1,2].

These findings on the beneficial role of V-defects are consistent with the results presented in Chapter 3 indicating that polarization barriers in green LEDs significantly contribute to a large ΔV_F [17,18]. The semipolar sidewalls of V-defects may then provide a lower polarization barrier for carrier injection into QWs relative to planar injection. A significant portion of the experimental research published on V-defects for voltage reduction is for GaN growth on silicon substrates, where TD densities are on the order of 10^9 cm^{-2}. These high TD densities in turn make it possible to realize LEDs with V-defect densities on the order of 10^9 cm^{-2}. For conventional GaN growth on sapphire substrates, TD densities are on the order of low 10^8 cm^{-2}, leading to lower V-defect densities. There have also been several investigations into V-defect engineering for green LEDs on sapphire substrates [19-

21]. Zhou *et al*. demonstrated that increasing the period of the InGaN/GaN superlattice resulted in larger V-defects, which in turn led to a reduction in V_F in green LEDs [19]. The V-defect density in these studies varied from 1.2×10^8 cm^{-2} to 1.6×10^8 cm^{-2}, which is lower than the densities achieved on silicon by an order of magnitude. They also found that low-temperature GaN can act as an alternative to a superlattice for V-defect formation. In another recent study, Lee *et al*. studied 300 μm and 10 μm-size green LEDs with different size V-defects, where the V-defect size was controlled by growing moderate temperature GaN layers of varying thickness to generate V-defects [20]. For both LEDs sizes with an estimated V-defect density of 2×10^8 cm^{-2}, they measured a reduction in V_F with increasing V-defect size. These results show the promise of V-defect engineering on sapphire as well as silicon substrates.

In this chapter the TD density, and thus the V-defect density, is systematically increased in InGaN-based green LEDs grown on sapphire substrates by MOCVD [22]. The TD density, V-defect density, material quality, and LED device performance are characterized. Advanced characterization of V-defects in green LEDs on sapphire is also presented.

5.2 Role of V-defect Density

5.2.1 Methods

To characterize the change in TD density for varied growth conditions, UID GaN/*n*-GaN templates were grown by atmospheric pressure MOCVD on (0001) single side polish (SSP) sapphire substrates and patterned sapphire substrates (PSS). The GaN template

growth is further divided into five steps to investigate the impact of changing NH_3 flow during these steps,

1. Nucleation layer
2. Temperature ramp from 505 °C to 900 °C
3. Temperature ramp from 900 °C to 1220 °C
4. High temperature (HT) UID GaN growth
5. High temperature (HT) *n*-GaN growth

The sum of the NH_3, metalorganic (MO) carry, and gas carry was kept constant at 7 slm for each layer. For example, if the NH_3 flow in the nucleation layer was 4 slm, then the MO carry was 1.5 slm and the gas carry was 1.5 slm. If the NH_3 flow in the nucleation layer was decreased to 3 slm, then the MO carry and gas carry were both increased to 2 slm. For each template growth, PSS and SSP sapphire substrates were co-loaded and measured. Table 5.1 shows the conditions used in three separate experiments. In Experiment 1, the NH_3 flow was varied in the nucleation layer and the temperature ramp from 505 °C to 900 °C. In Experiment 2, the NH_3 was varied in the temperature ramp from 900°C to 1220 °C. Lastly, in Experiment 3, the NH_3 flow was varied in both the temperature ramp from 900°C to 1220 °C and the HT UID GaN layer. As will be shown in the next section, the growth parameters changed during Experiment 3 led to the desired effect of an increase in the TD density for the SSP samples. Therefore, these conditions were adopted for the remained of the experiments and the substrate type investigated was limited to SSP. Nevertheless, brief results from Experiments 1 and 2 as well as PSS results from Experiment 3 will be presented in Section 5.2.2.

Table 5.1. The five steps that comprise the MOCVD growth of GaN templates on sapphire substrates. The NH_3 flow conditions for each step are shown for Experiments 1, 2, and 3. Multiple values indicate a series where different NH_3 flows were explored.

Growth step	Experiment 1 NH_3 flow (slm)	Experiment 2 NH_3 flow (slm)	Experiment 3 NH_3 flow (slm)
Nucleation	2, 4, or 6	4	4
Ramp 505 °C to 900 °C	2, 4, or 6	4	4
Ramp 900 °C to 1220 °C	3	1, 3, or 5	1, 3, 4, or 5
HT UID GaN	3	3	1, 3, 4, or 5
HT *n*-GaN	3	3	3

The four samples grown on SSP substrates from Experiment 3 are referred to as GaN-1, GaN-3, GaN-4, and GaN-5, where the number represents the NH_3 flow. For these samples, a ~40 nm thick nucleation layer was grown at 505 °C using 4 slm NH_3 flow followed by a temperature increase to 900 °C, also under 4 slm NH_3 flow. Next, the temperature was increased from 900 °C to 1220 °C and a 2.2 μm thick UID GaN layer was subsequently deposited at 1220 °C; X slm NH_3 flow was used during these steps, where X = 1, 3, 4, 5. NH_3 flows of 1, 3, 4, and 5 slm correspond to V/III molar flow ratios of 758, 2275, 3034, and 3792, respectively. The UID GaN was followed by a 2.2-μm *n*-GaN ([Si] = 5×10^{18} cm^{-3}) layer grown at 1220 °C using 3 slm NH_3 flow. All other growth conditions were kept constant, including TMG precursor flow and growth time. A schematic of the GaN template structures is shown in Fig. 5.1.

XRD ω-rocking curve measurements of the template samples from Experiments 1, 2, and 3 on SSP and PSS were performed on a Panalytical MRD PRO using Cu Kα1 radiation (λ = 1.5405 Å). The 0002- and $20\bar{2}1$-reflections were measured in a symmetric and skew symmetric geometry, respectively, and the full width half maximum (FWHM) values were

determined. An Asylum MFP-3D atomic force microscope (AFM) in standard tapping mode was used to characterize surface morphology and spectral reflectance measurements using a Filmetrics system were used to determine total film thickness. Lastly, TDs were imaged using a ThermoFisher Apreo C FEG scanning electron microscope (SEM) equipped with a cathodoluminescence (CL) detector. CL imaging was done in panchromatic mode using 5 kV and 1.6 nA beam conditions.

Green LEDs on SSP sapphire substrates were grown by MOCVD with either 3, 4, or 5 slm NH_3 flow during the 900 °C to 1220 °C temperature ramp and UID GaN growth. The LED samples with 3, 4, and 5 slm NH_3 flow are referred to as LED-3, LED-4, and LED-5, respectively. A 30-period *n*-type 2.5 nm/5 nm $In_{0.05}Ga_{0.95}N$/GaN superlattice ([Si] = 5×10^{18} cm^{-3}) grown at 890 °C was used to form V-defects at TDs. The five-QW active region was grown undoped and consisted of 3-nm $In_{0.22}Ga_{0.78}N$ QWs, 2-nm $Al_{0.10}Ga_{0.90}N$ capping layers, 4-nm low temperature (LT) GaN barriers, and 6-nm high temperature (HT) GaN barriers. The QW, AlGaN cap, HT GaN, and LT GaN growth temperatures were 775 °C, 775 °C, 860 °C, and 915 °C, respectively. The active region was followed by a *p*-AlGaN electron blocking layer, *p*-GaN, and a *p*+-GaN contact layer. An additional three LED-like structures with varying NH_3 flow were grown and interrupted at the top of the last (*p*-side) GaN QB. The interrupted growth samples with 3, 4, and 5 slm NH_3 flow are referred to as IG-3, IG-4, and IG-5, respectively. It should be noted that all growth temperatures given are the thermocouple temperature, not the actual surface temperature. Schematics of the interrupted growth and LED structures are shown in Fig. 5.1.

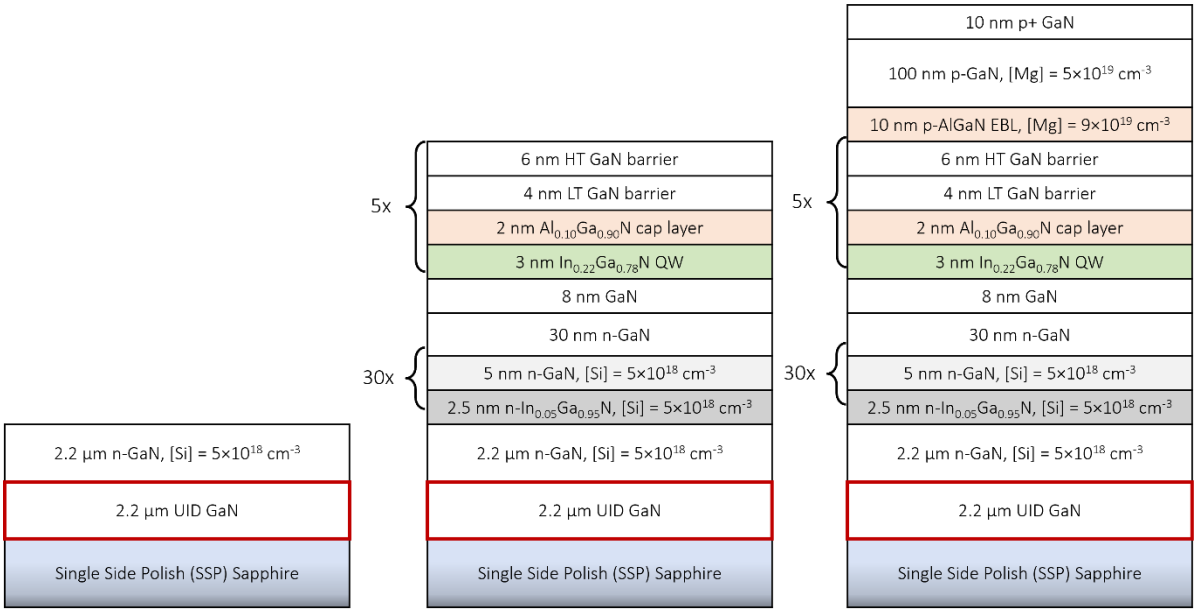

Figure 5.1. Schematics showing the epitaxial structure for the template samples GaN-1, GaN-2, GaN-3, GaN-5 (left), the interrupted growth samples IG-3, IG-4, IG-5 (center), and LED samples LED-3, LED-4, LED-5 (right). The layer indicated in red shows where the NH_3 flow was varied for each set of samples.

SEM images using a FEI Nova Nano 650 FEG SEM at 2 kV were obtained on the interrupted growth samples (IG-3, IG-4, IG-5) to characterize the size and density of V-defects at the surface of the active region. The full LED samples (LED-3, LED-4, LED-5) underwent a post-growth anneal in N_2/O_2 at 600 °C for 15 minutes to activate the Mg-doped layers. The samples were then fabricated into LEDs using a $SiCl_4$ RIE for mesa isolation, PECVD for SiO_2 sidewall passivation, and electron-beam deposition for contact deposition. Ti/Au was used as the contact to *n*-GaN and Pd/Au as the contact to *p*-GaN for simple fabrication and reliable voltage determination. The final device size was 0.025 mm^2. Devices were measured on-wafer and the power was measured from back-side emission. With metal contacts, this device design was not optimized for light extraction and on-wafer measurements yielded only relative power.

5.2.2 Results

Figure 5.2(a) shows the FWHM values (Δω) from XRD ω-scans of the template samples from Experiment 1 with 2, 4, or 6 slm NH_3 flow on SSP or PSS. The Δω of the on-axis 0002-reflection $\Delta\omega_{0002}$ is approximately constant on both PSS and SSP while the Δω of the off-axis $20\bar{2}1$-reflection $\Delta\omega_{20\bar{2}1}$ decreases slightly with increasing NH_3 flow for both substrate types. The XRD results from Experiment 2 are shown in Fig. 5.2(b). Again, $\Delta\omega_{0002}$ is relatively constant on both PSS and SSP. Under these growth conditions, however, $\Delta\omega_{20\bar{2}1}$ increases with increasing NH_3 flow for both substrate types, with the trend being more pronounced for templates on SSP. Lastly, Fig. 5.2(c) shows the Δω measured for template samples GaN-1, GaN-3, GaN-4, and GaN-5 from Experiment 3. For these conditions, $\Delta\omega_{0002}$ has a relatively constant value of ~250 arcsec with increasing NH_3 flow while $\Delta\omega_{20\bar{2}1}$ increases from ~250 arcsec to ~700 arcsec with increasing NH_3 flow.

The rocking curve width of the $20\bar{2}1$-reflection, measured in a skew symmetric geometry, is a measure of subgrain twist in the epitaxial layer. As the simplest estimate, the edge-component TDD is proportional to the square of the off-axis rocking curve width [23,24]. The peak broadening observed for the $20\bar{2}1$ reflection therefore indicates a significant change in the edge-component TDD was achieved when the NH_3 flow was increased from 1 to 5 slm during the 900 °C to 1220 °C temperature ramp and HT UID GaN growth. In contrast, the relatively constant value of $\Delta\omega_{0002}$ indicates there is a negligible increase in the screw-component TDD.

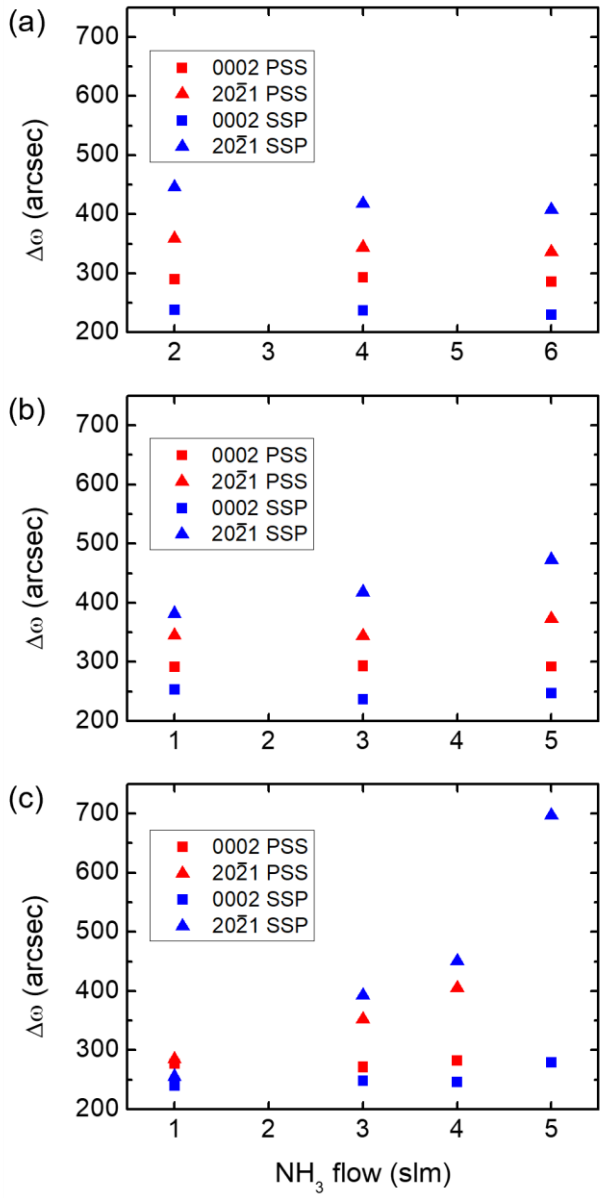

Figure 5.2. Δω values from XRD ω-rocking curve scans of the 0002- and 20$\bar{2}$1-reflections for templates on SSP and PSS. (a) Experiment 1: NH_3 flow varied in the nucleation layer and during the temperature ramp from 505 °C to 900 °C. (b) Experiment 2: NH_3 flow varied during the temperature ramp from 900 °C to 1220 °C. (c) Experiment 3: NH_3 flow varied during the temperature ramp from 900 °C to 1220 °C and in the HT UID GaN layer.

A high V/III ratio decreases island size during early stages of HT GaN growth by promoting a faster transition from a 3D island growth to a 2D layer-by-layer growth mode [25,26]. A higher density of small islands leads to an increase in edge TD formation at

island coalescence [27,28]. A schematic showing the evolution of GaN nucleation and growth to form a coalesced buffer layer on sapphire is presented in Fig. 5.3; the edge TDs formed at the island coalescence boundaries are indicated as vertical lines.

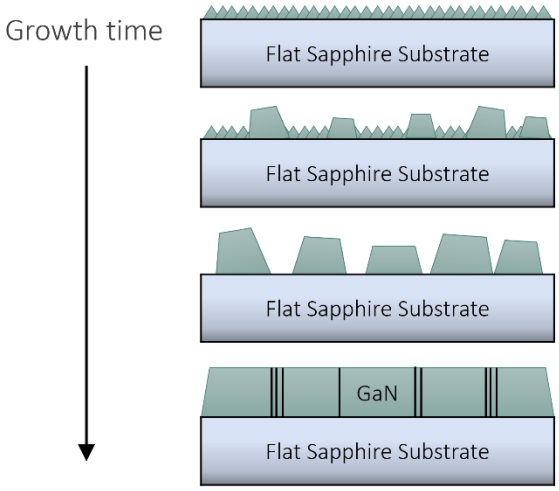

Figure 5.3. Schematic showing the evolution of GaN nucleation and growth to form a coalesced buffer layer on sapphire.

The morphology of the GaN-1, GaN-3, and GaN-5 samples were characterized using AFM and the 5 × 5 μm^2 scans are shown in Fig. 5.4. For 1 slm NH_3 flow and 3 slm NH_3 flow, the templates show a relatively smooth morphology with clearly defined terraces and steps – this morphology is consistent with step-flow growth. The GaN-5 sample also exhibits step-flow growth morphology; however, significant step pinning occurs at screw-component threading dislocations. This trend is consistent with previous reports where an increase in the V/III ratio decreases the equilibrium vapor pressure of the solid, thus increasing the driving force for growth and resulting in more step pinning [29]. From these data, it was confirmed that while the GaN-5 sample was expected to have a high TD density,

the morphological quality of the template is high, thus allowing for the growth of high-performance green LEDs.

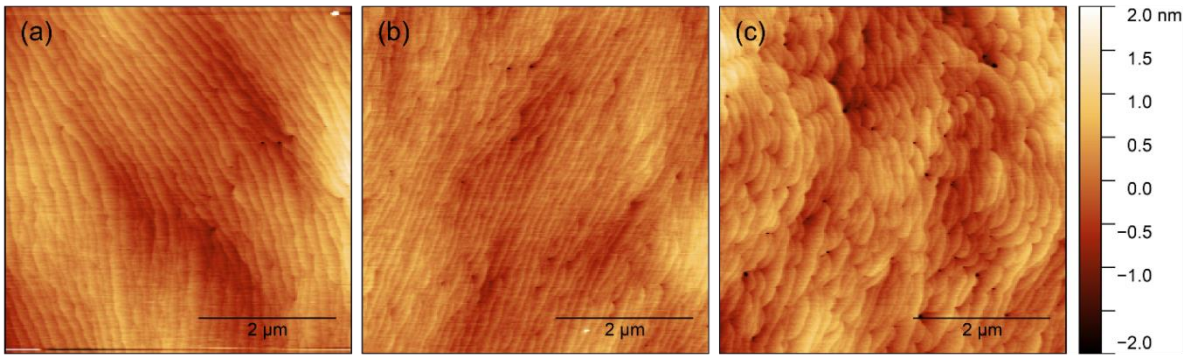

Figure 5.4. AFM measurements (5 × 5 µm^2) of GaN template samples on flat sapphire substrates using (a) 1 slm (GaN-1), (b) 3 slm (GaN-3), and (c) 5 slm (GaN-5) NH_3 flow during the temperature ramp after the nucleation layer and during the HT UID GaN growth. This figure was published in [22] Copyright Elsevier (2021).

Wafer maps of total thickness, as measured by spectral reflectance, allow for the growth rate and growth uniformity to be compared for different growth conditions. The total GaN template film thickness is plotted as a function of wafer position in Fig. 5.5, where locations -22 cm and 22 cm indicate the outer edge of the wafer and location 0 indicates the center of the wafer. The GaN-3 and GaN-5 samples have comparable thicknesses and growth rate uniformity, while the GaN-1 sample has a significantly reduced thickness. Because the regime of interest is one where the TD density is increased, not decreased, less attention is given to the poor growth rate and uniformity of the GaN-1 sample. For the GaN-3, GaN-4, and GaN-5 samples, the template thicknesses are expected to be similar and uniform, and therefore the change in NH_3 should not introduce undesirable secondary effects related to growth rate.

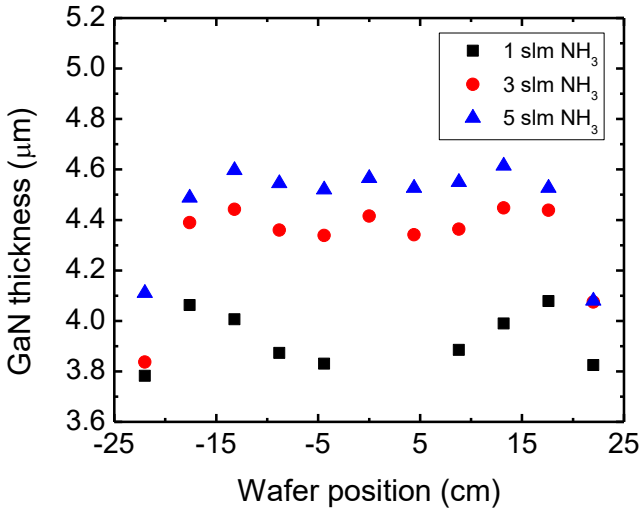

Figure 5.5. GaN film thickness maps across a 2-inch SSP wafer for GaN-1, GaN-3, and GaN-5. Measurements were performed using spectral reflectance.

XRD ω-rocking curve, AFM, and film thickness data support that a systematic increase in the TD density of GaN on SSP substrates was achieved without compromising the template morphology or uniformity. Panchromatic CL measurements were then performed to image the TDs; Fig. 5.6(a) – 5.6(c) shows the results for the GaN-3, GaN-4, and GaN-5 samples. Consistent with previous measurements, an appreciable increase in the TD density was observed with increasing NH_3 flow from 3 to 5 slm. The high TD density in these samples makes quantification challenging due to clustering of dislocations. However, dislocation counting from CL images yielded approximate TD densities of 4×10^8, 6×10^8, 1×10^9 cm^{-2} for the GaN-3, GaN-4, and GaN-5 samples, respectively. Figure 5.7 shows the dependence of TD density (as measured by CL) on $\Delta\omega^2_{20\bar{2}1}$ from XRD measurements. The increase in TD density with $\Delta\omega^2_{20\bar{2}1}$ signifies an increase in the edge-component TD density. This finding agrees with previous evidence that increasing the V/III ratio results in a large density of small islands and therefore more island coalescence boundaries.

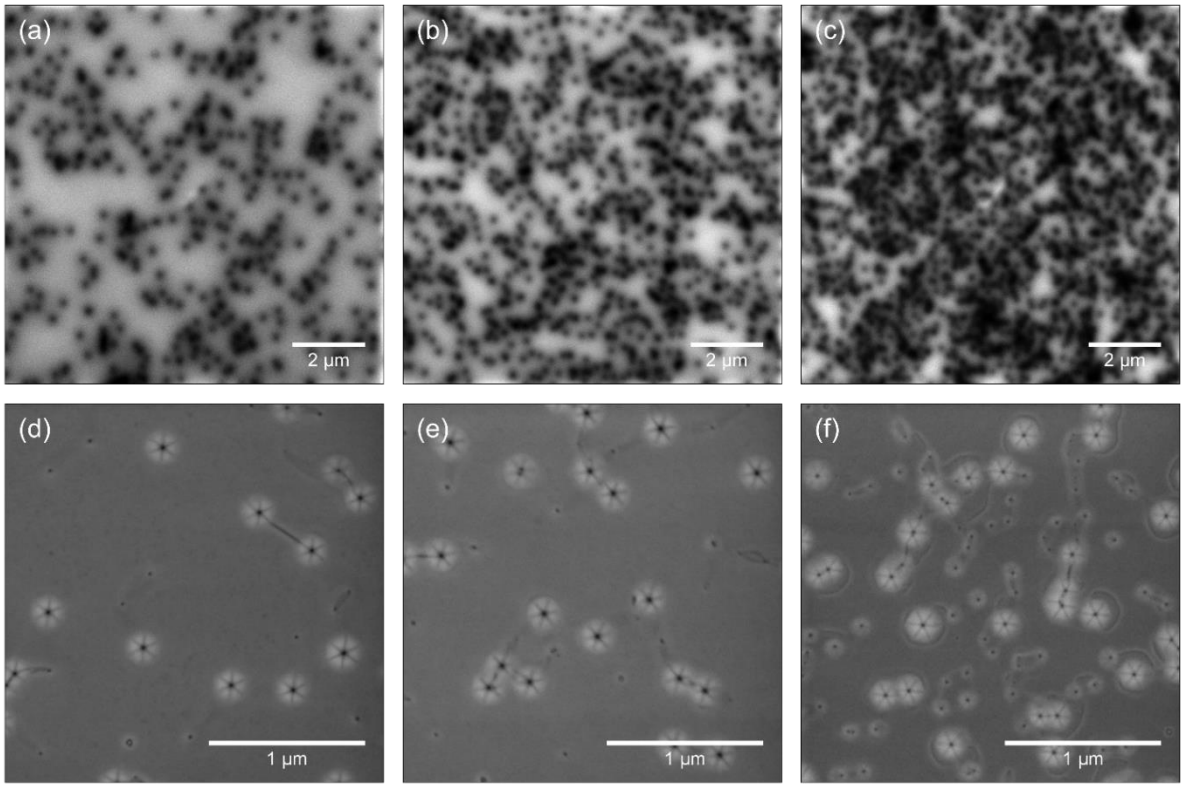

Figure 5.6. Panchromatic CL images (5 kV, 1.6 nA) of GaN template samples using (a) 3 slm (GaN-3), (b) 4 slm (GaN-4), and (c) 5 slm (GaN-5) NH_3. Secondary electron SEM images (2 kV) at the top surface of the active region for interrupted growth samples with (d) 3 slm (IG-3), (e) 4 slm (IG-4), and (f) 5 slm (IG-5) NH_3 flow. This figure was published in [22] Copyright Elsevier (2021).

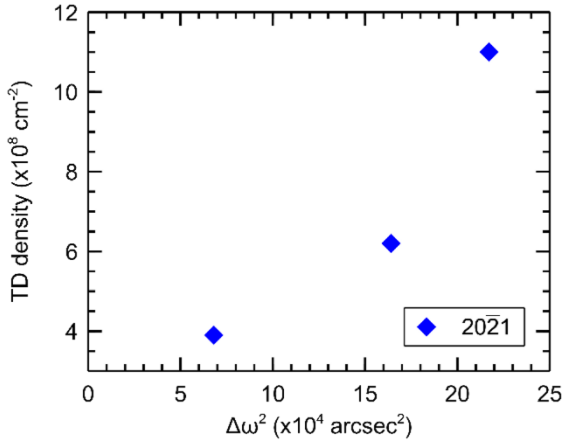

Figure 5.7. Dependence of TD density (as measured by CL) on $\Delta\omega^2_{20\bar{2}1}$ from XRD measurements of the GaN-3, GaN-4, and GaN-5 samples. This figure was published in [22] Copyright Elsevier (2021).

From SEM images collected on IG-3, IG-4, and IG-5 samples, an increase in V-defect density with NH_3 flow is observed in Fig. 5.6(d) – 5.6(f). Populations of small defects (less than ~150 nm across with no visible semipolar sidewalls) and large V-defects (greater than ~150 nm across) are present in all samples; however, the sample IG-5 has a particularly high density of small defects. Table 5.2 summarizes the average size of large V-defects, density of large defects, density of small defects, and total density of defects for each sample. Approximately a 2.5-fold increase in the density of large V-defects and 5.5-fold increase in the density of small defects was achieved by increasing the NH_3 flow from 3 to 5 slm during the temperature ramp and HT GaN growth. However, the high density of small defects indicates that there is a population of dislocations that do not form V-defects during the SL growth. Indeed, the density of total defects in the interrupted growth samples (4.1×10^8, 6.2×10^8, 1.7×10^9 cm^{-2} for IG-3, IG-4, IG-5, respectively) is in close agreement with the density of TDs measured in the template samples (4×10^8, 6×10^8, 1×10^9 cm^{-2} for GaN-3, GaN-4, GaN-5, respectively).

Table 5.2. Average size of large defects D_L, density of large defects ρ_L, density of small defects ρ_S, and total density of defects ρ_T, for interrupted growth samples IG-3, IG-4, and IG-5 with varying NH_3 flow. This table was published in [22] Copyright Elsevier (2021).

NH_3 flow (slm)	D_L (nm)	ρ_L (cm^{-2})	ρ_S (cm^{-2})	ρ_T (cm^{-2})
3	184 ± 15	2.0×10^8	2.2×10^8	4.1×10^8
4	206 ± 17	2.6×10^8	3.6×10^8	6.2×10^8
5	174 ± 27	5.0×10^8	1.2×10^9	1.7×10^9

The J-V characteristics of the final LED devices reveal a systematic decrease in voltage with increasing V-defect density. The trend is consistent from 0.1 to 100 A cm^{-2},

with a total voltage decrease of 0.13 V at 20 A cm^{-2}. Figure 5.8(a) shows the linear J-V curves from 0 to 4 V and Fig. 5.8(b) shows a reduced view of the semi-log J-V curves to emphasize the trend in V_F at low J, where the series resistance contribution is minimal. The average forward voltage V_F, relative power L_r, peak wavelength λ_{peak}, and spectrum FWHM $\Delta\lambda$ measured at 20 A cm^{-2} for each sample is summarized in Table 5.3. Along with the decrease in voltage with increasing V-defect density, from LED-3 to LED-5 there is a slight decrease in relative power from 0.53 to 0.43 mW (note again these are on-wafer powers measured on the LED backside into a photodiode), an increase in λ_{peak} from 516 to 523 nm, and an increase in $\Delta\lambda$ from 26 to 32 nm.

The decrease in V_F with increasing V-defect density agrees with 3D numerical modeling performed by Li *et al*. where a higher V-defect density enables hole injection via the semipolar sidewall QWs [14]. However, undesirable slight decrease in the light output power was measured experimentally; this effect is attributed to the high density of small defects, which are likely a combination of threading dislocations and small V-defects formed later in growth. While the TD density was successfully increased by approximately one order of magnitude, the accompanying density of large V-defects was only increased by a factor of 2.6. The TDs that do not have an associated large V-defect likely act as centers for significant nonradiative recombination. There also appears to be a population of TDs associated with small V-defects. The semipolar sidewalls of small V-defects, which open at the top of the SL or within the active region, do not penetrate through the entire active region. It is therefore unlikely that small V-defects provide the same path for hole injection into deeper QWs as large V-defects. In work by Jiang *et al*. these different sized of V-defects were imaged in cross-sectional scanning transmission electron microscopy and it

was proposed that large V-defects with well-defined sidewalls are more beneficial for passivation of TDs and deeper hole injection [16].

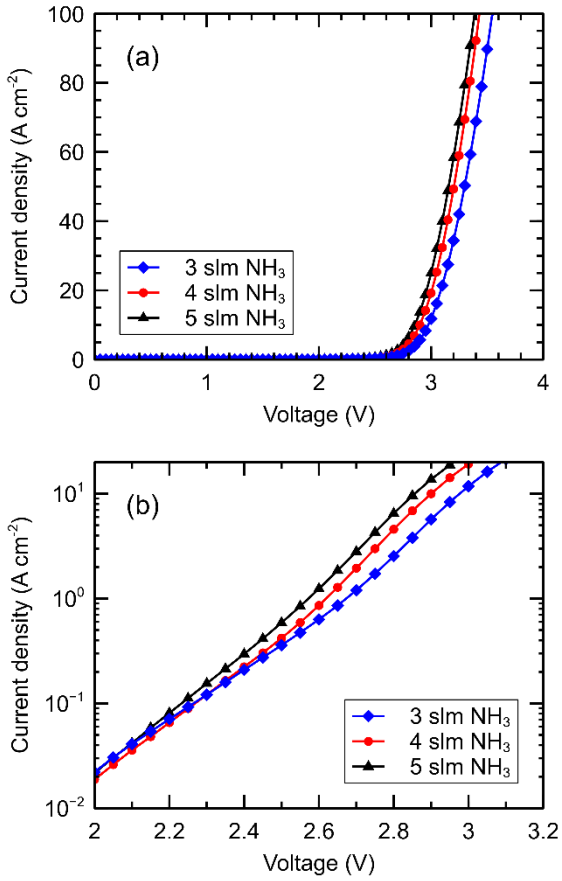

Figure 5.8. (a) *J-V* curves for LED samples with varying template NH_3 flow and thus threading dislocation and V-defect densities. (b) Reduced view of semi-log *J-V* curves to emphasize the trend in V_F at low *J*, where the series resistance contribution is minimal. This figure was published in [22] Copyright Elsevier (2021).

Table 5.3. Average forward voltage V_F, relative power L_r, peak wavelength λ_{peak}, and spectrum FWHM Δλ measured at 20 A cm^{-2} for LED samples LED-3, LED-4, and LED-5 with varying NH_3 flow. This table was published in [22] Copyright Elsevier (2021).

NH_3 flow (slm)	V_F (V)	L_r (mW)	λ_{peak}(nm)	Δλ (nm)
3	3.07	0.53	516	26
4	3.02	0.50	521	28
5	2.94	0.43	523	32

If the increase in TD density resulted in an equal increase in the density of large V-defects, it expected that a more significant voltage reduction (and even an increase in light output power) would have been observed. Nevertheless, the observed decrease in V_F with higher V-defect density is consistent with previous modeling predictions [14] and experimental results that demonstrate the positive impact of V-defects on electrical efficiency [1,2,16]. The absence of improvement in output power is attributed to nonradiative recombination that likely occurs at the high density of TDs which do not contain large V-defects. Experimental evidence on the benefits of V-defects for electrical efficiency have been predominantly reported for III-nitride materials on silicon substrates. These results therefore underscore the potential of using V-defect engineering for voltage reduction in green LEDs on sapphire substrates.

5.3 V-defect Characterization

Important data on the V-defect structure and site-III atomic fraction were measured using advanced materials characterization techniques including high-angle annular dark-field scanning transmission electron microscopy (HAADF-STEM), transmission electron microscopy-based energy dispersive X-ray spectroscopy (TEM-EDX), and atom probe

tomography (APT). The materials characterization presented here was performed by Dr. Feng Wu. Figure 5.9 shows a cross-section HAADF STEM image of a V-defect formed in a green LED on sapphire. From this cross-section, the V-defect is seen to nucleate at a TD in the InGaN/GaN SL, which is consistent with expectations based on literature reports and the SEM presented in Section 5.2.2.

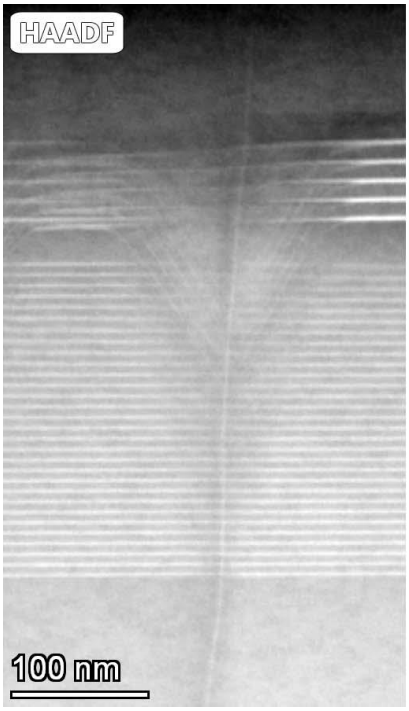

Figure 5.9. Cross-section HAADF-STEM image of a V-defect nucleated at a TD in the InGaN/GaN SL. This green LED structure was grown on PSS with a 30-period SL and a five-period QW active region.

In Fig. 5.10(a), the HAADF-STEM image highlights the MQW structure in the vicinity of a V-defect; the semipolar sidewall QWs are seen to be thinner than the *c*-plane QWs. Figures 5.10(b) and 5.10(c) show EDX images of gallium and indium, respectively, in the same V-defect region where there is reduced indium incorporation in the sidewall QWs relative to the planar QWs. The gallium and indium atomic fraction profiles (as measured by

EDX) around the V-defect are shown in Fig. 5.10(d). Peaks 1-4 show the site-III fraction in the planar region while peaks 5-9 show the site-III fraction in the sidewall region; again, the sidewall region shows lower indium incorporation by a factor of ~3-4. The peak numbers correspond to the labeled regions in Fig. 5.10(a).

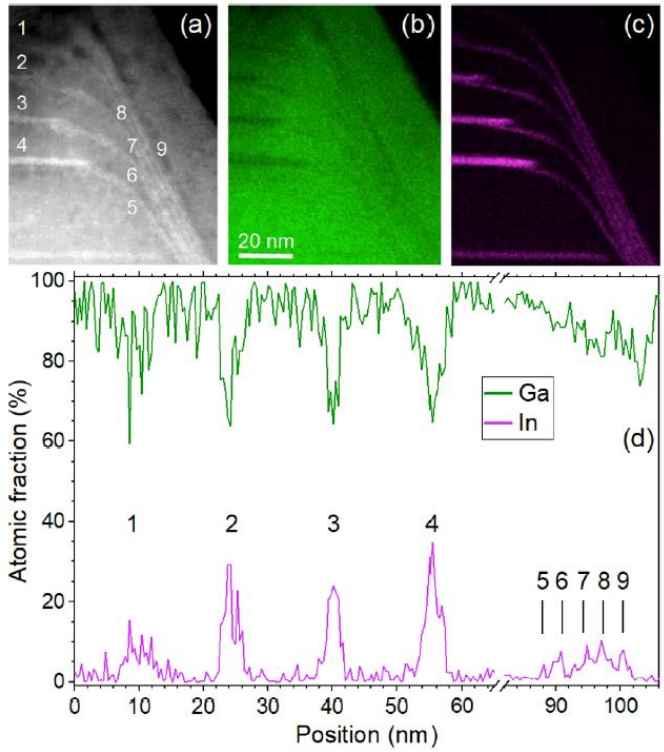

Figure 5.10. (a) HAADF-STEM image of V-defect region in a five-QW green LED on PSS. EDX images of (b) gallium and (c) indium concentrations in the same V-defect region. (d) Site-III atomic fraction profiles where the numbers correspond to the regions in part (a). From these images, the V-defect sidewalls are observed to be thinner and have lower indium incorporation relative to the planar regions. Reproduced from [30], with the permission of AIP Publishing.

A 3D APT reconstruction of a green LED grown on sapphire (sample grown by Dr. Abdullah Alhassan) is shown in Fig. 5.11(a). The APT tip is taken in the vicinity of a V-defect to capture the semipolar sidewall QWs and QBs. A schematic of the V-defect

geometry is overlaid to highlight the V-defect initiation in the SL. From APT, the 1D concentration profiles can be extracted. Figure 5.11(b) shows the site-III atomic percentage along the black dashed line shown in Fig. 5.11(a). While the planar QWs are expected to have a composition of ~20% indium, the sidewall QWs are seen to have a much lower indium faction closer to ~3%. The sidewall QW indium fraction determined from both TEM-EDX and APT are in relatively close agreement. In both cases, planar QWs with ~20% indium contain semipolar sidewall QWs with less than 5% indium. The structural characterization of V-defects as well as quantification of the sidewall QW composition provide important information for understanding the band diagram in these 3D *p-n* junctions. These values can be used as input parameters for 2D V-defect simulations [14,15].

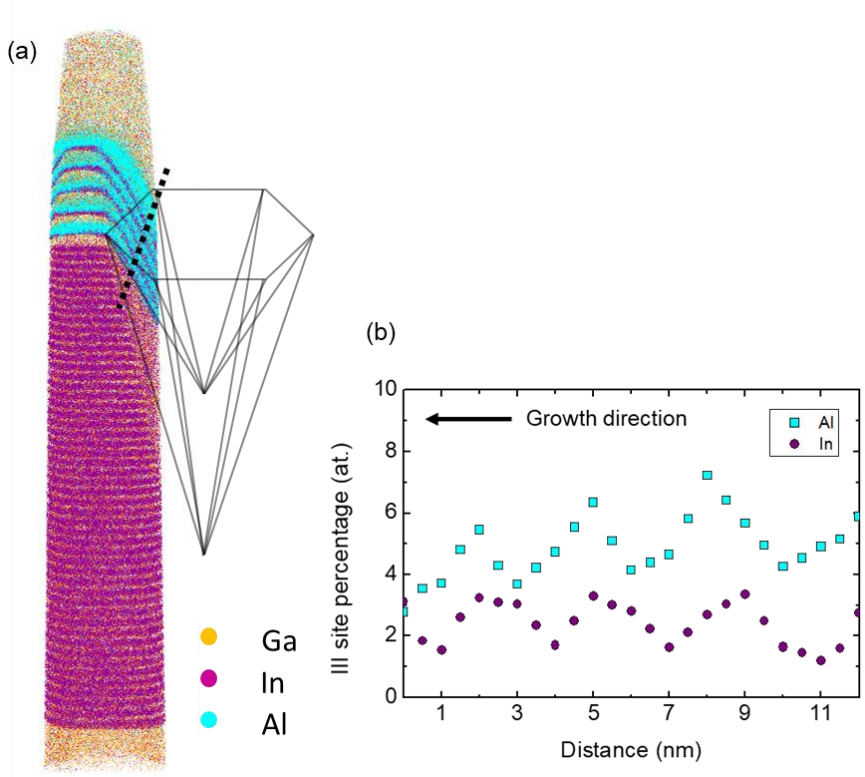

Figure. 5.11. (a) APT 3D reconstruction of a green LED on sapphire in the vicinity of a V-defect. A schematic of the V-defect geometry is overlaid to aid visualization of V-defect initiation in the SL. (b) Site-III atomic percentage along the black dashed line shown in part (a).

5.4 Conclusions

The role of V-defect density on device performance for green LEDs grown on sapphire substrates was investigated experimentally. By increasing the V/III ratio during high temperature UID GaN growth, higher densities of TDs and V-defects were achieved. From XRD rocking curve measurements, $\Delta\omega_{0002}$ remained constant while $\Delta\omega_{20\bar{2}1}$ increased significantly with NH_3 flow, indicating a negligible change in screw-component dislocations but a large increase in edge dislocations. By comparing the V-defect density at the top of the active region from SEM to the TD density from CL, it was observed that not all TDs opened

into large V-defects (greater than ~150 nm across). After SL and active region growth, a significant population of TDs without V-defects, or with only small V-defects (less than ~150 nm across), still exist. A decrease in V_F from 3.07 V to 2.94 V with increasing V-defect density from 2.0×10^8 to 5.0×10^8 cm^{-2} was measured in fabricated LEDs. These findings agree with previous simulations and experiments which indicate that the semipolar sidewall QWs in V-defects provide a lower energy barrier for hole injection into deeper QWs due to the lower polarization charge densities at the InGaN/GaN and AlGaN/GaN interfaces. The opening of all TDs into large V-defects with well-defined sidewall structure is predicted to lead to further reduction in V_F as well as reduction in nonradiative recombination at TDs. The results presented here highlight the promise of V-defect engineering for voltage reduction in long-wavelength III-nitride LEDs grown on sapphire substrates.

References

[1] F. Jiang, J. Zhang, L. Xu, J. Ding, G. Wang, X. Wu, X. Wang, C. Mo, Z. Quan, X. Guo, C. Zheng, S. Pan, and J. Liu, Photonics Res. **7**, 144 (2019).

[2] S. Zhang, J. Zhang, J. Gao, X. Wang, C. Zheng, M. Zhang, X. Wu, L. Xu, J. Ding, Z. Quan, and F. Jiang, Photonics Res. **8**, 1671 (2020).

[3] David, M.J. Grundmann, J.F. Kaeding, N.F. Gardner, T.G. Mihopoulos, and M.R. Krames, Appl. Phys. Lett. **92**, 053502 (2008).

[4] J.H. Zhu, S.M. Zhang, H. Wang, D.G. Zhao, J.J. Zhu, Z.S. Liu, D.S. Jiang, Y.X. Qiu, and H. Yang, Journal of Applied Physics **109**, 093117 (2011).

[5] B. Heying, E.J. Tarsa, C.R. Elsass, P. Fini, S.P. DenBaars, and J.S. Speck, Journal of Applied Physics **85**, 6470 (1999).

[6] X.H. Wu, C.R. Elsass, A. Abare, M. Mack, S. Keller, P.M. Petroff, S.P. DenBaars, J.S. Speck, and S.J. Rosner, Appl. Phys. Lett. **72**, 692 (1998).

[7] I.-H. Kim, H.-S. Park, Y.-J. Park, and T. Kim, Appl. Phys. Lett. **73**, 1634 (1998).

[8] A.E. Romanov, T.J. Baker, S. Nakamura, and J.S. Speck, J. Appl. Phys. **100**, 023522 (2006).

[9] S. Tomiya, Y. Kanitani, S. Tanaka, T. Ohkubo, and K. Hono, Appl. Phys. Lett. **98**, 181904 (2011).

[10] F. Wu, C. Lynsky, J. Ewing, M. Iza, S. Nakamura, S.P. DenBaars, and J.S. Speck, *In Preparation*.

[11] Y.-L. Hu, R.M. Farrell, C.J. Neufeld, M. Iza, S.C. Cruz, N. Pfaff, D. Simeonov, S. Keller, S. Nakamura, S.P. DenBaars, U.K. Mishra, and J.S. Speck, Appl. Phys. Lett. **100**, 161101 (2012).

[12] S.M. Ting, J.C. Ramer, D.I. Florescu, V.N. Merai, B.E. Albert, A. Parekh, D.S. Lee, D. Lu, D.V. Christini, L. Liu, and E.A. Armour, Journal of Applied Physics **94**, 1461 (2003).

[13] Z. Quan, L. Wang, C. Zheng, J. Liu, and F. Jiang, J. Appl. Phys. **116**, 183107 (2014).

[14] C.-K. Li, C.-K. Wu, C.-C. Hsu, L.-S. Lu, H. Li, T.-C. Lu, and Y.-R. Wu, AIP Advances **6**, 055208 (2016).

[15] C.-H. Ho, J.S. Speck, C. Weisbuch, and Y.-R. Wu, ArXiv:2109.08824 [Physics] (2021).

[16] X. Jiang, C. Zheng, C. Mo, X. Wang, J. Zhang, Z. Quan, J. Liu, and F. Jiang, Optical Materials **89**, 505 (2019).

[17] G. Lheureux, C. Lynsky, Y.-R. Wu, J.S. Speck, and C. Weisbuch, J. Appl. Phys. **128**, 235703 (2020).

[18] C. Lynsky, A.I. Alhassan, G. Lheureux, B. Bonef, S.P. DenBaars, S. Nakamura, Y.-R. Wu, C. Weisbuch, and J.S. Speck, Phys. Rev. Materials **4**, 054604 (2020).

[19] S. Zhou, X. Liu, H. Yan, Y. Gao, H. Xu, J. Zhao, Z. Quan, C. Gui, and S. Liu, Scientific Reports **8**, 11053 (2018).

[20] D.-H. Lee, D. Kang, T.-Y. Seong, M. Kneissl, and H. Amano, J. Phys. D: Appl. Phys. **53**, 045106 (2019).

[21] S. Zhou and X. Liu, Physica Status Solidi (a) **214**, 1600782 (2017).

[22] C. Lynsky, R.C. White, Y.C. Chow, W.Y. Ho, S. Nakamura, S.P. DenBaars, and J.S. Speck, Journal of Crystal Growth **560–561**, 126048 (2021).

[23] B. Heying, X.H. Wu, S. Keller, Y. Li, D. Kapolnek, B.P. Keller, S.P. DenBaars, and J.S. Speck, Appl. Phys. Lett. **68**, 643 (1996).

[24] P. Gay, P.B. Hirsch, and A. Kelly, Acta Metallurgica **1**, 315 (1953).

[25] T. Yang, K. Uchida, T. Mishima, J. Kasai, and J. Gotoh, Physica Status Solidi (a) **180**, 45 (2000).

[26] S. Kim, J. Oh, J. Kang, D. Kim, J. Won, J.W. Kim, and H.-K. Cho, Journal of Crystal Growth **262**, 7 (2004).

[27] P. Fini, X. Wu, E.J. Tarsa, Y. Golan, V. Srikant, S. Keller, S.P. Denbaars, and J.S. Speck, Jpn. J. Appl. Phys. **37**, 4460 (1998).

[28] X.H. Wu, P. Fini, E.J. Tarsa, B. Heying, S. Keller, U.K. Mishra, S.P. DenBaars, and J.S. Speck, Journal of Crystal Growth **189–190**, 231 (1998).

[29] M.A. Laurent, S. Keller, and U.K. Mishra, Physica Status Solidi (a) **216**, 1800523 (2019).

[30] R. Yapparov, Y.C. Chow, C. Lynsky, F. Wu, S. Nakamura, J.S. Speck, and S. Marcinkevičius, Journal of Applied Physics **128**, 225703 (2020).

6

Red micro-LEDs

6.1 Introduction

Chapters 3, 4, and 5 were primarily focused on understanding and improving the electrical efficiency of green LEDs on sapphire substrates. In this chapter, the experience gained from MOCVD growth of green LEDs is leveraged to extend the wavelength to red. Specific emphasis is placed on long-wavelength LED growth on (111)-oriented silicon substrates and LED device sizes smaller than $100 \times 100\ \mu m^2$.

Today, the primary driving force for red III-nitride LED development is the display industry. In Chapter 1, the advantages of micro-LED (μLED) displays over incumbent technologies as well as current manufacturing approaches were briefly discussed. In addition to complexities in array assembly [1], an important challenge faced by μLEDs is the well-documented decrease in EQE with device size [2,3]. As the surface area to volume ratio increases, nonradiative recombination at the sidewall increases [4-6]. Surface recombination is exacerbated by mesa isolation using plasma-assisted dry etching, which induces sidewall damage and introduces SRH nonradiative recombination centers. Various chemical treatment and sidewall passivation techniques have proven to be effective at minimizing nonradiative sidewall recombination [7,8] and blue and green μLEDs have been demonstrated with reduced size-dependent EQE characteristics [8,9].

In μLED displays, typically the blue and green emitters are III-nitride LEDs with an InGaN active layer, while the red emitters are III-phosphide LEDs with an AlGaInP active layer. AlGaInP red LEDs are a mature technology with high efficiencies and narrow spectral FWHM [10-12]. However, the surface recombination velocity and diffusion length are computationally and empirically shown to be larger for conventional zinc-blende semiconductors, such as (Al,Ga,In)P, than for InGaN alloys [6,13,14]. With a high surface area to volume ratio, μLEDs based on AlGaInP are therefore severely impacted by surface recombination. The same passivation techniques used for InGaN μLEDs have been applied to AlGaInP μLEDs and while improvement was achieved, the EQE still showed a strong size-dependence [12]. An attractive alternative is to use InGaN-based LEDs for the red emitter.

With QW indium fractions of ~0.3, red III-nitride LEDs suffer from the same efficiency challenges present at green wavelengths. Nevertheless, the promise of surpassing red AlGaInP efficiencies at small device sizes, as well as realizing an RGB display from one materials system, has led to a growing body of research dedicated to red III-nitride LED development. Pasayat *et al*. demonstrated a 6 × 6 μm^2 InGaN red μLED with an on-wafer EQE of 0.2% using GaN on porous GaN pseudo-substrates to grow strain-relaxed InGaN [15]. The authors attribute their results to a reduction in the compositional pulling effect [16], which posits that the incorporation efficiency of indium decreases as strain due to lattice mismatch increases [17,18]. A similar approach was taken by White *et al*. where red μLEDs were grown on relaxed InGaN substrates ("InGaNOS" substrates provided by SOITEC) [19]. An 80 × 80 μm^2 device emitting at 609 nm with 0.83% EQE was achieved. Impressive large-area (1 × 1 mm^2) red LED results were reported by Zhang *et al*. using V-

defect engineering on silicon substrates [20]. At 622 nm, the authors realized an overall peak WPE of 16.8% and V_F of 1.96 V at 0.8 A/cm^2.

In this chapter, a similar V-defect engineering approach to that used by Zhang *et al*. is explored for μLED device sizes. Epitaxial optimization of the red LED active region is first detailed, followed by materials characterization using a variety of techniques, including HAADF-STEM, TEM-EDX, and TRPL spectroscopy. The device fabrication methods and on-wafer μLED device results are then presented. Raytracing simulations were performed to estimate the LEE of different device configurations to obtain an EQE correction factor.

6.2 Epitaxial Growth and Material Optimization

The primary goal of this research was to demonstrate red μLEDs on silicon substrates. Due to the numerous challenges associated with growing GaN on silicon, it was determined that purchasing these templates would allow for faster development of the red-emitting active region. Therefore, GaN on (111)-oriented silicon templates were purchased from Enkris Semiconductor and re-growths by MOCVD were performed to grow full LED structures. Performing re-growths also allowed for many experiments to be performed on co-loaded silicon and sapphire substrates. Enkris GaN-on-Si templates were diced into 13 × 13 mm^2 squares and then cleaned using a standard solvent clean (acetone, isopropanol, H_2O) prior to growth.

While this chapter focuses on V-defect engineering to realize red LEDs on silicon, an alternative approach using GaN-on-porous-GaN pseudo-substrates was also considered. Porous GaN is formed in highly Si-doped layers using an electrochemical etch process and enables the formation of a relaxed InGaN layer on which high indium content QWs can be

grown. The use of GaN-on-porous-GaN pseudo-substrates has been demonstrated to enable long-wavelength LEDs on sapphire [15,16]. The nonstandard epitaxial structure of the Enkris template, shown in Fig. 6.1, was designed to allow for a porous GaN LED process. It is not anticipated that the structure will significantly impact devices which use V-defect engineering, however a more optimized template *n*-GaN structure, similar to those used on sapphire throughout this dissertation, was developed later in this project.

One unique challenge posed when developing GaN LEDs on silicon is the optically absorbing substrate. While advanced processing methods that involve substrate removal can be used to circumvent this issue in the final fabricated devices, the substrate complicates the procedure used at UCSB for rapid LED feedback. Typically for LED and laser structures grown on transparent substrates such as sapphire, "quick test" allows for measuring certain key device parameters. In quick test, the wafer first undergoes a post-growth anneal in N_2/O_2 at 600 °C for 15 minutes to activate the Mg-doped layers. To contact the *p*-GaN, a mask is used to apply indium metal in a uniform array of circles to the epi surface. The *n*-GaN is contacted by first scribing the epi surface and then applying indium metal in this region. During quick test, the indium *n*- and *p*-contacts are probed to collect *L-I-V* and spectral data; these data are then used to make decisions on future growths and determine which devices should be processed. However, the power measured in quick test comes from backside collection into a calibrated photodetector. With an absorbing substrate, such as silicon, this quick test setup prohibits proper power measurements. Early device optimization, which was primarily focused on achieving stable red emission, relied on topside measurements using a spectrometer. From the spectral data, the wavelength and FWHM of different growths could be compared. The spectrometer position and integration time were often fixed on a given

day so that the integrated EL intensity of a series of samples could be compared; although sensitivity of spectrometer position meant this approach was impractical for comparing data collected during different measurement sessions. Later in the project an integrating sphere setup was constructed to enable quantitative quick test power measurements of GaN-on-Si LEDs.

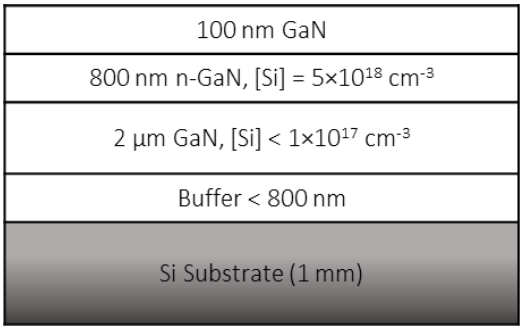

Figure 6.1. Epitaxial structure of template purchased from Enkris Semiconductor. The substrate is 1-mm thick, (111)-oriented silicon.

6.2.1 Increasing Wavelength

Initial growths were performed to first assess the reference green LED recipe transfer from sapphire to silicon substrates and then to increase the wavelength from green to red. Green LED re-growth on GaN-on-Si templates started with 500 nm *n*-GaN ([Si] = 5×10^{18} cm^{-3}) followed by a 30-period *n*-type 2.5 nm/5 nm $In_{0.05}Ga_{0.95}N$/GaN superlattice ([Si] = 5×10^{18} cm^{-3}) to form V-defects at TDs [21,22]. The active region was grown undoped and consisted of five periods of 3-nm $In_{0.22}Ga_{0.78}N$ QWs, 2-nm $Al_{0.10}Ga_{0.90}N$ capping layers, 4-nm low LT GaN barriers, and 6-nm HT GaN barriers. The QW, AlGaN cap, LT GaN, and HT GaN growth temperatures were 815 °C, 815 °C, 890 °C, and 945 °C, respectively. The active region was followed by a 10-nm *p*+-AlGaN electron blocking layer ([Mg] = 1×10^{20}

cm^{-3}), 100 nm of *p*-GaN ([Mg] = 5×10^{19} cm^{-3}), and a 10-nm *p*+-GaN contact layer. No major changes to the growth parameters were required when transitioning from sapphire to silicon.

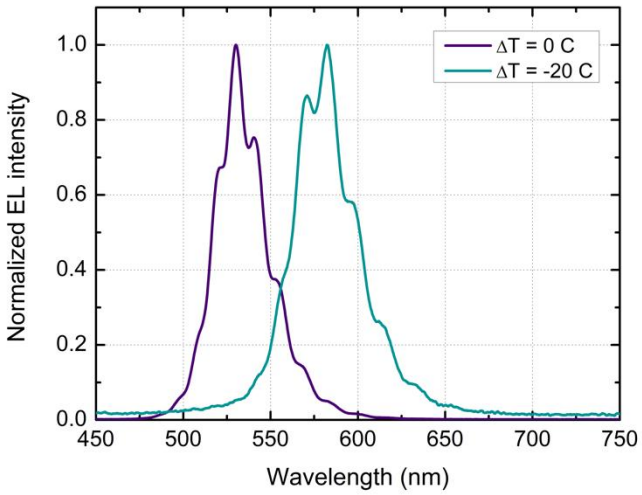

Figure 6.2. Normalized EL spectra collected from quick test at 5 mA for LEDs with active region temperatures of ΔT = 0 °C and ΔT = -20 °C. The peak wavelengths of the LEDs with ΔT = 0 °C and ΔT = -20 °C are 533 and 581 nm, respectively and the FWHM values are 36 and 43 nm, respectively.

To then increase the wavelength, the active region and *p*-side layers were decreased in increments of 20 °C. The quick test EL spectra of the reference green LED with ΔT = 0 °C and the LED with ΔT = -20 °C are shown in Fig. 6.2. Fabry-Pérot interference fringes are observed in quick test measurements of GaN LEDs on silicon; Gaussian fits of the spectral data are used to determine peak EL wavelength and FWHM. For ΔT = 0 °C, the peak wavelength and FWHM are 533 nm and 36 nm, respectively, and for ΔT = -20 °C, the peak wavelength and FWHM are 581 nm and 43 nm, respectively. Weak and inhomogeneous light emission was measured for samples with ΔT = -40 °C and ΔT = -60 °C (EL spectra not shown here) and therefore future experiments focused on conditions using ΔT = -20 °C.

Another growth parameter explored to increase the wavelength further was the aluminum fraction of the AlGaN cap layer. Several reports support that the AlGaN cap layer aluminum fraction plays an important role in improving efficiency and increasing the emission wavelength in long-wavelength LEDs [23-26]. Several mechanisms by which the AlGaN cap improves long-wavelength device performance have been proposed. Koleske *et al*. utilize AlGaN capping layers followed by high temperature GaN QB growth to improve the efficiency of LEDs emitting from 530-590 nm [24]. The authors cite several advantages of this growth approach, including increasing the indium incorporation, improving the morphology of the upper QW interface, reducing nonradiative recombination centers, and red-shifting the wavelength by increasing the polarization-induced electric field in the QW.

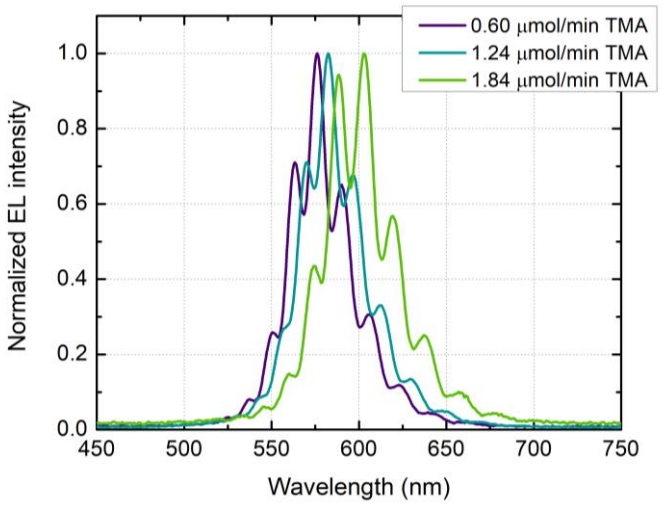

Figure 6.3. Normalized EL spectra collected from quick test at 5 mA for LEDs with varying TMA flow rate in the AlGaN cap layer. The peak wavelengths of the LEDs with 0.60, 1.24, and 1.84 µmol/min TMA are 577, 584, and 599 nm, respectively and the FWHM values are 43, 45, and 48 nm, respectively.

For the reference green LED, the TMA flow rate in the AlGaN cap layer was 0.283 µmol/min (0.8 sccm), which resulted in a film with 10% aluminum. To increase the LED

wavelength without reducing the QW temperature, a series of LEDs were grown with varying TMA flow in the cap layer. Figure 6.3 shows the normalized EL spectra collected from quick test at 5 mA for devices with 0.60, 1.24, and 1.84 μmol/min TMA flow rates; these molar flow rates correspond to volumetric flow rates of 1.7, 3.5, and 5.2 sccm. The peak wavelength increases from 577 to 599 nm with increasing TMA while the FWHM increases from 43 to 48 nm.

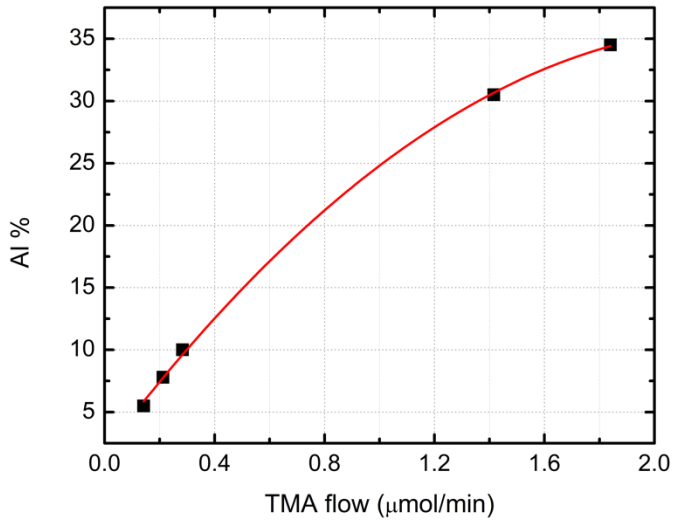

Figure 6.4. Dependence of aluminum percentage in AlGaN cap calibration samples, as measured by XRD, on TMA molar flow rate. The red line is a quadratic fit of the data to highlight the saturation in aluminum incorporation.

Previous XRD ω-2θ measurements of thick AlGaN calibration samples showed a linear increase in aluminum fraction with TMA flow rates ranging from 0.14 to 0.28 μmol/min. Measurements on calibration samples with 1.42 and 1.84 μmol/min TMA show that the aluminum incorporation begins to saturate at these high flow rates. The aluminum percentage measured by XRD for varying TMA flow rates is given in Fig. 6.4; the black squares represent data points, and the red line is a quadratic fit of the data to highlight the

decreasing aluminum incorporation. The longest wavelength emission was achieved using 1.84 μmol/min TMA which corresponds to an aluminum composition of approximately 35%. It is hypothesized that the red-shift with increasing aluminum fraction observed here is the result of the larger polarization-induced electric field in the QW

For all AlGaN cap calibrations shown in Fig. 6.4, the NH_3 and TEG flow rates were fixed at 3.2 slm and 6.24 μmol/min (27 sccm). The 0.28 μmol/min TMA growth conditions used in the reference green LED resulted in a growth rate of 0.9 Å/sec while the highest TMA flow used in the 599-nm wavelength LED had a growth rate of 1.4 Å/sec. In all the LED growths, the AlGaN cap growth time was not changed to compensate for the different growth rates; therefore, the cap thickness was closer to 3 nm for the 599-nm wavelength LED. The cap thickness expected from XRD calibrations was consistent with the thickness observed in HAADF STEM images of a seven-QW red-emitting LED which used 1.84 μmol/min TMA in the AlGaN cap (Fig. 6.5). For the NH_3 and TEG flow rate conditions used here, increasing the TMA flow rate is not expected to result in more aluminum incorporation in the AlGaN layer based on the data in Fig. 6.4. It may be of interest to explore a much higher range of aluminum compositions than shown here for red-emitting LEDs [23]. Future work should investigate different NH_3 and TEG flow rates to achieve increased aluminum incorporation.

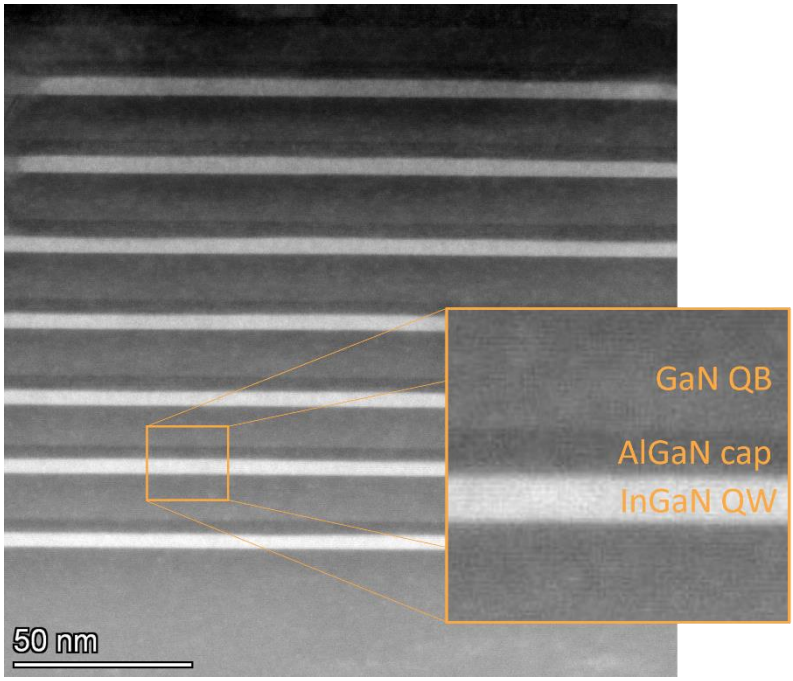

Figure 6.5. HAADF STEM images (courtesy of Dr. Feng Wu) of a seven-QW red-emitting LED grown on silicon. The AlGaN cap layer composition determined from XRD calibration growths was 35% aluminum and the thickness was approximately 3 nm.

After employing a 35% aluminum AlGaN cap to increase the wavelength to 599 nm, a series of LEDs were grown with varying number of QWs to explore the impact on EL wavelength. A red-shift with increasing QW number is expected. As the active region width is increased, the residual electric field of the *p*-*n* junction is decreased. This will reduce the extent to which the polarization-related electric field in the QW is canceled out. The result is an increase in the net electric field across the QW and a red-shift due to the QCSE. Figure 6.6 shows the normalized EL spectra for LEDs where the active region period was increased from five to nine. From five to seven QWs a red-shift in peak EL wavelength from 599 to 631 nm is observed along with an increase in the FWHM from 48 to 59 nm. Surprisingly, a large blue-shift occurred when the QW period was increased further to nine. Possible explanations for the blue-shift include InGaN stress relaxation which reduced the net electric

field in the QW and thus the QCSE or run-to-run growth variation that caused a decrease in the indium incorporation. Because the spectral FWHM remained narrow for this LED, it seems unlikely that the blue-shift was induced by InGaN relaxation.

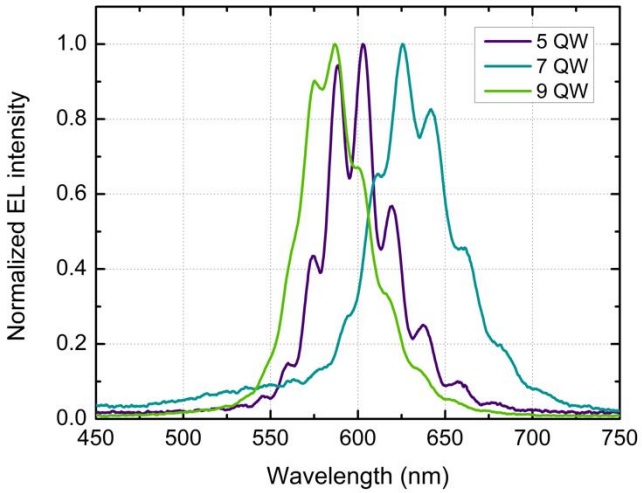

Figure 6.6. Normalized EL spectra collected from quick test at 5 mA for LEDs with varying active region period. The peak wavelengths of the LEDs with five, seven, and nine QWs are 599, 631, and 586 nm, respectively and the FWHM values are 48, 59, and 48 nm, respectively.

By decreasing the active region temperature by 20 °C, increasing the aluminum fraction in the AlGaN cap layer from 10% to 35%, and increasing the number of QWs from five to seven, the LED emission wavelength on silicon was increased from 533 nm to 631 nm. These growth studies represent initial steps to achieve red emission but room for further optimization, such as increasing the AlGaN cap composition further, still exist.

6.2.2 Improving Stability

One challenge that presented itself when growing red-emitting LEDs on silicon was achieving stable, repeatable growths. The low active region growth temperatures needed to

realize red emission mean that careful optimization of parameters is required to operate in a stable growth regime. This section focuses on efforts to optimize the QW thickness, temperature, growth rate, and ratio of TMI/TEG flow. The goal was to improve device performance while realizing robust growth conditions. Unless otherwise noted, all growths shown here are full LEDs on silicon and the spectra are measured using the quick test procedure described above.

The large lattice mismatch between InN and GaN along with the piezoelectric nature of III-nitride compounds lead to QW thickness having a significant impact on device performance. The net electric field across the QW spatially separates electron and hole wavefunctions; this effect becomes more significant for higher indium composition QWs. Thicker QWs will result in a greater degree of spatial separation. The QW morphology also begins to degrade as the thickness or indium composition of the InGaN layer increases. It is therefore desirable to decrease the QW thickness for high indium content QWs to improve wavefunction overlap and improve epitaxial film quality. LEDs with QW thicknesses ranging from 1.5 nm to 3.0 nm were investigated and the normalized EL spectra collected from quick test at 5 mA are given in Fig. 6.7.

A substantial blue-shift in wavelength from 639 nm to 491 nm was observed when decreasing the QW thickness from 3.0 to 1.5 nm. This can be understood in analogy with the simple case of a finite potential well of width L where the eigenstate E_n is inversely proportional L^2. The LED with the 3.0 nm QW exhibits a large peak in EL at ~415 nm. Presently, the origin of the blue emission is unknown. Characterization aimed at identifying the origin of the peak is presented in Appendix B.

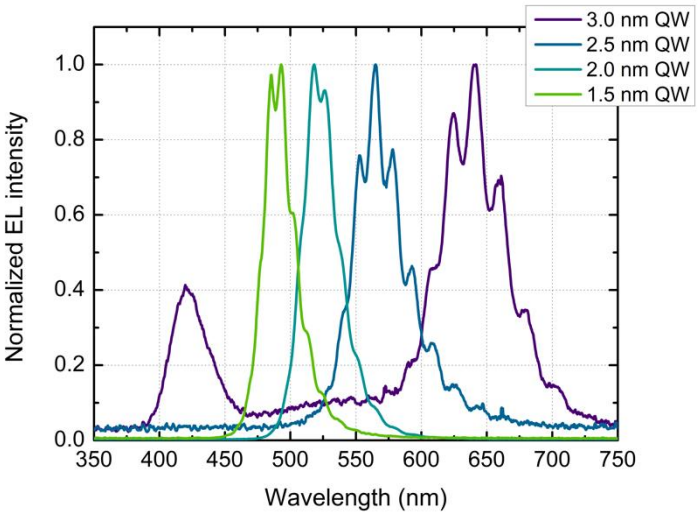

Figure 6.7. Normalized EL spectra collected from quick test at 5 mA for LEDs with varying QW thickness. The peak wavelengths of the LEDs with QW widths of 3.0, 2.5, 2.0, and 1.5 nm are 639, 568, 523, and 491 nm, respectively.

To counter the undesirable blue-shift with decreasing well width, the temperature needs to be decreased to promote indium incorporation. Therefore, the QW width and temperature must be optimized to balance the advantages of thinner QWs with the disadvantages of lower QW growth temperature. Due to the significant temperature decrease required to red-shift back to >600 nm emission, only the 3.0 and 2.5 nm QW width LEDs were chosen for this optimization. It was found that a temperature offset of approximately -12.5 °C was sufficient to increase the wavelength of a 2.5 nm QW LED to red emission. Figure 6.8 compares the normalized EL wavelength, as measured by quick test at 5 mA, for a 3.0 nm QW LED with $\Delta T = 0$ °C and a 2.5 nm QW LED with $\Delta T = -12.5$ °C. The peak wavelength of the 3.0 and 2.5 nm QW LEDs were 622 and 612 nm, respectively. While exact wavelength matching was not achieved, it is expected that the wavelengths are similar enough for the devices to be compared. A slightly larger ΔT of -15 °C would have likely achieved better wavelength agreement.

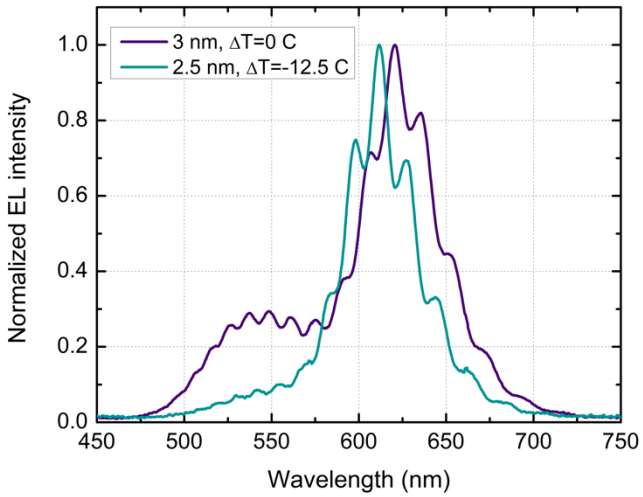

Figure 6.8. Normalized EL spectra collected from quick test at 5 mA. The purple curve shows LED-A with QW thickness = 3.0 nm, ΔT = 0 °C, GR = 1 Å/sec, and peak wavelength = 622 nm. The blue curve shows LED-B with QW thickness = 2.5 nm, ΔT = -12.5 °C, GR = 0.66 Å/sec, and peak wavelength = 612 nm.

Along with the reduced QW thickness and temperature, the LED shown in Fig. 6.8 was also grown with a reduced growth rate (GR). The reference GR used for the 3.0 nm QW was 1 Å/sec while the 2.5 nm QW was grown using 0.66 Å/sec. The GR was reduced by decreasing the TEG flow rate from 6.24 μmol/min (27 sccm) to 4.16 μmol/min (18 sccm) while maintaining a constant TMI flow rate of 5.47 μmol/min (70 sccm). Unfortunately, due to reactor challenges, experiments isolating the effects of GR from QW width were compromised; therefore, conclusions drawn about the impact of changing these parameters are largely speculative. It is expected that a slower GR will improve the InGaN surface morphology as adatoms have more time to diffuse to a step edge. Indeed, green LEDs with improved light output power were realized by Hikosaka *et al*. when the QW growth rate was reduced [27]. Processed device data still allows for the relative efficiency to be compared between the structures even though an exact explanation for the differences is lacking. The

processed device results for these two samples are presented and discussed in Section 6.3.2. The LEDs with 3.0 and 2.5 nm QWs are referred to as LED-A and LED-B, respectively.

In the EL spectra of the 3.0 nm QW LED in Fig. 6.8 a prominent shoulder at approximately 550 nm can be seen. This peak is hypothesized to be the result of phase separation in the InGaN layer and is supported by the observation of regions of green emission (see Fig. 6.28 in Section 6.3.2). The thinner QWs grown at lower temperature and GR appear to suppress the green emission shoulder. Additional characterization should be performed in future studies to determine whether the green emission is due to phase separation.

Another growth parameter that was studied to improve wavelength stability and device performance was the TMI/TEG molar flow ratio. The reference green LED conditions use TEG and TMI flows of 6.24 μmol/min (27 sccm) and 5.47 μmol/min (70 sccm), respectively, and thus a TMI/TEG ratio = 0.88. In the previously described experiment where the TEG flow was reduced but the TMI was kept fixed, the TMI/TEG ratio increased to 1.31. Using these conditions as a reference point and keeping the GR fixed at 0.66 Å/sec (corresponding to TEG flow rate of 4.16 μmol/min, or 18 sccm), the TMI flow was reduced from 5.47 μmol/min (70 sccm) to 3.66 μmol/min (46.8 sccm) and 2.82 μmol/min (36 sccm). The flow rate conditions correspond to TMI/TEG ratios of 1.31, 0.88, and 0.68. The QW width for these samples was 2.5 nm. In Fig. 6.9, the quick test EL results show that the wavelength blue-shifts with decreasing TMI/TEG ratio. The wavelength change indicates that in this growth regime, the indium incorporation efficiency exhibits a strong dependence on TMI supply [28].

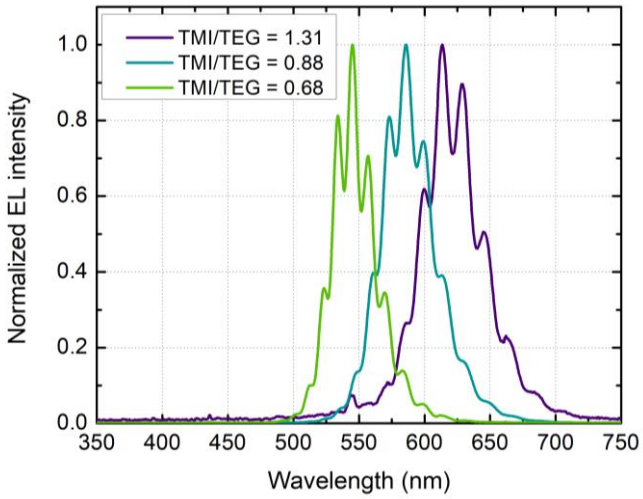

Figure 6.9. Normalized EL spectra collected from quick test at 5 mA for LEDs with varying TMI/TEG molar flow ratio. For TMI/TEG = 1.31, 0.88, and 0.68, the peak wavelengths = 620, 587, and 545 nm, respectively.

Additional experiments were performed where the TMI flow was further increased from 5.47 μmol/min (70 sccm) to 7.82 μmol/min (100 sccm) and 10.17 μmol/min (130 sccm); these conditions represent TMI/TEG molar flow ratios of 1.31, 1.89, and 2.44. Increasing the TMI flow led to significant degradation of QW luminescence (spectra not shown here), which may be a result of indium droplet formation [29]. To compensate for the increase in indium incorporation, an LED with the 1.89 TMI/TEG ratio conditions was grown with ΔT = 5 °C in the QW. Improved luminescence was observed, and the correct wavelength achieved; however, this sample exhibited a large green-emitting shoulder peak. For this reason, the TMI/TEG molar flow ratios of 1.31 and 0.88 were chosen for further study.

To increase the wavelength for the 0.88 TMI/TEG ratio conditions, the QW growth temperature was decreased. One reference LED was grown with TMI/TEG = 1.31 and ΔT = 0 °C and one LED was grown with TMI/TEG = 0.88 and ΔT = -2 °C. The QW width for

these samples was 2.5 nm. The relative quick test EL spectra are shown in Fig. 6.10; from these data the sample with TMI/TEG = 0.88 shows slightly improved luminescence. The structures with TMI/TEG = 0.88 and TMI/TEG = 1.31 are referred to as LED-C and LED-D, respectively. The final processed device results for LED-C and LED-D are further discussed in Section 6.3.2.

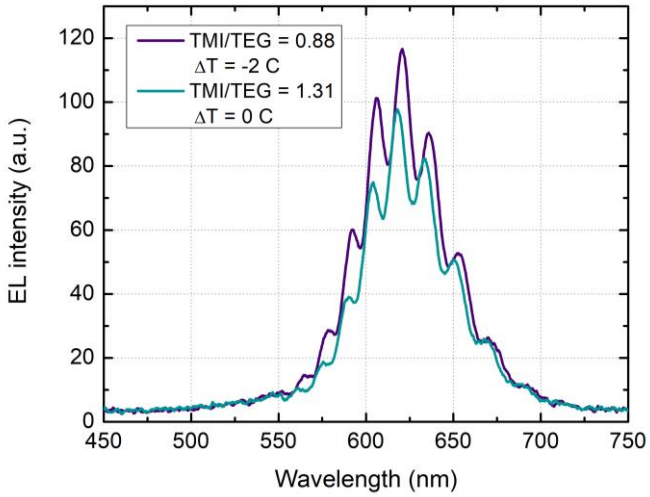

Figure 6.10. EL spectra collected from quick test at 5 mA for LEDs with varying TMI/TEG molar flow ratio and QW growth temperature. For both LED-C with TMI/TEG = 0.88 and ΔT = -2 °C and LED-D with TMI/TEG = 1.31 and ΔT = 0 °C, the peak wavelength is approximately 620 nm.

6.2.3 Materials Characterization

AFM was used to characterize the top LED surface when increasing the wavelength and moving to growth on silicon rather than sapphire substrates. Figure 6.11 shows 5 × 5 μm^2 AFM scans of green, yellow, and amber LEDs grown on co-loaded PSS and silicon substrates. On PSS, large V-defects with relatively uniform size distribution are observed for the green [Fig. 6.11(a)] and yellow [Fig. 6.11(b)] LEDs while several smaller defects and roughening of the *p*-GaN is seen for the amber [Fig. 6.11(c)] LED. The average V-defect

density on PSS is 1.4×10^{8} cm^{-2}. Relative to PSS growth, there is an increase in small defects in the green [Fig. 6.11(d)] and yellow [Fig. 6.11(e)] LEDs grown on Si. Figure 6.11(f) shows that these small defects, which are likely V-defects nucleated in the active region, become numerous for the amber LED on silicon. From AFM, the average V-defect density on silicon is 3.5×10^{8} cm^{-2}. While an increase in the V-defect density was achieved when moving from PSS to silicon, the density on silicon is still below what is expected based on estimations that the TDD is in the high 10^{8} or low 10^{9} cm^{-2} range. An opportunity may therefore exist to nucleate additional TDs in the SL to form large V-defects. From secondary electron SEM images at the surface of a seven-QW red LED on silicon, the average density and diameter of large V-defects are calculated to be 3.5×10^{8} cm^{-2} and 150 nm, respectively (Fig. 6.12).

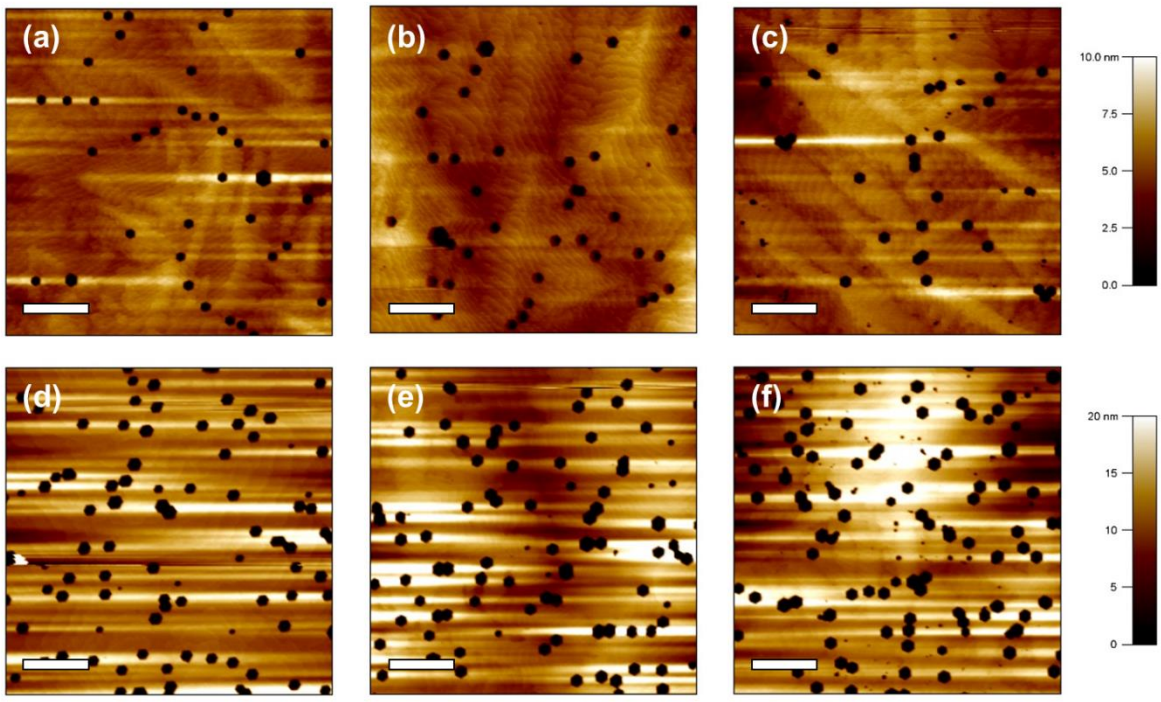

Figure 6.11. 5×5 μm^2 AFM scans of (a) green, (b) yellow, and (c) amber LEDs on PSS and (d) green, (e) yellow, and (f) amber LEDs on silicon. The average V-defect density on PSS is 1.4×10^{8} cm^{-2} and on silicon is 3.5×10^{8} cm^{-2}. Scale bars are 1 μm.

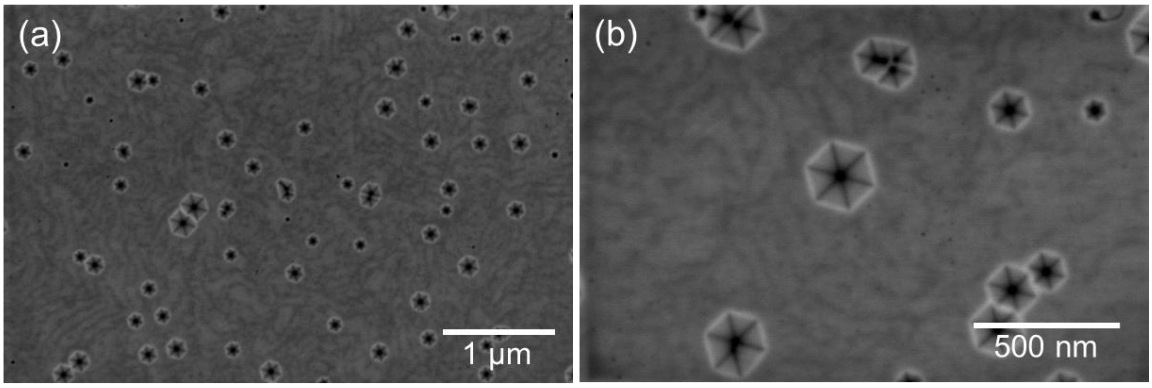

Figure 6.12. Secondary electron SEM images (2 kV) at magnifications of (a) 25,000X and (b) 65,000X at the top surface of a seven-QW red LED on silicon. The average density and diameter of large V-defects are 3.5×10^{8} cm^{-2} and 150 nm, respectively.

From AFM scans (Fig. 6.11) and SEM images (Fig. 6.12) of the *p*-GaN surface it is observed that V-defects generated in the SL and active region are not filled in during LED *p*-side growth. For the current conditions, growth is primarily conformal. The implications of unfilled V-defects are not yet fully understood; however, it is plausible that they could impact reliability or other electrical device properties. The growth temperature of the *p*-GaN layer was increased to achieve more lateral growth and planarize the LED surface. Figure 6.13(a) shows an AFM scan of an LED using the reference, 100 nm of low temperature *p*-GaN grown at 917 °C. When the temperature of the top 50 nm of *p*-GaN was increased to 945 °C, while keeping the bottom 50 nm at 917 °C, an improvement in V-defect filling was observed in AFM [Fig. 6.13(b)]. Unfortunately, quick test measurements indicated the EL intensity was reduced for the device with higher *p*-GaN temperature. Future optimization is required to identify growth conditions for the *p*-side of the LED that will enable planarization without negatively impacting luminescence intensity. Other possible

conditions which could be explored include using TMI as a surfactant or decreasing the relative thickness of the high temperature *p*-GaN layer to reduce the thermal load.

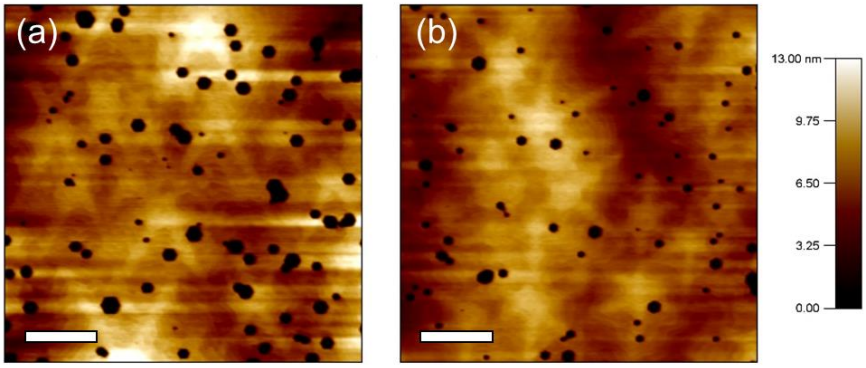

Figure 6.13. 5 × 5 μm^2 AFM scans of red LEDs on silicon grown with (a) 100 nm low temperature *p*-GaN at 917 °C and (b) 50 nm low temperature followed by 50 nm high temperature *p*-GaN at 945 °C. V-defect filling is improved for higher *p*-GaN temperature growth. Scale bars are 1 μm.

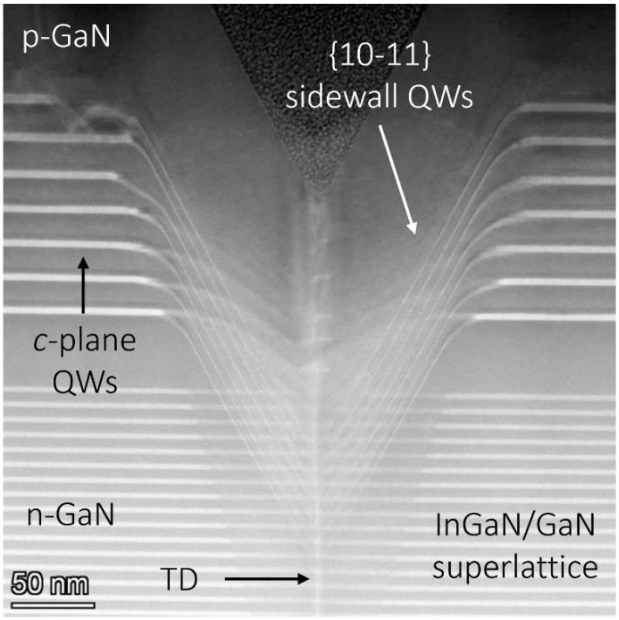

Figure 6.14. Cross section HAADF STEM of a V-defect nucleated in the SL of a red LED on silicon. The nucleation of the V-defect the threading dislocation can be seen. The {10$\bar{1}$1} sidewall QWs and QBs are seen to have reduced thickness compared to the planar QWs and QBs.

HAADF-STEM and TEM-EDX were used to characterize the active region and V-defects in red LEDs on silicon. These data are courtesy of Dr. Feng Wu. Figure 6.14 shows a cross section HAADF STEM image of a V-defect which is nucleated at a TD. The V-defect can be seen to initiate in the InGaN/GaN SL layers below the active region. Well defined $\{10\bar{1}1\}$ sidewall QWs and QBs are observed, although the thickness of both layers is reduced relative to the planar regions. The *p*-GaN layer is seen to be conformal around the V-defect. Cross section HAADF-STEM and TEM-EDX of the V-defect sidewall are shown in Fig. 6.15 where EDX allows for compositional analysis of the LED layers. The sidewall QWs have lower indium composition compared to the planar QWs while the aluminum composition is more similar between the two regions. Quantification of the indium and aluminum composition in the planar and sidewall regions using EDX as well as APT will be the subject of future studies.

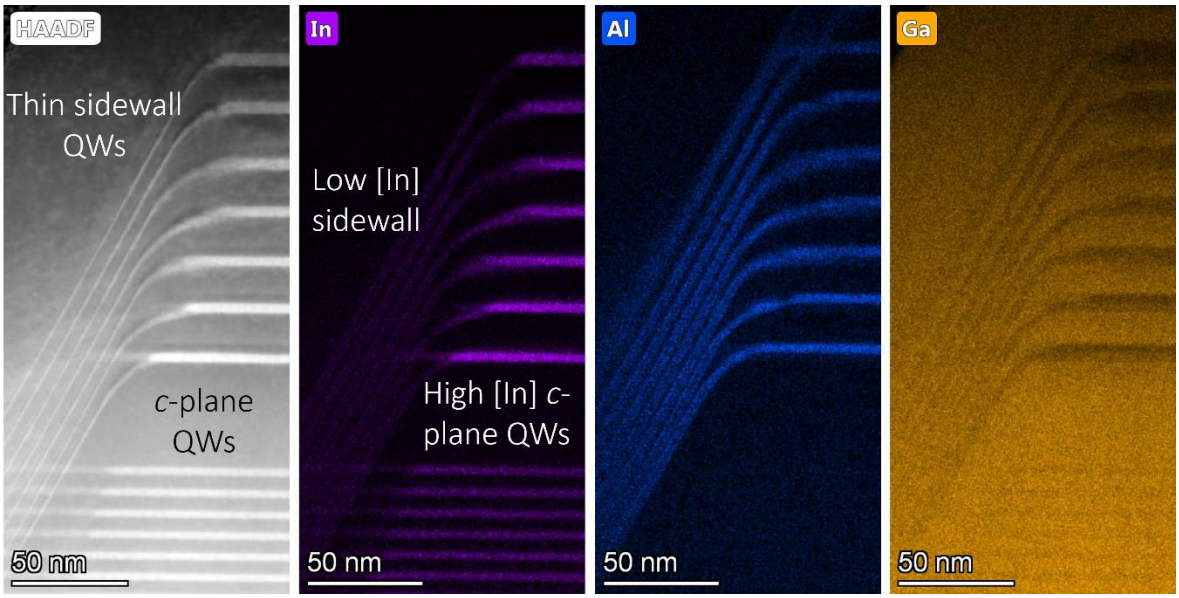

Figure 6.15. Images of the V-defect sidewall in cross section HAADF STEM and TEM-EDX. EDX compositional analysis of the indium, aluminum, and gallium show reduced indium incorporation in the sidewall QWs relative to the planar QWs.

Cross-section HAADF-STEM also allows for important characterization of the QW thickness. Due to the high indium compositions required for red LEDs, it becomes challenging to calibrate the QW growth rate using the standard approach, which involves growing thick InGaN layers and determining the composition and thickness from HRXRD ω-2θ measurements. TEM thus provides an attractive, and accurate, method for directly measuring the QW thickness. Figure 6.16 shows a cross-section HAADF STEM image of the planar QW region in a red LED. For this specific sample, the target QW thickness was 3 nm, which is in good agreement with the thickness measured by TEM. The diffuse upper interface of the QW presents some difficulty in determining the exact thickness. Nevertheless, good control over the QW thickness and uniformity is demonstrated in these red LED growths.

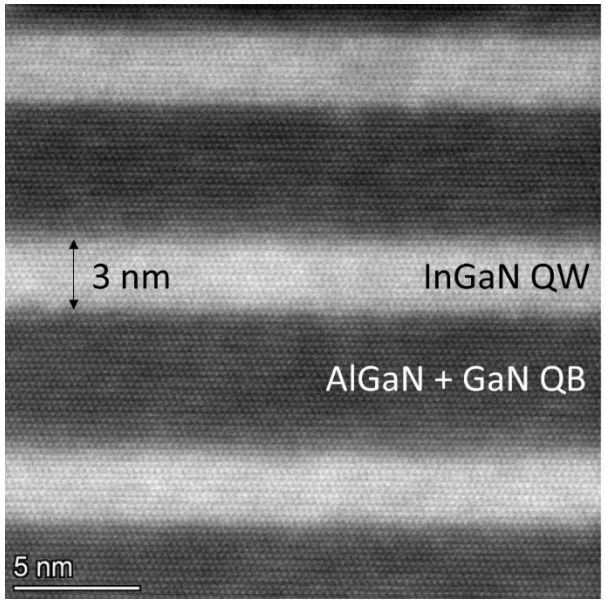

Figure 6.16. Cross-section HAADF-STEM showing the planar QWs and QBs where the target QW thickness was 3 nm.

6.2.4 Time-Resolved Photoluminescence Spectroscopy

TRPL and quasi-cw PL spectroscopy measurements were performed on long-wavelength LEDs on silicon and PSS substrates. The TRPL and quasi-cw PL measurements and analysis shown here were performed at KTH Royal Institute by Professor Saulius Marcinkevičius and Rinat Yapparov. The samples were grown at UCSB.

In the TRPL measurements, PL was excited with 200 fs pulses from a self mode-locking Ti:sapphire laser at central wavelengths of 390 nm and 450 nm and a 2 MHz repetition frequency. To record time-resolved PL transients, the PL decay time should be much shorter than the pulse repetition period. This was achieved using a 500 ns interval between pulses. The average pulse power was 80 μW and the spot diameter was ~30-50 μm. The dependence on excitation power was studied using neutral density filters with attenuation up to 100 times (down to 0.8 μW). For temperature dependent measurements, experiments were performed in the 5-300 K range. The time-resolved measurements allow for the determination of the relative IQE and, in certain cases, the absolute IQE.

For the quasi-cw PL measurements, PL was excited with 150 fs pulses at a wavelength of 390 nm and repetition frequency of 76 MHz. The average power was 3 mW and the spot diameter was ~30 μm. The interval between the laser pulses was much smaller than the PL decay time, hence the quasi-cw conditions. The temperature range studied was 5-290 K. The relative IQE was estimated by dividing the time- and spectrally-integrated PL at a given temperature to the value at 5 K. The relative IQE is the upper limit to the absolute IQE.

A total of six samples were measured. The samples had EL emission at either red or yellow wavelengths and were on either silicon or PSS substrates. Relative IQE (as measured

by temperature dependent quasi-cw PL) was determined for all six samples, while absolute IQE (as measured by temperature dependent TRPL) was calculated for two samples. Room temperature PL transients were also measured for all samples. Table 6.1 summarizes the sample details as well as which experiments were carried out. Samples Y1 PSS and Y1 Si were co-loaded during the same growth, as were R1 PSS and R1 Si.

Table 6.1. Long-wavelength LED samples measured using quasi-cw PL and TRPL techniques. The peak wavelength determined from quick test at 20 mA and the substrate type for each sample are provided. The × symbol denotes the type of measurement performed on each sample.

Sample	λ at 20 mA (nm)	Substrate	Quasi-cw PL	Temperature dependent TRPL	Room temperature transient
Y1 PSS	572	PSS	×	×	×
Y1 Si	572	Si	×		×
R1 PSS	602	PSS	×		×
R1 Si	607	Si	×		×
R2 Si	608	Si	×	×	×
R3 Si	602	Si	×		×

The transients measured with excitation at 390 nm, 2 MHz, and 80 μW for sample Y1 PSS are shown in Fig. 6.17(a). The transients contain fast and slow decay components with decay times on the order of 3-10 ns and hundreds of ns, respectively. The origin of the fast decay component is currently unclear. Possibly, it reflects the fast recombination of strongly localized excitons. It is present at all temperatures and because it was not observed to be dependent on excitation power (data not shown here), fast carrier trapping to nonradiative recombination centers can be ruled out as a mechanism. However, since the fast PL decay component, especially at high excitation powers, contains only a small

fraction of the total emission energy, it does not play a major role in determination of the IQE. Hence, the radiative and nonradiative recombination times, and therefore the IQE, were determined using the slow PL decay component. The PL decay time (slow component) τ_{PL}, radiative recombination time τ_R, and nonradiative recombination time τ_{NR} for sample Y1 PSS are shown in Fig. 6.17(b). The values of τ_{PL} at different temperatures are determined by fitting the transients with a double exponential function. The radiative recombination time is inversely proportional to the amplitude of a PL transient [33] and therefore, the temperature dependence of τ_R can also be directly determined relative to the low temperature value. The nonradiative recombination time can then be calculated using the following equation,

$$\frac{1}{\tau_{PL}} = \frac{1}{\tau_R} + \frac{1}{\tau_{NR}}. \tag{6.1}$$

As discussed in detail in Refs. [30-32], nonradiative recombination at low temperature can be considered negligible if the temperature dependence of τ_{PL} and τ_R converge in the low temperature range. If this condition is met, which is the case for sample Y1 PSS, the high temperature IQE values can be taken as absolute. The temperature dependence of the absolute IQE is plotted in Fig. 6.17(c), where IQE is calculated according to

$$IQE(T) = \frac{\tau_{NR}(T)}{\tau_R(T) + \tau_{NR}(T)}. \tag{6.2}$$

The room temperature IQE is approximately 40% for sample Y1 PSS. The radiative lifetime exhibits a weak temperature dependence, which is attributed to recombination of localized excitons being the prevailing recombination mechanism.

The same measurements and calculations were performed on sample R2 Si; the results are shown in Figs. 6.17(d)-6.17(f). Similar to sample Y1 PSS, the transients contain fast and slow decay components, and the slow component was used to determine τ_{PL}. For R2 Si, the low temperature τ_{PL} and τ_R converge, indicating that IQE values can be taken as absolute. The radiative recombination time shows weak temperature dependence below 250 K. The large increase above 250 K is attributed to increased free carrier recombination, which has a linear dependence on temperature. The room temperature IQE of R2 Si is just under 10%, which is significantly lower than what was measured for Y1 PSS.

The room temperature PL transients (excitation at 450 nm, 2 MHz, 80 μW) for the PSS and silicon samples are reported in Figs. 6.18(a) and 6.18(b), respectively. The PL intensity of samples on silicon are approximately one order of magnitude lower than samples on PSS. This is partly due to the reduced IQE by a factor of ~5 and part due to the reduced light extraction on Si. The origin of the reduced IQE on silicon will be the subject of future studies. In Fig. 6.18(a), the intensity of R1 PSS and Y1 PSS are similar and the room temperature IQE of R1 PSS is estimated to be ~20-30%. From the transients in Fig. 6.18(b), the decay times for R1 Si, R2 Si, R3 Si, and Y1 Si are 78, 98, 73, and 85 ns, respectively. The similar decay times indicate that the samples on silicon should have similar IQEs to the value calculated from temperature dependent TRPL for sample R2 Si.

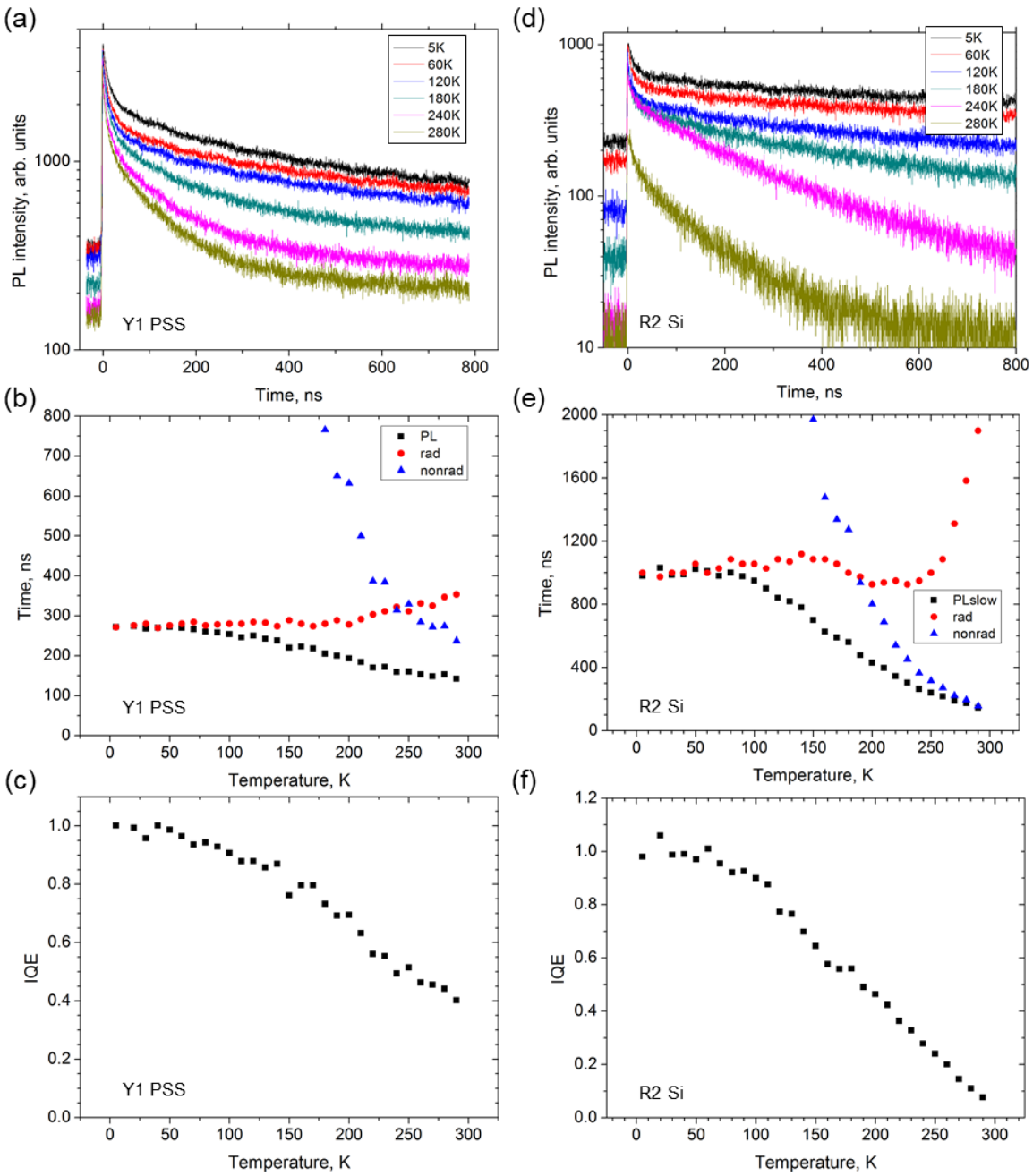

Figure 6.17. Y1 PSS sample (a) temperature dependent transients (5-280 K) with excitation at 390 nm, 2MHz, and 80 μW, (b) PL decay (slow component), radiative recombination, and nonradiative recombination times, and (c) absolute IQE. R2 Si sample (d) temperature dependent transients (5-280 K) with excitation at 390 nm, 2 MHz, and 80 μW, (e) PL decay (slow component), radiative recombination, and nonradiative recombination times, and (f) absolute IQE.

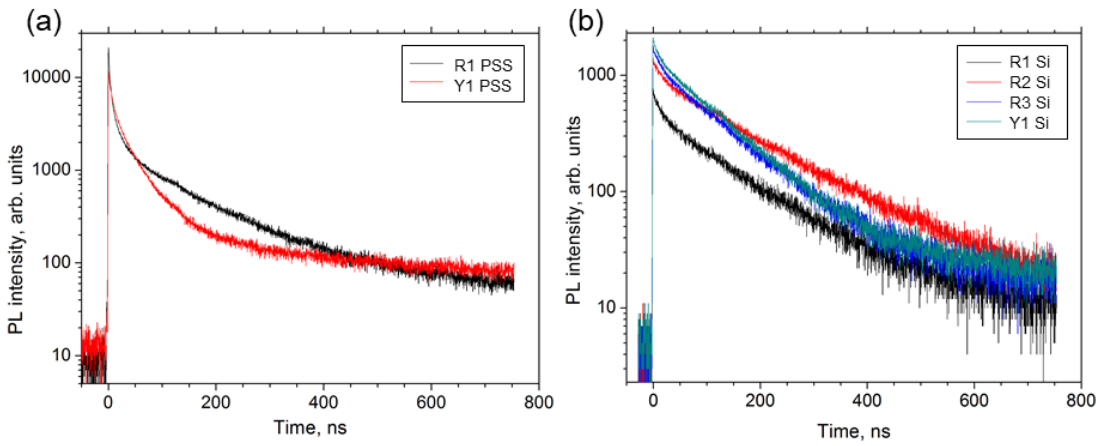

Figure 6.18. Room temperature (300 K) transients with excitation at 450 nm, 2 MHz, and 80 μW for (a) sample on PSS and (b) samples on Si.

In Fig. 6.19, the relative IQE (calculated from quasi-cw PL measurements) for samples on PSS and silicon are shown. These data assume the IQE is 100% at 5 K, which may or may not be accurate, and therefore the curves provide an upper limit of the absolute IQE. Nevertheless, the quasi-cw PL experiments allow for all samples to be compared. For both substrates, the Y1 samples have higher relative IQE compared to the R1-R3 samples. This result is consistent with expectations that longer wavelength LEDs will have lower IQE [33]. Similar to what was observed in Fig. 6.17, the samples on PSS have higher IQE than those on silicon by a factor of ~5.

Samples R2 Si and R3 Si have nearly identical epitaxial structures to the sample (LED-E) with the highest reported EQE for a UCSB-grown red μLED on Si. These results are discussed in Sections 6.3.2 and 6.3.3. The absolute IQE determined for R2 Si is consistent with the approximate value expected based on the measured EQE and simulated LEE.

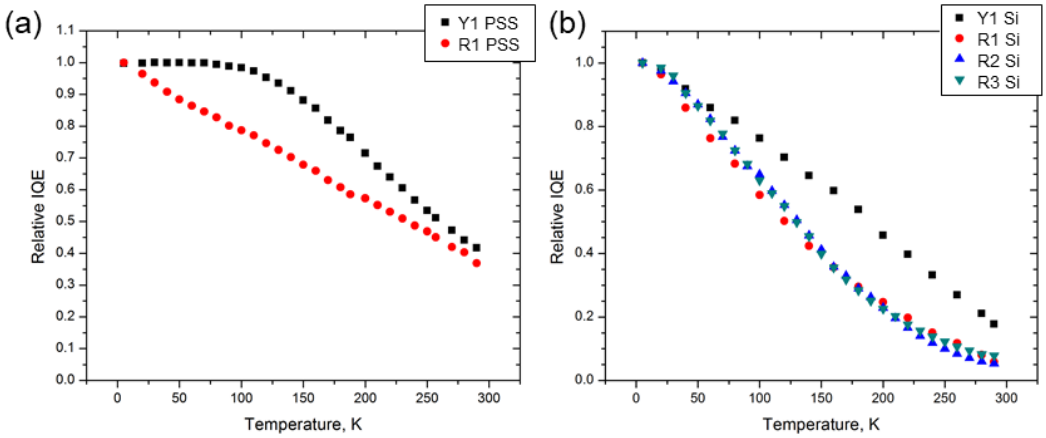

Figure 6.19. Relative IQE measured by quasi-cw PL for (a) samples on PSS and (b) samples on silicon. The PL excitation is at 390 nm, 76 MHz, and 3 mW.

6.3 Red micro-LED Devices

6.3.1 Methods

The μLED device design and fabrication process used here were developed at UCSB and are discussed extensively in other reports [2,7]. μLEDs were fabricated with the following dimensions: 5 × 5 μm^2, 10 × 10 μm^2, 20 × 20 μm^2, 40 × 40 μm^2, 60 × 60 μm^2, 80 × 80 μm^2, and 100 × 100 μm^2.

The epitaxially grown material was first cleaned with aqua regia (3:1 HCl:NHO_3) and then solvent to remove indium metal from quick test and any surface contamination. 110 nm of indium-tin oxide (ITO), which is a transparent conducting oxide that serves as the contact to *p*-GaN, was then deposited using electron-beam deposition. Next, 500 nm of SiO_2 was blanket sputtered to later serve as the hard mask. The LED mesas were lithographically defined using positive resist. The SiO_2 was etched using a CF_4/CHF_3-based inductively coupled plasma reactive ion etch (ICP RIE) and the ITO was etched using a CH_3/H_2/Ar-based RIE. The photoresist was then removed, and the mesa defined by etching down to the *n*-GaN using a $SiCl_4$-based RIE. The SiO_2 hard mask was wet etched using buffered HF. An

omnidirectional reflector (ODR) was deposited using ion beam deposition to improve light extraction and serve as a metal isolation dielectric layer. The ODR consisted of 3x alternating SiO_2/Ta_2O_5 followed by an Al_2O_3 layer for improved metal adhesion. In the wavelength range of 430 to 450 nm, this ODR stack was calculated to have 95.5% reflectance; it is noted that the ODR stack should be optimized in the future for the 600 to 630 nm wavelength range. Following ODR lift-off, a 25-nm SiO_2 film was deposited using atomic layer deposition (ALD) at 300 °C for sidewall passivation [7]. The ALD SiO_2 was removed from select areas using a buffered HF wet etch. Electron-beam deposition was used to deposit the 500/100/500 nm Al/Ni/Au metal stack which serves as a common *n*- and *p*-contact. A schematic of the full process flow is illustrated in Fig. 6.20(a). Figures 6.20(b) and 6.21(c) show the processed device cross-section and top view schematics, respectively.

An integrating sphere was used to measure the EQE characteristics of final fabricated devices. From Eq. 2.9, the EQE = LEE × IQE. Because the processed devices considered here are measured on wafer and have absorbing silicon substrates, the LEE is expected to be considerably lower than state-of-the-art device architectures, which conservatively have LEE values of approximately 85%. The combination of low LEE on silicon, small μLED device sizes, and low efficiency of long-wavelength III-nitride devices contribute to very low measured signal in the integrating sphere.

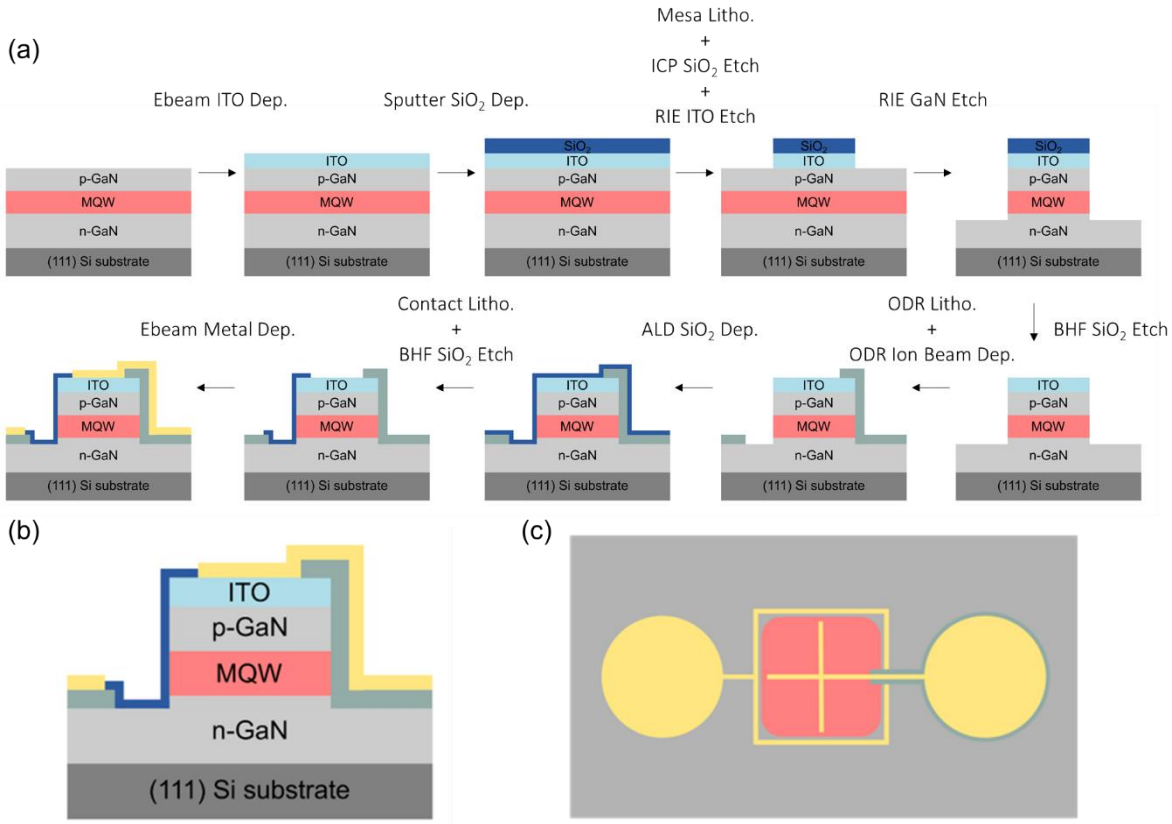

Figure 6.20. Schematics showing the μLED device (a) process flow, (b) cross-section, and (c) top-view. The schematics are not drawn to scale.

Monte-Carlo raytracing simulations were performed by Dr. Pavel Shapturenka at UCSB using Synopsys LightTools to gauge the absolute LEE of a processed on-wafer device on silicon, as well as a maximum-LEE configuration to benchmark an efficiency correction factor for packaged, substrate-removed devices. For on-wafer simulations, device mesas of various edge lengths (5, 20, and 100 μm), 700 nm etch depth, and 20-degree sidewalls were initialized with distinct, constant refractive index and absorption values for Si, *p*-GaN, *n*-GaN, ITO, SiO_2, and metal contacts. 1,000,000 distinct rays were generated from a 100-nm rectangular volume source meant to represent the active region, with its angular emission profile apodized by $1 + \cos^2(\theta)$ to favor dipole emission in the -/+ Z direction (from the dominant twofold degenerate band transitions). Source emission was

Gaussian and centered at 620 nm with a 35 nm FWHM. For high-LEE flip-chip simulations, mesas were inverted and placed on a 3-μm silver layer (reflectivity = 90%). The top side of the inverted mesa was roughened with a Lambertian-scattering surface with 50/50 first-pass transmission probability.

6.3.2 Device Results

Using the process flow described in the previous section, LED-A and LED-B were fabricated into μLEDs. These samples were described in Section 6.2.2 and their epitaxial structures are shown in Fig. 6.21. LED-A contains a 3.0 nm QW grown at 1 Å/sec while LED-B contains a 2.5 nm QW grown at 0.66 Å/sec with ΔT = -12.5 °C to produce the desired wavelength.

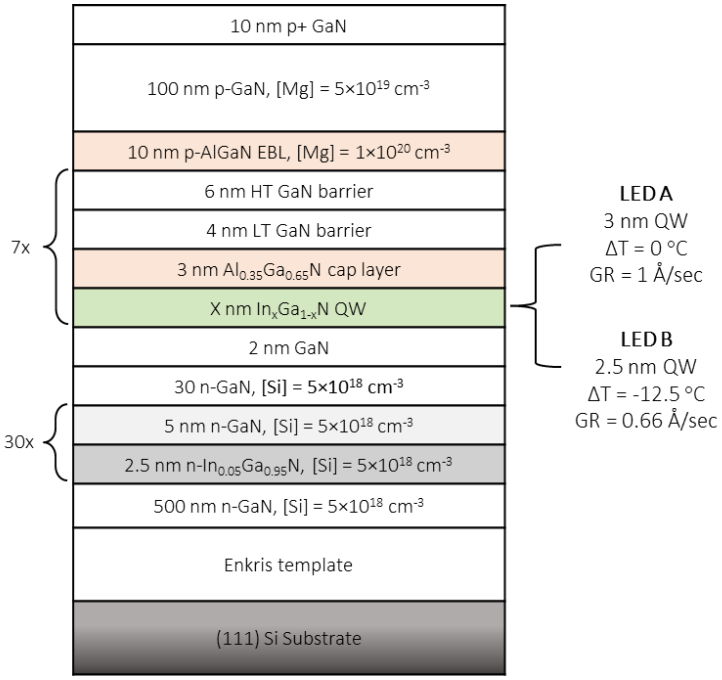

Figure 6.21. Schematic showing epitaxial structure of LED-A and LED-B.

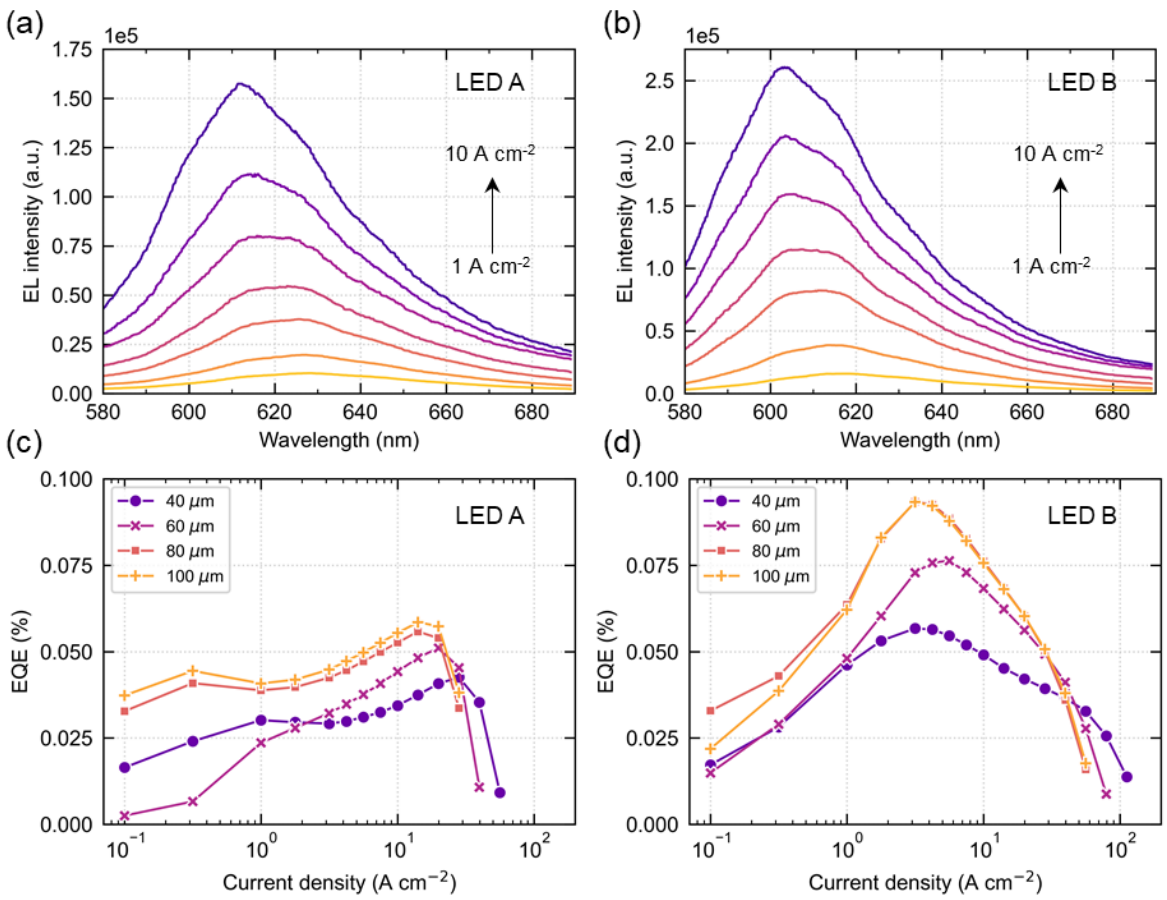

Figure 6.22. EL spectra from 1 A cm^{-2} (yellow curve) to 10 A cm^{-2} (purple curve) for (a) LED-A and (b) LED-B 80 × 80 μm^2 devices. EQE curves for (c) LED-A and (d) LED-B devices ranging from 40 × 40 μm^2 to 100 × 100 μm^2.

The EL spectra from 1 A cm^{-2} (yellow curve) to 10 A cm^{-2} (purple curve) for 80 × 80 μm^2 devices are shown in Figs. 6.22(a) and 6.22(b) for LED-A and LED-B, respectively. Fig. 6.22(c) shows the EQE curves for LED-A for 40 × 40 μm^2, 60 × 60 μm^2, 80 × 80 μm^2, and 100 × 100 μm^2 devices. The peak EQE for all device sizes from LED-A are quite low (< 0.06%) and the peak occurs at high current density (>10 A cm^{-2}). In comparison, the EQE curves in Fig. 6.22(d) for LED-B show improved peak EQE values and the peak occurs at approximately 3 A cm^{-2}, which is consistent with expectations for long-wavelength μLED devices with significant SRH nonradiative recombination. Due to experimental challenges

with the MOCVD reactor, it cannot be conclusively stated whether slower growth rate or thinner QWs contributed to the improved performance of LED-B over LED-A. It is hypothesized that both parameters likely played a beneficial role. The slower GR is expected to yield smoother QW morphology and reduce the likelihood of undesirable V-defect nucleation in the active region while thinner QWs will lead to improved wavefunction overlap.

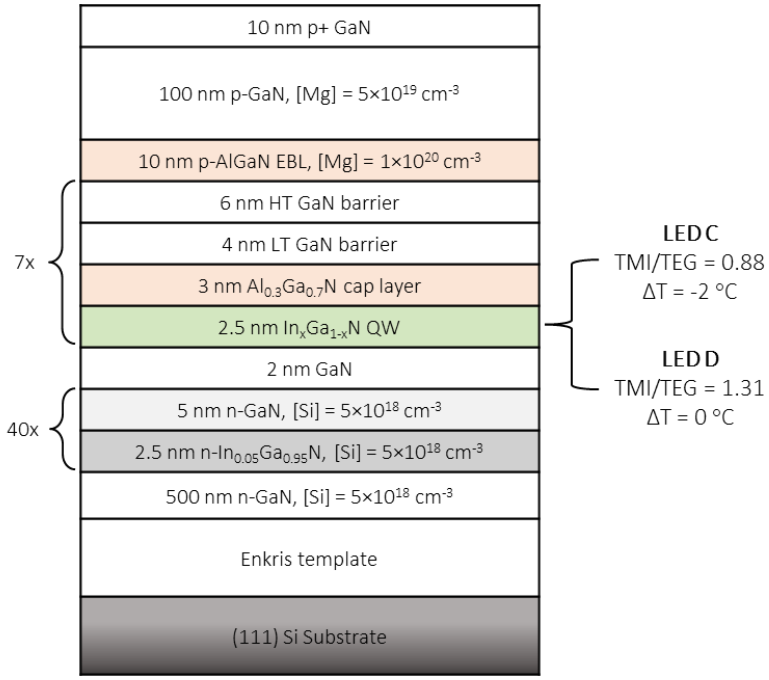

Figure 6.23. Schematic showing epitaxial structure of LED-C and LED-D.

LEDs with varying QW TMI/TEG molar flow and growth temperature were processed into μLED devices. The epitaxial structures for LED-C and D are depicted in Fig. 6.23. Growth conditions for LED-C were 4.16 μmol/min (18 sccm) TEG, 3.66 μmol/min (46.8 sccm), TMI/TEG = 0.88, and ΔT = -2 °C. Conditions used for LED-D were 4.16 μmol/min (18 sccm) TEG, 5.47 μmol/min (70 sccm), TMI/TEG = 1.31, and ΔT = 0 °C. The

EL spectra from 1 A cm^{-2} (yellow curve) to 10 A cm^{-2} (purple curve) for 80 × 80 μm^2 devices are shown in Figs. 6.24(a) and 6.24(b) for LED-C and LED-D, respectively. EQE curves for LED-C are given in Fig. 6.24(c) for 40 × 40 μm^2, 60 × 60 μm^2, and 80 × 80 μm^2 devices, which reach their peak EQE at current densities between 5.6 and 7.5 A cm^{-2}. The 80 × 80 μm^2 device has the highest peak EQE of approximately 0.1% where the corresponding wavelength is ~625 nm. EQE curves for the same size devices on LED-D are shown in Fig. 6.24(d); peak EQE is reached at a lower current density of 3.2 A cm^{-2}. A much lower peak EQE of approximately 0.06% was measured for the 80 × 80 μm^2 device although the wavelength for LED-D is red-shifted by ~10 nm. Despite the shorter wavelength, which is expected to result in improved EQE values, the higher EQE realized using TMI/TEG ratio = 0.88 for LED-C led to these conditions being incorporated into future growths.

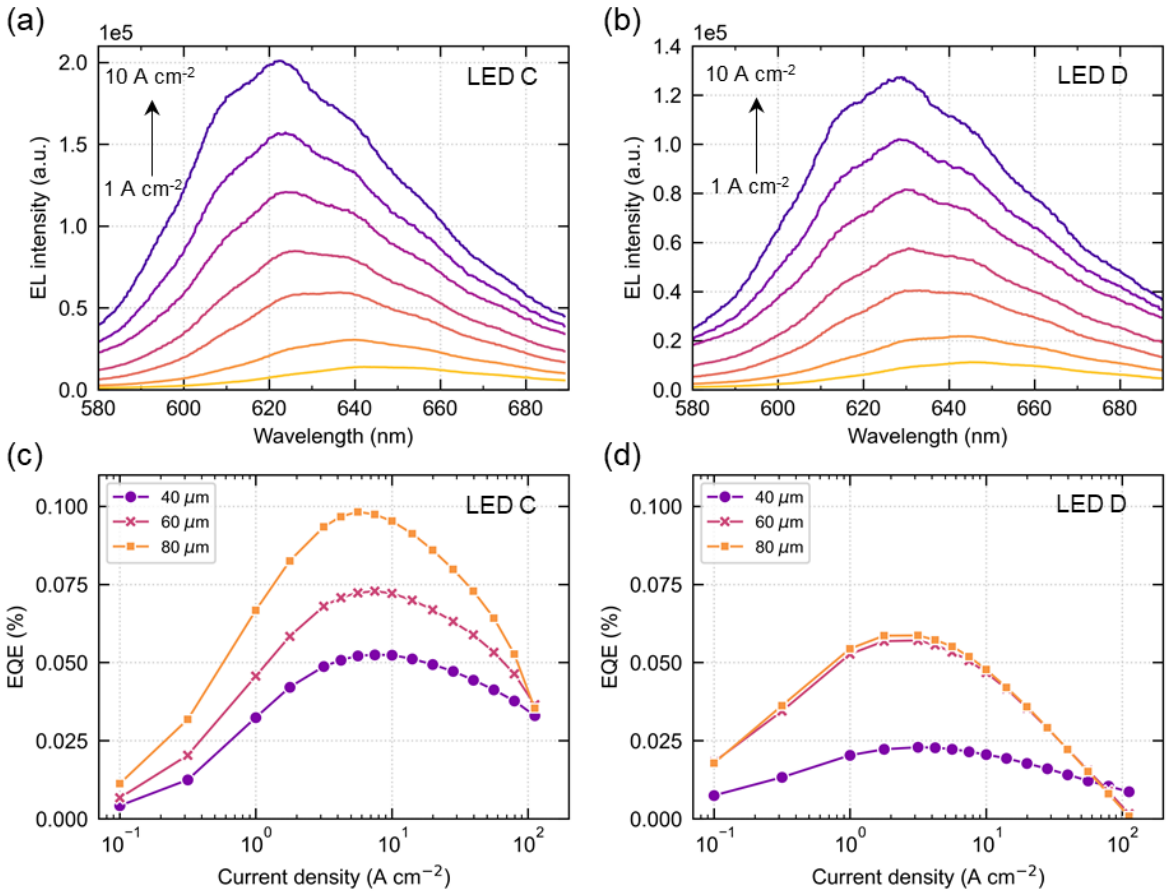

Figure 6.24. EL spectra from 1 A cm^{-2} (yellow curve) to 10 A cm^{-2} (purple curve) for (a) LED-C and (b) LED-D 80 × 80 μm^2 devices. EQE curves for (c) LED-C and (d) LED-D devices ranging from 40 × 40 μm^2 to 80 × 80 μm^2.

To-date, the best red μLED on silicon results obtained at UCSB are for LED-E. The epitaxial structure of LED-E is shown in Fig. 6.25. The LED was re-grown on the Enkris template beginning with a 500-nm *n*-GaN layer ([Si] = 5×10^{18} cm^{-3}). A 30-period *n*-type 2.5 nm/5 nm $In_{0.05}Ga_{0.95}N$/GaN superlattice ([Si] = 5×10^{18} cm^{-3}) was grown to form V-defects at TDs followed by a 2-nm UID GaN spacer layer. The active region was grown undoped and consisted of seven periods of 2.5-nm InGaN QWs, 3-nm $Al_{0.30}Ga_{0.70}N$ capping layers, 4-nm LT GaN barriers, and 6-nm HT GaN barriers. The QW, AlGaN cap, LT GaN, and HT GaN growth temperatures were 762 °C, 762 °C, 859 °C, and 914 °C, respectively. QW flow rates

were 4.16 μmol/min (18 sccm) TEG and 3.66 μmol/min (46.8 sccm) TMI, resulting in TMI/TEG = 0.88. The active region was followed by a 10-nm *p*-AlGaN electron blocking layer ([Mg] = 1×10^{20} cm^{-3}), 75 nm of *p*-GaN ([Mg] = 5×10^{19} cm^{-3}), and a 10-nm *p*+-GaN contact layer.

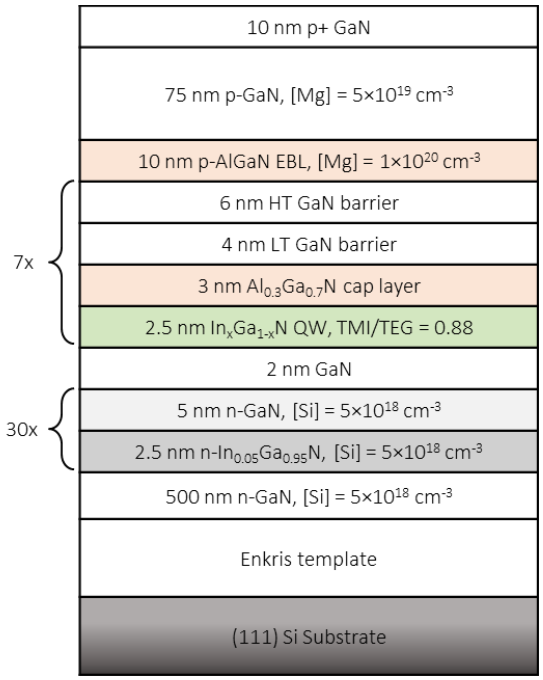

Figure 6.25. Schematic showing epitaxial structure of LED-E.

The fabricated μLED characteristics for LED-E are given in Fig. 6.26. The EL spectra from 1 A cm^{-2} (yellow curve) to 10 A cm^{-2} (purple curve) for an 80 × 80 μm^2 device is shown in Fig. 6.26(a) and the peak wavelength as a function of current density from 0 to 50 A cm^{-2} is plotted in Fig. 6.26(b) for device sizes ranging from 5 × 5 μm^2 to 80 × 80 μm^2. The EQE curves for the same range of devices are shown in Fig. 6.26(c). The 80 × 80 μm^2 device has a peak EQE of 0.17% at J = 4.2 A cm^{-2} and λ = 619 nm. The EQE curve for the 60 × 60 μm^2 device almost exactly follows that of the 80 × 80 μm^2 device. The value of the

peak EQE decreases slightly with device size down to 20 × 20 μm^2, where it reaches 0.16%, while the current density corresponding to peak is increased to 20 A cm^{-2}. For the smaller device sizes of 10 × 10 μm^2 and 5 × 5 μm^2, the peak EQE drops more sharply down to 0.13% and 0.07%, respectively; however, the current density at peak remains approximately constant at 20 A cm^{-2}. The *J-V* curves for all measured device sizes are shown in Fig. 6.26(d) where the average forward voltage at 20 A cm^{-2} is 3.06 V. The *J-V* characteristics are expected to be size-independent although a spread is observed here where, with the exception of the 5 × 5 μm^2 device, the voltage increases with device size. One possible explanation for the trend in the *J-V* curves is the difference in current spreading for different size devices. It is also important to note that the setup in which these devices are measured is not optimized for electrical device characterization but rather for light collection. Future measurements will use an improved probe station setup, rather than an integrating sphere, to measure the *J-V* characteristics. This will allow for important measurements of the low current density regime as well as the reverse leakage behavior.

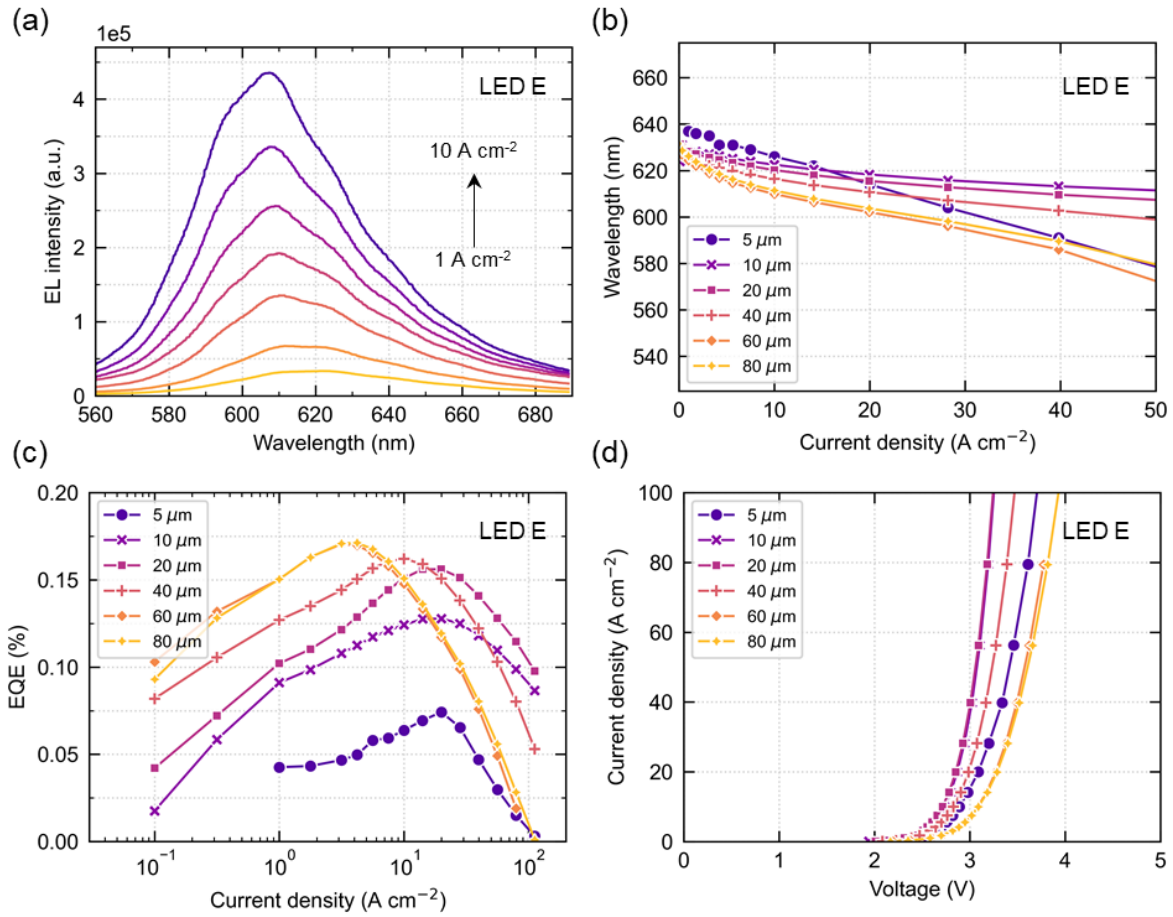

Figure 6.26. (a) EL spectra of 80 × 80 μm^2 device from 1 A cm^{-2} (yellow curve) to 10 A cm^{-2} (purple curve), (b) peak wavelength as a function of current density, (c) EQE curves, and (d) *J-V* curves for LED-E devices ranging from 5 × 5 μm^2 to 80 × 80 μm^2.

Figure 6.27. shows images of EL emission for varying device sizes on LED-E at 1 and 5 A cm^{-2}. At 1 A cm^{-2} and for the smallest devices at 5 A cm^{-2}, regions of green emission are observed. The poor light extraction on silicon also makes it easier to see that the QW emission from this sample is inhomogeneous; there are regions of higher and lower emission intensity. Future studies should closely monitor EL images of processed devices to move toward growth conditions that achieve more uniform emission.

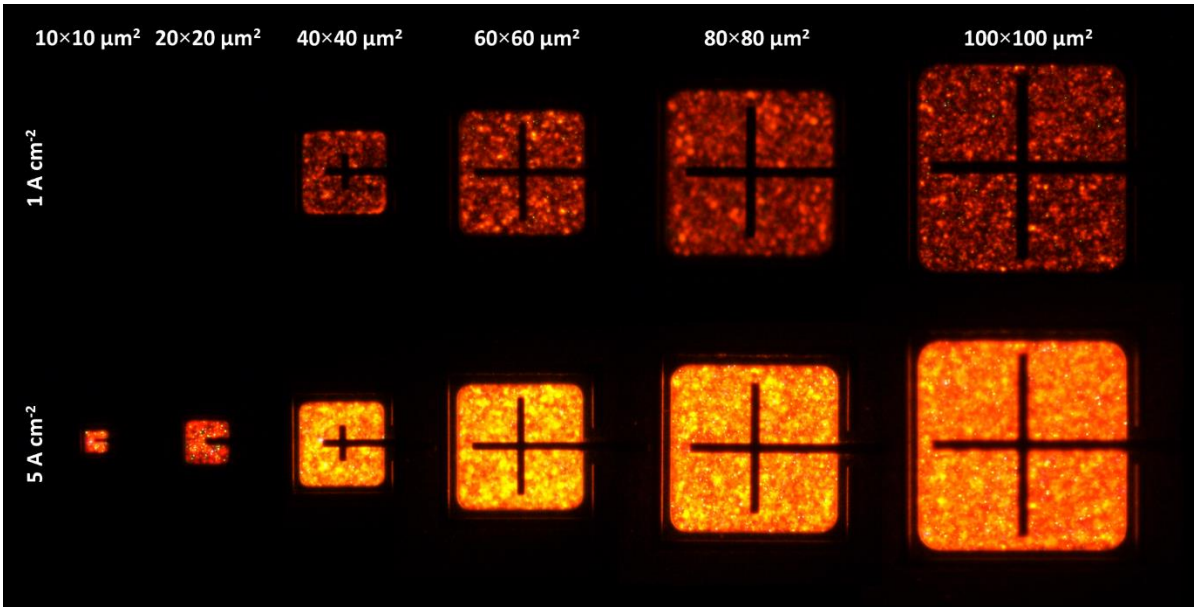

Figure 6.27. LED-E EL images of 40 × 40 μm^2 to 100 × 100 μm^2 devices at 1 A cm^{-2} and 10 × 10 μm^2 to 100 × 100 μm^2 devices at 5 A cm^{-2}.

6.3.3 Light Extraction Correction

Results from the Monte Carlo raytracing simulations, which provided an estimate of the LEE for red μLED devices of varying sizes and configurations, were used to calculate an EQE correction factor. The high-LEE flip-chip configuration was simulated to have LEE = 87.3% and 82.3% for 5 × 5 μm^2 and 20 × 20 μm^2 mesas, respectively. The configuration used in on-wafer simulations is shown in Fig. 6.28 and is representative of the device design employed for LEDs A-E presented in the previous section. The 5 × 5 μm^2 and 20 × 20 μm^2 mesas were simulated to have LEE = 5.33% and 4.97%, respectively. A correction factor is calculated based on the lower LEE mesa size of 20 × 20 μm^2 and is equal to 16.6. The EQE curves for LED-E were recalculated using this correction factor. Figure 6.29 shows the EQE expected for LED-E if the LEE was 82.3% rather than 4.97%. For the 60 × 60 μm^2 and 80 × 80 μm^2 devices, the peak EQE increases to 2.8% while for the 20 × 20 μm^2 device, the peak EQE increases to 2.7%.

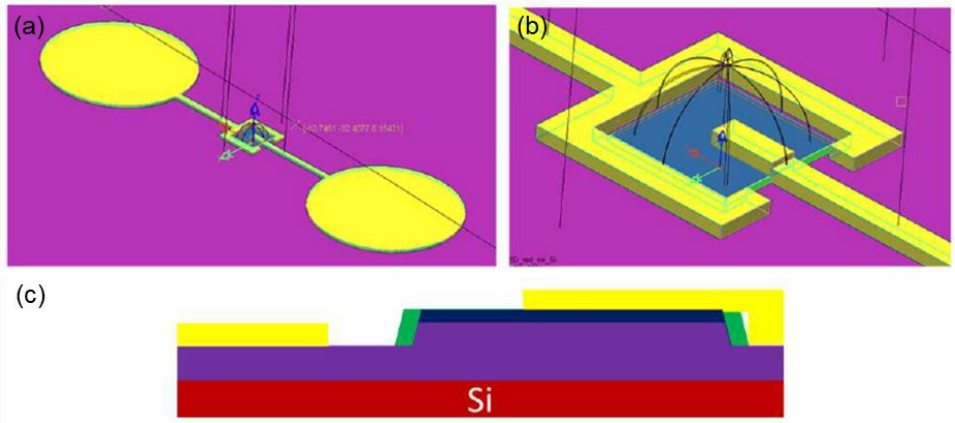

Figure 6.28. On-wafer configuration using Synopsys LightTools for Monte Carlo raytracing simulations. A 20 × 20 μm^2 mesa with sloped sidewalls, ITO, sidewall SiO_2, and metal contacts and pads was simulated. Schematics of (a) the full simulated device, including pads, (b) the mesa structure, and (c) the device cross-section. Figure and simulations are courtesy of Dr. Pavel Shapturenka.

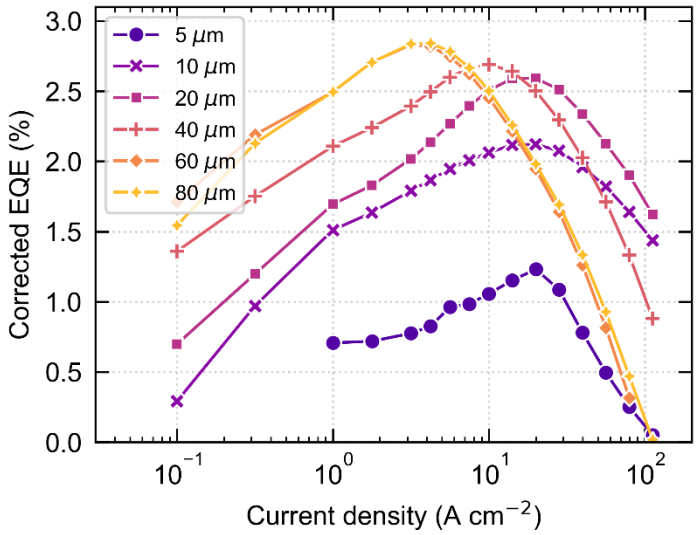

Figure 6.29. EQE curves of LED-E using correction factor = 16.6. The correction factor amounts to assuming a LEE = 82.3% rather than 4.97%. The peak EQE increases to 2.84%.

6.4 Conclusions

Epitaxial growth optimization of long-wavelength III-nitride LEDs was presented in this chapter with the goal of using V-defect engineering to realize high efficiency red μLEDs

on silicon substrates. The growth conditions of a reference green LED on sapphire were used as the starting point from which to increase the emission wavelength and to transfer the growth process to (111)-oriented silicon substrates. Initial optimization efforts were focused on the InGaN QW, AlGaN cap, and GaN QB layers in the active region. By decreasing the active region temperature by 20 °C, increasing the AlGaN cap layer aluminum fraction from 10% to 35%, and increasing the number of QWs from five to seven, the LED emission wavelength on silicon was increased from green at 533 nm to red at 631 nm. To achieve more robust QW optical properties and increase the LED efficiency, various QW growth conditions were explored. Namely, the QW thickness, growth rate, TMI/TEG molar flow ratio, and temperature were studied and adjusted to achieve higher efficiencies at wavelengths greater than 610 nm.

Advanced materials characterization techniques including AFM, SEM, and HAADF STEM were leveraged to study the V-defect density, size, and structure in red LEDs on silicon. TEM-based EDX enabled qualitative comparisons to be made between the alloy compositions on the sidewall QWs and the planar QWs. HAADF STEM images also showed that the planar QW and capping layer thickness were uniform and close to the targeted values. To measure the carrier recombination times and determine the absolute IQE for a yellow LED on PSS and a red LED on silicon, TRPL spectroscopy was employed. The IQE for the yellow LED on PSS and the red LEDs were ~40% and ~8%, respectively. Quasi-cw PL measurements, which provides an upper bound for the actual IQE, on several samples showed that the relative IQE was lower for red wavelengths than yellow and lower for LEDs on silicon compared to those on PSS.

Lastly, μLED devices were fabricated and their optical and electrical properties measured. Results for several devices highlight the evolution of the LED epitaxial structure. An optimized red LED structure with high efficiency was ultimately achieved. The on-wafer (with no substrate removal) EQE was 0.17% for 60 × 60 μm^2 and 80 × 80 μm^2 red μLEDs on silicon with a wavelength of 619 nm. To better estimate the EQE that would be measured if these devices utilized a high-LEE flip-chip configuration, Monte Carlo raytracing simulations were performed. An improvement in the LEE by a factor of 16.6 was calculated. Using this correction factor, the highest efficiency red LED sample with $\lambda \sim 620$ nm is expected to have peak EQE values of 1.2%, 2.2%, 2.7%, 2.7%, 2.8%, and 2.8% for 5 × 5 μm^2, 10 × 10 μm^2, 20 × 20 μm^2, 40 × 40 μm^2, 60 × 60 μm^2, and 80 × 80 μm^2 μLED devices, respectively. The research presented in this chapter highlights the promise of using V-defect engineering to realize high efficiency red μLEDs. However, many opportunities still exist for optimization of the device fabrication and epitaxial growth and will be further discussed in Chapter 7.

References

[1] K. Ding, V. Avrutin, N. Izyumskaya, Ü. Özgür, and H. Morkoç, Applied Sciences **9**, 1206 (2019).

[2] D. Hwang, A. Mughal, C.D. Pynn, S. Nakamura, and S.P. DenBaars, Appl. Phys. Express **10**, 032101 (2017).

[3] F. Olivier, S. Tirano, L. Dupré, B. Aventurier, C. Largeron, and F. Templier, Journal of Luminescence **191**, 112 (2017).

[4] F. Olivier, A. Daami, C. Licitra, and F. Templier, Appl. Phys. Lett. **111**, 022104 (2017).

[5] S.S. Konoplev, K.A. Bulashevich, and S.Yu. Karpov, Physica Status Solidi (a) **215**, 1700508 (2018).

[6] K.A. Bulashevich and S.Y. Karpov, Physica Status Solidi (RRL) – Rapid Research Letters **10**, 480 (2016).

[7] M.S. Wong, D. Hwang, A.I. Alhassan, C. Lee, R. Ley, S. Nakamura, and S.P. DenBaars, Opt. Express, OE **26**, 21324 (2018).

[8] M.S. Wong, C. Lee, D.J. Myers, D. Hwang, J.A. Kearns, T. Li, J.S. Speck, S. Nakamura, and S.P. DenBaars, Appl. Phys. Express **12**, 097004 (2019).

[9] J.M. Smith, R. Ley, M.S. Wong, Y.H. Baek, J.H. Kang, C.H. Kim, M.J. Gordon, S. Nakamura, J.S. Speck, and S.P. DenBaars, Appl. Phys. Lett. **116**, 071102 (2020).

[10] R.-H. Horng, H.-Y. Chien, K.-Y. Chen, W.-Y. Tseng, Y.-T. Tsai, and F.-G. Tarntair, IEEE Journal of the Electron Devices Society **6**, 475 (2018).

[11] M.R. Krames, M. Ochiai-Holcomb, G.E. Höfler, C. Carter-Coman, E.I. Chen, I.-H. Tan, P. Grillot, N.F. Gardner, H.C. Chui, J.-W. Huang, S.A. Stockman, F.A. Kish, M.G. Craford, T.S. Tan, C.P. Kocot, M. Hueschen, J. Posselt, B. Loh, G. Sasser, and D. Collins, Appl. Phys. Lett. **75**, 2365 (1999).

[12] M.S. Wong, J.A. Kearns, C. Lee, J.M. Smith, C. Lynsky, G. Lheureux, H. Choi, J. Kim, C. Kim, S. Nakamura, J.S. Speck, and S.P. DenBaars, Opt. Express **28**, 5787 (2020).

[13] M. Boroditsky, I. Gontijo, M. Jackson, R. Vrijen, E. Yablonovitch, T. Krauss, C.-C. Cheng, A. Scherer, R. Bhat, and M. Krames, Journal of Applied Physics **87**, 3497 (2000).

[14] J.-T. Oh, S.-Y. Lee, Y.-T. Moon, J.H. Moon, S. Park, K.Y. Hong, K.Y. Song, C. Oh, J.-I. Shim, H.-H. Jeong, J.-O. Song, H. Amano, and T.-Y. Seong, Opt. Express, OE **26**, 11194 (2018).

[15] S.S. Pasayat, C. Gupta, M.S. Wong, R. Ley, M.J. Gordon, S.P. DenBaars, S. Nakamura, S. Keller, and U.K. Mishra, Appl. Phys. Express **14**, 011004 (2021).

[16] S.S. Pasayat, R. Ley, C. Gupta, M.S. Wong, C. Lynsky, Y. Wang, M.J. Gordon, S. Nakamura, S.P. Denbaars, S. Keller, and U.K. Mishra, Appl. Phys. Lett. **117**, 061105 (2020).

[17] S. Pereira, M.R. Correia, E. Pereira, K.P. O'Donnell, C. Trager-Cowan, F. Sweeney, and E. Alves, Phys. Rev. B **64**, 205311 (2001).

[18] M. Hao, H. Ishikawa, T. Egawa, C.L. Shao, and T. Jimbo, Appl. Phys. Lett. **82**, 4702 (2003).

[19] R.C. White, H. Li, M. Khoury, C. Lynsky, M. Iza, S. Keller, D. Sotta, S. Nakamura, and S.P. DenBaars, Crystals **11**, 1364 (2021),

[20] S. Zhang, J. Zhang, J. Gao, X. Wang, C. Zheng, M. Zhang, X. Wu, L. Xu, J. Ding, Z. Quan, and F. Jiang, Photonics Res. **8**, 1671 (2020).

[21] I.-H. Kim, H.-S. Park, Y.-J. Park, and T. Kim, Appl. Phys. Lett. **73**, 1634 (1998).

[22] X.H. Wu, C.R. Elsass, A. Abare, M. Mack, S. Keller, P.M. Petroff, S.P. DenBaars, J.S. Speck, and S.J. Rosner, Appl. Phys. Lett. **72**, 692 (1998).

[23] J.-I. Hwang, R. Hashimoto, S. Saito, and S. Nunoue, Appl. Phys. Express **7**, 071003 (2014).

[24] D.D. Koleske, A.J. Fischer, B.N. Bryant, P.G. Kotula, and J.J. Wierer, Journal of Crystal Growth **415**, 57 (2015).

[25] S. Saito, R. Hashimoto, J. Hwang, and S. Nunoue, Appl. Phys. Express **6**, 111004 (2013).

[26] T. Shioda, H. Yoshida, K. Tachibana, N. Sugiyama, and S. Nunoue, Physica Status Solidi (a) **209**, 473 (2012).

[27] T. Hikosaka, T. Shioda, Y. Harada, K. Tachibana, N. Sugiyama, and S. Nunoue, Physica Status Solidi c **8**, 2016 (2011).

[28] S. Ploch, T. Wernicke, M. Frentrup, M. Pristovsek, M. Weyers, and M. Kneissl, Appl. Phys. Lett. **101**, 202102 (2012).

[29] J. Ou, Y.-C. Pan, W.-H. Lee, C.-K. Shu, H.-C. Lin, M.-C. Lee, W.-H. Chen, C.-I. Chiang, H. Chang, and W.-K. Chen, Jpn. J. Appl. Phys. **38**, 4958 (1999).

[30] A. Hangleiter, T. Langer, P. Henning, F.A. Ketzer, H. Bremers, and U. Rossow, in *Gallium Nitride Materials and Devices XIII* (SPIE, 2018), pp. 132–139.

[31] S. Marcinkevičius, R. Yapparov, Y.C. Chow, C. Lynsky, S. Nakamura, S.P. DenBaars, and J.S. Speck, Appl. Phys. Lett. **119**, 071102 (2021).

[32] P. Henning, S. Sidikejiang, P. Horenburg, H. Bremers, U. Rossow, and A. Hangleiter, Appl. Phys. Lett. **119**, 011106 (2021).

[33] F. Nippert, S.Yu. Karpov, G. Callsen, B. Galler, T. Kure, C. Nenstiel, M.R. Wagner, M. Straßburg, H.-J. Lugauer, and A. Hoffmann, Appl. Phys. Lett. **109**, 161103 (2016).

7

Conclusions and Future Work

7.1 Conclusions

This dissertation focused on the development of long-wavelength III-nitride LEDs. Attention was first devoted to identifying the source of excess voltage in *c*-plane green LEDs. Several approaches to mitigating excess voltage were then proposed and studied. Lastly, the efforts on green LED development were extended to longer wavelengths, with a specific emphasis on red LEDs on silicon substrates.

In Chapter 3, a combined experimental and simulation-based approach using Localization Landscape theory of disorder [1-5] was used to explore the impact of QW number on forward voltage V_F in *c*-plane green LEDs [6,7]. An increase in V_F with increasing QW number was observed in both experimentally grown and simulated structures. From these results, polarization-induced barriers and sequential filling of QWs were proposed as two mechanisms which contribute to the increase in V_F. The higher QW indium fraction in green LEDs relative to blue results in a larger polarization discontinuity at the QW/QB interface and thus a larger polarization-related barrier. This barrier means that with more QWs, it becomes increasingly difficult for electrons to reach the most active *p*-side QW. 3D simulations were performed where the polarization coefficients were artificially reduced to 0%; even without the presence of polarization, a voltage penalty was

still observed for green multiple QW LEDs. This led to the identification of a second mechanism, sequential carrier injection of QWs, which is related to the depth of the QW potential. This effect was found to be more pronounced in high indium composition QWs where band offsets between the QW and QB are large. In addition to helping explain the historically low WPE of green LEDs, these results highlight important considerations for heterostructure design of long-wavelength III-nitride LEDs.

To overcome the barriers to carrier transport identified in Chapter 3, InGaN quantum barriers were proposed in Chapter 4 as one potential design approach. 3D device simulations which included random alloy fluctuations were used to understand carrier behavior in a disordered potential [8]. The simulated J-V characteristics and carrier density spatial overlap indicated that increasing the indium fraction in the InGaN QBs led to a reduced polarization discontinuity at the QW/QB interface, thereby reducing V_F and improving carrier density spatial overlap. Simulated maps of electron and hole current through the device also showed preferential pathways for vertical transport in structures with InGaN QBs. A positive correlation between hole (electron) current in the *p*-side (*n*-side) barrier and indium fraction along with a negative correlation between the strain ε_{zz} and indium fraction, revealed that preferential pathways exist in regions of high indium content and reduced strain. Experimentally, multiple QW green LEDs with InGaN quantum barriers exhibited lower V_F and blue-shifted wavelengths relative to LEDs with GaN quantum barriers, consistent with simulation data.

Chapter 5 investigated V-defect engineering on sapphire substrates to reduce excess forward voltage ΔV_F in *c*-plane green LEDs. V-defect engineering was demonstrated in other reports to be an effective approach to realize high WPE, long-wavelength LEDs by

improving hole injection in lower, *n*-side QWs [9,10]. However, these demonstrations were achieved on silicon substrates which allow for V-defect densities in the low 10^9 cm^{-2} range, whereas V-defect densities on sapphire are typically an order of magnitude lower. In Chapter 4, the TD density, and therefore the V-defect density, were systematically increased for green LEDs on sapphire [11]. Increasing the V/III ratio during high temperature GaN growth results in higher TD densities, as measured by XRD ω-rocking curve scans and cathodoluminescence. Based on SEM images at the top of the active region, the V-defect density was also observed to increase, although not to the same extent as the TD density. LED device characterization showed the desired reduction in V_F with higher V-defect density. Unfortunately, this was accompanied by a decrease in the light output power, which is attributed to the high density of TDs which did not contain a V-defect. The opening of all TDs into large V-defects, with well-defined sidewall structure, is predicted to lead to further reduction in V_F as well as reduction in nonradiative recombination at TDs.

Lastly in Chapter 6, the LED emission wavelength was increased from green (~525 nm) to red (~610 nm) and μLED devices with 5 × 5 μm^2 to 100 × 100 μm^2 mesa sizes were studied. This chapter primarily focused on red LED growth on silicon substrates; however, some results for yellow LEDs and LEDs on PSS were also presented. The epitaxial growth optimization process was discussed, including initial efforts to increase the wavelength from green to red and to improve the wavelength stability. Important data on the V-defect structure and alloy compositions were measured using advanced materials characterization techniques including HAADF STEM and TEM-EDX. Temperature dependent TRPL spectroscopy of select samples enabled absolute IQE measurements. A yellow-emitting LED on PSS and red-emitting LED on silicon were measured to have IQEs of ~40% and ~8%,

respectively. An on-wafer EQE value of 0.17% was achieved for 60 × 60 μm^2 and 80 × 80 μm^2 red μLEDs on silicon with a wavelength of 619 nm. Monte Carlo raytracing simulations provided estimates of the LEE for red μLED devices of varying sizes and configurations. A high-LEE flip-chip configuration was simulated to have LEE = 82.3%, whereas the on-wafer (no substrate removal) configuration gave LEE = 4.97%. Using these data, a correction factor was applied to the measured EQE. Therefore, if a high-LEE fabrication process was used, an increase in the peak EQE from 0.17% to 2.8% is expected. An EQE of 2.8% for a red μLED is among the highest reported values in the literature.

7.2 Future Work

The fields of long-wavelength LED and μLED device research continue to grow at a rapid pace and are driven primarily by the need for more efficient, self-emissive pixel designs for next-generation display technologies and color-mixed LEDs for solid-state lighting. There remain many opportunities to build upon the research presented in this dissertation to advance long-wavelength LEDs. Two specific areas that are identified for future work are V-defect engineering and red LED optimization.

7.2.1 V-defect Engineering

Despite the impressive demonstrations of high efficiency long-wavelength LEDs on silicon using V-defect engineering [9,10], these LEDs still exhibit current droop and decreasing EQE with increasing emission wavelength. The results were also achieved on silicon, which necessitates more involved LED processing to realize high LEE. Continued

research in the field of V-defect engineering is required to mitigate droop and demonstrate high WPE on the more conventional LED substrate, PSS.

The presence of droop in V-defect engineered long-wavelength LEDs indicates that even with the lower polarization barrier sidewall, all QWs are not fully injected. Thus, the full potential of V-defects to laterally inject all QWs in a MQW stack has yet to be realized. It was shown in Chapter 5 that increasing the screw-component TDD on sapphire was challenging using growth conditions alone. One alternate approach to achieving higher V-defect density on PSS is to increase the pattern pitch. The pattern pitch has units of length and is defined as the sum of the bottom pattern diameter plus the spacing length between the patterned structures. A typical value of the PSS pattern pitch is 3 μm. GaN growth on PSS is analogous to the epitaxial lateral overgrowth (ELOG) technique where growth on a masked substrate is used to reduce the TDD [12-14]. In cross-sectional bright field TEM under two-beam diffraction conditions (g = [0002]), Kim *et al*. observe screw-component TDs at the apex of the PSS cone-shaped pattern [14]. It is possible that with a higher pattern pitch, the density of screw-component TDs, and thus the V-defect density [15], could be increased.

It is also conceivable that lateral injection could be achieved using other methods besides V-defect nucleation in the InGaN/GaN SL. *Ex-situ* wet or dry etching (such as those described in Refs. [16] and [17]), followed by a clean and *p*-GaN regrowth, could be used to expose the deeper QWs and enable improved hole injection. Another possibility is that sidewall QWs provide a large enough barrier to prevent efficient lateral hole injection. In this case, *in-situ* etching methods could be explored to remove the sidewalls and expose the planar QWs. For future V-defect engineering research, it would be advantageous to determine a characterization method and/or unique heterostructure design that allows for the

unambiguous, direct observation of deeper QW injection. For example, a structure incorporating marker QWs that emit at different wavelengths could be considered.

7.2.2 Red LED Optimization

There are still many opportunities for growth optimization of red LEDs on silicon using a V-defect engineering approach. In Chapter 6, the highest aluminum fraction AlGaN cap layers explored had 35% aluminum. Other literature reports have shown that very high aluminum percentages, upwards of 90%, can be advantageous for red LEDs [18]. Increasing the aluminum fraction of the cap is also associated with higher V_F [19] and so a balance must be struck between optical and electrical efficiency. Growth conditions, such as growth rate, V/III ratio, and total gas flow should be examined to improve the aluminum incorporation efficiency and measure the effect of different AlGaN cap compositions on μLED device performance. Along with the cap layer, improvements in the QW and GaN QB growth conditions may lead to improved device EQE. Microscope images of μLED devices under electrical injection in Fig. 6.27 showed relatively inhomogeneous luminescence with bright regions, dark regions, and even some regions of green emission. Interrupted growths along with AFM is recommended to characterize the surface morphology at the top of the active region. These measurements may provide insight into the inhomogeneous light emission and, in conjunction with growth optimization, may yield high indium fraction QWs with improved morphology.

Other growth optimization could target the *n*- and *p*-GaN regions. In the SL on the *n*-side of the LED, the indium composition and relative thickness of the InGaN and GaN layers in the SL could be studied [20,21]. The TDD for GaN-on-Si is estimated to be in the

low 10^9, however, the V-defect density at the surface of the *p*-GaN was observed to be 3.5×10^8 cm^{-2}. Zhang *et al*. reported high efficiency red LEDs with an optimized V-defect density on the order of 10^9 cm^{-2} [10], which supports efforts to use SL growth conditions that lead to a higher fraction of TDs opening into V-defects [22]. Higher indium or thicker InGaN in the SL could produce the desired result. On the *p*-side of the device, improved *p*-GaN growth conditions for V-defect filling could be explored to improve efficiency [23]. Increasing the growth temperature, decreasing the growth rate, or introducing TMI flow are several approaches that may promote lateral growth. The AlGaN EBL and Mg-doping concentration after the last QB are expected to play an important role on hole injection and therefore should also be carefully optimized [24-26].

Lastly, an important area of development for red μLEDs on silicon substrates is the device fabrication and substrate removal. The significant impact of the absorbing substrate on the LEE was discussed in Chapter 6. Monte Carlo raytracing simulations calculated LEE values of approximately 5% for red μLEDs on silicon. In contrast, a high-LEE flip-chip configuration is simulated to have an LEE of close to 85%. Incorporating a high-LEE flip-chip fabrication process, such as the one described in detail in Ref. [27], will enable accurate assessment of red μLEDs as well as comparison with other state-of-the-art results.

References

[1] M. Filoche and S. Mayboroda, PNAS **109**, 14761 (2012).

[2] M. Filoche, M. Piccardo, Y.-R. Wu, C.-K. Li, C. Weisbuch, and S. Mayboroda, Phys. Rev. B **95**, 144204 (2017).

[3] D.N. Arnold, G. David, D. Jerison, S. Mayboroda, and M. Filoche, Phys. Rev. Lett. **116**, 056602 (2016).

[4] C.-K. Li, M. Piccardo, L.-S. Lu, S. Mayboroda, L. Martinelli, J. Peretti, J.S. Speck, C. Weisbuch, M. Filoche, and Y.-R. Wu, Phys. Rev. B **95**, 144206 (2017).

[5] See http://yrwu-wk.ee.ntu.edu.tw/ for "Optoelectronic device simulation laboratory".

[6] C. Lynsky, A.I. Alhassan, G. Lheureux, B. Bonef, S.P. DenBaars, S. Nakamura, Y.-R. Wu, C. Weisbuch, and J.S. Speck, Phys. Rev. Materials **4**, 054604 (2020).

[7] G. Lheureux, C. Lynsky, Y.-R. Wu, J.S. Speck, and C. Weisbuch, J. Appl. Phys. **128**, 235703 (2020).

[8] C. Lynsky, G. Lheureux, B. Bonef, K.S. Qwah, R.C. White, S.P. DenBaars, S. Nakamura, Y.-R. Wu, C. Weisbuch, and J.S. Speck, *Submitted*.

[9] F. Jiang, J. Zhang, L. Xu, J. Ding, G. Wang, X. Wu, X. Wang, C. Mo, Z. Quan, X. Guo, C. Zheng, S. Pan, and J. Liu, Photonics Res. **7**, 144 (2019).

[10] S. Zhang, J. Zhang, J. Gao, X. Wang, C. Zheng, M. Zhang, X. Wu, L. Xu, J. Ding, Z. Quan, and F. Jiang, Photonics Res. **8**, 1671 (2020).

[11] C. Lynsky, R.C. White, Y.C. Chow, W.Y. Ho, S. Nakamura, S.P. DenBaars, and J.S. Speck, Journal of Crystal Growth **560–561**, 126048 (2021).

[12] B. Beaumont, Ph. Vennéguès, and P. Gibart, Physica Status Solidi (b) **227**, 1 (2001).

[13] H.-Y. Shin, S.K. Kwon, Y.I. Chang, M.J. Cho, and K.H. Park, Journal of Crystal Growth **311**, 4167 (2009).

[14] Y.H. Kim, H. Ruh, Y.K. Noh, M.D. Kim, and J.E. Oh, Journal of Applied Physics **107**, 063501 (2010).

[15] X.H. Wu, C.R. Elsass, A. Abare, M. Mack, S. Keller, P.M. Petroff, S.P. DenBaars, J.S. Speck, and S.J. Rosner, Appl. Phys. Lett. **72**, 692 (1998).

[16] M. Kodama, M. Sugimoto, E. Hayashi, N. Soejima, O. Ishiguro, M. Kanechika, K. Itoh, H. Ueda, T. Uesugi, and T. Kachi, Appl. Phys. Express **1**, 021104 (2008).

[17] J.G. Nedy, N.G. Young, K.M. Kelchner, Y. Hu, R.M. Farrell, S. Nakamura, S.P. DenBaars, C. Weisbuch, and J.S. Speck, Semicond. Sci. Technol. **30**, 085019 (2015).

[18] J.-I. Hwang, R. Hashimoto, S. Saito, and S. Nunoue, Appl. Phys. Express **7**, 071003 (2014).

[19] T. Shioda, H. Yoshida, K. Tachibana, N. Sugiyama, and S. Nunoue, Physica Status Solidi (a) **209**, 473 (2012).

[20] W. Qi, J. Zhang, C. Mo, X. Wang, X. Wu, Z. Quan, G. Wang, S. Pan, F. Fang, J. Liu, and F. Jiang, Journal of Applied Physics **122**, 084504 (2017).

[21] X. Jiang, C. Zheng, C. Mo, X. Wang, J. Zhang, Z. Quan, J. Liu, and F. Jiang, Optical Materials **89**, 505 (2019).

[22] Z.J. Quan, J.L. Liu, F. Fang, G.X. Wang, and F.Y. Jiang, Opt Quant Electron **48**, 195 (2016).

[23] C. Xu, C. Zheng, X. Wu, S. Pan, X. Jiang, J. Liu, and F. Jiang, J. Semicond. **40**, 052801 (2019).

[24] Q. Mao, J. Liu, Z. Quan, X. Wu, M. Zhang, and F. Jiang, ECS J. Solid State Sci. Technol. **4**, R44 (2014).

[25] X. Liu, J. Liu, Q. Mao, X. Wu, J. Zhang, G. Wang, Z. Quan, C. Mo, and F. Jiang, Semicond. Sci. Technol. **31**, 025012 (2016).

[26] Y. Li, F. Yun, X. Su, S. Liu, W. Ding, and X. Hou, Journal of Applied Physics **116**, 123101 (2014).

[27] F. Jiang, J. Zhang, S. Qian, and Z. Quan, *Light-Emitting Diodes: Materials, Processes*, *Devices and Applications*, Ed. by J. Li and G.Q. Zhang, (Springer, 2019), p. 133–170.

Appendices

A. Python3 Code

Data preparation of 3D-DDCC output files

```
# The Data_Preparation_1QW5In_CL file is responsible for the
modification of data files output from the 3D-DDCC to enable
further analysis in Python3. This specific script is for a 1QW LED
with 5% indium in the QB but can be used for other LED structures.

import os
import pandas as pd
import numpy as np
import glob


__author__ = "Cheyenne Lynsky, Christian Robertson, Guillaume
Lheureux, Clayton Qwah"


directory=os.path.dirname(os.path.realpath(__file__))

# os.chdir(directory)
#%% Extract data & create node/position/volume element maps

def write_space_df(file, head_len=5):

"""
This function is inteded to take in a 3D .msh file and output a
Pandas DataFrame object that contains the x, y, and z coordinates
indexed to their Node numbers.
"""

    # Check input parameter types.
    if type(file) is not str or type(head_len) is not int:
        print('Input parameters of incorrect type.')
        return

    # Only run method if the file type is a .msh
    if file.endswith('.msh'):
        print("Extracting 3D space coordination...")

        # Dynamically determines the node space size.
```

```
        data_info = pd.read_csv(file, nrows=head_len, header=None)
        num_nodes = int(data_info.iloc[head_len-1, 0])
        raw_data = pd.read_csv(file, skiprows=head_len,
           nrows=num_nodes, header=None, delim_whitespace=True,
           names=['x', 'y', 'z'], engine='python')
        return raw_data
    else:
        print("Error! File extension is not correct!")
        return


def extract_data(file, head_len=12):

"""
This function is the most general extractor that pulls energy
bands, ionized dopants, and temperature. The extractors read output
files and convert them into Pandas DataFrames containing the data
as values and using the Node numbers as indices.
"""

    # Check input parameter types.
    if type(file) is not str or type(head_len) is not int:
        print('Input parameters of incorrect type.')
        return

    # Only run with file extension is correct and set the column
    header
    if file.endswith('.out'):
        head = 'Ec'
    elif file.endswith('.ef'):
        head = 'Ef'
    elif file.endswith('.Ev'):
        head = 'Ev'
    elif file.endswith('.nda'):
        head = 'NDA'
    elif file.endswith('.T'):
        head = 'Temperature'
    elif file.endswith('.L'):
        head = 'Landscape_Electrons'
    elif file.endswith('.Lp'):
        head = 'Landscape_Holes'

    else:
        print("Error! File extension is not correct!")
        return

    print("Extracting " + head + " data...")

    data_info = pd.read_csv(file, nrows=head_len, header=None)
    num_nodes = int(data_info.iloc[head_len-1, 0])
    my_data = pd.read_csv(file, skiprows=head_len, nrows=num_nodes,
      delim_whitespace=True, header=None, names=[head],
```

```
      engine='python')
    return my_data


def extract_carriers(file, head_len=12):

"""
This function extracts the free carrier concentrations. Since the
.np file contains both holes and electrons as separate halves, the
function grabs sequentially then combines them with a unified Node
index.
"""

    # Check input parameter types.
    if type(file) is not str or type(head_len) is not int:
        print('Input parameters of incorrect type.')
        return

    # Only run method if the file type is a .np
    if file.endswith('.np'):

        data_info = pd.read_csv(file, nrows=head_len, header=None)
        num_nodes = int(data_info.iloc[head_len-1, 0])

        print("Extracting electron concentration...")

        ndat = pd.read_csv(file, skiprows=head_len,
           nrows=num_nodes, header=None, names=['n'],
           delim_whitespace=True,  engine='python')

        print("Extracting hole concentration...")

        pdat = pd.read_csv(file, skiprows=2*head_len+num_nodes-2,
           nrows=num_nodes, header=None, names=['p'],
           delim_whitespace=True, engine='python')
        output = pd.concat([ndat, pdat], axis=1, join='outer')
        return output
    else:
        print("Error! File extension is not correct!")
        return


def extract_recombination(file, head_len=12):

"""
This function extracts the recombination rates from their
corresponding files. The files are parsed slightly different which
causes errors in the extractor. The recombination rates are indexed
to Node.
"""

    # Check input parameter types.
```

```
    if type(file) is not str or type(head_len) is not int:
        print('Input parameters of incorrect type.')
        return

    # Only run with file extension is correct and set the column
    header
    if file.endswith('.nonRad'):
        head = 'Non-Radiative'
    elif file.endswith('.Auger'):
        head = 'Auger'
    elif file.endswith('.Rad'):
        head = 'Radiative'
    else:
        print("Error! File extension is incorrect!")
        return

    print("Extracting " + head + " recombination data...")

    data_info = pd.read_csv(file, nrows=head_len, header=None)
    num_nodes = int(data_info.iloc[head_len-1, 0])
    rec_data = pd.read_csv(file, header=None, skiprows=head_len,
     nrows=num_nodes, delim_whitespace=True, names=[head],
     engine='python')
    return rec_data


def extract_composition(file):

"""
This function is an extractor that reads composition output files
and converts them into Pandas DataFrames containing the composition
data as values and using the Node numbers as indices.
"""

    #remove header from file
    comp_header=10
    #extract information about composition map
    comp_map_info=pd.read_csv(file,nrows=comp_header)
    #extract number of nodes
    num_nodes = int(comp_map_info.iloc[comp_header-1, 0])
    #extract composition data

    print('Extracting composition data')

    my_data = pd.read_csv(file, skiprows=comp_header+1,
     nrows=num_nodes, delim_whitespace=True, header=None,
     names=['Node','Comp'], engine='python')
    return my_data


def extract_strain(file):
```

```
"""
This function is an extractor that reads strain output files and
converts them into Pandas DataFrames containing the strain data as
values and using the Node numbers as indices.
"""
    #remove header from file
    strain_header=10
    #extract information about strain map
    strain_map_info=pd.read_csv(file,nrows=strain_header)
    #extract number of nodes
    num_nodes = int(strain_map_info.iloc[strain_header-1, 0])
    #extract strain data

    print('Extracting strain data')

    my_data = pd.read_csv(file, skiprows=strain_header+1,
      nrows=num_nodes, delim_whitespace=True, header=None,
      names=['Node','Strain'], engine='python')
    return my_data


def write_volume_df(file, head_len = 1116001):

"""
This function is inteded to take in a 3D .msh file and output a
PandasDataFrame object that contains the Node Numbers indexed to
their Volume Element Numbers.
"""

    # Check input parameter types.
    if type(file) is not str or type(head_len) is not int:
        print('Input parameters of incorrect type.')
        return

    # Only run method if the file type is a .msh
    if file.endswith('.msh'):
        print("Extracting 3D space coordination...")

        # Dynamically determines the volume space size.
        vol_info = pd.read_csv(file, skiprows=head_len,
           header=None)
        vol_node_info = vol_info.iloc[:-1,0]
        num_elements = int(len(vol_node_info))
        raw_data = pd.read_csv(file, skiprows=head_len, index_col =
           0, nrows=num_elements, header=None,
           delim_whitespace=True, names=['tag1', 'tag2', 'tag3',
           'tag4','node 1', 'node 2', 'node 3', 'node 4'],
           engine='python')
        # return raw_data
        print(num_elements)
        return raw_data
```

```
    else:
        print("Error! File extension is not correct!")
        return


def extract_current(file, head_len=12):

"""
This function is an extractor that pulls electron and hole current.
The extractor reads output files and convert them into Pandas
DataFrames containing the data as values and using the Volume
Element numbers as indices.
"""

    # Check input parameter types.
    if type(file) is not str or type(head_len) is not int:
        print('Input parameters of incorrect type.')
        return

    # Only run with file extension is correct and set the column
    header
    if file.endswith('.Jns'):
        head = 'Electron_Current'
    elif file.endswith('.Jps'):
        head = 'Hole_Current'

    else:
        print("Error! File extension is not correct!")
        return

    print("Extracting " + head + " data...")
    data_info = pd.read_csv(file, nrows=head_len, header=None)
    num_elements = int(data_info.iloc[head_len-1, 0])
    my_data = pd.read_csv(file, skiprows=head_len,
      nrows=num_elements, delim_whitespace=True, header=None,
      names=[head], engine='python')
    return my_data


#%% Functions to create unified files

def create_unified_node_data_file(model_ID, node_map):

"""
This function creates a unified data file that contains all
parameters associated with a particular model, indexed to Node.
"""

    if type(model_ID) is not str or type(node_map) is not
pd.DataFrame:
        print('Input parameters of incorrect type.')
        return
```

```
    # The Node map is used as the base on which the other data sets
      are added.
    output_data = node_map

    # The success variable is used to prevent the function from
      adding data when the file analyzed is not parseable.
    success = True

    for file in glob.glob(model_ID + '.*'):
        print('Analyzing ' + file + '. Please wait...')
        if file.endswith('.np'):
            my_data = extract_carriers(file)
        elif file.endswith(('.Auger', '.nonRad', '.Rad')):
            my_data = extract_recombination(file)
        elif file.endswith(('.out', '.ef', '.Ev', '.nda',
           '.T','.L','.Lp')):
            my_data = extract_data(file)
        else:
            print(file + ' is not parseable at this time.')
            success = False

        if success:
            output_data = pd.concat([output_data, my_data], axis=1,
                join='outer')

        success = True

    # Reorder the headers to be easier to read
    output_data = output_data[['x', 'y', 'z', 'Ec', 'Ev', 'Ef',
      'NDA', 'n', 'p', 'Radiative', 'Non-Radiative',
      'Auger','Temperature','Landscape_Electrons','Landscape_Holes']
      ]

    #output_data.to_csv(model_ID + '.unified', index_label='Node')
    return output_data


def create_unified_vol_data_file(model_ID, vol_map):

"""
This function creates a unified data file that contains all
parameters associated with a particular model, indexed to Volume
element.
"""

    if type(model_ID) is not str or type(vol_map) is not
pd.DataFrame:
        print('Input parameters of incorrect type.')
        return

    # The Volume map is used as the base on which the other data
```

```
      sets are added.
    output_data_vol = vol_map

    # The success variable is used to prevent the function from
      adding data when the file analyzed is not parseable.
    success = True

    for file in glob.glob(model_ID + '.*'):
        print('Analyzing ' + file + '. Please wait...')
        if file.endswith(('.Jns', '.Jps')):
            my_data_vol = extract_current(file)
        else:
            print(file + ' is not parseable at this time.')
            success = False

        if success:
            output_data_vol = pd.concat([output_data_vol,
                my_data_vol], axis=1, join='outer')

        success = True

    # Reorder the headers to be easier to read and get rid of
      "tags"
    output_data_vol = output_data_vol[["Electron_Current",
      "Hole_Current","node 1", "node 2", "node 3", "node 4"]]

    #output_data.to_csv(model_ID + '.unified', index_label='Node')
    return output_data_vol

#%% Create unified files

# Extract map of nodes
node_map = write_space_df('LED5In.msh')

# Extract map of volume elements
vol_map = write_volume_df('LED5In.msh')

# Detect files in directory
filelist=[]
for fname in os.listdir(directory):
            if 'LED5In-out.vg_0.00.vd_' in fname:
               filelist.append(fname[0:34])

# Extract different filenames  for different biases
filelist = list(dict.fromkeys(filelist))

# Create unified data file for each bias
for file in filelist:
    # Create Node and Volume unified dataframes for each bias
    mydf = create_unified_node_data_file(file, node_map)
    mydf_vol = create_unified_vol_data_file(file, vol_map)
```

```
    # Attach composition and strain dataframe to Node unified
      dataframe
    composition_map=extract_composition('In_map.out')
    composition_map=composition_map.set_index('Node')
    strainzz_map=extract_strain('strainzz_point.txt')
    strainzz_map=strainzz_map.set_index('Node')
    mydf=pd.concat([mydf,composition_map,strainzz_map], axis=1,
      join='outer')

    # Reset index from Volume to standard index 0, 1, 2 etc.
    mydf_vol.reset_index(inplace=True)
    mydf_vol = mydf_vol.rename(columns = {'index':'Volume'})

    # Change to Node index and calculate avg. current at each node
    mydf_vol_reord = mydf_vol.melt(id_vars = ["Electron_Current",
      "Hole_Current", "Volume"], value_name = "Node ID")
    mydf_vol_avg = mydf_vol_reord.groupby("Node
      ID")["Electron_Current", "Hole_Current"].mean()

    # Create master data frame containing all data indexed to Node
    masterdf = pd.concat([mydf, mydf_vol_avg], axis=1,
      join='outer')

masterdf.to_csv(file + '.unified', index_label='Node ID')
```

Creating correlation plots

```
# Correlation_Plotting is responsible for creating correlation
plots between values of a specific node in a given domain.

"""
Created on Wed Mar 31 14:16:57 2021

@author: Cheyenne Lynsky
"""

import os
import pandas as pd
import matplotlib.pyplot as plt
import mpl_scatter_density
import matplotlib as mpl
from matplotlib.colors import LinearSegmentedColormap
import numpy as np

# directory=os.path.dirname(os.path.realpath(__file__))
directory = os.chdir(r'C:\Users\Cheyenne Lynsky\Desktop\Box
Sync\Data\InGaN Barrier Paper Data\Unified Files\5In')
```

```
# Read unified file of interest as created by Data_Preparation.py
script and output Pandas DataFrame indexed to Node ID
uni_file = 'LED5In-out.vg_0.00.vd_2.90.vs_0.00.unified'
unidf = pd.read_csv(uni_file, index_col = 0)

#%% Define plot ranges and properties

# Specify the range of Z values for the p-side quantum barrier and
the corresponding composition, strain, and hole current
pside_QB = unidf[(unidf["z"] > 5.2e-6) & (unidf["z"] < 5.7e-6)]
Comp_p = pside_QB["Comp"].tolist()
Strain_p = pside_QB["Strain"].tolist()
Strain_p_scaled = [element * 1000 for element in Strain_p]
Jps_p = pside_QB["Hole_Current"].tolist()

# Specify the range of Z values for the n-side quantum barrier and
the corresponding composition, strain, and hole current
nside_QB = unidf[(unidf["z"] > 4.1e-6) & (unidf["z"] < 4.7e-6)]
Comp_n = nside_QB["Comp"].tolist()
Strain_n = nside_QB["Strain"].tolist()
Jns_n = nside_QB["Electron_Current"].tolist()

# Color scheme to be used for density scatter plots
white_viridis = LinearSegmentedColormap.from_list('white_viridis',
[
    (0, '#ffffff'),
    (1e-20, '#440053'),
    (0.2, '#404388'),
    (0.4, '#2a788e'),
    (0.6, '#21a784'),
    (0.8, '#78d151'),
    (1, '#fde624'),
], N=256)

mpl.rcParams['ps.fonttype'] = 42
mpl.rcParams['pdf.fonttype'] = 42
mpl.rcParams['font.family'] = 'Arial'
plt.rcParams['font.size'] = '8'

#%% Make Hole Current vs In Fraction correlation figure

fig1 = plt.figure(figsize=(1.9,1.8), dpi=600)
ax1 = fig1.add_subplot(1, 1, 1, projection = 'scatter_density')
density1 = ax1.scatter_density(Comp_p, Jps_p)
ax1.scatter_density(Comp_p, Jps_p, cmap=white_viridis)
fig1.colorbar(density1, label = 'Number of points per pixel',
orientation = 'vertical', pad = 0)
ax1.tick_params(axis='both', which='major', direction='in', length
= 5, pad = 5, bottom = True, top = True, left = True, right = True)
ax1.tick_params(axis='both', which='minor', direction='in', length
= 2, pad = 5, bottom = True, top = True, left = True, right = True)
ax1.set_xlim(0, 0.1)
```

```
ax1.set_ylim(0,0.08)
ax1.set_xticks(np.arange(0,0.15,0.05))
ax1.set_xticks(np.arange(0,0.1,0.01), minor = True)
ax1.set_yticks(np.arange(0,0.08,0.01), minor = True)
ax1.set_xlabel('Indium fraction')
ax1.set_ylabel('Hole current (A cm$^{-2}$)')
# fig1.savefig('Jp_In_correlation.png', bbox_inches = 'tight')

#%% Make Electron Current vs In Fraction correlation figure

fig2 = plt.figure(figsize=(1.9,1.8), dpi=600)
ax2 = fig2.add_subplot(1, 1, 1, projection = 'scatter_density')
density2 = ax2.scatter_density(Comp_n, Jns_n)
ax2.scatter_density(Comp_n, Jns_n, cmap=white_viridis)
fig2.colorbar(density2, label='Number of points per pixel',
orientation = 'vertical', pad = 0)
ax2.tick_params(axis='both', which='major', direction='in', length
= 5, pad = 5, bottom = True, top = True, left = True, right = True)
ax2.tick_params(axis='both', which='minor', direction='in', length
= 2, pad = 5, bottom = True, top = True, left = True, right = True)
ax2.set_xlim(0, 0.1)
ax2.set_ylim(0,0.08)
ax2.set_xticks(np.arange(0,0.15,0.05))
ax2.set_xticks(np.arange(0,0.1,0.01), minor = True)
ax2.set_yticks(np.arange(0,0.08,0.01), minor = True)
ax2.set_xlabel('Indium fraction')
ax2.set_ylabel('Electron current (A cm$^{-2}$)')
# fig2.savefig('Jn_In_correlation.png', bbox_inches = 'tight')


#%% Make Strain vs In Fraction (p-side) correlation figure

fig3 = plt.figure(figsize=(1.9,1.8), dpi=600)
ax3 = fig3.add_subplot(1, 1, 1, projection = 'scatter_density')
density3 = ax3.scatter_density(Comp_p, Strain_p_scaled)
ax3.scatter_density(Comp_p, Strain_p_scaled, cmap=white_viridis)
fig3.colorbar(density3, label = 'Number of points per pixel',
orientation = 'vertical', pad = 0)
ax3.tick_params(axis='both', which='major', direction='in', length
= 5, pad = 5, bottom = True, top = True, left = True, right = True)
ax3.tick_params(axis='both', which='minor', direction='in', length
= 2, pad = 5, bottom = True, top = True, left = True, right = True)
ax3.set_xlim(0, 0.1)
ax3.set_ylim(-1, 7)
ax3.set_xticks(np.arange(0,0.15,0.05))
ax3.set_xticks(np.arange(0,0.1,0.01), minor = True)
ax3.set_yticks(np.arange(-1,7,1), minor = True)
ax3.set_xlabel('Indium fraction')
ax3.set_ylabel('$\epsilon_{zz}$ (10$^{-3}$)')
# fig3.savefig('Strainzz_In_correlation.png', bbox_inches =
'tight')
```

B. Characterization of Blue Peak in Red LEDs

One prominent feature of many red LED devices presented Chapter 6 is a peak at approximately 410 nm seen in EL. An example of a device with this peak is the 3.0 nm QW LED shown in Fig. 6.7. The presence of the blue emission peak in red devices has been intermittent and its origin has yet to be identified. It was observed that this peak is present in long-wavelength LEDs grown on both silicon and sapphire substrates. Many experiments were conducted to identify the origin and minimize or eliminate the peak. Several studies targeted SL growth conditions, testing the hypothesis that the emission was coming from the low indium composition InGaN layers in that region. However, removing the TMI flow in the SL had no impact on the wavelength or intensity of the blue peak, indicating that this InGaN layer does contribute to blue emission. Other experiments included varying the *p*-GaN growth temperature, electron blocking layer Mg-doping, spacer thickness between the SL and active region, SL growth temperature, SL Si-doping, SL period, and QW thickness. None of these experiments yielded evidence pointing to the origin of the blue peak.

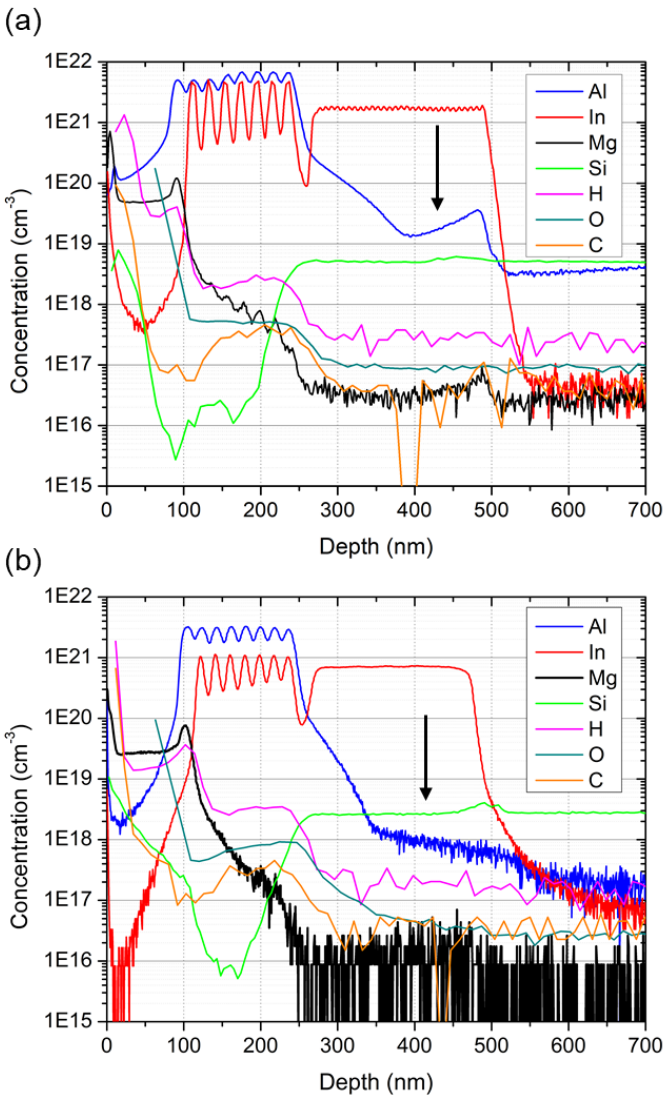

Figure B.1. SIMS measurements of LEDs on silicon that (a) showed and (b) did not show a blue emission peak in EL. The arrows highlight the region where the background aluminum signal is high in part (a) and low in part (b).

Secondary ion mass spectroscopy (SIMS) measurements on LEDs with and without a prominent blue peak did not show a significant difference in the concentration of carbon or oxygen atmospheric impurities. One observed difference however was the aluminum profile. Two LEDs grown on sapphire and four LEDs grown on silicon which displayed the blue peak were measured by SIMS. All six samples had a similar aluminum profile with a plateau

that extended through almost the full depth of the SL. Figure B.1(a) shows the SIMS measurements for one of the LEDs on silicon with a blue peak. To date, only one LED without the blue peak, which was grown on silicon, has been measured by SIMS [Fig. B.1(b)]. In contrast with the aluminum profile shown in Fig. B.1(a), this sample does not have the same high [Al] throughout the entire SL region. This is highlighted as one observation that could be investigated further to determine whether there is a real correlation between the aluminum profile and the blue peak.

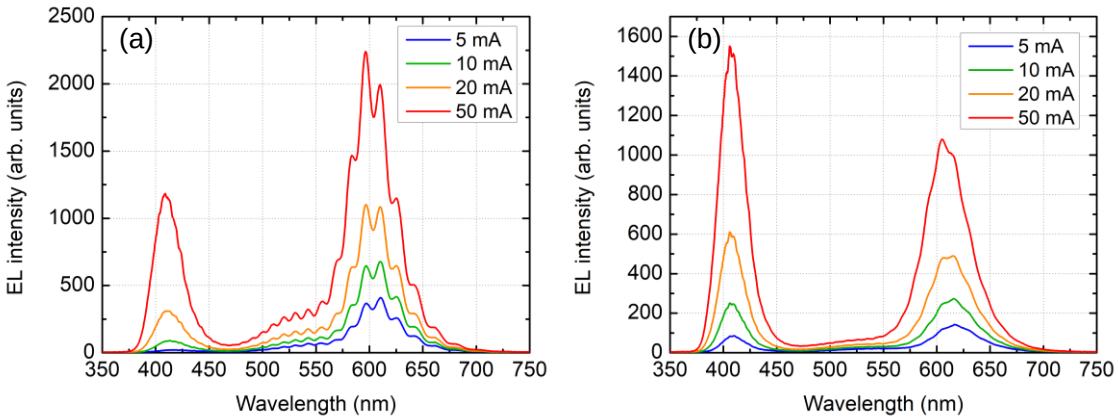

Figure B.2. EL spectra measured at 5, 10, 20, and 50 mA by quick test for red LEDs on (a) silicon and (b) sapphire substrates. The intensity of the blue peak increases with current for both cases. For the LED on sapphire, the blue peak intensity exceeds that of the QW peak at 20 and 50 mA.

Another feature of the blue peak is that its EL intensity relative to QW luminescence increases with drive current. The quick test EL spectra from 5 to 50 mA for LEDs on silicon and sapphire are shown in Fig. B.2(a) and Fig B.2(b), respectively. In the case of the LED on sapphire, the blue peak intensity exceeds that of the QW peak at 20 and 50 mA. This effect was also observed in processed devices which had a prominent blue peak. In those samples, the blue emission was approximately 20% as intense as the QW emission at peak

EQE and became more intense than the QW emission in the current density range of 70-100 A cm^{-2} (Fig. B.3).

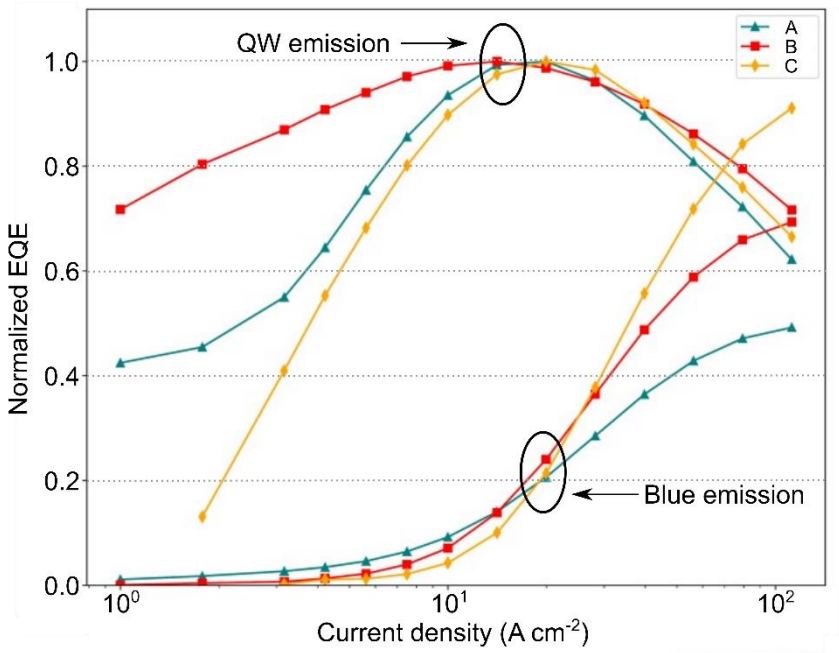

Figure B.3. Normalized EQE curves for three processed LED devices. The top curves correspond to the QW emission contribution to the measured EQE while the bottom curves correspond to the blue emission.

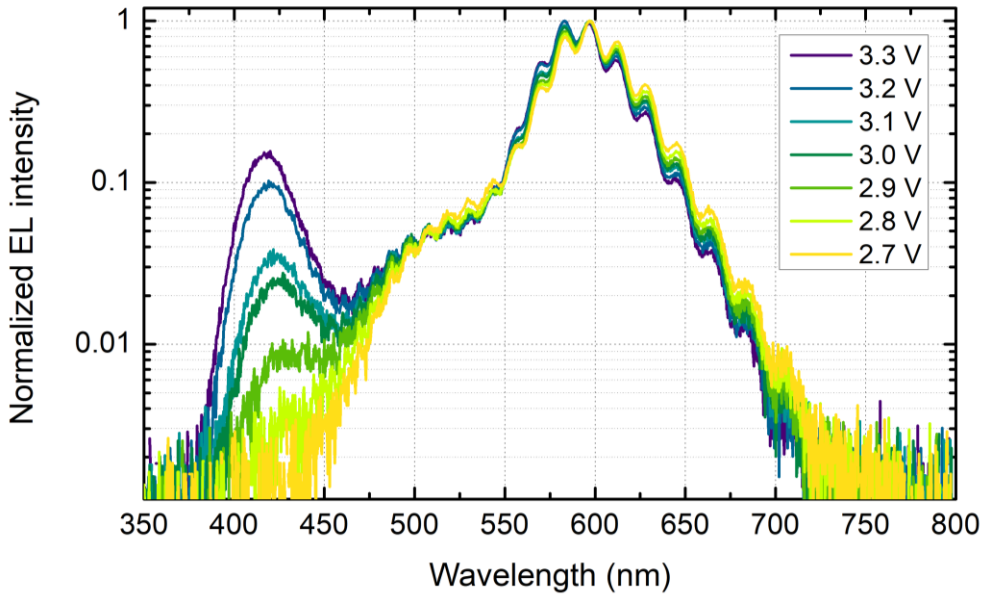

Figure B.4. Log scale normalized EL intensity spectra from 2.7 to 3.3 V. The turn-on voltage of the blue peak is seen to occur at approximately 2.9 V.

Figure B.4 shows normalized EL spectra on a log scale collected at different applied voltages for a processed red LED sample. The voltage was increased from 2.7 to 3.3 V in increments of 0.1 V and the EL spectra was recorded at each point. This range of applied voltages corresponded to a current range of 2.0 to 12.1 mA. The curves were normalized based on the QW peak emission. From these data, the turn-on voltage of the blue peak found to occur at approximately 2.9 V.

While the origin of the blue peak has not been conclusively identified, the characterization data presented in this appendix represent a starting point from which to build upon.